Assessment of the Seismic Performance of Inadequately Detailed Reinforced Concrete Columns

A Thesis
submitted in partial fulfilment
of the requirements for the Degree
of
Master of Engineering
at the
University of Canterbury
by
Alistair Boys

University of Canterbury
Christchurch, New Zealand
2009

Abstract

Currently in NZ, there is a significant proportion of building stock designed prior to 1995 with inadequate transverse reinforcement in the reinforced concrete columns. Recent earthquakes (such as the 1994 Northridge and 1999 Kocaeli earthquakes) and research has highlighted the susceptibility of these columns to lose shear and axial load carrying capacity. In view of the current focus in New Zealand towards assessing and upgrading the performance of existing structures, a model to quantify the performance of these columns is required.

Special focus in this research is towards the performance of columns designed to support gravity only as these 'gravity' columns did not have the detailing requirements associated with the lateral force resisting system. Previous research has typically focused on the performance of these columns under in-plane seismic actions only. To increase the understanding of these columns it is necessary to extend the current research to capture the full bi-directional performance.

In this thesis, results of experimental investigations performed on representative Reinforced Concrete columns are discussed. The investigation consisted of uni- and bi-directional tests performed on six cantilever 'gravity' columns. Two detailing configurations were tested under three different loading protocols; uni-directional quasi-static, bi-directional quasi-static, and bi-directional quasi-earthquake loading. The test specimens are representative of columns designed to carry gravity only, constructed during the period from the introduction of deformed bars in the mid 1960's through to the early 1990's.

An assessment of existing capacity models is carried out for the uni-directional tests and then extended for bi-directional loading. The adequacy of the proposed 'Limit Surface Model' is verified using the quasi-earthquake tests to ensure the appropriateness of the model under realistic displacement histories. Additionally, a conservative 'Simplified Backbone Model' is proposed and assessed.

Acknowledgements

Firstly I would like to thank the University of Canterbury and especially my supervisors, Professor Des Bull and Dr Stefano Pampanin for their excellent critical input and direction when I lacked focus.

Considerable assistance was provided by the technical staff in the civil engineering laboratory at the University of Canterbury. Particular gratitude is due to John Maley; without his help and technical advice this research would not have been possible.

Financial support for the project was provided by the NZ Foundation for Research, Science and Technology, this support was invaluable to the project and sincere thanks are necessary.

Finally the help from my fellow postgraduate students and support from my friends and family is gratefully acknowledged.

Table of contents:

1.0 Introduction 1-1
1.1 General 1-1
1.2 Research Objectives 1-2
1.3 Thesis Outline 1-3
2.0 Review of Relevant Literature 2-1
2.1 Introduction 2-1
2.2 Assessment Procedures 2-1
2.2.1 NZSEE Assessment Guidelines 2-2
2.2.2 FEMA 356 2-6
2.3 Specific Research into inadequately detailed RC columns 2-10
2.3.1 Shear Failure 2-10
2.3.2 Axial Failure 2-12
2.3.3 Empirical Backbone 2-13
2.3.4 Splice Capacity and Type of Failure 2-16
3.0 Specimen Design and Loading Protocols 3-1
3.1 Specimen Selection 3-1
3.2 Experimental Setup and Data Acquisition 3-3
3.2.1 Test Apparatus 3-3
3.2.2 Instrumentation and Data Acquisition 3-4
3.3 Construction 3-5
4.0 Experimental Results for Uni-Directional Tests 4-1
4.1 Uni-directional Quasi-static Protocol 4-1
4.2 Material Testing 4-1
4.3 Specimen 24L-300-2D 4-2
4.3.1 Test Observations 4-2
4.3.2 Force versus Drift Response 4-3
4.4 Specimen 30L-300-2D 4-5
4.4.1 Test Observations 4-5
4.4.2 Force versus Drift Response 4-6
4.5 Relative Contributions to Displacement 4-7
4.6 Key Results 4-9
4.7 Comparison with Seismic Assessment Models 4-10
4.7.1 Shear Capacity Models 4-10
4.7.2 Drift Limit Models 4-13
5.0 Experimental Results for Bi-Directional Tests 5-1
5.1 Bi-directional Quasi-static Protocol 5-1
5.2 Material Testing 5-2
5.3 Specimen 24L-300-3D 5-3
5.3.1 Test Observations 5-3
5.3.2 Force versus Drift Response 5-4
5.4 Specimen 24L-300-3D-R 5-6
5.4.1 Test Observations 5-6
5.4.2 Force versus Drift Response 5-7
5.5 Specimen 30L-300-3D 5-8
5.5.1 Test Observations 5-8
5.5.2 Force versus Drift Response 5-10
5.6 Relative Contributions to Displacement 5-11
5.7 Model Development and Experimental Comparisons 5-15

5.7.1 Limits Surface Model for Bi-Directional Loading 5-15
5.7.2 Limit Surface Model Comparisons 5-16
5.7.3 Simplified Backbone Model for Bi-Directional Loading 5-19
5.7.4 Simplified Backbone Model Comparisons 5-20
6.0 Experimental Results for Quasi-Earthquake Test 6-1
6.1 Quasi-Earthquake Protocol 6-1
6.2 Experimental Results for Specimen 24L-300-EQ 6-5
6.2.1 Test Observations 6-5
6.2.2 Relative Contributions to Displacement 6-8
6.2.3 Force versus Drift Response and Comparison with Limit Surface Model 6-9
6.2.4 Simplified Backbone Model Comparisons 6-11
7.0 Model Performance and Implementation 7-1
7.1 Model Performance 7-1
7.2 Consequences of Relative Stiffness 7-2
7.3 Simplified Assessment of Existing Structures 7-4
7.4 Assessment using Non-Linear Time History Analysis 7-5
7.4.1 Software Package 7-5
7.4.2 Selection of Hysteresis Model 7-6
7.4.3 Implementation of Shear and Axial Failure Springs 7-7
8.0 Conclusions 8-1
8.1 Global Performance of Columns 8-1
8.2 Adequacy of the Drift Based Failure Models 8-1
8.3 Further Research Required 8-2
Appendix A Material Testing A-1
Appendix B Lateral and Axial Corrections B-1
B.1 Lateral Force and Displacement Corrections B-1
B.2 Axial Correction B-3
Appendix C Sample Model Calculations C-1
C.1 Calculations for specimen 24L-300-2D C-1
Appendix D Instrumentation Results D-1
D.1 Strain-Gauges D-1
D.2 Potentiometer Data D-8
Appendix E Test Photographs E-1
E.1 Construction E-1
E.2 Specimen 24L-300-2D E-2
E.3 Specimen 24L-300-3D E-5
E.4 Specimen 24L-300-3D-R E-10
E.5 Specimen 30L-300-2D E-16
E.6 Specimen 30L-300-3D E-19
E.7 Specimen 24L-300-EQ E-24

List of Figures:

Figure 1-1 California State University parking building, Northridge Earthquake 1994 1-1
Figure 1-2 Consequences of inadequate detailing 1-2
Figure 2-1 Degradation of shear strength with increasing curvature ductility 2-4
Figure 2-2 Generalised component F-d relations for modelling and acceptance criteria 2-8
Figure 2-3 Degradation of shear strength with increasing displacement ductility 2-10
Figure 2-4 Variability of displacement at shear failure inherent in shear strength model... 2-11
Figure 2-5 Drift capacity model for shear failure 2-12
Figure 2-6 FBD of the shear failure plane assumed in the axial failure model 2-13
Figure 2-7 Proposed backbone model..... 2-14
Figure 2-8 Shake-table test results compared with backbone model and FEMA 356..... 2-16
Figure 2-9 Notations for capacity equations and illustration of splitting failure modes 2-19
Figure 2-10 Potential failure modes for rectangular and circular members 2-20
Figure 3-1 Details of test specimens..... 3-2
Figure 3-2 Elevation of Experimental Apparatus 3-3
Figure 3-3 Experimental apparatus with test specimen 3-4
Figure 3-4 Configuration of strain gauges..... 3-4
Figure 3-5 Configuration of potentiometers 3-5
Figure 3-6 Base-block reinforcing steel, formwork and concrete casting..... 3-6
Figure 3-7 Lap-splice detail at column base with strain gauges attached..... 3-6
Figure 3-8 Column prior to and during casting 3-6
Figure 4-1 Uni-directional drift protocol 4-1
Figure 4-2 Damage sequence for specimen 24L-300-2D 4-3
Figure 4-3 Experimental Data for Specimen 24L-300-2D 4-4
Figure 4-4 Damage sequence for specimen 30L-300-2D 4-5
Figure 4-5 Experimental Data for Specimen 30L-300-2D 4-6
Figure 4-6 Comparative Specimen Damage @ 2% Drift Cycles 4-9
Figure 4-7 Relative Contributions to Total Displacement for Specimen 24L-300-2D 4-8
Figure 4-8 Relative Contributions to Total Displacement for Specimen 30L-300-2D 4-8
Figure 4-9 Effect of splice length on damage sustained..... 4-10
Figure 4-10 Shear strength model comparisons for Specimen 24L-300-2D 4-11
Figure 4-11 Impact of variability on Sezen model 4-12
Figure 4-12 Effect of yield displacement on Sezen Shear Strength model 4-12
Figure 4-13 Determination of yield drift for Sezen Model..... 4-13
Figure 4-14 Illustration of the FEMA 356 backbone..... 4-14
Figure 4-15 Backbone model and limit comparisons for Specimen 24L-300-2D..... 4-15
Figure 4-16 Elwood Backbone model comparison for specimen 24L-300-2D..... 4-16
Figure 4-17 Elwood Backbone model comparison for specimen 30L-300-2D..... 4-17
Figure 5-1 Bi-directional loading protocol 5-1
Figure 5-2 Components of bi-directional loading protocol 5-2
Figure 5-3 Damage sequence of specimen 24L-300-3D 5-4
Figure 5-4 Experimental data for specimen 24L-300-3D..... 5-5
Figure 5-5 Damage sequence of specimen 24L-300-3D-R 5-7
Figure 5-6 Test results for specimen 24L-300-3D-R..... 5-8
Figure 5-7 Damage sequence of specimen 30L-300-3D 5-9
Figure 5-8 Test results for specimen 30L-300-3D..... 5-10
Figure 5-9 Illustration of plane sections 5-11
Figure 5-10 Contributions to Total Displacement for Specimen 24L-300-3D..... 5-12
Figure 5-11 Contributions to Total Displacement for Specimen 30L-300-3D..... 5-13

Figure 5-12 Damage Comparison between Specimens 24L-300-3D and 30L-300-3D 5-13
Figure 5-13 Contributions to Total Displacement for Specimen 24L-300-3D-R..... 5-14
Figure 5-14 Backbone calculated for in-plane and 45° loading with fitted limit curve 5-15
Figure 5-15 Limit Surface Model comparisons for specimen 24L-300-3D 5-16
Figure 5-16 Limit Surface Model comparisons for specimen 24L-300-3D-R 5-17
Figure 5-17 Limit Surface Model comparisons for specimen 30L-300-3D 5-18
Figure 5-18 Backbone for 45° loading resolved to in-plane component 5-19
Figure 5-19 Derivation of simplified backbone model using Specimen 24L-300-3D 5-20
Figure 5-20 Model comparisons for specimen 24L-300-3D 5-21
Figure 5-21 Model comparisons for specimen 24L-300-3D-R 5-22
Figure 5-22 Model comparisons for specimen 30L-300-3D 5-22
Figure 6-1 Illustration of Limit Surface for specimen 24L-300-EQ..... 6-1
Figure 6-2 Model of specimen 24L-300-EQ 6-2
Figure 6-3 Hysteresis properties of the inelastic spring used in simplified model..... 6-2
Figure 6-4 Quasi-earthquake protocol with modelled drift limit surface 6-4
Figure 6-5 Principal components of the Quasi-EQ protocol 6-4
Figure 6-6 Loading protocol and photographic sequence for specimen 24L-300-EQ 6-5
Figure 6-7 Photographic sequence of damage sustained prior to 1st large drift 'peak' 6-6
Figure 6-8 Damage sustained by specimen at 1st large drift 'peak' (shear failure) 6-7
Figure 6-9 Damage sustained by specimen at 2nd large drift 'peak'..... 6-7
Figure 6-10 Damage sustained by specimen at 3rd large drift 'peak' 6-8
Figure 6-11 Photographs of the damage the specimen sustained at axial failure 6-8
Figure 6-12 Contributions to Total Displacement for Specimen 24L-300-EQ 6-9
Figure 6-13 Experimental results for specimen 24L-300-EQ..... 6-10
Figure 7-1 Comparison between assumed and realistic displacement profile..... 7-3
Figure 7-2 Typical hysteresis rule and moment-axial interaction surface for NLTHA..... 7-6
Figure 7-3 Representation of the shear and axial failure springs..... 7-7
Figure 8-1 Probabilistic backbone model (Elwood and Moehle 2006)..... 8-2

List of Tables:

Table 2-1 Structural Performance Levels and Requirements (FEMA356) 2-7
Table 2-2 Effective stiffness values (Table 6-5 FEMA356)..... 2-8
Table 2-3 Modelling parameters and Acceptance criteria for RC columns (FEMA356)..... 2-9
Table 3-1 Experimental Program..... 3-2
Table 4-1 Summary of material properties for unidirectional test specimens 4-2
Table 5-1 Summary of material properties for all test specimens 5-2
Table 6-1 Summary of material properties for the Quasi-Earthquake test specimen 6-1

1.0 Introduction

1.1 General

Currently, it is widely recognised that reinforced concrete (RC) columns with inadequate transverse reinforcement perform poorly during seismic events. This is evident in post-earthquake photographs from events such as the Northridge earthquake in 1994. Figure 1-1 shows the failure of the internal gravity columns and the consequences of this failure. This has resulted in an increasing number of investigations into the seismic performance of these columns, notably the work carried out under the Pacific Earthquake Engineering Research (PEER) program in the United States.

a) Internal view of collapsed columns **b) Exterior view of consequences**

Figure 1-1 California State University parking building, Northridge Earthquake 1994 (Photographs courtesy of EERC Library)

In New Zealand (NZ) a significant proportion of reinforced concrete (RC) buildings designed prior to 1995 contain columns (particularly those designed to support gravity loads only) with insufficient transverse reinforcement. These columns have been shown (by seismic events and research) to be susceptible to shear failure and subsequent loss of axial capacity. Additionally, columns constructed in NZ during this period typically have lap-splices at the base of the columns, with cranks in the longitudinal reinforcing bars at the end of the splice. As a consequence these columns are also potentially susceptible to:

1. Buckling failure of the crank, particularly if sufficient lateral restraint is not provided by stirrups at the upper end of the crank.
2. Degradation of tension capacity of the lap-splice during cyclic loading.
3. Expulsion of the cover induced by splitting of the concrete at the splice.

Figure 1-2 a) illustrates the likely consequence of poorly restrained lap-splices, and Figure 1-2 b) shows the more general consequences of inadequate transverse reinforcement.

a) Consequences of lap-splice failure
Indian Hills Medical Centre, Northridge, 1994
(Photograph courtesy of NZSEE)

b) Consequences of insufficient transverse steel
Olive View Hospital, Sylmar, 1971
(Photograph courtesy of EERC Library)

Figure 1-2 Consequences of inadequate detailing

Typically, research into these columns has concentrated on uni-directional loading, with considerably less emphasis on the effects of bi-directional loading. For the most part previous research has had minimal focus on lap-splices and does not consider the NZ norm of using cranked bars at the top of the splice. The testing to date is has been predominantly performed under quasi-static loading protocols, which are perceived to be excessively demanding for structural elements with inadequate detailing.

1.2 Research Objectives

The research presented in this thesis aims to extend the understanding of the performance of these inadequately detailed RC columns with a focus on NZ specific typologies but with outcomes easily generalised for all similar structures worldwide. The main objectives of the research are outlined below:

- Compare the performance of the variety of capacity models available in the various assessment guidelines

- Verify the drift based models for shear and axial failure under uni-directional loading
- Extend the existing uni-directional drift based assessment models for assessment of bi-directional loading effects
- Identify load and detailing dependent failure mechanisms such as bar buckling, lap-splice degradation and splitting, and associated expulsion of the cover concrete.
- For each of the failure mechanisms determine displacement based limits to enable the hierarchy of significant events to be assessed, and illustrate the performance consequences of each failure mechanism.
- Calibrate an appropriate hysteresis rule for use in Non-Linear Time History Analysis (NLTHA), and implement shear and axial failure springs thereby allowing full behaviour of the columns to be assessed (including the potential for load redistribution after axial failure has occurred).

1.3 Thesis Outline

This thesis is comprised of nine chapters, progressing from a review of the relevant literature, to design of the experimental program and subsequently assessing the performance of the specimens and the ability of the various models to capture the behaviour exhibited. Further investigations are made into the implementation of the performance models into NLTHA and the consequences of structural configuration.

Chapter 2 comprises a summary of the literature relevant to the columns of interest. The first section investigates the recommendations of two specific assessment procedures and guidelines (NZSEE Assessment Guidelines and FEMA 356). For these procedures an overview of the complete process of assessing buildings is investigated, followed by the recommendations regarding modelling the columns of interest. The second section summarises specific research into the performance of these columns with regard to; shear and flexural capacity, likely drift limits for shear and axial failure, and the capacity and failure mechanisms associated with inadequately detailed lap-splices.

Design of the experimental program is outlined in chapter 3. Included in this section are the design of the test specimens, experimental configuration, applied loading, and the data acquisition system, followed by a sequence of construction photographs. Six cantilever column specimens with two detailing configurations are proposed, with testing under uni-

and bi-directional loading protocols. All six specimens represent columns designed to carry gravity load only (i.e. internal columns nominally considered separate from the lateral force resisting system by designers), designed with minimum transverse reinforcement and detailing allowable by NZ codes (NZS 1900, 1964 for example) in the period from 1964 (corresponding to the introduction of deformed bars) to 1995 when the code requirements for these columns were made more stringent.

Chapters 4, 5, and 6, report on the experimental results from the uni-directional, bi-directional, and quasi-earthquake loading protocols respectively. In each of these chapters, the first section develops the applied loading protocols, followed by the material testing of the specimens. The following section presents the force-displacement results for each specimen in addition to photographs illustrating key events in the degradation and subsequent failure of the columns. Performance comparisons are made for the columns with differing detailing provisions, illustrating the effects of the provided lap-splice length. The chapters also investigate contributions to the displacement of the column as the tests progress. The displacements are separated into contributions from rotation at the base of the column and the residual contribution from both flexure and shear.

Comparisons between the experimental results and the various models outlined in Chapter 3 are presented at the end of Chapters 4 to 6. The performance of the models presented in the assessment guidelines (NZSEE and FEMA 356) are shown to be overly conservative. The uni-directional drift-based models for shear and axial failure are verified and then extended to bi-directional loading. Finally, a failure limit surface model for bi-directional loading is developed and then verified with the data from the quasi-earthquake test specimen.

Chapter seven is separated into two main sections. The first section summarises the performance of the proposed backbone model and the associated drift limit curve for bi-directional loading. In conjunction with the performance assessment the limitation of the assumed displacement profile is illustrated and an approach for mitigation is presented. The second section outlines the application of the models for the assessment of existing structures. It is proposed that a preliminary assessment of a structure is made using the ‘Simplified Backbone Model’ with further modelling using NLTHA and the full ‘Limit Surface Model’.

Recommendations are also made regarding the appropriate NLTHA techniques and modelling of the hysteretic behaviour of the members. The implementation of shear and axial failure springs is discussed along with the implications of extending these springs to full 3D failure limits. This will enable the post axial-failure performance of the structure to be assessed; especially with regard to the potential for load redistribution to adjacent elements.

Conclusions from this research are presented in Chapter 8. The global performance of inadequately detailed columns is summarised, illustrating the potential to lose axial capacity at levels of drift lower than would be acceptable in a design level earthquake. A summary of the validity and performance of the proposed models is made. Finally recommendations are made regarding further research, to enable a more probabilistic approach to column performance.

2.0 Review of Relevant Literature

2.1 Introduction

There is a considerable quantity of relevant previous research on the assessing the seismic performance of existing structures in general, and specifically on the various failure mechanisms these inadequately detailed RC columns are susceptible to. This literature can be broken into two categories. The first category consists of documents produced by various international organisations, and the second being specific research into the performance of inadequately detailed sub-assembly specimens. To reflect these distinct categories the review is broken into corresponding sections. Typically, the guidelines offer recommendations on the assessment process, including data collection of in-situ material properties, modelling the structure, and the various analysis techniques available. Recommendations are made as to the likely lower bound and characteristic strengths of materials when actual values are not available.

2.2 Assessment Procedures

There are a number of guidelines for assessing existing buildings currently in use worldwide; these include NZSEE Assessment Guidelines (2006), FEMA 356 (2000), and ATC 40 (1996). Typically, these guidelines are holistic in their approach to the problem of assessing existing structures, with minimal specific advice on the performance of individual structural components. Two of these will be considered in full (NZSEE and FEMA 356).

Note that prior to the submission of this thesis FEMA 356 has been superseded by ASCE 41 Supplement 1 (2007), which makes a significant number of changes to the assessment of RC columns during seismic events. This thesis will not specifically consider ASCE 41 but recommends the reader to compare the outcomes and conclusions with the procedures set out in the supplement.

2.2.1 NZSEE Assessment Guidelines

As a result of changes to the New Zealand Building Act 2004 extending the range of buildings deemed to be earthquake-prone, the New Zealand Society for Earthquake Engineering (NZSEE) produced a report entitled, "Assessment and Improvement of the Structural Performance of Buildings in Earthquakes" (2006). The aim of these recommendations is to enable Territorial Authorities and engineers to assess and classify existing buildings in terms of the expected performance during earthquakes.

The guidelines outline the following process to prioritise remediation of at risk buildings:

1. A two-stage assessment process of Initial Evaluation with a subsequent Detailed Assessment if required.
2. Recommendations regarding possible Improvement Measures and minimum requirements for upgraded performance.

The Initial Evaluation process involves estimating the likely structural performance of a building during an earthquake and quantifying the performance given the, building; typology, era, location, and soil classification. Building performance is measured against the current earthquake design code (NZS1170.5:2004) and quantified as the "percentage of new building standard" (%NBS). Results of the Initial Evaluation procedure are categorised as follows (verbatim from the guidelines):

- A %NBS of 33 or less means that the building is assessed as potentially Earthquake Prone in terms of the Building Act and a more detailed evaluation of it will typically be required.
- A %NBS of greater than 33 means that the building is regarded as outside the requirements of the Act. No further action on it will be required by law, however it may still be considered as representing an unacceptable risk and further work on it may be recommended.
- A %NBS of 67 or greater means that the building is not considered to be a significant earthquake risk.

Given that a more detailed assessment is required, the guidelines provide recommendations for the assessment of these inadequately detailed RC columns. There are three main facets in the assessment; the material strengths of the RC column, the shear and flexural strengths, and

the moment capacity of the lap-splice. It is recommended that material strengths for the concrete and reinforcing steel are obtained by testing where possible. In lieu of test data, a conservative estimate of the probable concrete strength is 1.5 times the nominal compressive strength, and for the period encompassing 1930-1970 the approximate mean value for the yield strength of structural grade steel may be taken as 300 MPa.

Flexural strength of a section should be determined using the appropriate material strengths and moment-curvature analysis of the section. Shear strength of a section may be calculated as the sum of the contributions from the concrete mechanism, transverse steel and the applied axial load as given by Equation (2-1). The reduction factor incorporates a factor of 0.85 to capture the lower bound value of the experimental data used to validate the model. An additional strength reduction factor of 0.85 is applied to ensure a conservative estimation of the shear strength.

$$V_p = 0.72\left(V_c + V_s + V_n\right) \quad \text{(MPa)} \qquad (2\text{-}1)$$

The shear force resisted by the concrete mechanism is given by:

$$V_c = v_c 0.8 A_g \qquad (2\text{-}2)$$

$$v_c = k\sqrt{f_c'} \qquad (2\text{-}3)$$

Where:

v_c = nominal shear stress carried by the concrete mechanism

k = degradation factor based on member curvature ductility (given by relationships illustrated in Figure 2-1)

f'_c = compressive strength of concrete

Shear resistance provided by the transverse steel assumes a shear failure plane at an angle of 30° to the longitudinal axis of the column and is given by:

$$V_s = \frac{A_v f_{yt} d''}{s} \cot 30° \qquad (2\text{-}4)$$

Where:

A_v = total effective area of transverse steel crossing the failure plane (in the direction of the applied shear)

f_{yt} = yield strength of transverse reinforcement

s = spacing of transverse reinforcement

d'' = Depth of the concrete core measured parallel to the applied shear

The contribution of axial load to the shear strength is given by:

$$V_n = N.\tan\alpha \tag{2-5}$$

Where:

α = the angle between the centre of the compressive stress blocks at the top and the base of the column (use centre-line at top for cantilever tests)

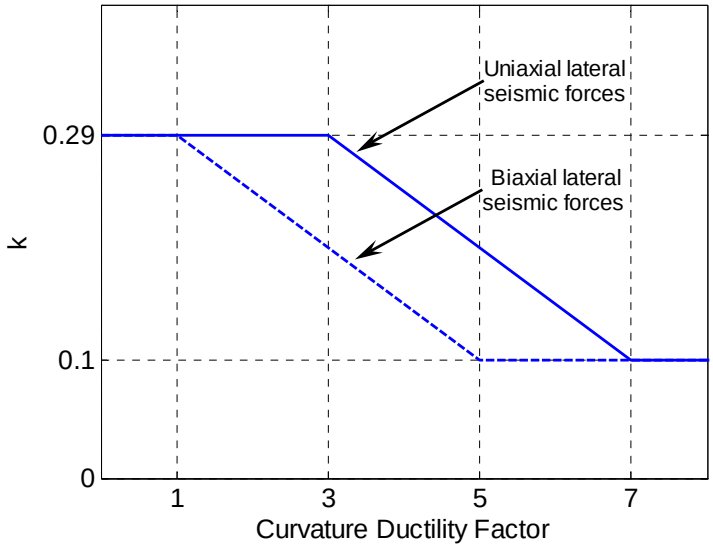

Figure 2-1 Degradation of shear strength with increasing curvature ductility (NZSEE2006)

An upper limit to the available curvature ductility of columns with inadequate transverse reinforcement can be calculated using Equation (2-6) below. This equation is referenced from the Concrete Structures Standard (Eq C8-4 NZS3101:1995), and is used to determine the required volumetric ratio of transverse reinforcement for a given column. By rearranging the relationship and incorporating the relevant parameters, a conservative estimate of the available ductility can be made.

$$\frac{A_{sh}}{S_h h''} = \left\{ \frac{A_g}{A_c} \frac{\left\{ \left(\varphi_u / \varphi_y \right) - 33\rho_t m + 22 \right\}}{111} \frac{f_c'}{f_{yt}} \frac{N^*}{\phi f_c' A_g} \right\} - 0.006 \qquad (2\text{-}6)$$

Where:

A_{sh} = total area of transverse reinforcement in direction of consideration, at spacing, s_h

s_h = centre-to-centre spacing of transverse reinforcement

h'' = dimension of the concrete core perpendicular to transverse reinforcement, measured to the outside of the peripheral hoops

A_g = gross area of section

A_c = area of concrete core, measured to the outside of peripheral hoops

φ_u/φ_y = curvature ductility factor

ρ_t = ratio of longitudinal column reinforcement = A_{st}/A_g

m = $f_y/0.85f_c'$

f_c' = concrete compressive strength

f_{yt} = yield strength of transverse reinforcement

N^* = design axial load

Moment capacity of the lap-splice connections at the base of the columns (M_{lap}) is calculated initially as a function of the full moment capacity (M_n) and the splice length provided. A final moment capacity (M_f) is also calculated assuming that splice failure has occurred, targeting the residual moment capacity of the spliced connection.

$$M_{lap} = M_n - \frac{\vartheta_p}{0.025}\left(M_n - M_f\right) \qquad (2\text{-}7)$$

Where:

$M_f \le M_{lap} \le M_n$

ϑ_p = plastic rotation demand on the section

M_f = greater of:

$$M_f = \begin{cases} \dfrac{l_{lap}}{l_d} M_n \\ \\ 0.5N(D-a) \end{cases} \tag{2-8}$$

There are a number of limitations in this process with regard to buildings with inadequately detailed RC columns. Firstly the steps in the Initial Evaluation process do not specifically calculate the available ductility for the columns of interest. Instead the suggested approach is based on reconfiguring a design equation that is inherently conservative. Secondly the detailed procedure typically focuses on lateral strength/moment capacity, with little regard to the displacement dependent failure mechanisms of these columns. And finally the focus is primarily on in-plane uni-directional behaviour of the columns.

2.2.2 FEMA 356

FEMA 356, entitled "Prestandard and Commentary for the Seismic Assessment of Buildings" (2000), outlines the performance assessment of existing buildings and categorises rehabilitation objectives. The process outline incorporates obtaining as-built information, determining the site-specific seismic hazard, assessing the performance of the structure via one of four analysis procedures; linear static (LSP), linear dynamic (LDP), non-linear static (NSP), non-linear dynamic (NDP). The basic performance requirements will depend on the nature of the building in question but minimum objectives are laid out in Table 2-1 below (only the section relevant to concrete frames is shown).

Structural components are separated into primary and secondary elements. Primary elements are those deemed to provide the lateral capacity of the structure to resist the ground motion induced seismic forces. Secondary elements are those that do not significantly or reliably contribute to the lateral resistance. Inadequately detailed RC columns are best assessed using either of the non-linear analysis procedures (static or dynamic) to enable the effect of the inelastic mechanisms to be assessed on the structural performance of the building as a whole. The following section outlines the default steps in assessing the performance and is conservative in nature, however experimentally validated models may be substituted.

Table 2-1 Structural Performance Levels and Requirements (FEMA356)

Table C1-3 Structural Performance Levels and Damage [1, 2, 3]—Vertical Elements

		Structural Performance Levels		
Elements	**Type**	**Collapse Prevention S-5**	**Life Safety S-3**	**Immediate Occupancy S-1**
Concrete Frames	Primary	Extensive cracking and hinge formation in ductile elements. Limited cracking and/or splice failure in some nonductile columns. Severe damage in short columns.	Extensive damage to beams. Spalling of cover and shear cracking (<1/8" width) for ductile columns. Minor spalling in nonductile columns. Joint cracks <1/8" wide.	Minor hairline cracking. Limited yielding possible at a few locations. No crushing (strains below 0.003).
	Secondary	Extensive spalling in columns (limited shortening) and beams. Severe joint damage. Some reinforcing buckled.	Extensive cracking and hinge formation in ductile elements. Limited cracking and/or splice failure in some nonductile columns. Severe damage in short columns.	Minor spalling in a few places in ductile columns and beams. Flexural cracking in beams and columns. Shear cracking in joints <1/16" width.
	Drift	4% transient or permanent	2% transient; 1% permanent	negligible permanent 1% transient;

1. Damage states indicated in this table are provided to allow an understanding of the severity of damage that may be sustained by various structural elements when present in structures meeting the definitions of the Structural Performance Levels. These damage states are not intended f or use in post-earthquake evaluation of damage or for judging the safety of, or required level of repair to, a structure following an earthquake.
2. Drift values, differential settlements, crack widths, and similar quantities indicated in these tables are not intended to be used as acceptance criteria for evaluating the acceptability of a rehabilitation design in accordance with the analysis procedures provided in this standard; rather, they are indicative of the range of drift that typical structures containing the indicated structural elements may undergo when responding within the various Structural Performance Levels. Drift control of a rehabilitated structure may often be governed by the requirements to protect nonstructural components. Acceptable levels of foundation settlement or movement are highly dependent on the construction of the superstructure. The values indicated are intended to be qualitative descriptions of the approximate behavior of structures meeting the indicated levels.
3. For limiting damage to frame elements of infilled frames, refer to the rows for concrete or steel frames.

Figure 2-2 illustrates the generalised force-deformation relationships (i.e. force-displacement, moment-curvature etc). Point *A* is the unloaded member, point *B* represents yielding of the member with elastic behaviour to this point. The stiffness of the elastic portion of the curve is given in Table 2-2 for the various member types. Point *C* represents the point at which the member loses a significant proportion of capacity (force, moment etc), reduced to residual capacity at *D*, and maintains this capacity until point *E* when complete loss of capacity occurs. Figure 2-2 a) is constructed in terms of rotation or displacement (columns and beams), Figure 2-2 b) is constructed in terms of drift (shear walls), and Figure 2-2 illustrates the desired performance criteria for the different damage states for both primary and secondary elements.

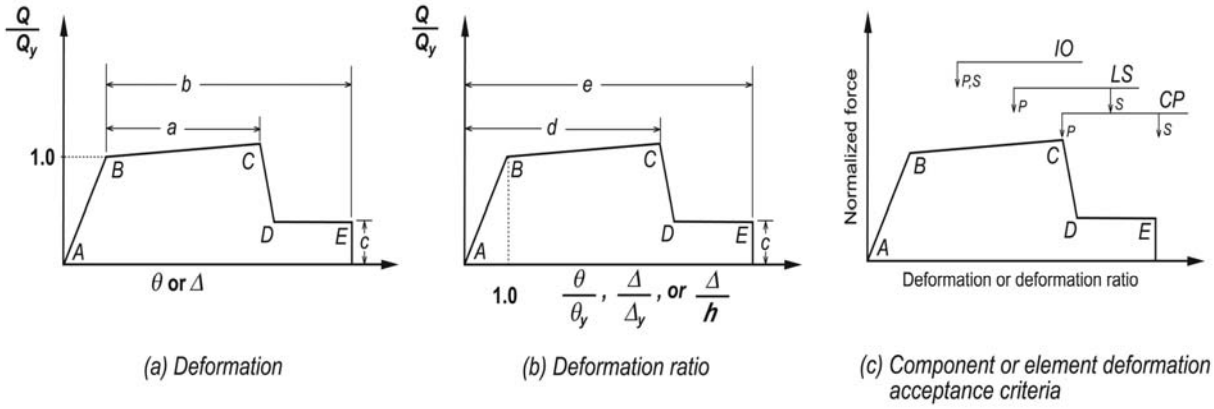

Figure 2-2 Generalised component F-d relations for modelling and acceptance criteria (Taken from Figure C2-1 FEMA356)

Appropriate values for deformation indexes '*a*', '*b*', and '*c*' for 'primary' and 'secondary' RC columns members are given in Table 2-3. The indexes listed correspond to inelastic rotations beyond yield, thus are a measure of ductility. The associated acceptance criteria refer to the maximum allowable inelastic rotations, thus if these values are exceeded during structural analysis the member is deemed not to have "satisfied the required performance level".

Table 2-2 Effective stiffness values (Table 6-5 FEMA356)

Component	Flexural Rigidity	Shear Rigidity	Axial Rigidity
Beams—nonprestressed	$0.5E_cI_g$	$0.4E_cA_w$	—
Beams—prestressed	E_cI_g	$0.4E_cA_w$	—
Columns with compression due to design gravity loads $\geq$0.5 A	$0.7E_cI_g$	$0.4E_cA_w$	E_cA_g
Columns with compression due to design gravity loads $\leq$0.3 A or with tension	$0.5E_cI_g$	$0.4E_cA_w$	E_sA_s
Walls—uncracked (on inspection)	$0.8E_cI_g$	$0.4E_cA_w$	E_cA_g
Walls—cracked	$0.5E_cI_g$	$0.4E_cA_w$	E_cA_g
Flat Slabs—nonprestressed	See Section 6.5.4.2	$0.4E_cA_g$	—
Flat Slabs—prestressed	See Section 6.5.4.2	$0.4E_cA_g$	—

Note: It shall be permitted to take I_g for T-beams as twice the value of I_g of the web alone. Otherwise, I_g shall be based on the effective width as defined in Section 6.4.1.3. For columns with axial compression falling between the limits provided, linear interpolation shall be permitted. Alternatively, the more conservative effective stiffnesses shall be used.

Table 2-3 Modelling parameters and Acceptance criteria for RC columns (Table 6-8 FEMA356)

Conditions			Modeling Parameters[4]			Acceptance Criteria[4]				
			Plastic Rotation Angle, radians		Residual Strength Ratio	Plastic Rotation Angle, radians				
						Performance Level				
							Component Type			
							Primary		Secondary	
			a	b	c	IO	LS	CP	LS	CP
i. Columns controlled by flexure[1]										
$\frac{P}{A_g f_c}$	Trans. Reinf.[2]	$\frac{V}{b_w d\sqrt{f_c}}$								
0.1	C	3	0.02	0.03	0.2	0.005	0.015	0.02	0.02	0.03
0.1	C	6	0.016	0.024	0.2	0.005	0.012	0.016	0.016	0.024
0.4	C	3	0.015	0.025	0.2	0.003	0.012	0.015	0.018	0.025
0.4	C	6	0.012	0.02	0.2	0.003	0.01	0.012	0.013	0.02
0.1	NC	3	0.006	0.015	0.2	0.005	0.005	0.006	0.01	0.015
0.1	NC	6	0.005	0.012	0.2	0.005	0.004	0.005	0.008	0.012
0.4	NC	3	0.003	0.01	0.2	0.002	0.002	0.003	0.006	0.01
0.4	NC	6	0.002	0.008	0.2	0.002	0.002	0.002	0.005	0.008
ii. Columns controlled by shear[1, 3]										
All cases[5]			—	—	—	—	—	—	.0030	.0040
iii. Columns controlled by inadequate development or splicing along the clear height[1,3]										
Hoop spacing d/2			0.01	0.02	0.4	0.005	0.005	0.01	0.01	0.02
Hoop spacing > d/2			0.0	0.01	0.2	0.0	0.0	0.0	0.005	0.01
iv. Columns with axial loads exceeding $0.70P_o$[1, 3]										
Conforming hoops over the entire length			0.015	0.025	0.02	0.0	0.005	0.01	0.01	0.02
All other cases			0.0	0.0	0.0	0.0	0.0	0.0	0.0	0.0

1. When more than one of the conditions i, ii, iii, and iv occurs for a given component, use the minimum appropriate numerical value from the table.
2. "C" and "NC" are abbreviations for conforming and nonconforming transverse reinforcement. A component is conforming if, within the flexural plastic hinge region, hoops are spaced at $d/3$, and if, for components of moderate and high ductility demand, the strength provided by the hoops (V_s) is at least three-fourths of the design shear. Otherwise, the component is considered nonconforming.
3. To qualify, columns must have transverse reinforcement consisting of hoops. Otherwise, actions shall be treated as force-controlled.
4. Linear interpolation between values listed in the table shall be permitted.
5. For columns controlled by shear, see Section 6.5.2.4.2 for acceptance criteria.

Shear capacity of the columns has contributions from the transverse steel provided and the concrete as shown in Equation (2-9). The shear capacity has reduction factors to account for imposed ductility demands (k), and density of the concrete (λ). The ductility capacity reduction factor k varies from 1.0 at low ductility demands to 0.7 for high ductility demands. The concrete contribution to the shear capacity considers the relative magnitude of the applied shear (V) and the resulting moment (M), and the ratio is limited to the range $2 \le M/V < 3$.

$$V_n = k\left[\frac{A_s f_y d}{s} + \lambda k\left(\frac{0.5\sqrt{f_c'}}{M/Vd}\sqrt{1+\frac{N_u}{0.5\sqrt{f_c'}A_g}}\right)0.8A_g\right] \quad \text{(S.I. units)} \qquad (2\text{-}9)$$

Capacity of the lap-splice connection at the base of the columns is given in terms of the ratio of provided splice length to the development length requirements in ACI 318, thus if a splice length is provided with 80% of the required development length the lap-splice may only develop 80% of the yield strength of the spliced longitudinal bars. When splice is provided with transverse reinforcement at spacing not greater than one-third of the section depth then the calculated capacity may be taken for high ductility demands. For larger spacing, the developed stress shall be assumed to degrade to 20% of calculated capacity at ductility requirements greater than 2.0.

2.3 Specific Research into inadequately detailed RC columns

2.3.1 Shear Failure

An investigation into the shear capacity of columns with inadequate transverse reinforcement was carried out by Sezen and Moehle (2004). Experimental data from 50 uni-directional laboratory tests with relevant details was used to derive and empirical model for the degradation of shear capacity with increasing ductility. The relationship derived is dependent on the section dimensions, material properties, transverse detailing provided and the axial load applied (Figure 2-3 and Equation (2-10))**.**

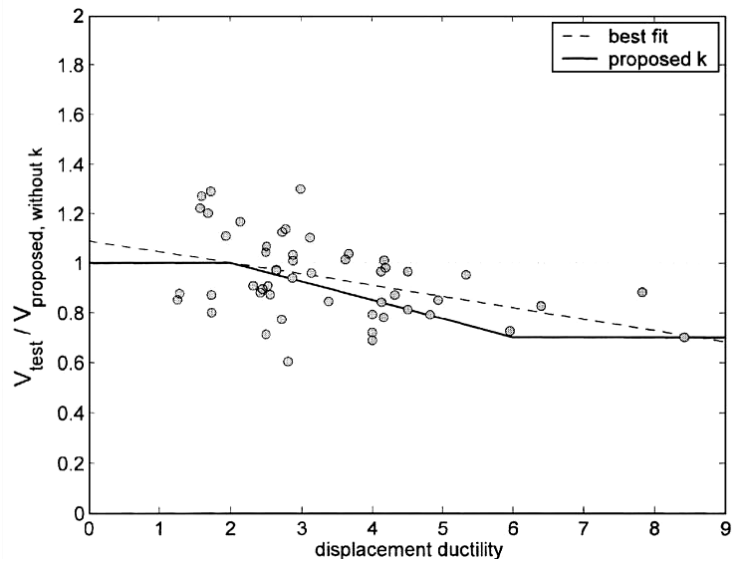

Figure 2-3 Degradation of shear strength with increasing displacement ductility (Figure 10 Sezen and Moehle 2004)

$$V_n = V_s + V_c = k\frac{A_v f_y d}{s} + k\left(\frac{0.5\sqrt{f'_c}}{a/d}\sqrt{1+\frac{P}{0.5\sqrt{f'_c}\,A_g}}\right)0.8A_g \qquad \text{(S.I. units)} \qquad (2\text{-}10)$$

Elwood and Moehle (2005b), illustrated that a small error in predicting the shear strength of the section may lead to considerable variability in the displacement at shear failure (Figure 2-4). As a consequence they proposed an empirical drift-based failure model to assess shear capacity, derived from the same database Sezen used to derive the shear strength model.

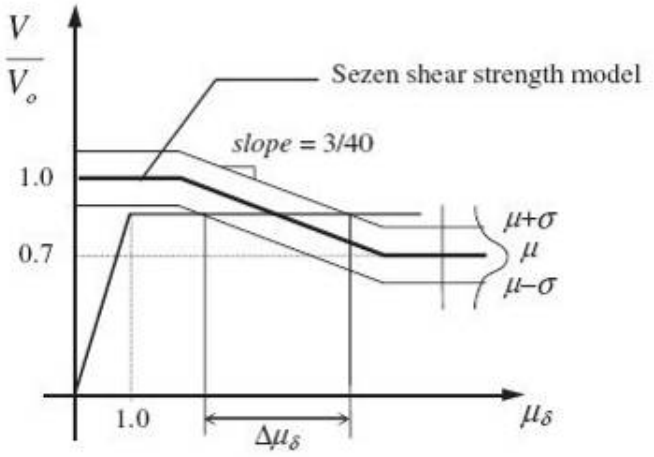

Figure 2-4 Variability of displacement at shear failure inherent in shear strength model (Figure 7 Elwood and Moehle 2005b)

The proposed model shown in Equation (2-11 is dependent on the detailing provided, concrete strength and the applied axial and shear forces. Figure 2-5 illustrates the drift capacity model and gives a comparison to the shear strength model developed by Sezen and Moehle. Comparing the model with the information from the experimental database it was found that there was no correlation between the shear strength and the error in calculated failure drift.

$$\delta_s = \frac{3}{100} + 4\rho'' - \frac{1}{40}\frac{\upsilon}{\sqrt{f'_c}} - \frac{1}{40}\frac{P}{A_g f'_c} \geq \frac{1}{100} \qquad \text{(S.I. units)} \qquad (2\text{-}11)$$

Where; ρ" = transverse steel area ratio, υ = nominal shear stress at section capacity, f'_c = concrete compressive strength, P = column axial load, and A_g = gross cross-sectional area.

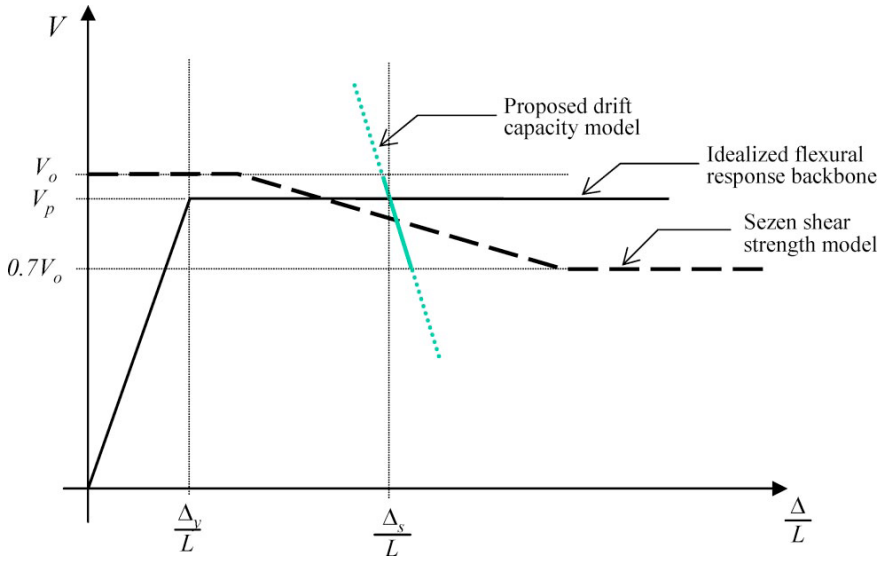

Figure 2-5 Drift capacity model for shear failure (Figure 16 Elwood and Moehle 2005b)

2.3.2 Axial Failure

Loss of axial load capacity of columns has been shown by previous earthquakes to have catastrophic results if the load cannot be redistributed. An investigation into the axial capacity of columns that have previously sustained shear failure was carried out by Elwood and Moehle (2005a). The model assumes a critical shear failure plane along which axial failure occurs and the drift at axial failure was calibrated empirically using a database of twelve full-scale columns tested in double curvature. Figure 2-6 illustrates the Free-body diagram of the shear failure plane and the forces from each of the contributing components, assuming shear capacity has reduced to zero.

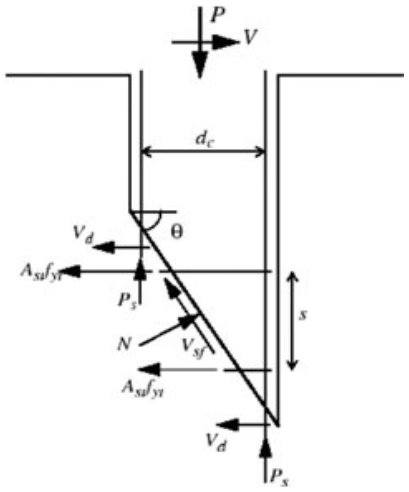

Figure 2-6 FBD of the shear failure plane assumed in the axial failure model (Figure 6 Elwood and Moehle 2006)

Drift at axial failure is dependent on the amount and spacing of the transverse reinforcement and the inclination of the failure surface as given by Equation (2-12.

$$\delta_a = \frac{4}{100}\frac{1+\tan^2 65°}{\tan 65° + P\left(\dfrac{s}{A_{st} f_{yt} d_c \tan 65°}\right)} \qquad \text{(S.I. units)} \qquad (2\text{-}12)$$

Where; 65° is the inclination of the assumed shear failure plane, A_{st} is the area of transverse reinforcement parallel to the applied shear, with a spacing s, f_{yt} is the yield stress of the transverse reinforcement, and d_c is the depth of column core measured parallel to the applied shear force.

2.3.3 Empirical Backbone

By combining the drift-based models for shear and axial failure in conjunction with yield drift for the section Elwood and Moehle (2006) proposed an empirical backbone model to capture the performance limits of columns with inadequate transverse reinforcement. The backbone consists of a tri-linear relationship; shear capacity increases linearly to the plastic limit at the yield displacement, constant plastic capacity until the shear limit is reached and linear degradation of capacity to drift at axial failure (see Figure 2-7).

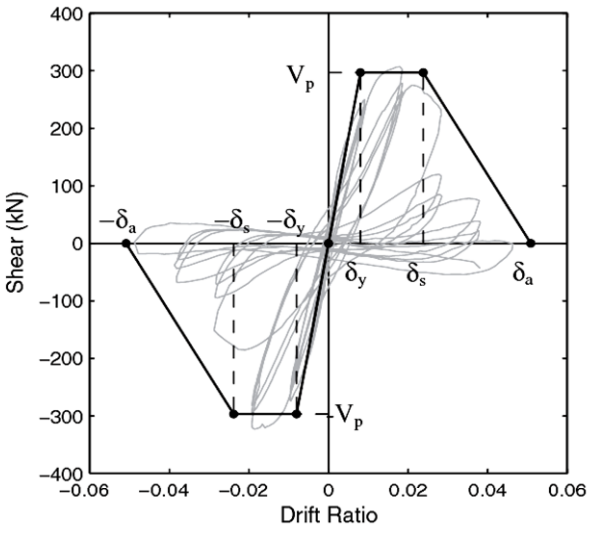

Figure 2-7 Proposed backbone model (Figure 2 Elwood and Moehle 2006)

The plastic shear capacity, V_p, of the section is given by Equation (2-13) (applies to double-curvature columns) and the calculated drift at yield is given as the sum of contributions from flexure, shear, and bar slip as given in Equations (2-14) thru (2-19).

$$V_p = \frac{2M_p}{L} \qquad \text{(S.I. units)} \qquad (2\text{-}13)$$

Where:

M_p = plastic moment capacity of the section

L = clear span of the column

The effective yield drift ratio:

$$\delta_y = \delta_{flex} + \delta_{shear} + \delta_{slip} \qquad \text{(S.I. units)} \qquad (2\text{-}14)$$

For a double-curvature column, the moment-area theorem gives the flexural contribution to the yield drift:

$$\delta_{flex} = \frac{L}{6}\phi_y \qquad \text{(S.I. units)} \qquad (2\text{-}15)$$

Where:

ϕ_y = yield curvature from section analysis of the column

Idealising the columns as a homogeneous material the shear deformation can be estimated by:

$$\delta_{shear} = \frac{2M_p}{5/6\,A_g GL} \qquad \text{(S.I. units)} \qquad (2\text{-}16)$$

Where:

A_g = gross cross-sectional area of the column

G = shear modulus of the column, given by Equation (2-17

$$G = \frac{E}{2(1-\nu)} \qquad \text{(S.I. units)} \qquad (2\text{-}17)$$

Where:

E = modulus of elasticity of the concrete

v = poisson's ratio (take as 0.2)

The drift ratio contribution due to bar-slip is dependent on the applied axial load, bar diameter and bond stress:

$$\delta_{slip} = \frac{d_b f_s \phi_y}{8u} \qquad \text{(S.I. units)} \qquad (2\text{-}18)$$

Where:

d_b = longitudinal bar diameter

u = average bond stress (approximated by $0.5\sqrt{f'_c}$)

f_s = axial load dependent bar stress, given by Equation (2-19) below

$$f_s = \begin{cases} f_y & \Leftarrow \quad P \le 0.2 f'_c A_g \\ f_y\left(\frac{5}{3} - \frac{10P}{3f'_c A_g}\right) & \Leftarrow \quad 0.2 f'_c A_g \le P \le 0.5 f'_c A_g \\ 0 & \Leftarrow \quad P \ge 0.5 f'_c A_g \end{cases} \qquad \text{(S.I. units)} \qquad (2\text{-}19)$$

Elwood and Moehle (2006) performed comparisons of the backbone model with the FEMA 356 model, for two dynamic experimental tests. The experimental tests were performed using a shake-table on two-bay uni-directional frames with the central column susceptible to shear/axial failure to allow post-failure load redistribution to be assessed. Force-displacement data for the two tests are shown below in Figure 2-8, with the backbone and FEMA 356

models and overlain. Clearly illustrated is the enhanced predictive capability of the backbone model when compared to the FEMA 356 model. FEMA 356 performs poorly in assessing the performance; initial stiffness is overestimated, the predicted drift ratio at shear failure is less than 50% of test results, and the post shear-failure response predicted is inadequate. Axial failure did not occur in either test, although the test with increased axial load deformed axially which resulted in axial load redistribution to the exterior columns.

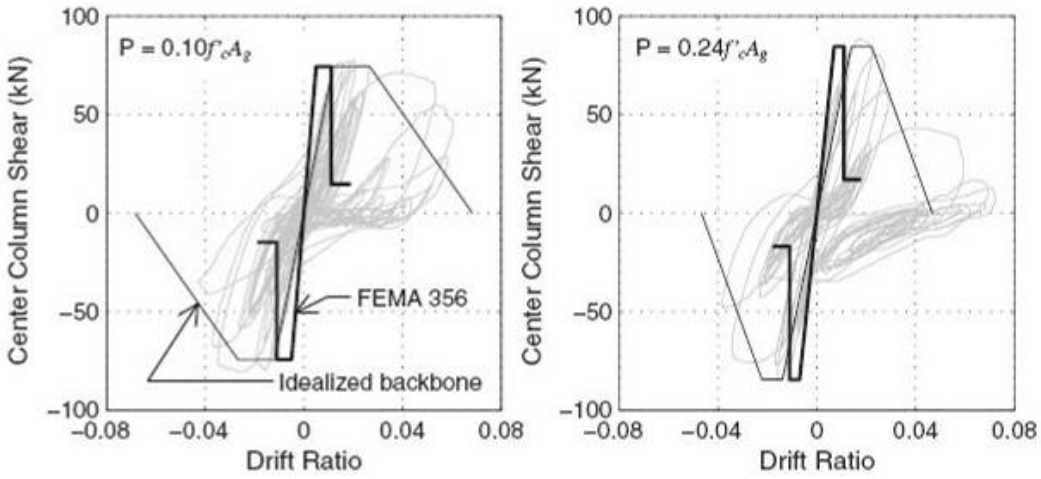

Figure 2-8 Shake-table test results compared with backbone model and FEMA 356 (Figure 10 Elwood and Moehle 2006)

2.3.4 Splice Capacity and Type of Failure

The performance of lap-splices at the base of RC columns with inadequate transverse reinforcing may limit the available flexural capacity and ductility. Two facets to the performance of the lap-splices are important, the capacity of the splice (related to the flexural capacity of the RC column), and the failure mechanism that occurs (related to the ductility of the RC column) given the capacity is exceeded.

The tensile capacity of the splice has been shown by previous researchers (Kim et al. 2006; Orangun et al. 1977; Zuo and Darwin 2000) to be dependent on bar diameter, concrete strength, cover, reinforcement configuration and the confinement provided by the transverse reinforcement. Two failure mechanisms are highlighted; firstly a simple pullout of the bars can occur after crushing of the concrete adjacent to the deformations on the bars, and secondly the splice can initiate splitting of the concrete. The type of failure occurring will depend on the configuration of the reinforcement and cover provided.

Orangun et al (1977) propose a model for the average bond stress capacity of lap-splices given an approximation of a triangular bond stress distribution along the lap-splice length. The average bond stress capacity is the sum of contributions from the unconfined lap-splice and the transverse steel provided.

$$u'_{cal} = u_{cal} + u_{tr} = \left[\left(0.10 + \frac{c}{4d_b} + \frac{25d_b}{6l_s}\right)\sqrt{f'_c}\right] + \left[0.0025\,\frac{A_{tr}f_{yt}}{sd_b}\sqrt{f'_c}\right] \quad \text{(S.I. units)} \quad (2\text{-}20)$$

Where:

u'_{cal}	=	average bond stress capacity (sum of the unconfined splice and the transverse steel contributions)
u_{cal}	=	average bond stress capacity from unconfined concrete
u_{tr}	=	average bond stress capacity from transverse steel
f'_c	=	concrete compressive strength
d_b	=	longitudinal bar diameter
l_s	=	lap-splice length
c	=	smallest clear concrete cover
A_{tr}	=	area of transverse reinforcement normal to the splitting plane
f_{yt}	=	yield strength of transverse reinforcement

Limits are proposed; $c/d_b \leq 2.5$ results in a splitting failure, as opposed to a pullout failure, and the contribution from the transverse reinforcement should be limited to a maximum $0.25\sqrt{f'_c}$. Harries et al (2006) suggest that the transverse reinforcement contribution should be neglected when the cyclic capacity of the splice is calculated.

Zuo and Darwin (2000) investigated the tension capacity of lapped splices for a range of bar profiles, concrete strengths, and quantity and type of aggregates. They found that the contribution to the tensile capacity of the splice due to the unconfined concrete is proportional to $f'^{1/4}_c$, and that the additional contribution from the transverse steel is best characterised as proportional to $f'^{3/4}_c$. This is a modification to their previous work (Darwin et al. 1996) that modelled both contributions as proportional to $f'^{1/4}_c$, and is the rationale behind the format Equation (2-23) takes.

$$\frac{T_b}{f'^{1/4}_c} = \frac{T_c + T_s}{f'^{1/4}_c} = \frac{A_b f_s}{f'^{1/4}_c} \tag{2-21}$$

The contributions from the unconfined concrete and the transverse steel are given by Equations (2-22) and (2-23) respectively. These have been converted from the original imperial units to S.I. units for convenience.

$$\frac{T_c}{f'^{1/4}_c} = \left[1.43 l_d \left(c_{\min} + 0.5 d_b\right) + 56.23 A_b\right]\left(0.1\frac{c_{\max}}{c_{\min}} + 0.9\right) \quad \text{(S.I. units)} \tag{2-22}$$

$$\frac{T_s}{f'^{1/4}_c} = \left(8.97 t_r t_d \frac{NA_{tr}}{n} + 742\right)\sqrt{f'_c} \quad \text{(S.I. units)} \tag{2-23}$$

Where:

T_c	=	tensile capacity of splice contribution from unconfined concrete (N)
T_s	=	tensile capacity of splice contribution from transverse steel (N)
f'_c	=	concrete compressive strength (MPa)
d_b	=	longitudinal bar diameter (mm)
l_d	=	lap-splice length (mm)
A_b	=	area of single spliced bar (mm^2)
A_{tr}	=	area of transverse reinforcing bar crossing the splitting plane (mm^2)
c_{min}, c_{max}	=	minimum, maximum value of c_s or c_b (mm, $c_{max}/c_{min} \leq 3.5$, refer Figure 2-9)
c_s	=	minimum value of c_{si} +6.35, c_{so} (mm)
c_{si}	=	½ of clear spacing between bars (mm)
c_{so}, c_b	=	side or bottom cover of reinforcing bars
N	=	number of transverse reinforcing bars (stirrups or ties) crossing l_d
n	=	number of bars spliced along the splitting plane (smaller of c_s, c_b)
t_r	=	factor accounting for bar profile (refer Equation (2-24), can be taken as 1 for bars with standard profile (Darwin et al. 1996))
t_d	=	factor accounting for bar diameter (refer Equation (2-25))
R_r	=	Ratio of projected rib area normal to bar axis to the product of the nominal bar perimeter and the centre to centre rib spacing

$$t_r = 9.6R_r + 0.28 \qquad \text{(S.I. units)} \quad (2\text{-}24)$$

$$t_d = 0.72\left(d_b / 25.4\right) + 0.28 \qquad \text{(S.I. units)} \quad (2\text{-}25)$$

Figure 2-9 illustrates the notation for the series of equations above, and the configuration dependent modes of splitting failure. The mode of failure is independent from the transverse reinforcement provided and should be determined prior to calculating the number of spliced bars on the splitting plane and the number of stirrups/ties contributing to the transverse steel component. Thus in Figure 2-10 a) below, the side split failure n = 3 and N = 2 x number of stirrup sets along splice length and similarly for the cover splitting failure.

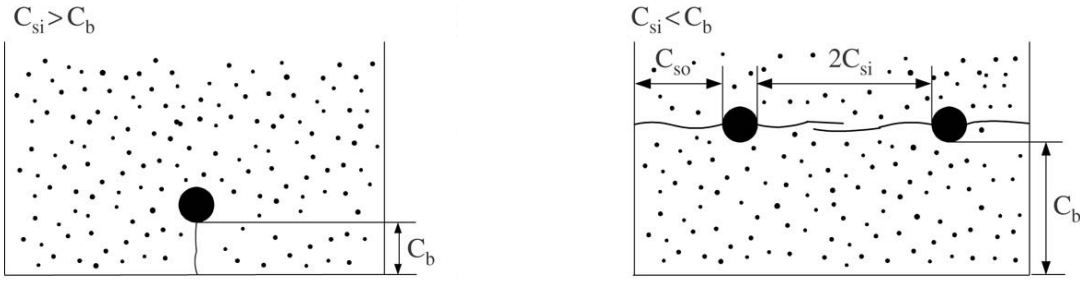

a) Cover splitting failure **b) Side splitting failure**

Figure 2-9 Notations for capacity equations and illustration of splitting failure modes (Kim et al. 2006)

Kim et al (2006) propose a modification to the model to account for the behaviour of circular columns. The two failure modes are illustrated in Figure 2-10 (b) in addition to the modified notation as appropriate for circular members. The modified definitions of the parameters used in Equation (2-22) are:

c_{min} = Cover, c (mm)

c_{max} = 0.5 S_c + 6.35 (mm)

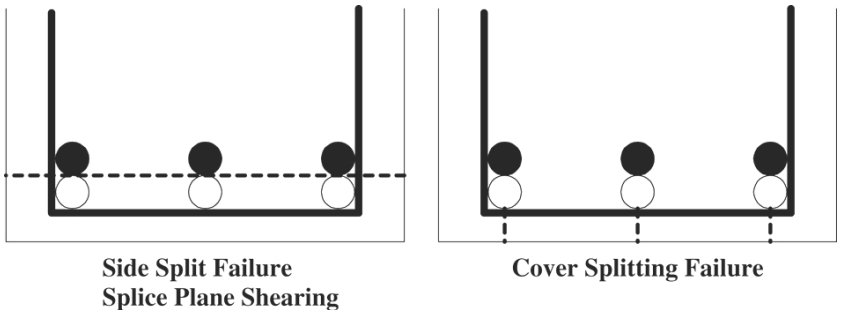

a) potential failure modes for rectangular members

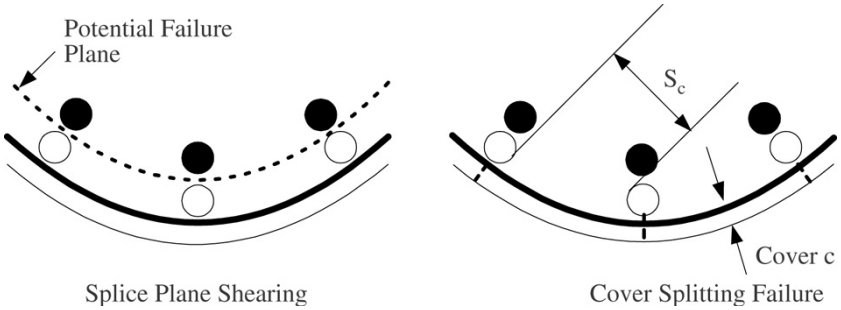

b) potential failure modes for circular members

Figure 2-10 Potential failure modes for rectangular and circular members

References:

Darwin, D., Tholen, M. L., Idun, E. K., and Zuo, J. (1996). "Splice Strength of High Relative Rib Area Reinforcing Bars." *ACI Structural Journal*, 93(1), 95-107.

Elwood, K. J., and Moehle, J. P. (2005a). "Axial Capacity Model for Shear-Damaged Columns." *ACI Structural Journal*, 102(4), 578-587.

Elwood, K. J., and Moehle, J. P. (2005b). "Drift Capacity of Reinforced Concrete Columns with Light Transverse Reinforcement." *Earthquake Spectra*, 21(1), 71-89.

Elwood, K. J., and Moehle, J. P. (2006). "Idealised Backbone Model For Existing Reinforced Concrete Columns and Comparisons With FEMA 356 Criteria." *Struct. Design Tall Spec. Build.*, 15, 553-569.

FEMA356. (2000). "Prestandard and Commentary for the Seismic Assessment of Buildings." FEMA.

Harries, K. A., Ricles, J. R., Pessiki, S., and Sause, R. (2006). "Seismic Retrofit of Lap Splices in Nonductile Square Columns Using Carbon Fiber-Reinforced Jackets." *ACI Structural Journal*, 103(6), 874-884.

Kim, T. H., Kim, B. S., Chung, Y. S., and Shin, H. M. (2006). "Seismic performance assessment of reinforced concrete bridge piers with lap splices." *Engineering Structures*, 28, 935-945.

NZS1170.5:2004. (2004). "Structural Design Actions, Part 5: Earthquake Actions - New Zealand".
NZS3101:1995. (1995). "Concrete Structures Standard."

NZSEE. (2006). "Assessment and Improvement of the Structural Performance of Buildings in Earthquakes." New Zealand Society for Earthquake Engineering.

Orangun, C. O., Jirsa, J. O., and Breen, J. E. (1977). "A Reevaluation of Test Data on Development Length and Splices." *ACI Journal, Proceedings*, 74(3), 114-122.

Sezen, H., and Moehle, J. P. (2004). "Shear Strength Model for Lightly Reinforced Concrete Columns." *Journal of Structural Engineering*, 130(11), 1692-1703.

Zuo, J., and Darwin, D. (2000). "Splice Strength of Conventional and High Relative Rib Area Bars in Normal and High-Strength Concrete." *ACI Structural Journal*, 97(4), 630-641.

3.0 Specimen Design and Loading Protocols

3.1 Specimen Selection

The test columns were designed to replicate existing columns constructed during the period of interest from the early 1960's (corresponding to the introduction of deformed bars) through to 1995 when the revised edition of NZS 3101 was released. NZS 3101: 1995 increased the detailing requirements (primarily the volume and spacing of the transverse reinforcing) for 'gravity' columns to match the requirements for columns in MRF's. This was in recognition of displacement compatibility between the lateral force resisting system and the nominally gravity load columns. Consultation with practising engineers was undertaken to ensure realistic specimen geometry, detailing and imposed loads for the period of interest.

The test specimens (shown in Figure 3-1 below) are full scale 450mm square cantilever columns with a height of 1624 mm. All specimens have the following common details;

- 4 - D25 Grade 300 reinforcing bars. This corresponds to a longitudinal reinforcing ratio (ρ_s) of 1% by volume. Grade 300 reinforcing best represents the steel in use during this period, with nominal yield strength of 275 MPa.
- R10 stirrups are provided at 300mm spacing, corresponding to the minimum diameter and maximum spacing allowable, (reinforcing ratio (ρ_t) of 0.12%).
- Cranked bars at the top of the lap-splice with 1:6 slope as required by NZS 1900 and NZS3101 (prior to and post 1982 respectively).
- Target concrete compressive strength (f'_c) of 32 MPa. This reflects a period typical design specification f'_c of 24 MPa and a likely increase of 33%.

Two lap-splice lengths are chosen; 600 mm (24 d_b, minimum requirements NZS 1900 and NZS 3101) and 750 mm (30 d_b, to reflect a more conservative design). The stirrup layout for the 600 mm lap-splice specimen is not ideal in terms of providing lateral buckling restraint to the upper end of the cranked bars as the stirrup is located 8 d_b above the upper crank. NZS 1900: 1960 is ambiguous, specifying an 8 d_b limit without explicitly stating that this was to be taken from the lower crank which equates to the 2 d_b limit currently used. This detailing reflects the worst case scenario with regard to inadequate design specifications and poor site practises.

Axial load for the specimens was selected to be in the region of 10MPa; this is at the upper end of the range of likely axial loads for 'gravity' columns and approximates a 6 storey building. For testing purposes this corresponds to an axial force of 2000kN, although for one test this was reduced to 1000kN to assess the effect of axial load on the rate of capacity degradation.

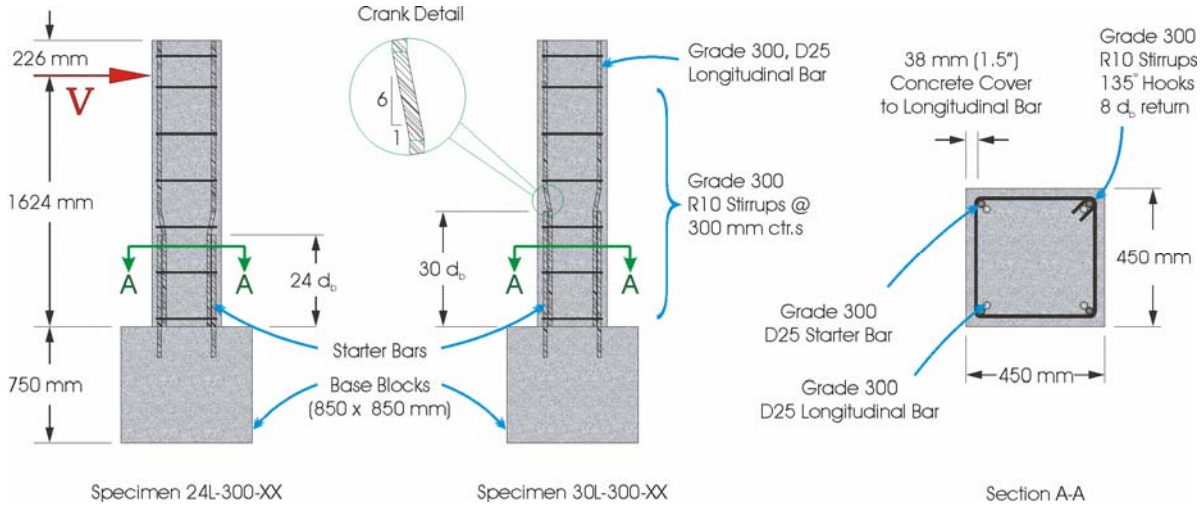

Figure 3-1 Details of test specimens

The full experimental program is shown in Table 3-1 below. The designations given to each of the six specimens is of the form XXL-300-XX, where:

- XXL- Length of lap-splice in bar diameters
- -300- Spacing of the transverse reinforcement in mm
- -XX Designates the loading protocol (developed in next section)

Table 3-1 Experimental Program

Designation	Lap length	Tie Details	Axial Load	Loading Protocol
24L-300-2D	600mm (24 d_b)	R10 @ 300mm	2000kN (0.3f'_cA_g)	2D Quasi-Static
24L-300-3D	600mm (24 d_b)	R10 @ 300mm	2000kN (0.3f'_cA_g)	3D Quasi-Static
24L-300-3D-R	600mm (24 d_b)	R10 @ 300mm	1000kN (0.15f'_cA_g)	3D Quasi-Static
30L-300-2D	750mm (30 d_b)	R10 @ 300mm	2000kN (0.3f'_cA_g)	2D Quasi-Static
30L-300-3D	750mm (30 d_b)	R10 @ 300mm	2000kN (0.3f'_cA_g)	3D Quasi-Static
24L-300-EQ	600mm (24 d_b)	R10 @ 300mm	2000kN (0.3f'_cA_g)	3D Quasi-EQ

3.2 Experimental Setup and Data Acquisition

3.2.1 Test Apparatus

The test apparatus allows the cantilever columns to be loaded axially in addition to bi-axial bending. Figure 3-2 below illustrates the schematic of the lateral force application via a self-equilibrating frame and counterweight. Universal bearing pivots are located at the top and base of the column allowing the Lateral Ram to extend (or contract) and causing the reaction frame to rotate at the base and induce bending in the column. Axial load is applied using the Dartec, which has an adjustable reaction head and a ram extending from the floor.

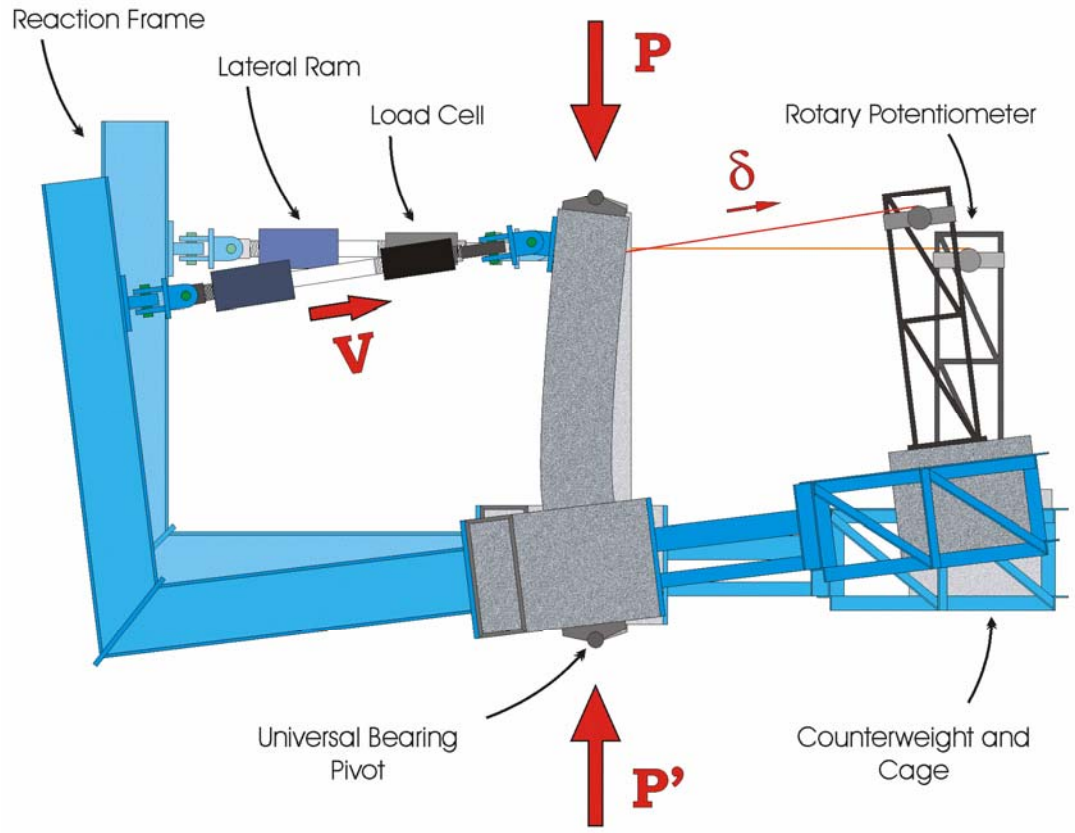

Figure 3-2 Elevation of Experimental Apparatus

The experimental apparatus configured for bi-directional bending is shown below in Figure 3-3. The two primary axes are shown, illustrating the reaction frame and lateral ram for the two orthogonal directions. In the centre is the DARTEC, providing the axial load via a fixed reaction head and a 10,000kN capacity hydraulic ram at the base. Partially obscured behind the near corner leg of the DARTEC is a test specimen (following testing).

Figure 3-3 Experimental apparatus with test specimen

3.2.2 Instrumentation and Data Acquisition

In addition to the force-displacement data captured by load-cells and rotational potentiometers, section data was collected via strain gauges and linear potentiometers. A total of 24 strain gauges were used for each specimen, configured as shown below in Figure 3-4. There are three gauges on both the starter and the lapped bars in each of the column corners; this allows the strain profile to be determined and the degradation of the splice capacity to be calculated as the test progresses.

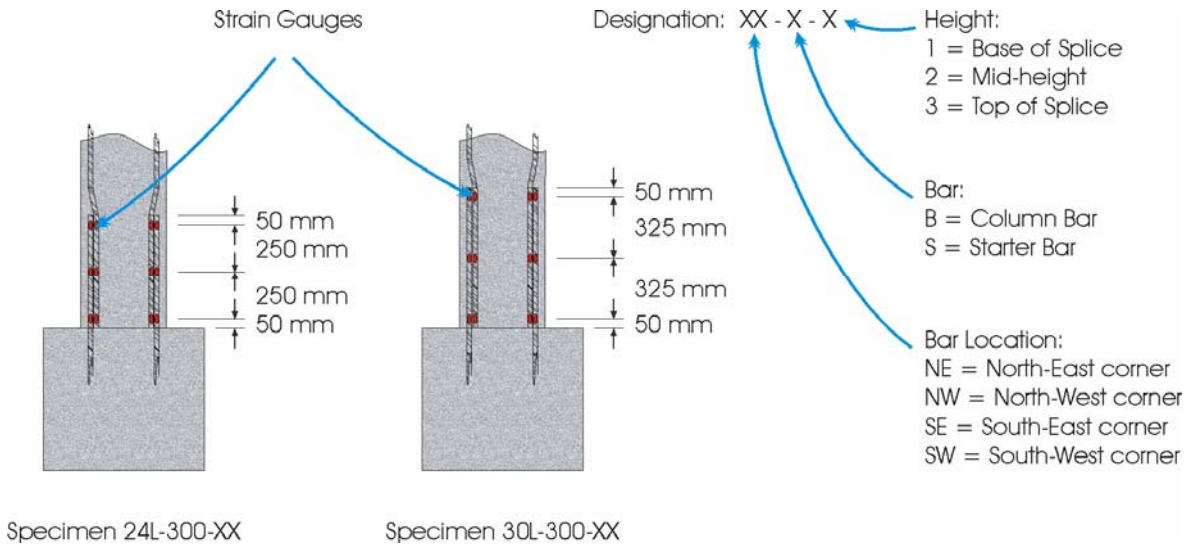

Figure 3-4 Configuration of strain gauges

Figure 3-5 below illustrates the potentiometer configuration for specimen 6; each of the four column faces is as shown. This enables the flexural, shear and interface crack rotation (due to bar-slip) components of the displacement to be calculated for the specimen at each angle of loading. However, specimens 1-5 only contain the B1 and B2 potentiometers on each face thus only the flexural and interface rotation can be calculated and the shear must be inferred.

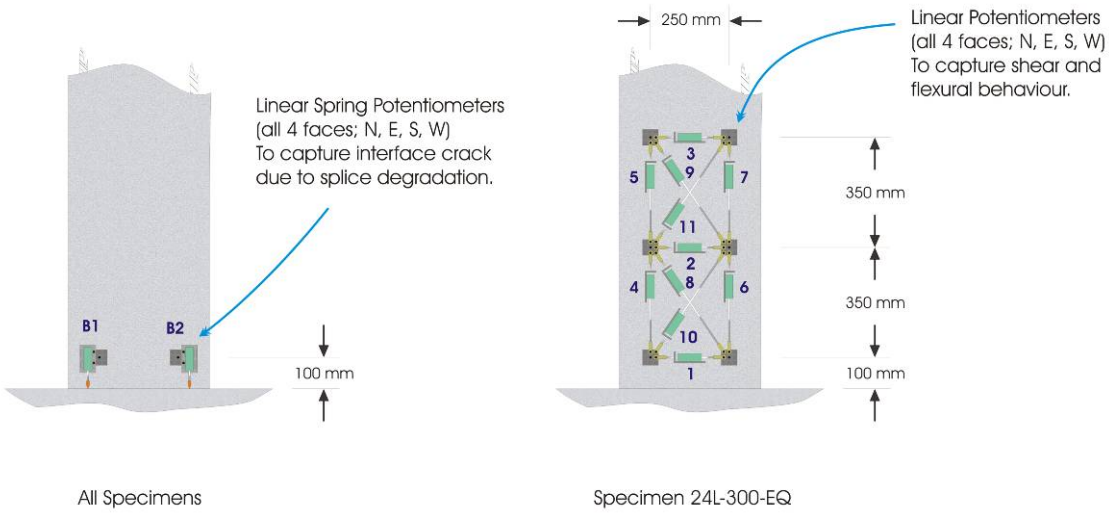

Figure 3-5 Configuration of potentiometers

3.3 Construction

Construction of all six specimens was performed in the manner of an assembly line to maximise the efficiency of the construction and testing process. Reduced costs associated with only one set of formwork and bracing being required also contributed to this decision. The following process was followed (Photographs for specimen 24L-300-2D are shown):

1) Base-block constructed and placed in formwork with all reinforcing, starter bars, mounting tubes, lifting mounts and bracing as required (Figure 3-6 a)).
2) Base-block casting using externally supplied concrete via a hopper and an overhead crane (Figure 3-6 b)).
3) Construct steel cage for column with longitudinal and transverse reinforcing, add strain gauges to longitudinal bars and seal (Figure 3-7 a) and b)).
4) Construct and place column formwork, add all mounting tubes, ducts for data acquisition and external formwork bracing (Figure 3-8 a)).
5) Cast column concrete (Figure 3-8 b)).
6) Place column in experimental apparatus and test.

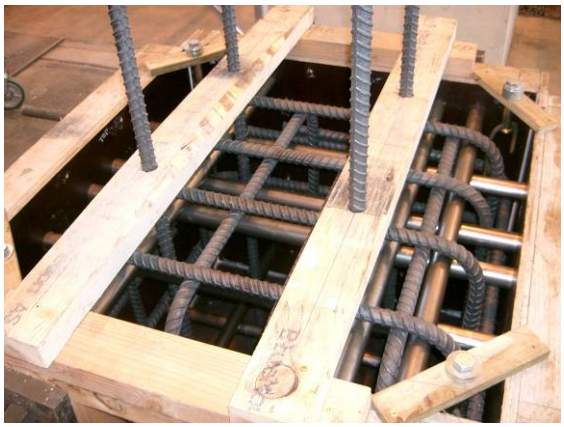

a) Base-block and formwork

b) Casting concrete base-block

Figure 3-6 Base-block reinforcing steel, formwork and concrete casting

a) Lap-splice at base of column

b) Lap-splice strain-gauge detail

Figure 3-7 Lap-splice detail at column base with strain gauges attached

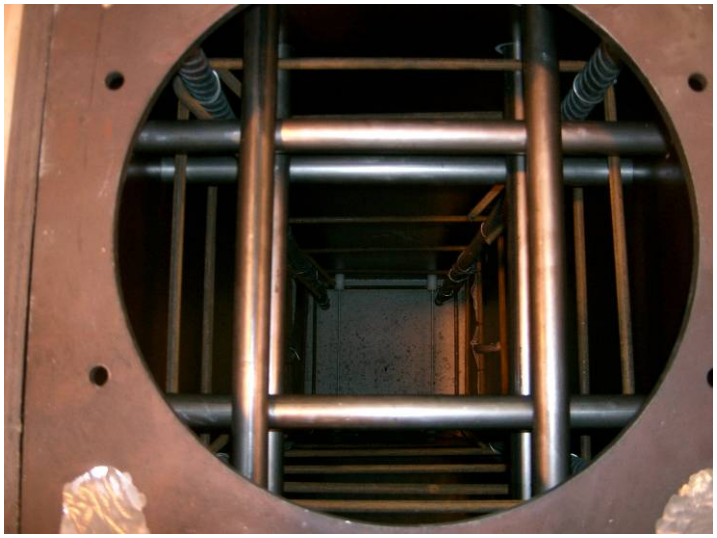

a) Interior view down column before casting

b) Column formwork and casting

Figure 3-8 Column prior to and during casting

4.0 Experimental Results for Uni-Directional Tests

4.1 Uni-directional Quasi-static Protocol

The loading protocol for uni-directional testing is of the same form as used by Melek et al. (2003) and is shown below in Figure 4-1. Three cycles to positive and negative peaks are undertaken at the following levels of drift; 0.1%, 0.25%, 0.5%, 0.75%, 1.0%, 1.5%, 2.0%, and 3.0%. This does not correspond exactly to the requirements outlined in ACI T1.1-01 (2001), which requires the initial drift level to lie within the elastic range of the member and all subsequent levels of drift to lie within the range of 1.25 to 1.5 times the preceding level of drift. The difference between the imposed protocol and the requirements arises due to the doubling of imposed drift from 0.25% to 0.50%, which corresponds to the region in which the section begins to perform inelastically (beyond this point the protocol complies). However due to the low level of demand at this level it is not envisaged that this will have a significant effect on the validity of the results presented.

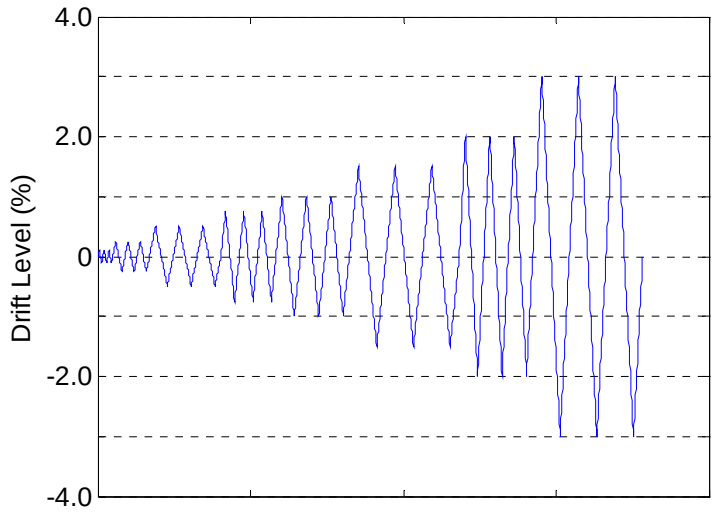

Figure 4-1 Uni-directional drift protocol

4.2 Material Testing

Prior to testing each specimen under the designed loading protocol, material tests were carried out on each of the component materials; longitudinal and transverse steel, and the concrete compressive strength. These results are summarised in Table 4-1 below. The yield

strengths of the longitudinal steel (f_y = 315 and 320 MPa) are very similar to the target capacity. Although the transverse steel provided was significantly stronger (f_{yt} = 439 MPa) than was specified, it has minimal effect on the behaviour of the specimen due to the very low transverse reinforcement ratio. The measured concrete compressive strengths (f'_c) were 33.6 and 33.9 MPa (refer to Appendix A for material testing results), which is close to the target strength of 32 MPa, and lies within the expected bounds of in-situ concrete for existing columns.

Table 4-1 Summary of material properties for unidirectional test specimens

Column Designation	f'_c (MPa)	N/f'_cA_g	f_y (MPa)	f_u (MPa)	f_{yt} (MPa)
24L-300-2D	33.6	0.29	315	465	439
30L-300-2D	33.9	0.29	320	465	439

4.3 Specimen 24L-300-2D

4.3.1 Test Observations

Observations made during the testing of Specimen 24L-300-2D are presented here. The progression of damage sustained by the specimen during testing is shown in Figure 4-2 a) through f). Key damage states observed and the level of drift at which they occurred are listed in the following bullet points:

- 1.0% drift cycles, first flexural cracks occur in the plastic hinge region along the length of the lap-splice (as shown in Figure 4-2 (a)).
- 1.5% drift cycles, shear cracks propagate from the flexural cracks initiated previously (Figure 4-2 (b)).
- 2.0% drift (1st cycle), shear cracks extend significantly (Figure 4-2 (c)).
- 2.0% drift (2nd and 3rd cycles), splice-splitting initiates cracking along the line of the lap-splice (Figure 4-2 (d)).
- 3.0% drift (1st positive drift cycle), expulsion of the splice cover concrete occurs with the associated significant reduction in lateral force capacity (Figure 4-2 (e)).

- 3.0% drift (1st negative drift cycle), full formation of the shear failure plane occurs and the specimen loses axial load carrying capacity (Figure 4-2 (f)).

Post-failure observations include:

- Buckling of the poorly restrained cranked longitudinal bar at the top of the lap-splice, as shown in Figure 4-2 (g), this figure also illustrates the shear failure wedge sustained by the specimen.
- Figure 4-2 (h) shows the 'bursting' of the stirrup restraining the shear failure wedge as a result of the two halves driving past each other.

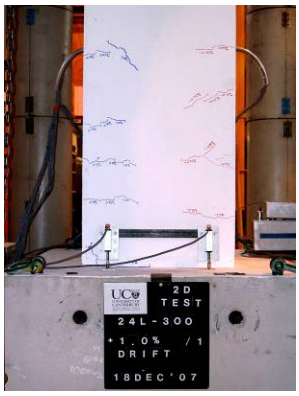

a) 1.0% Drift

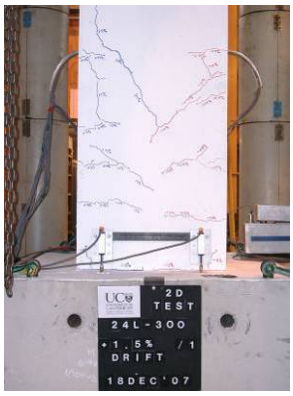

b) 1.5% Drift

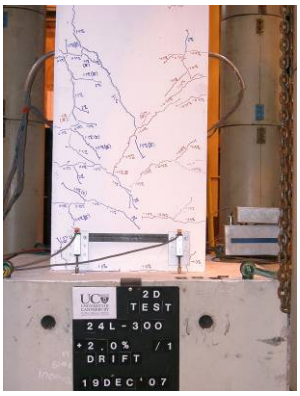

c) 2.0% Drift – 1st Cycle

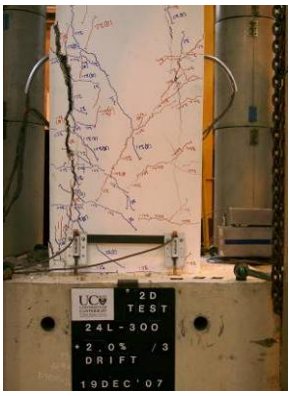

d) 2.0% Drift – 3rd Cycle

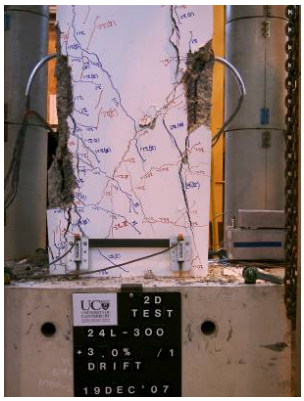

e) +3.0% Drift (Shear Failure)

f) -3.0% Drift (Axial Failure)

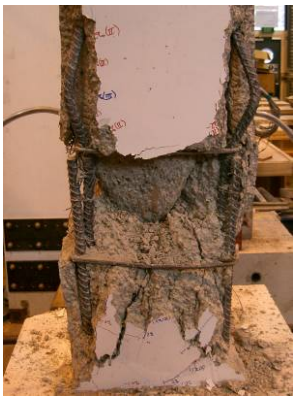

g) Buckling of Cranked Bars

h) Burst Stirrup at Hook

Figure 4-2 Damage sequence for specimen 24L-300-2D

4.3.2 Force versus Drift Response

The measured Force versus drift response of specimen 24L-300-2D is shown in Figure 4-3. Highlighted on the figure are the points during the loading that the specimen loses significant

lateral capacity and loss of axial capacity. Axial load of the specimen was applied using the Dartec, utilising a force controlled hydraulic actuator. As axial degradation occurred the ram would extend to maintain the imposed 2000kN axial load. Termination of the test occurred upon the axial deformation reaching a pre-determined (for safety reasons) limit of 25mm.

The figure illustrates marked cyclic deterioration of the lateral capacity and a noticeable degree of 'pinching' of the hysteresis loops of the column during the test. As shown in the progression of damage photographs in Figure 4-2, this is associated with the damage to the lap-splice, resulting in reduced unloading stiffness as the splice recovers the slip resulting from the previous loading. The point annotated "Shear failure" in the figure corresponds to the point at which the shear resistance of the specimen can no longer sustain 80% of the peak lateral force recorded, as defined in (Elwood and Moehle 2005b). This definition makes no distinction whether the dominant contributing factor to the "Shear Failure" is due to a splice failure, flexural degradation, or a classical shear failure. However, as the following Chapters illustrate, this is of lesser significance than the ability to capture the global performance of the columns.

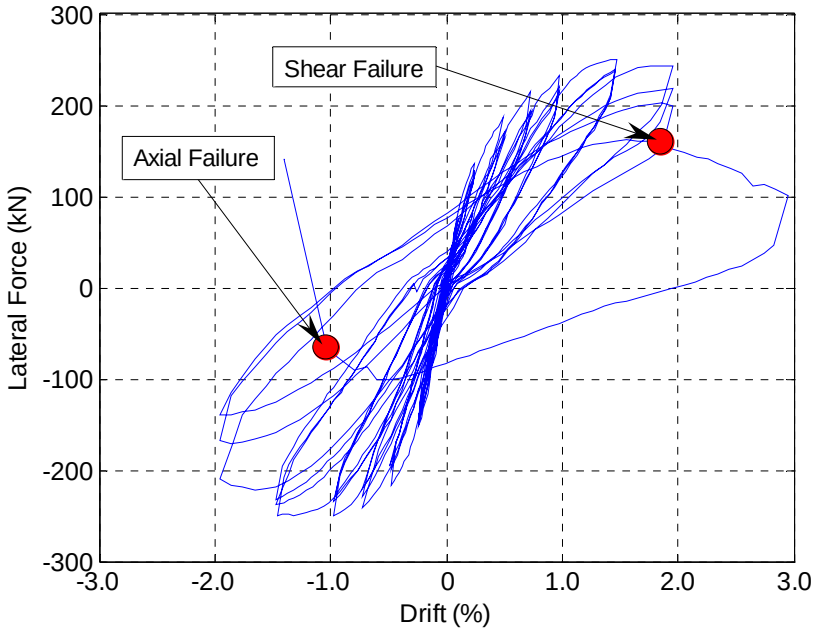

Figure 4-3 Experimental Data for Specimen 24L-300-2D

4.4 Specimen 30L-300-2D

4.4.1 Test Observations

Observations made during the testing of Specimen 30L-300-2D are presented here. The progression of damage sustained by the specimen during testing is shown in Figure 4-4 (a) through (f). Key damage states and the associated drift of occurrence are:

- 0.5% drift cycles, first minor flexural cracks occur in the plastic hinge region along the length of the lap-splice (as shown in Figure 4-4 (a)).
- 0.75% drift cycles, flexural cracks extend (Figure 4-4 (b)).
- 1.0% drift cycles, minor shear cracks extend from flexure cracks (Figure 4-4 (c)).
- 1.5% drift cycles, shear cracks extend (Figure 4-4 (d)).
- 2.0% drift cycles, shear crack extends to full width of the specimen (Figure 4-4 (e)).
- 3.0% drift (1st positive drift cycle), full formation of the shear failure plane occurs and the specimen loses lateral and axial load capacity simultaneously (Figure 4-4 (f)).

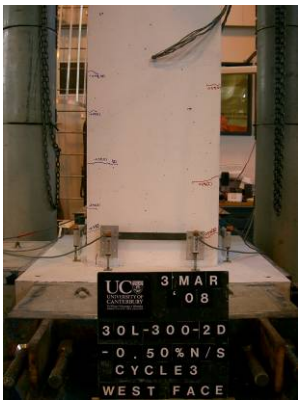

a) 0.5% Drift Cycles

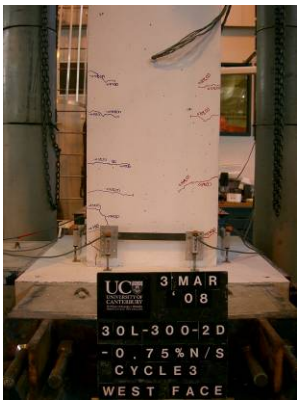

b) 0.75% Drift Cycles

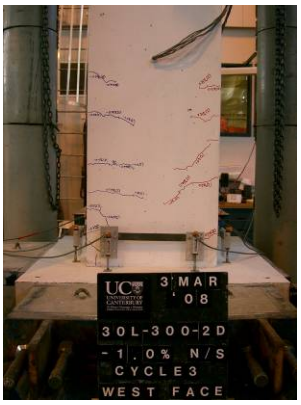

c) 1.0% Drift Cycles

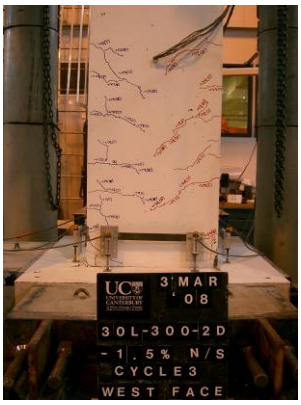

d) 1.5% Drift Cycles

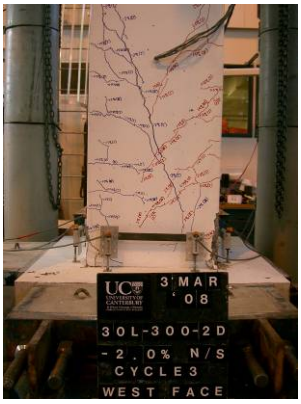

e) 2.0% Drift Cycles

f) 3.0% Drift 1st Cycle

g) Buckled Cranked Bars

h) Shear Failure Plane

Figure 4-4 Damage sequence for specimen 30L-300-2D

Post-failure observations include:

- Buckling of the restrained cranked longitudinal bar at the top of the lap-splice, as shown in Figure 4-2 (g), this figure also illustrates the shear failure wedge sustained by the specimen.
- Figure 4-2 (h) shows the reverse face of the shear failure plane and the damage to the cover concrete at the base of the specimen

4.4.2 Force versus Drift Response

The measured Force versus drift response of specimen 30L-300-2D is shown in Figure 4-5. Highlighted on the figure is the point that the specimen simultaneously loses both lateral and axial capacity. Termination of the test occurred upon the axial deformation reaching an imposed limit of 15mm, at which point the residual axial capacity was 618kN. The degradation of the lateral capacity resulting from the cyclic demands for this specimen is minimal.

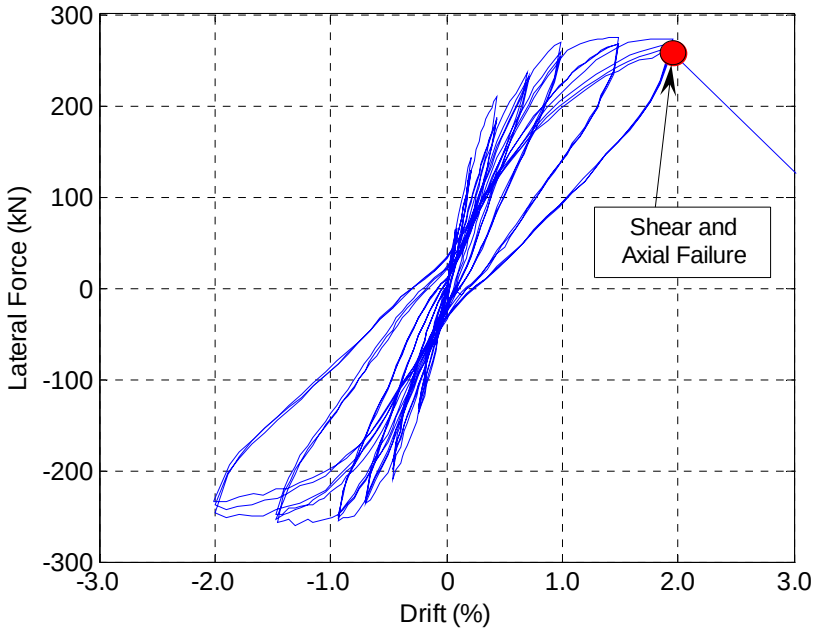

Figure 4-5 Experimental Data for Specimen 30L-300-2D

4.5 Relative Contributions to Displacement

Calculation of the relative contributions to the total displacement of the columns was determined using the potentiometers at the base of each column (raw potentiometer data for the all tests are shown in full in Appendix D. The total column displacement can be separated into contributions from the relative rotation at the base of the column and the combination of flexural and shear deformations over the full height of the column. A total of four potentiometers were used for the uni-directional tests, two each on the column faces parallel to the imposed displacement.

The rotation at the base of the column is determined by dividing the relative vertical displacements of the potentiometers by the lever arm (as shown in Equation (4-1)). Using the calculated rotation the displacement at the top is calculated using Equation (4-2).

$$\vartheta_{base} = {(\delta_1 - \delta_2)}/{l_{base}} \tag{4-1}$$

$$\delta_{base\_rotn} = \vartheta_{base} . H_{col} \tag{4-2}$$

Figure 4-6 and Figure 4-7 below illustrate the relative contributions progressively throughout the tests for Specimens 24L-300-2D and 30L-300-2D respectively. As the figures show the relative contributions are similar for the two tests, typically between 33-50%. However, on closer inspection it is evident that the proportion of the displacement attributable for the two specimens changes as the tests progress. The base rotation contribution for specimen with minimal splice length (24L-300-2D) remains fairly constant, even reducing as the specimen approaches failure (Figure 4-6). Specimen 30L-300-2D (Figure 4-7) displays the opposite trend, with the relative proportion from the rotation at the base of the column increasing in a linear manner. This is due to the additional lap-splice length in specimen 30L-300-2D resulting in limited damage to the splice region, and a consequent reduction in displacement associated with splice slippage. Figure 4-8 illustrates the comparative splice damage for the two specimens.

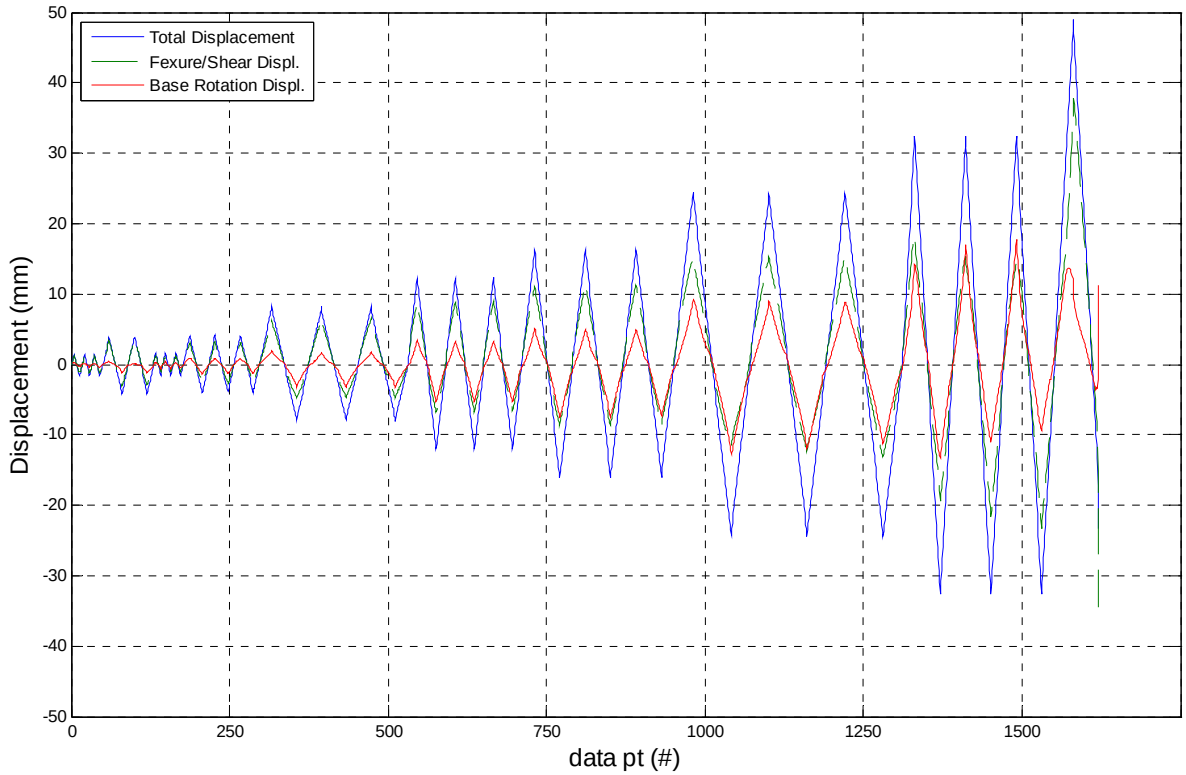

Figure 4-6 Relative Contributions to Total Displacement for Specimen 24L-300-2D

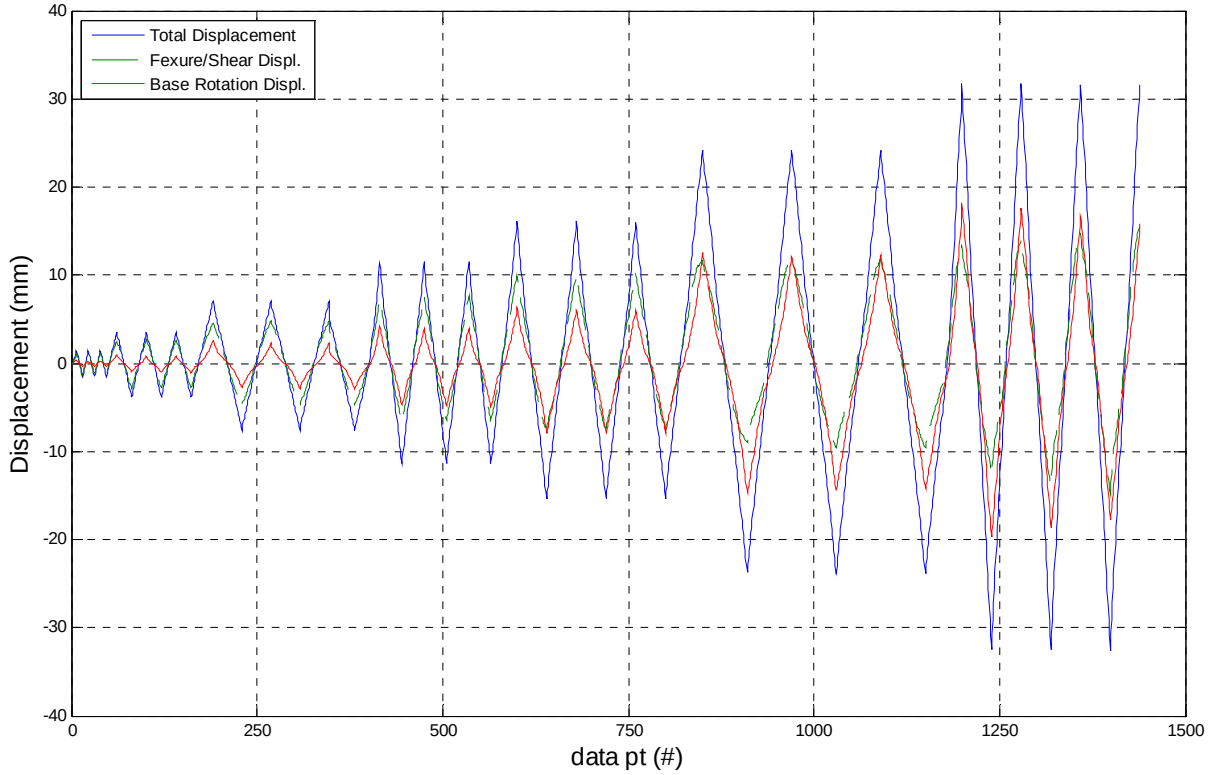

Figure 4-7 Relative Contributions to Total Displacement for Specimen 30L-300-2D

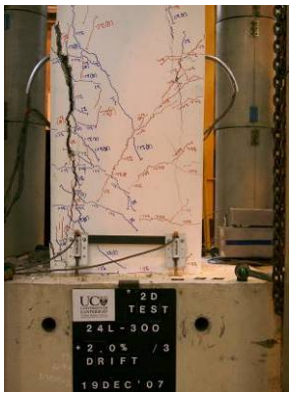

a) 24L-300-2D @ +2.0% Drift

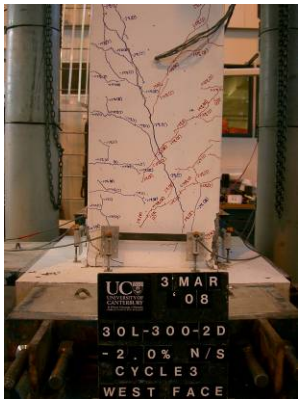

b) 30L-300-2D @ +2.0% Drift

Figure 4-8 Comparative Specimen Damage @ 2% Drift Cycles

4.6 Key Results

The key result from these uni-directional tests is the low drift level at which loss of axial capacity occurred (effectively 2% drift). This is considerably lower than would be necessary to provide life-safety during a design level seismic event.

The primary difference between the two uni-directional tests is the length of lap-splice provided (and consequently the effectiveness of the lateral restraint of the cranked longitudinal bars). Figure 4-9 below directly compares the damage sustained during the tests, as is evident the specimen with the minimum allowable splice length (24L-300-2D) exhibits considerable damage to the cover concrete at the splice. Comparatively this type of damage is almost non-existent until failure occurs in the specimen (30L-300-2D) with additional splice length provision. Also significant is the lack of cyclic deterioration for this specimen.

However, the global drift capacity between the two specimens is identical, suggesting that the performance of these drift sensitive columns is governed by a shear failure mechanism and subsequent loss of axial capacity along the shear failure plane, as proposed by Elwood and Moehle (2005a).

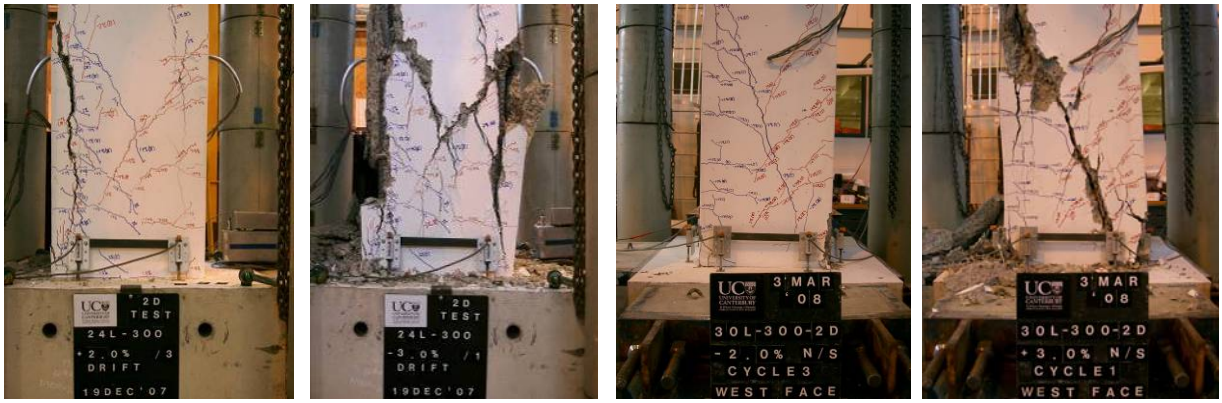

a) Specimen 24L-300-2D (2% cycles) | **b) Specimen 24L-300-2D (3% cycles)** | **c) Specimen 30L-300-2D (2% cycles)** | **c) Specimen 30L-300-2D (3% cycles)**

Figure 4-9 Effect of splice length on damage sustained

4.7 Comparison with Seismic Assessment Models

Comparisons between the experimental data and the various assessment models reviewed in Chapter 2.0 are made in this section. Firstly, the three shear capacity models; Sezen and Moehle (2004), FEMA 356 (2000), and NZSEE Guidelines (2006), are considered. Secondly, three drift capacity models are compared; FEMA 356, Elwood and Moehle (2006), and the ductility limit from the NZSEE Guidelines.

4.7.1 Shear Capacity Models

The three shear capacity models as given in Equations (4-3) to (4-5) below, each determine the nominal shear capacity of the section, which reduces as a function of the ductility level to a residual capacity. Each model considers contributions to the shear capacity from the concrete and the transverse steel provided. The NZSEE model also separates the concrete component into contributions from a purely concrete mechanism and an axial load mechanism. For each of the models shear failure is deemed to occur at the point where the capacity model intersects the flexural capacity of the section.

$$V_{NZSEE} = 0.72(V_c + V_s + V_N) = 0.72\left(k\sqrt{f_c'}\,0.8A_g + \frac{A_v f_{yt} d''}{s}\cot 30° + N.\tan\alpha \right) \quad (4\text{-}3)$$

$$V_{356} = V_s + V_c = k\frac{A_s f_y d}{s} + \lambda k\left(\frac{0.5\sqrt{f_c'}}{M/Vd}\sqrt{1+\frac{N_u}{0.5\sqrt{f_c'}A_g}}\right)0.8A_g \quad (4\text{-}4)$$

$$V_{Sezen} = V_s + V_c = k\frac{A_v f_y d}{s} + k\left(\frac{0.5\sqrt{f'_c}}{a/d}\sqrt{1+\frac{P}{0.5\sqrt{f'_c}A_g}}\right)0.8A_g \quad (4\text{-}5)$$

The shear capacity models are compared in Figure 4-10 with the flexural section capacity and the experimental results for specimen 24L-300-2D. For clarity only the positive quadrant of the data has been shown. The NZSEE model considerably overestimates the shear capacity, and the FEMA 356 model is also non-conservative. The Sezen and Moehle model predicts shear failure, but underestimates the drift at shear failure.

There are two problems with the approach made by these models:

1) Any error in calculating the nominal shear capacity will have a significant effect on the shear failure drift as a result of the low slope of the degrading section of the capacity relationship. This effect was highlighted by Elwood and Moehle (2005b) as illustrated in Figure 4-11.
2) The models are dependent on the yield drift and ductility, consequently any inaccuracy in calculating the yield drift will have a significant effect on the modelled capacity. This effect is illustrated in Figure 4-12 and developed further subsequently.

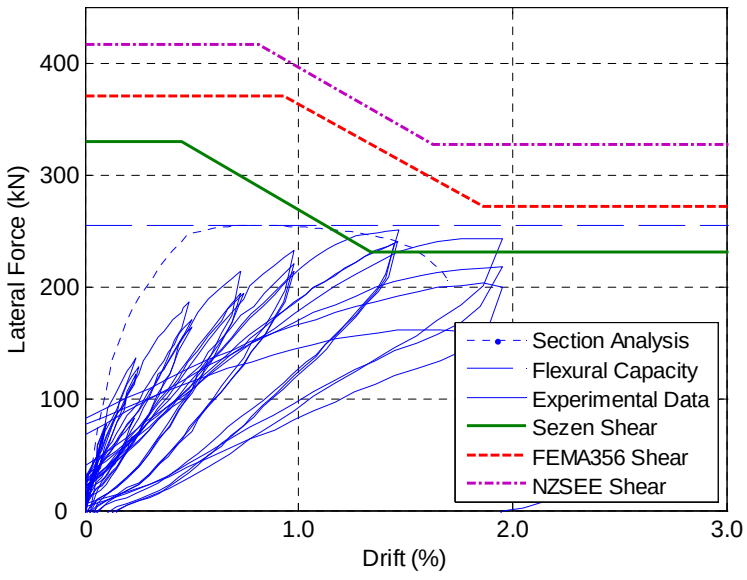

Figure 4-10 Shear strength model comparisons for Specimen 24L-300-2D

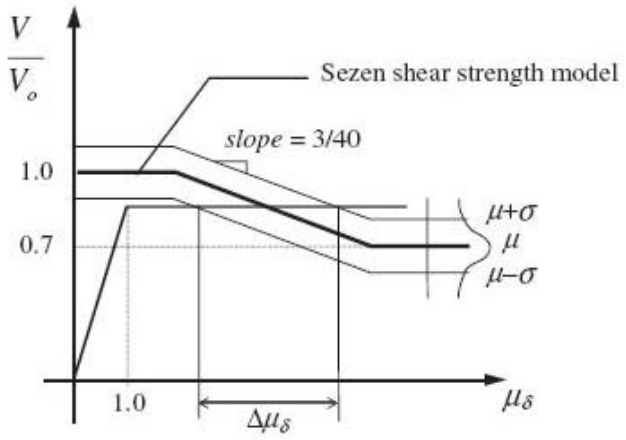

Figure 4-11 Impact of variability on Sezen model (Figure 7 Elwood and Moehle 2005b)

The impact of the yield drift is illustrated in Figure 4-12 below using the Sezen capacity model. Yield drifts are calculated analytically and taken from experimental results. The resulting shear failure drifts have a difference exceeding 2.0%, with the experimental shear failure bracketed by the predictions. For this comparison the analytical yield drift is determined from section analysis (neglecting bar slip and yield penetration), and the experimental yield drift is taken from experimental data. In both cases the yield drift is defined by drawing a secant through the point corresponding to 70% of the maximum shear force of the lateral load-drift relationship (as shown in Figure 4-13).

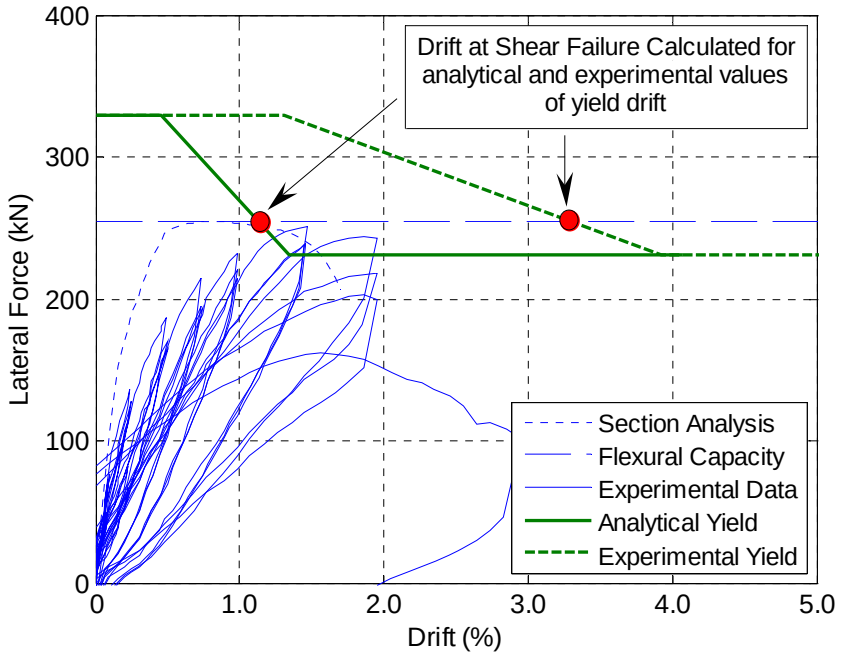

Figure 4-12 Effect of yield displacement on Sezen Shear Strength model

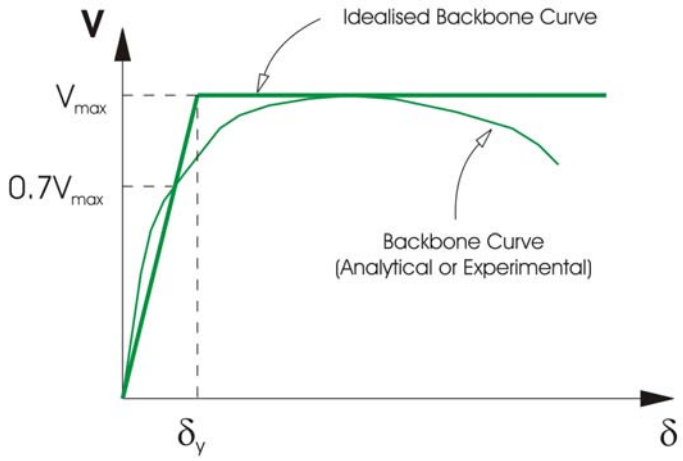

Figure 4-13 Determination of yield drift for Sezen Model

4.7.2 Drift Limit Models

The second category of models, provide backbones to describe the available shear capacity and drift levels at which significant degradation occurs. Three models are compared; NZSEE Assessment Guidelines, FEMA 356 backbone model, and the Elwood backbone model. A general outline of the process for each model is given below, with the full calculation process for each included in Appendix C.

The NZSEE assessment guidelines (2006) provide a conservative limit on the available ductility given the specimen details and axial load (Equation (4-6)). No specific information regarding lateral force capacity is given beyond the shear capacity relationship investigated previously in Section 4.7.1. The conservative nature is a result of the relationship being a reconfigured design equation.

$$\frac{\varphi_u}{\varphi_y}=\left(\frac{A_{sh}}{s_h h''}+0.006\right).\frac{A_c}{A_g}\frac{f_{yt}}{f_c'}\frac{\phi.f_c' A_g}{N^*}.111+33\rho_t m-22 \qquad (4\text{-}6)$$

FEMA 356 (2000) provides tabulated values for available plastic rotational capacity. Flexural yield of the backbone (point B) is determined by summing contributions from flexure and shear. Loss of lateral capacity (point C) and loss of residual capacity (point E), occur after an

inelastic rotational capacities interpolated from a table that considers; axial load ratio, shear stress and the compliance (or non-compliance) of the transverse reinforcement provided. The residual strength ratio (c) is taken as 20% of the lateral capacity of the section.

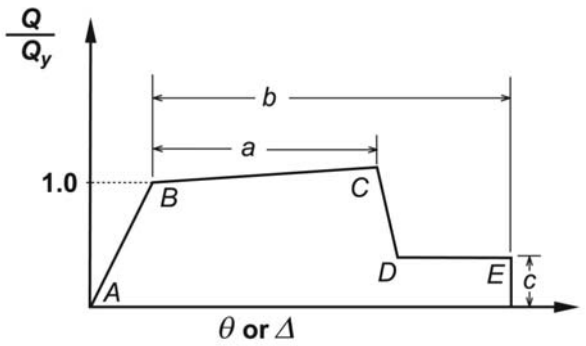

Figure 4-14 Illustration of the FEMA 356 backbone

The Elwood backbone (Elwood and Moehle 2006) calculates the inelastic section capacity and the drift at; yield, shear failure, and axial failure (Equations (4-7) to (4-9)). The yield drift has contributions from flexure, shear and slip. Drift at shear failure is dependent on the area ratio of transverse steel provided, the shear stress in the column and the applied axial load. The drift at axial failure is contingent on the existence of a shear-failure plane nominally at an angle of 65°, and depends on the axial load and the area, spacing and strength of the transverse reinforcement provided. However, the Elwood model backbone for specimen 24L-300-2D calculates the drift at axial failure to be lower than the drift at shear failure. And, as the model presupposes shear failure the drift at axial failure is adjusted to coincide with the drift at shear failure. This is evident in the vertical nature of the backbone shown in Figure 4-16 at approximately 2.2%.

$$\delta_y = \delta_{flex} + \delta_{shear} + \delta_{slip} \tag{4-7}$$

$$\delta_s = \frac{3}{100} + 4\rho'' - \frac{1}{40}\frac{\upsilon}{\sqrt{f'_c}} - \frac{1}{40}\frac{P}{A_g f'_c} \geq \frac{1}{100} \tag{4-8}$$

$$\delta_a = \frac{4}{100}\frac{1+\tan^2 65°}{\tan 65° + P\left(\frac{s}{A_{st} f_{yt} d_c \tan 65°}\right)} \tag{4-9}$$

Performance comparisons are made in Figure 4-15 between all three models and the experimental results from test specimen 24L-300-2D. As expected the curvature ductility limit proposed by the NZSEE Assessment Guidelines is shown to be conservative (and will also be subject to the determined value of yield curvature as highlighted previously). The FEMA 356 model is very conservative regarding the level of drift (less than 1.0%) at which the lateral strength of the section reduces to the residual capacity. In contrast the experimental data shows that the lateral capacity was maintained to a drift level of nearly 2.0%. The Elwood backbone however, more closely resembles the experimental results, although the initial stiffness of the backbone is underestimated for levels of drift below 0.5%. This is due to the inclusion of the slip component into the determination of the yield drift, and could easily be accounted for by adding an additional point into the backbone corresponding to first cracking of the section.

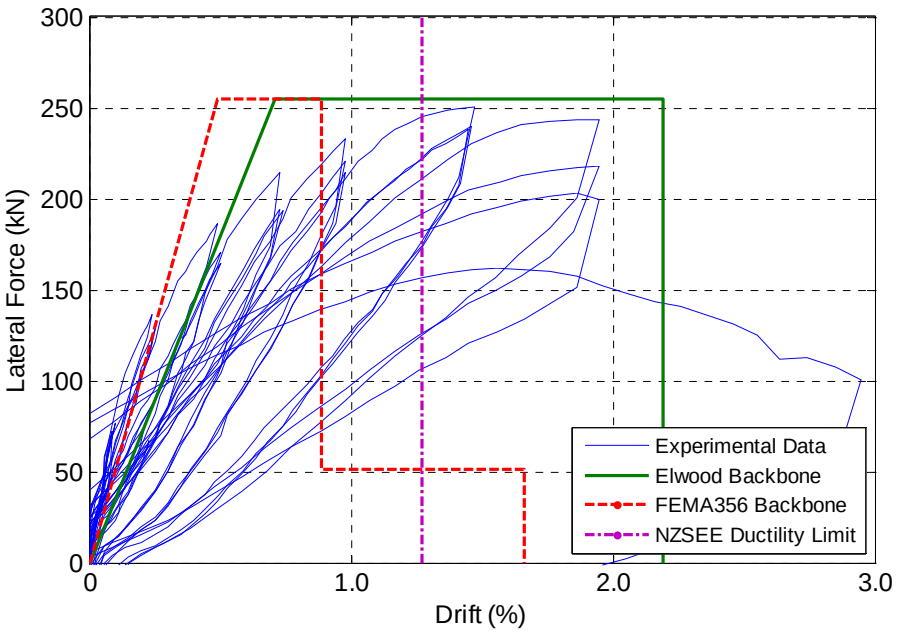

Figure 4-15 Backbone model and limit comparisons for Specimen 24L-300-2D

To determine the additional 'cracking' point in the modified backbone requires the cracking moment (M_{cr}), and drift (δ_{cr}). The cracking moment and displacement are functions of the stress required to crack the concrete (f_{cr}), the stress resulting from the axial load (f_N), and the transformed section second moment of area ($I_{transformed}$), as given by Equations (4-10) and (4-11). See Appendix C for calculations in full.

$$F_{cr} = \frac{M_{cr}}{L} = \frac{\left(f_{cr} + f_N\right)}{D/2} \cdot \frac{I_{transformed}}{L} \tag{4-10}$$

$$\delta_{cr} = \frac{\varphi_{cr} L}{3} = \frac{M_{cr}}{E_c I_{transformed}} \cdot \frac{L}{3} \tag{4-11}$$

Considering the modified Elwood model in isolation, Figure 4-16 and Figure 4-17 compare the model (including the 'cracking' point) and the experimental data for the uni-directional specimens 24L-300-2D and 30L-300-2D respectively. As is evident the modified backbone model captures the behaviour of the specimens with a high degree of accuracy. Specimen 24L-300-2D loses significant shear capacity just prior to the modelled drift limit, and although the axial failure is delayed for a further half cycle after the peak beyond the limit is reached, minimal additional excitation is required.

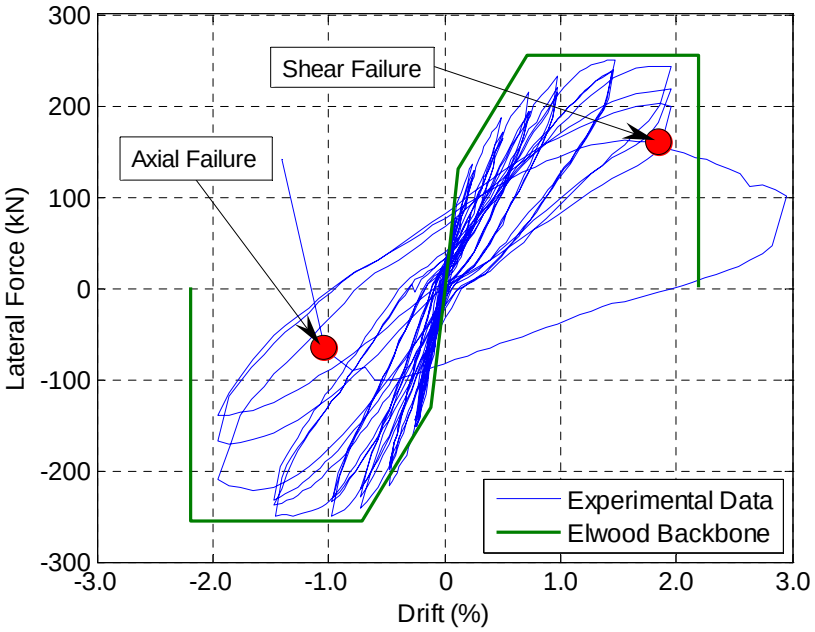

Figure 4-16 Elwood Backbone model comparison for specimen 24L-300-2D

Specimen 30L-300-2D has considerably more stable hysteresis as a result of the increased lap-splice length provided but shear and coincident axial failure occur at a similar drift as specimen 24L-300-2D. This highlights the independence of the modelled shear and axial failure drift from the capacity of the lap-splice.

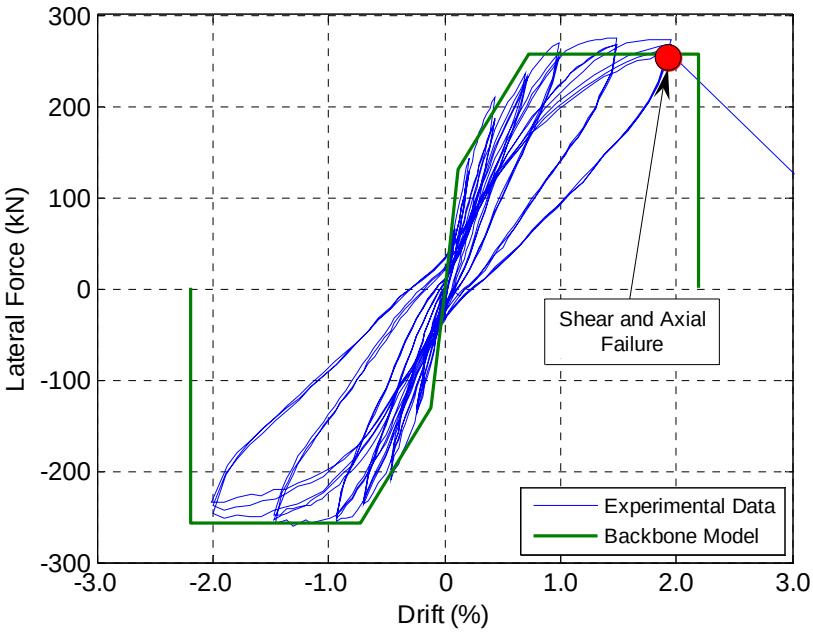

Figure 4-17 Elwood Backbone model comparison for specimen 30L-300-2D

References

ACI T1.1-01. (2001). "Acceptance Criteria for Moment Frames Based on Structural Testing."

Elwood, K. J., and Moehle, J. P. (2005a). "Axial Capacity Model for Shear-Damaged Columns." *ACI Structural Journal*, 102(4), 578-587.

Elwood, K. J., and Moehle, J. P. (2005b). "Drift Capacity of Reinforced Concrete Columns with Light Transverse Reinforcement." *Earthquake Spectra*, 21(1), 71-89.

Elwood, K. J., and Moehle, J. P. (2006). "Idealised Backbone Model For Existing Reinforced Concrete Columns and Comparisons With FEMA 356 Criteria." *Struct. Design Tall Spec. Build.*, 15, 553-569.

FEMA356. (2000). "Prestandard and Commentary for the Seismic Assessment of Buildings." FEMA.

Guidelines, N. (2006). "Assessment and Improvement of the Structural Performance of Buildings in Earthquakes." NZSEE Study Group Recommendations.

Melek, M., Wallace, J. W., and Conte, J. P. (2003). "Experimental Assessment of Columns with Short Lap Splices Subjected to Cyclic Loads." *PEER Report*, 04.

Sezen, H., and Moehle, J. P. (2004). "Shear Strength Model for Lightly Reinforced Concrete Columns." *Journal of Structural Engineering*, 130(11), 1692-1703.

5.0 Experimental Results for Bi-Directional Tests

5.1 Bi-directional Quasi-static Protocol

The bi-directional loading imposed is a development of the increasingly familiar 'cloverleaf' protocol. In this version the 'leaves' have been scaled such that the peak displacement in each of the principal component directions is equivalent to the drift for the associated level of drift for the uni-directional protocol shown previously. Each of the 'leaves' is traversed once only at each level of drift, and an additional uni-directional excursion is undertaken to each of the four principal axis. The imposed protocol and the path followed at each level is illustrated in Figure 5-1 with the excursions are labelled 1 through 8.

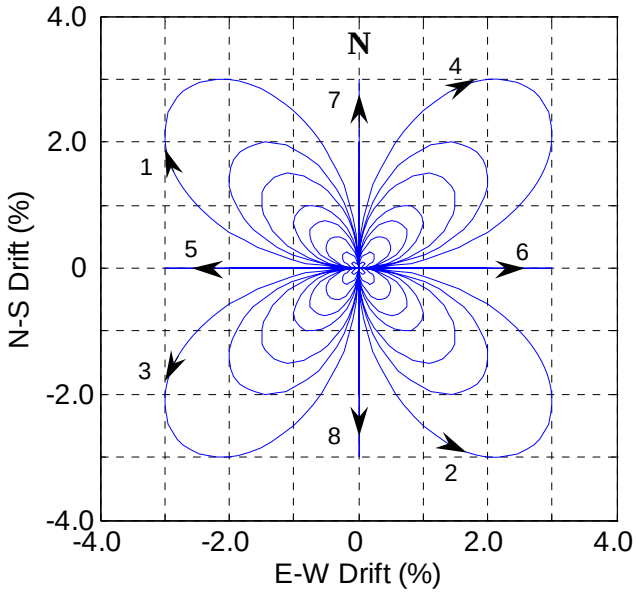

Figure 5-1 Bi-directional loading protocol

Resolving the bi-directional protocol into the principal components illustrates the rationale: in both principal axes the drift protocol undergoes an equivalent three peaks in the positive and negative directions (illustrated in Figure 5-2 below), equivalent to the uni-directional protocol. As a consequence the additional demands associated with bi-directional loading are able to be assessed, such as the increased rate of splice capacity degradation and onset of damage at drift levels significantly lower than associated with uni-directional loading. Of particular interest is the applicability of the drift based failure limits when applied to full bi-directional loading.

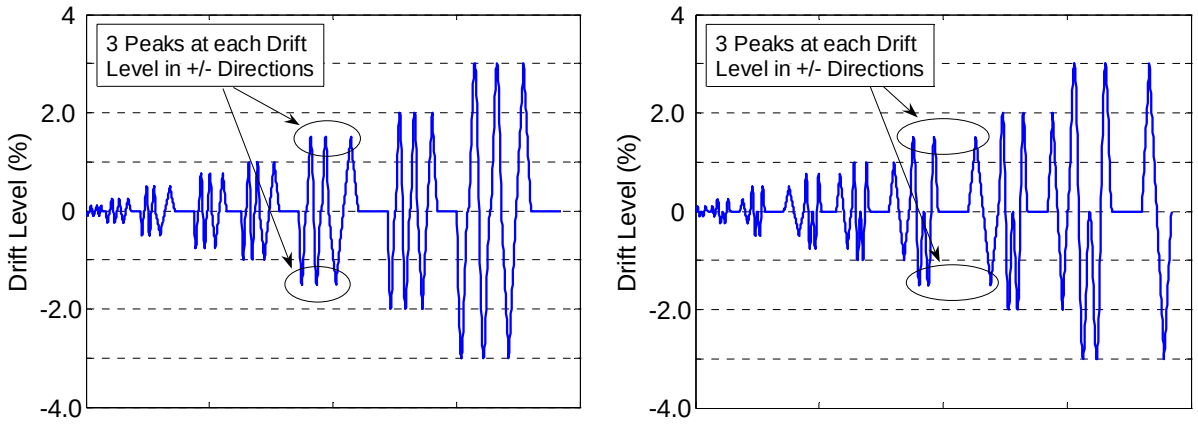

a) E-W Component **b) N-S Component**

Figure 5-2 Components of bi-directional loading protocol

5.2 Material Testing

Prior to testing each specimen under the designed loading protocol, material tests were carried out on each of the component materials; longitudinal and transverse steel, and the concrete compressive strength. These results are summarised in Table 5-1 below. The yield strength of the longitudinal steel (f_y = 315 MPa) is very similar to the target capacity. The yield strength of the transverse steel provided (f_{yt} = 439 MPa), as previously described in Chapter 4.2 will have a minimal effect. Concrete compressive strength (f'_c) ranges from 24.3 to 28.4 MPa, these strengths are lower than the target value, but lie within the range expected of in-situ concrete for the columns of interest.

Table 5-1 Summary of material properties for all test specimens

Column Designation	f'_c (MPa)	N/f'_cA_g	f_y (MPa)	f_u (MPa)	f_{yt} (MPa)
24L-300-3D	28.4	0.35	315	465	439
24L-300-3D-R	27.5	0.18	315	465	439
30L-300-3D	24.3	0.41	315	465	439

5.3 Specimen 24L-300-3D

5.3.1 Test Observations

Observations made during the testing of Specimen 24L-300-3D are presented here. The progression of damage sustained by the specimen during testing is shown in Figure 5-3 (a) through (e). Key damage states and the associated drift of occurrence are listed in the following bullet points:

- 0.5% drift cycles, first flexural cracks occur in the plastic hinge region along the length of the lap-splice (as shown in Figure 5-3 (a)).
- 0.75% drift cycles, shear cracks propagate from the flexural cracks initiated previously and splice splitting initiates cracking along the plane of the splices (Figure 5-3 (b)).
- 1.0% drift cycles, shear and splice-splitting cracks extend significantly (Figure 5-3 (c)).
- 1.5% drift (1st 'loop'), shear failure occurs (as defined previously) and considerable spalling of the splice cover concrete occurs splice (Figure 5-3 (d)).
- 1.5% drift (2nd 'loop'), loss of axial load carrying capacity occurs in addition to further expulsion of the splice cover concrete and buckling of the poorly restrained cranked longitudinal bars (Figure 5-3 (e)).

Post-failure observations include:

- Buckling of the poorly restrained cranked longitudinal bar at the top of the lap-splice, as shown in Figure 5-3 (f).
- Figure 5-3 (g) illustrates the shear failure 'cone' sustained by the specimen.
- The residual deformation of specimen 24L-300-3D is illustrated in Figure 5-3 (h).

Clearly evident from this test is the much reduced drift capacity associated with bi-directional loading as failure occurred at a drift of 1.5% (resolved to in-plane component). This capacity is considerably lower than the performance targets outlined in both the NZSEE Guidelines (2006), and FEMA 356 (2000).

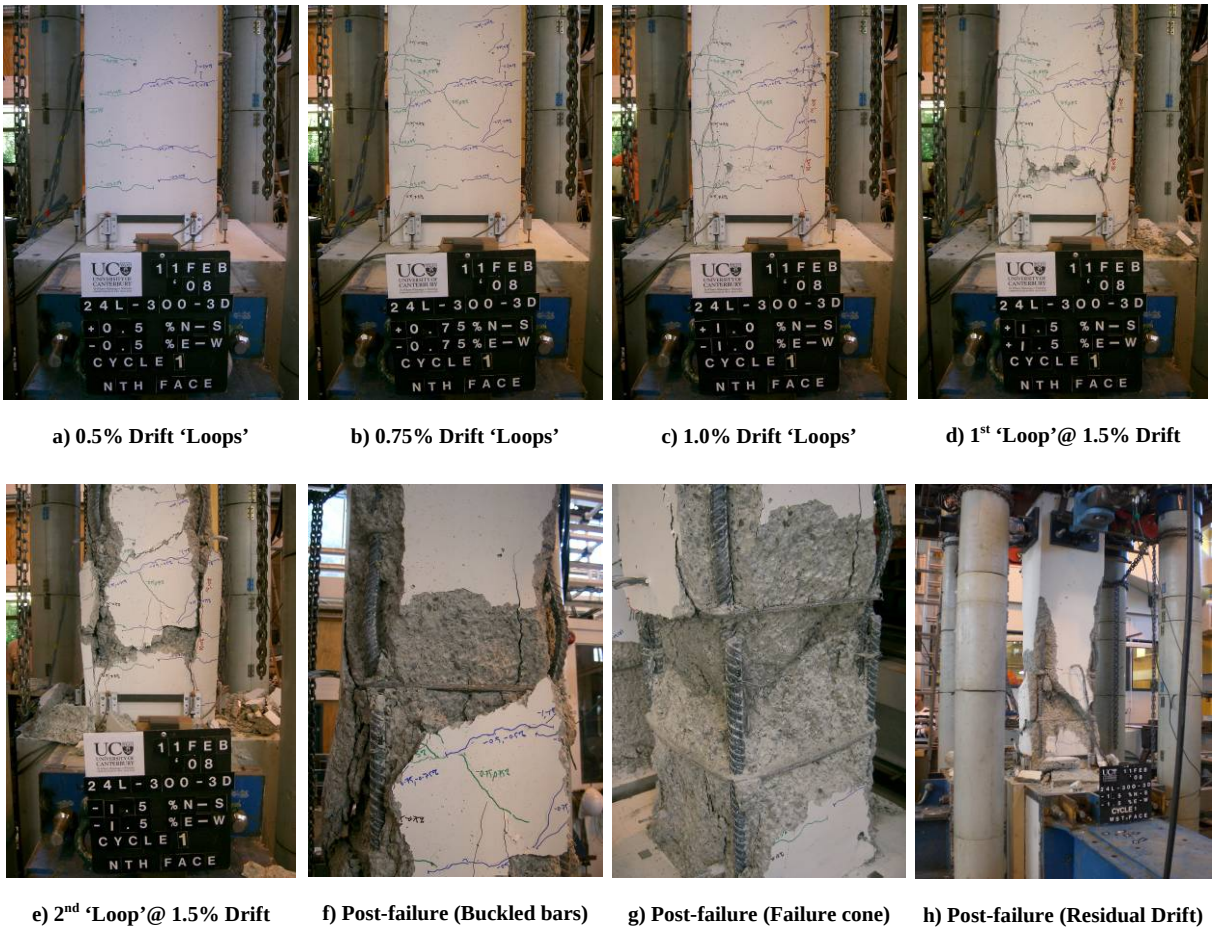

a) 0.5% Drift 'Loops' **b) 0.75% Drift 'Loops'** **c) 1.0% Drift 'Loops'** **d) 1st 'Loop'@ 1.5% Drift**

e) 2nd 'Loop'@ 1.5% Drift **f) Post-failure (Buckled bars)** **g) Post-failure (Failure cone)** **h) Post-failure (Residual Drift)**

Figure 5-3 Damage sequence of specimen 24L-300-3D

5.3.2 Force versus Drift Response

Figure 5-4 illustrates measured Force versus Drift response of specimen 24L-300-3D. Also shown in the figure are the imposed drift protocol in plan view, and the components in the N-S and E-W directions (the protocol is represented by dashed lines after specimen failure). The bi-directional loading and the lateral forces have been reduced to the in-plane components for clarity of presentation. The points at which shear and axial failure occur are highlighted on the figure. Due to the nature of the imposed protocol the shear (and axial) failures occur at different levels of drift in each of the component directions. Termination of the test occurred once more upon the axial deformation reaching an imposed limit of 15mm; however the residual axial capacity was not recorded.

Similar to the unidirectional testing in Chapter 4.0, Figure 5-4 illustrates marked cyclic deterioration of the lateral capacity and noticeable 'pinching' of the hysteresis loops as the test progresses. Onset of lap-splice degradation occurs considerably earlier than in the uni-directional loading tests. This is due to the higher strains in the longitudinal reinforcement associated with loading imposed to all quadrants of the bi-directional test specimens.

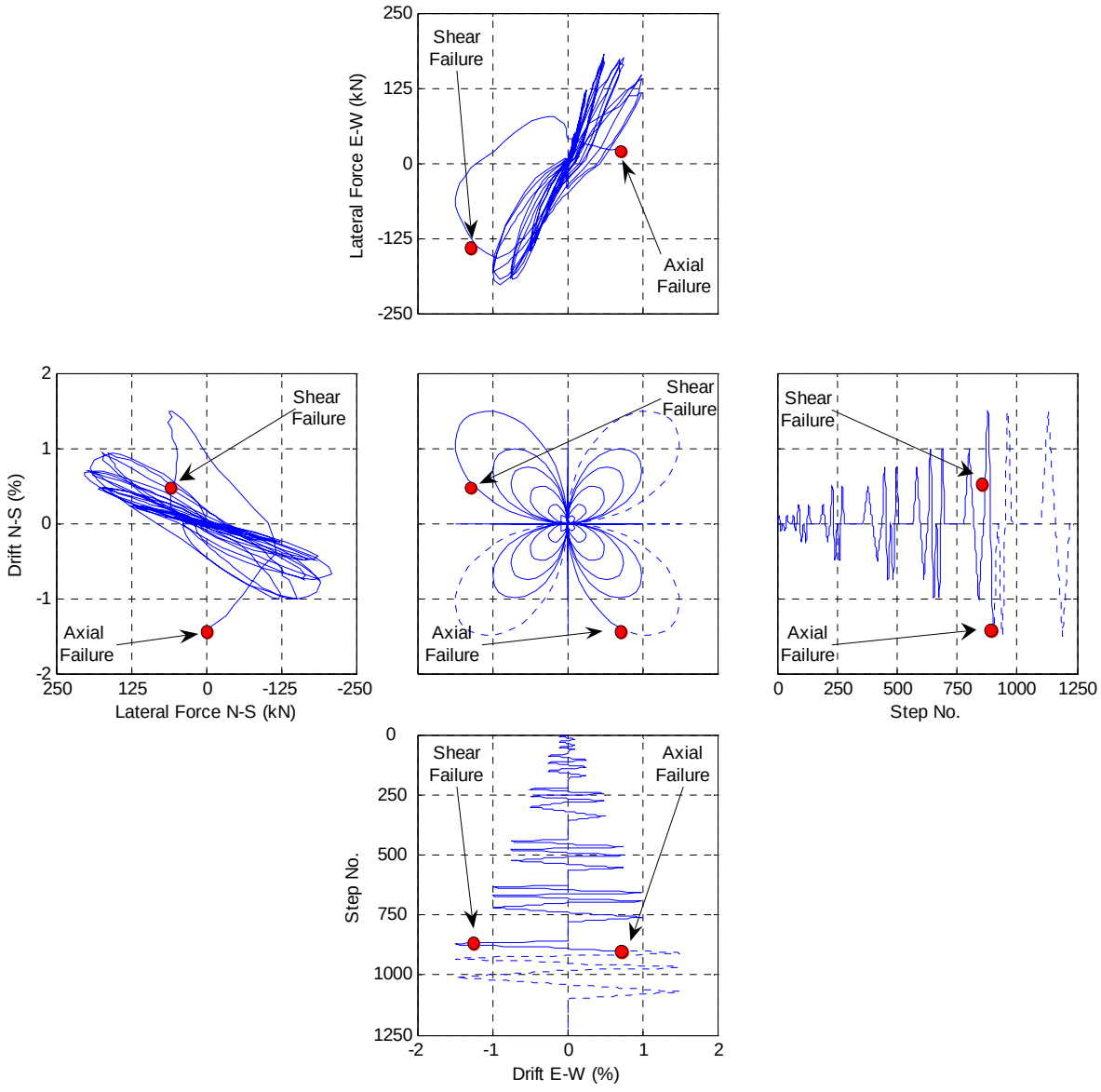

Figure 5-4 Experimental data for specimen 24L-300-3D

5.4 Specimen 24L-300-3D-R

5.4.1 Test Observations

Observations made during the testing of Specimen 24L-300-3D-R are presented here. The progression of damage sustained by the specimen during testing is shown in Figure 5-5 (a) - (g). Key damage states and the associated drift of occurrence are as follows:

- 0.5% drift cycles, first flexural and shear cracks occur in the plastic hinge region along the length of the lap-splice (as shown in Figure 5-5 (a)).
- 0.75% drift cycles, shear cracks propagate and splice splitting cracks begin to form along the plane of the splices (Figure 5-5 (b)).
- 1.0% drift cycles, splice-splitting cracks extend (Figure 5-5 (c)).
- 1.5% drift cycles, shear cracks extend and splice splitting cracks form completely (Figure 5-5 (d)).
- 2.0% drift cycles, expulsion of the splice cover concrete occurs (Figure 5-5 (e)).
- 3.0% drift (1st 'loop'), further expulsion of the splice cover concrete occurs and the inadequately restrained cranked longitudinal bars begin to buckle (Figure 5-5 (f)).
- 3.0% drift (3rd 'loop'), loss of axial capacity occurs and considerable quantities of cover concrete are expelled from all faces of the column (Figure 5-5 (g)).

Post-failure observations include:

- Figure 5-5 (h) illustrates the condition of the specimen at the end of testing. Loose concrete has been removed exposing the 'cone' of core concrete remaining, and the buckled longitudinal bars, note that buckling of the bars occurs both at the crank and at the mid-height of the splice on opposite sides.

This test illustrates the increase in drift capacity associated with reduced axial load. The capacity attained is considerably closer to the performance targets outlined in both the NZSEE Guidelines (2006), and FEMA 356 (2000).

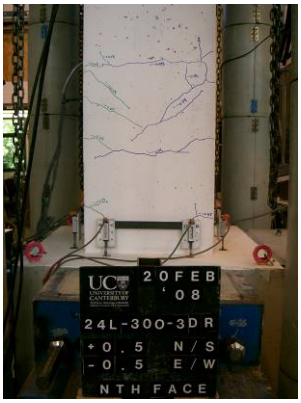

a) 0.5% Drift Cycles

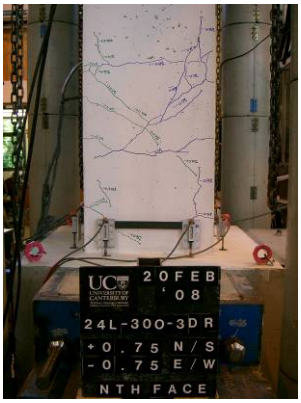

b) 0.75% Drift Cycles

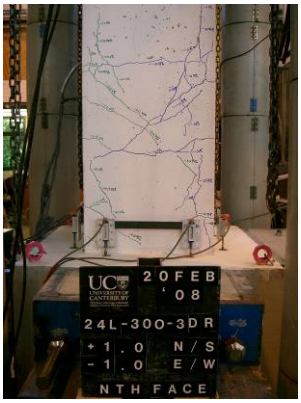

c) 1.0% Drift Cycles

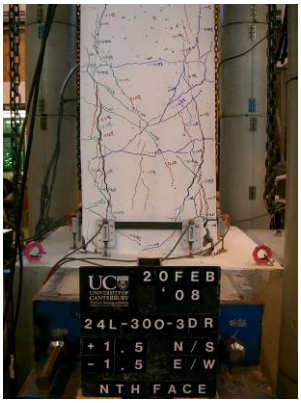

d) 1.5% Drift Cycles

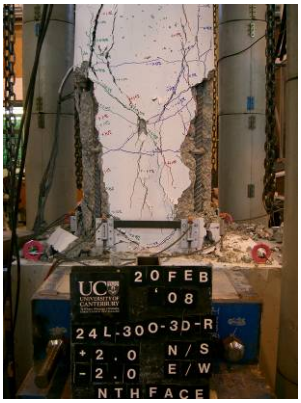

e) 2.0% Drift Cycles

f) 1st 'loop' 3.0% Drift Cycles

g) 3rd 'loop' 3.0% Drift Cycles

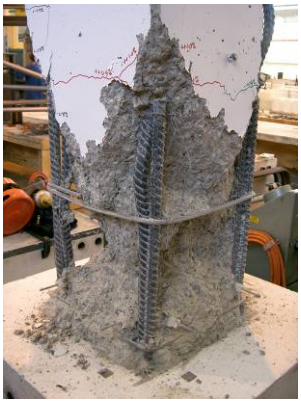

h) Post-failure Damage

Figure 5-5 Damage sequence of specimen 24L-300-3D-R

5.4.2 Force versus Drift Response

The imposed loading and resulting in-plane components of the Force-Drift relationships are shown in Figure 5-6. Shear failure of the specimen (as defined previously) occurs at a relatively low level of drift (just prior to 1.5%), and although the specimen exhibits a moderate amount of ductility beyond this, the shear capacity degrades substantially from this point forward. Axial failure of the specimen occurs during the 3rd 'loop' of the 3% drift level of the imposed protocol. Beyond shear failure the rate at which the shear capacity degrades is almost linear (this will be revisited in the subsequent modelling section). The reduced axial load has a significant effect on the performance of the lap-splice degradation. As can be seen from the figure each subsequent level of drift imparts a reduction in lateral capacity, which holds fairly constant for the cycles within the drift level. This is attributable to the increased drift imposing additional tensile strains on the lap-splice thus causing damage, however for subsequent cycles at each drift level the damage has been done hence the hysteresis loops for each drift level display a degree of stability.

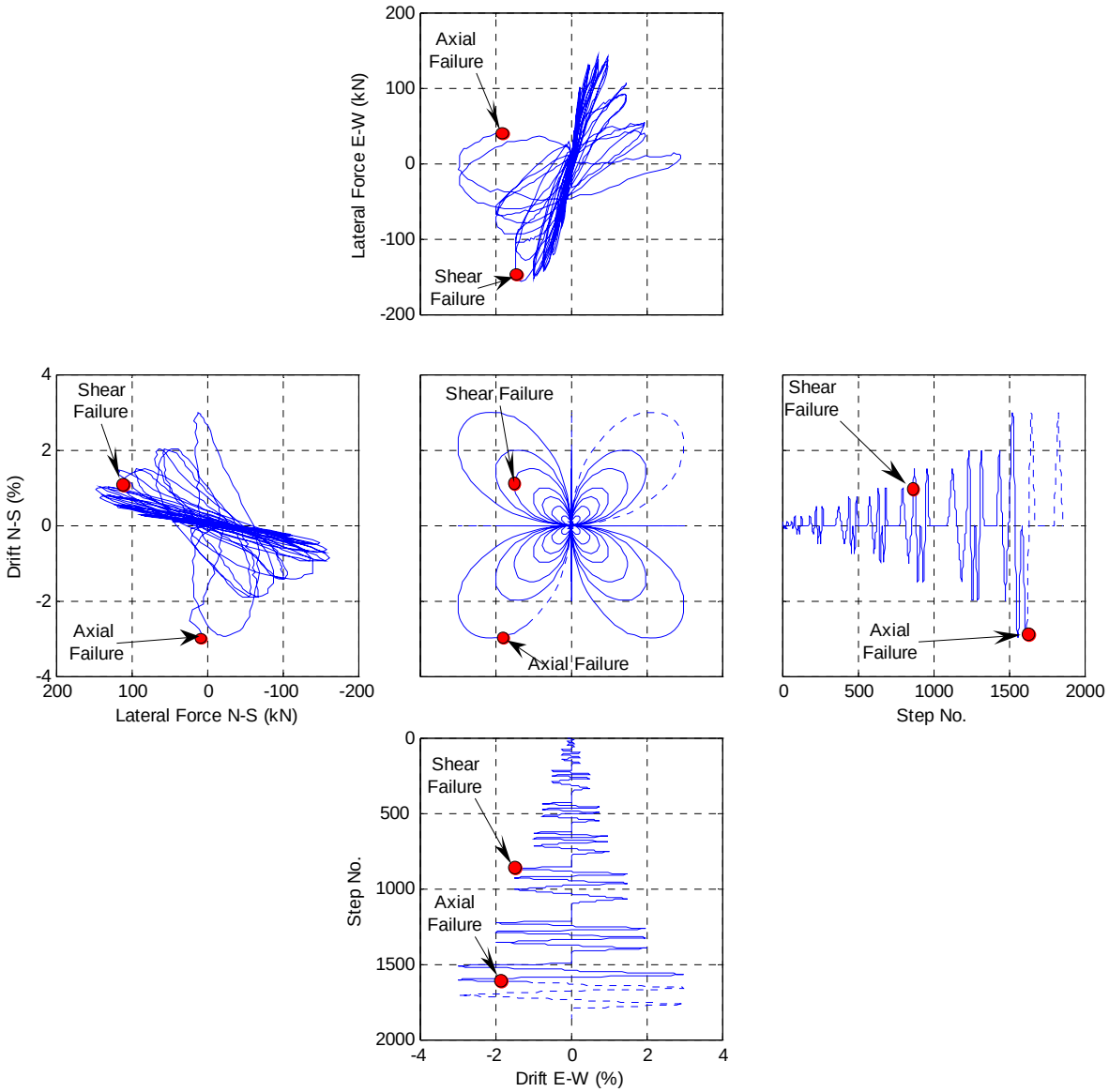

Figure 5-6 Test results for specimen 24L-300-3D-R

5.5 Specimen 30L-300-3D

5.5.1 Test Observations

Observations made during the testing of Specimen 30L-300-3D are presented here. The progression of damage sustained by the specimen during testing is shown in Figure 5-7 (a) through (f). Key damage states and the associated drift of occurrence are listed in the bullet points below:

- 0.5% drift cycles, first flexural cracks occur in the plastic hinge region along the length of the lap-splice (as shown in Figure 5-7 (a)).
- 0.75% drift cycles, shear cracks propagate from the flexural cracks initiated previously and splice splitting cracks begin to initiate along the plane of the splices (Figure 5-7 (b)).
- 1.0% drift cycles, shear cracks extend significantly and splice-splitting cracks fully form (Figure 5-7 (c)).
- 1.5% drift (1st 'loop'), shear failure occurs and considerable shear cracks form and splitting cracks open (Figure 5-7 (d)).
- 1.5% drift (2nd 'loop'), expulsion of the splice cover concrete occurs at the column corner corresponding to the maximum tensile force (Figure 5-7 (e)).
- 1.5% drift (3rd 'loop'), axial failure of the column occurs, along with expulsion of the splice cover concrete and separation of the cover concrete across the column faces.

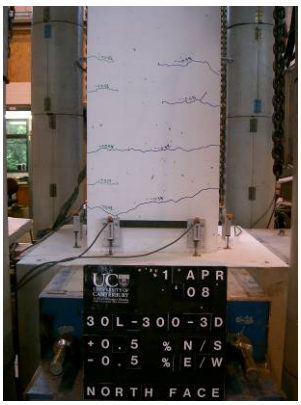

a) 0.5% Drift Cycles

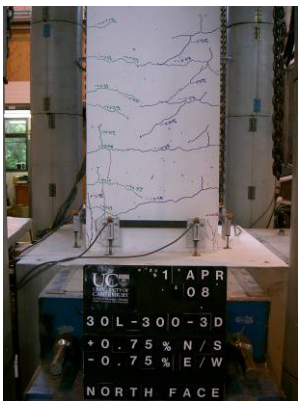

b) 0.75% Drift Cycles

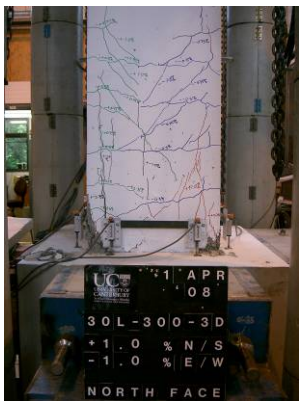

c) 1.0% Drift Cycles

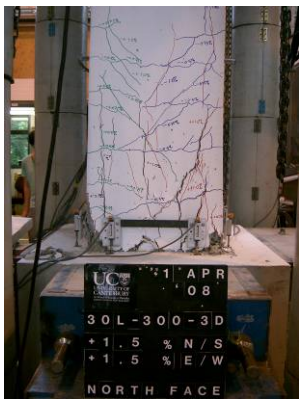

d) 1st Loop 1.5% Drift Cycles

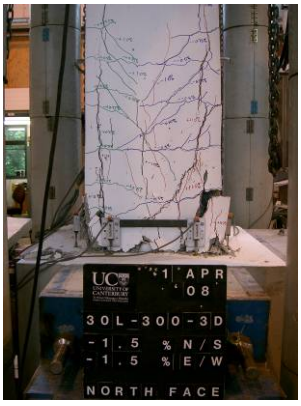

e) 2nd Loop 1.5% Drift Cycles

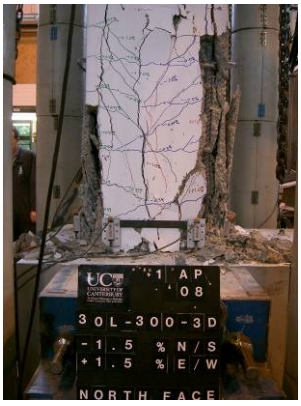

f) 3rd Loop 1.5% Drift Cycles

g) Concrete expulsion

h) Buckled longitudinal bars

Figure 5-7 Damage sequence of specimen 30L-300-3D

Post-failure observations include:

- Figure 5-7 (g) illustrates the separation of the cover concrete on the specimen faces.
- Buckling of the poorly longitudinal bars occurred at the mid-height of the lap-splice, as shown in Figure 5-7 (h)

5.5.2 Force versus Drift Response

The force-drift relationship for this specimen is shown in Figure 5-8 below. As was illustrated in the uni-directional tests, the additional length of lap-splice provided reduces the degradation of lateral capacity prior to shear failure at approximately 1% drift. Beyond this point degradation is considerable and sudden, with complete loss of axial capacity occurring two 'loops' later.

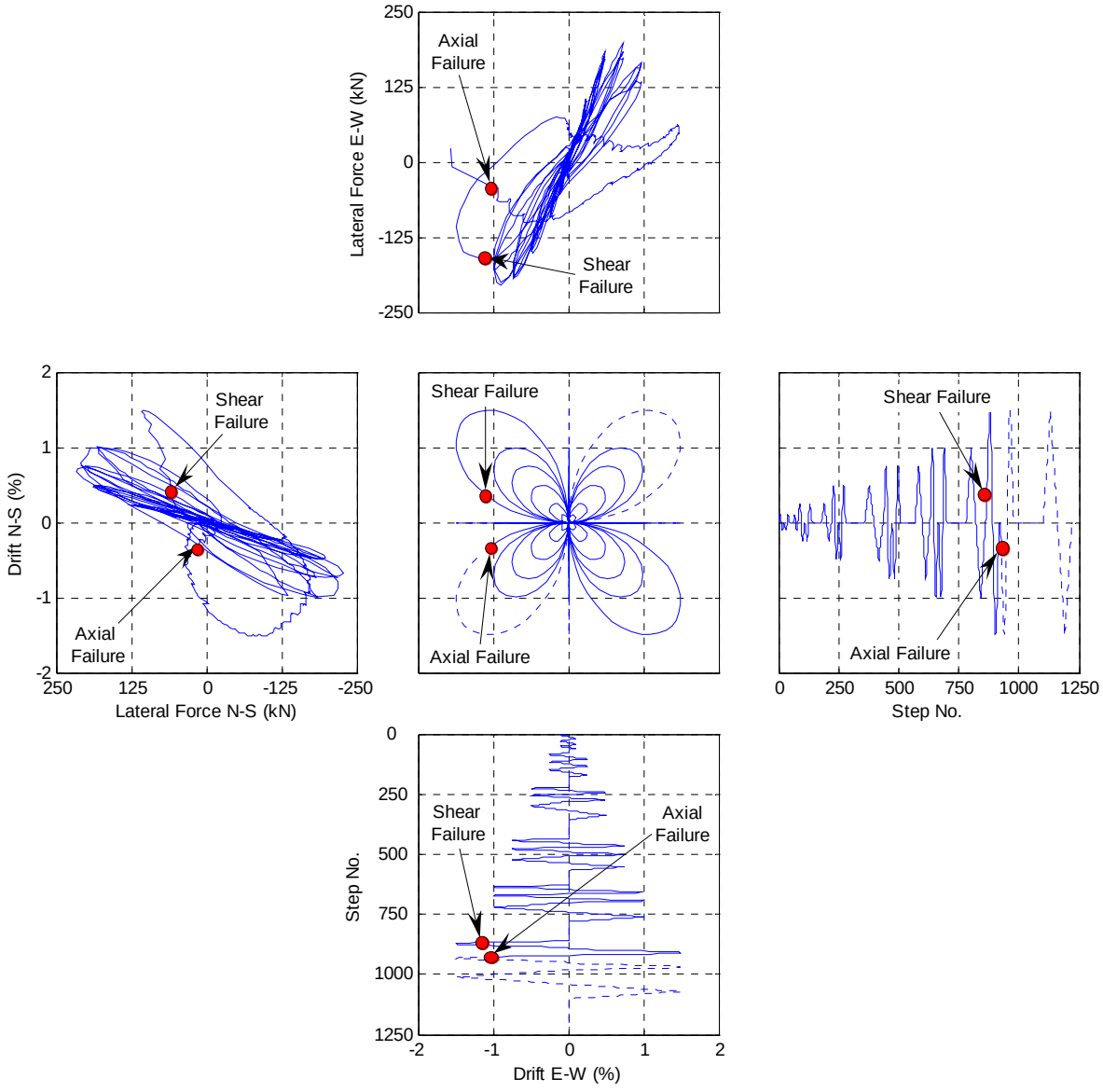

Figure 5-8 Test results for specimen 30L-300-3D

5.6 Relative Contributions to Displacement

Potentiometers were also attached to the base of the bi-directional tests to determine the base rotation induced contribution to the total displacement. To this end two linear potentiometers were attached to all four faces of the columns during testing. The potentiometers attached to each face are located to determine the relative rotation resulting from displacement in the direction parallel to the column face. However, the potentiometers will also capture displacement in the orthogonal direction. This effect is negated by the assumption that plane sections remain plane as the relative displacement of the two pots will only capture the displacement in the parallel direction.

This is verified in Figure 5-9 below, taken from the bi-directional testing for specimen 30L-300-3D. The figure illustrates the calculated North-South displacement caused by base rotation using the pots on both the East and West column faces. As can be seen the calculated contributions to displacement are very similar until data point 700 (corresponding to the 1.0% drift cycles), at which point the specimen has sustained significant damage. One further beneficial consequence of this effect is an element of redundancy in the acquisition of the base rotation potentiometer data. Typically the calculated base rotation is determined using the average of the two opposing sets of data (unless a lack of data requires otherwise).

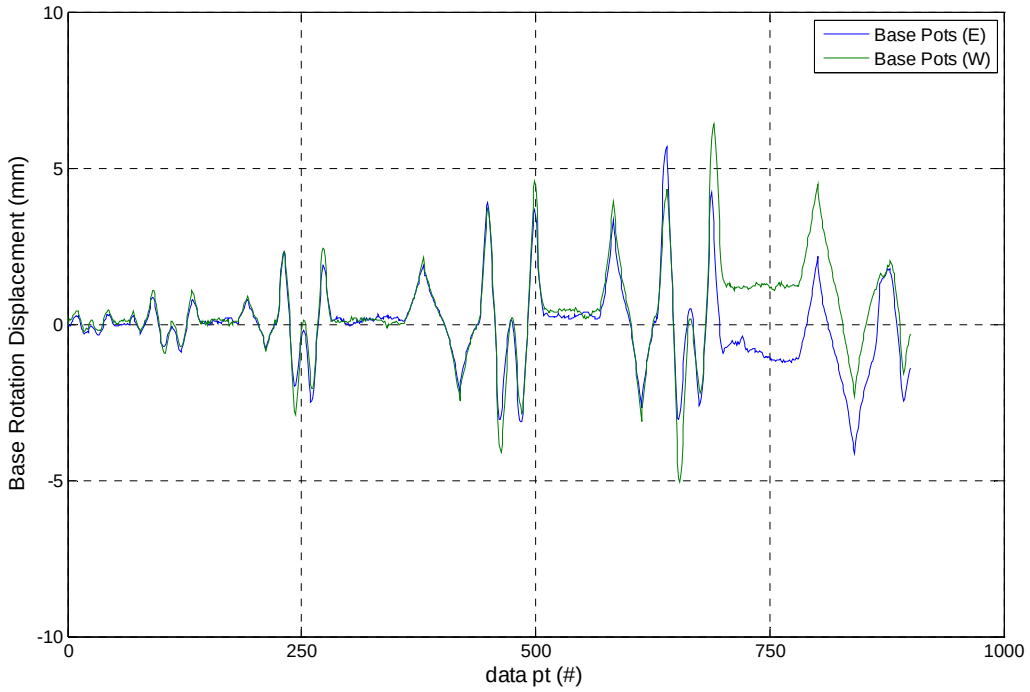

Figure 5-9 Illustration of plane sections

In Figure 5-10 below, the contributions to the total displacement for specimen 24L-300-3D are shown. Clearly evident is the significant reduction in the contribution arising from the base rotation. This is likely a result of the increased strain and associated levels of damage in the lap-splice region arising from the bi-directional displacement protocol.

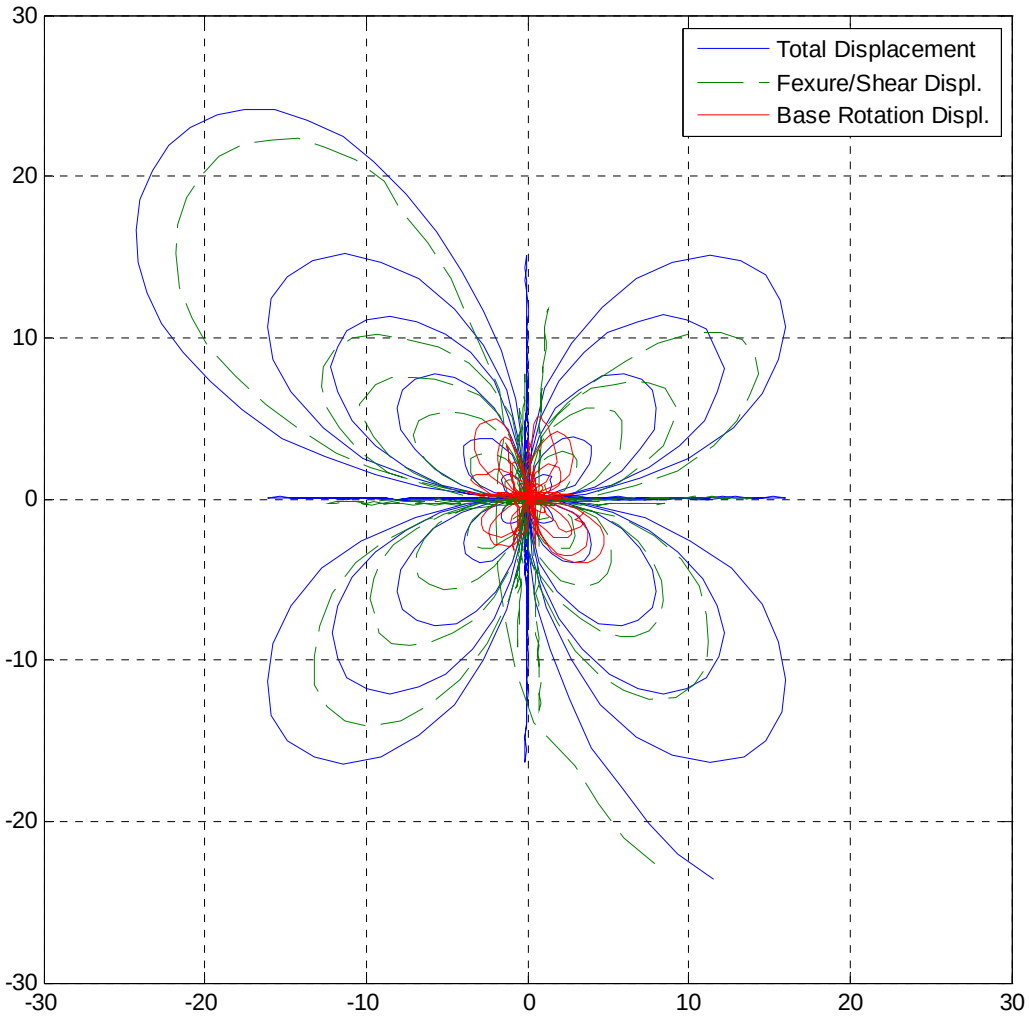

Figure 5-10 Contributions to Total Displacement for Specimen 24L-300-3D

The effect of the additional splice length on the relative contribution to displacement is illustrated in Figure 5-11 below. Similar to the uni-directional tests the contribution arising from the base rotation is significantly increased for this specimen, again due to the reduced level of damage to the splice region. The reduced level of damage is evident when comparing damage photographs (as shown in Figure 5-12) of the two specimens taken during testing.

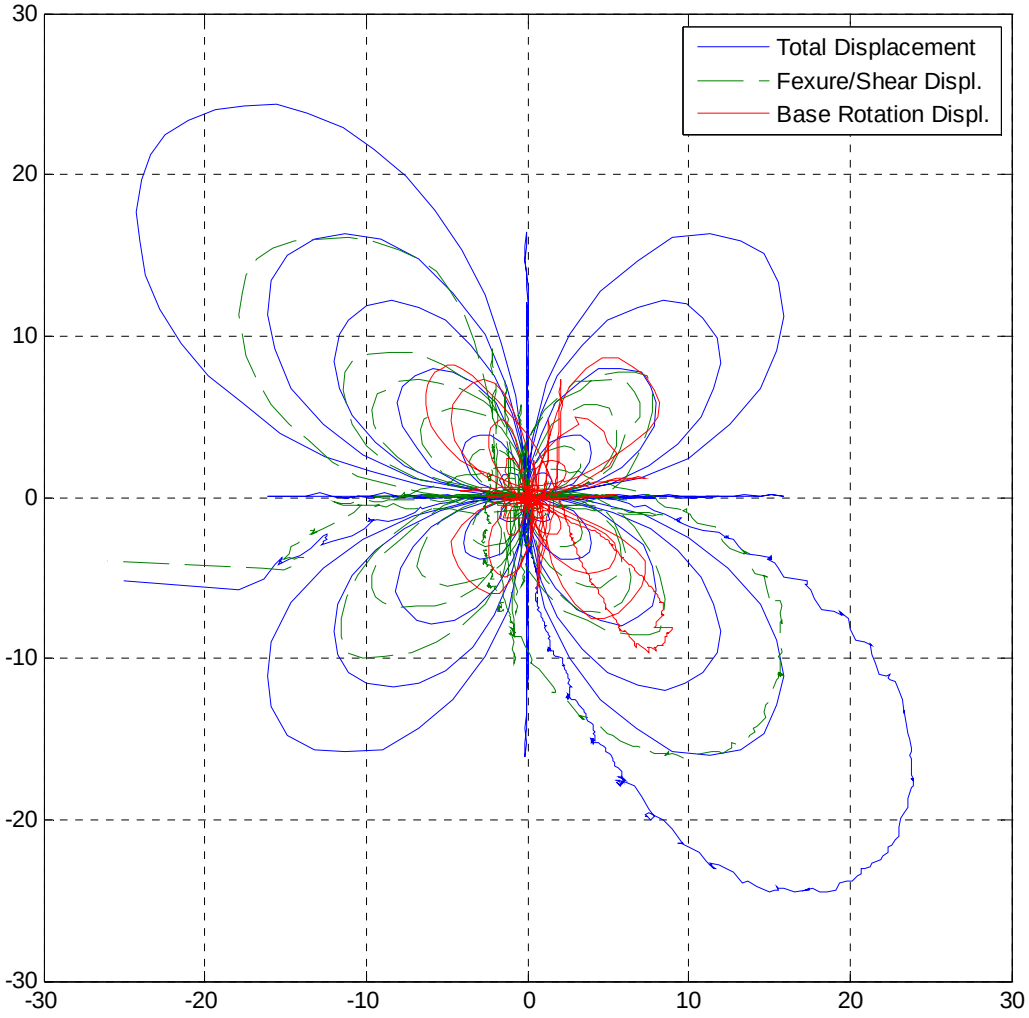

Figure 5-11 Contributions to Total Displacement for Specimen 30L-300-3D

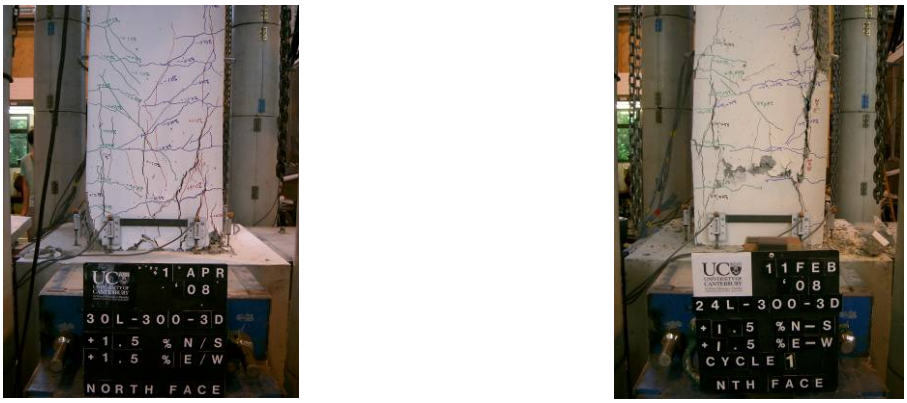

a) Specimen 30L-300-3D (1st Loop 1.5% Drift Cycles) **b) Specimen 24L-300-3D (1st 'Loop'@ 1.5% Drift)**

Figure 5-12 Damage Comparison between Specimens 24L-300-3D and 30L-300-3D

The final comparison (shown in Figure 5-13) is for specimen 24L-300-3D-R, which corresponds to the minimum allowable splice length and a reduced axial load of 1000kN. Clearly evident is the significant increase in the contribution to the total displacement from the base rotation component. This is caused by the reduction in axial load resulting in higher curvature (and hence displacement) corresponding to a similar level of tensile strain in the longitudinal bars. Associated with this is a reduction in splice damage and a greater base rotation, both of which increase the relative contribution from the rotation at the base of the column.

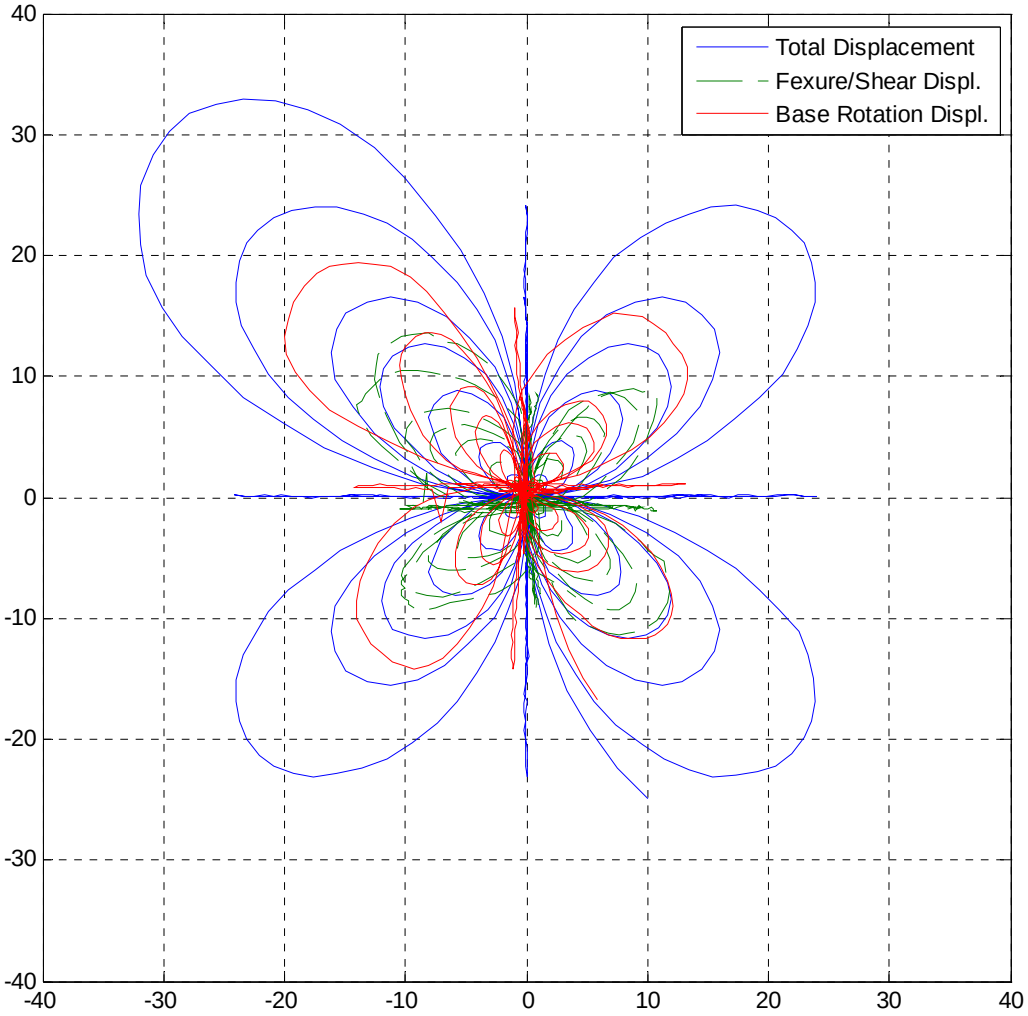

Figure 5-13 Contributions to Total Displacement for Specimen 24L-300-3D-R

5.7 Model Development and Experimental Comparisons

5.7.1 Limits Surface Model for Bi-Directional Loading

The Elwood backbone model verified in Chapter 4.0 calculates the shear and axial drift limits for uni-directional loading (at any loading angle) by assessing the section capacity and the density and effectiveness of the transverse reinforcement. Hence for a loading angle of 45° the stirrups have a reduced effectiveness (factor of $1/\sqrt{2}$) due to geometry, affecting both the shear and axial drift limits. Extending the uni-directional backbone model to encompass full bi-directional loading requires the shear and axial drift capacity to be determined for all angles of loading. However, the full relationship can be approximated by calculating capacities at a reduced number of angles and fitting a limit curve through these points.

The resulting Limit Surface model is derived by calculating the modified Elwood backbone (including the 'cracking' point) for loading angles of 0° and 45° and fitting the power law relationship shown in Equation (5-1) through the calculated points. The value of α, used in the relationship is adjusted to ensure the Limit Curve 'fits' the calculated drift values. Figure 5-14 below illustrates the concept, with two separate limit curves for shear and axial failure shown.

$$\left(\frac{\delta_x}{\delta_{x,calculated}}\right)^{\alpha}+\left(\frac{\delta_y}{\delta_{y,calculated}}\right)^{\alpha}=1 \qquad (5\text{-}1)$$

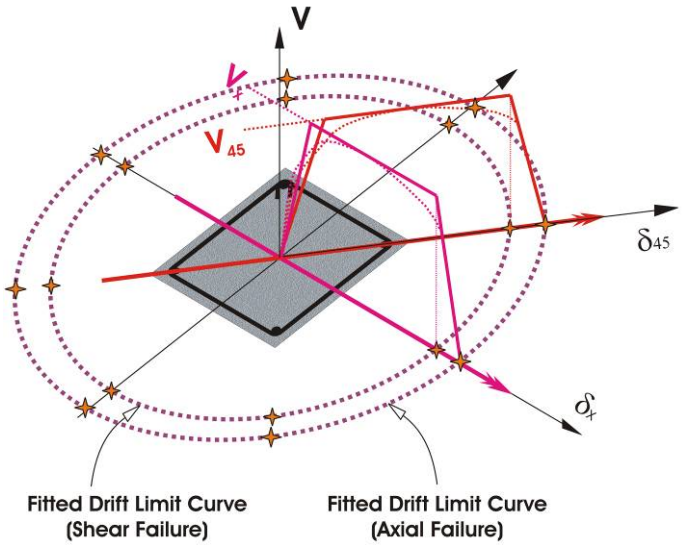

Figure 5-14 Backbone calculated for in-plane and 45° loading with fitted limit curve

5.7.2 Limit Surface Model Comparisons

A comparison between the experimental results and the limit surface model for specimen 24L-300-3D is shown in Figure 5-15. The calculated drift at axial failure coincides with the drift at shear failure due to the high axial load ratio, as for the previous uni-directional tests, thus only one limit curve is displayed. The experimental shear failure (as previously defined) occurs at a lower level of drift than the model suggests. This is likely due to the additional degradation associated with the increased strains imposed on the lapped longitudinal bars as the specimen traverses through the peak drift at 45°. Beyond shear failure the specimen undergoes the excursion to the peak drift coinciding with the limit curve, and axial failure occurs on the following 'leaf' of the protocol after minimal additional demand.

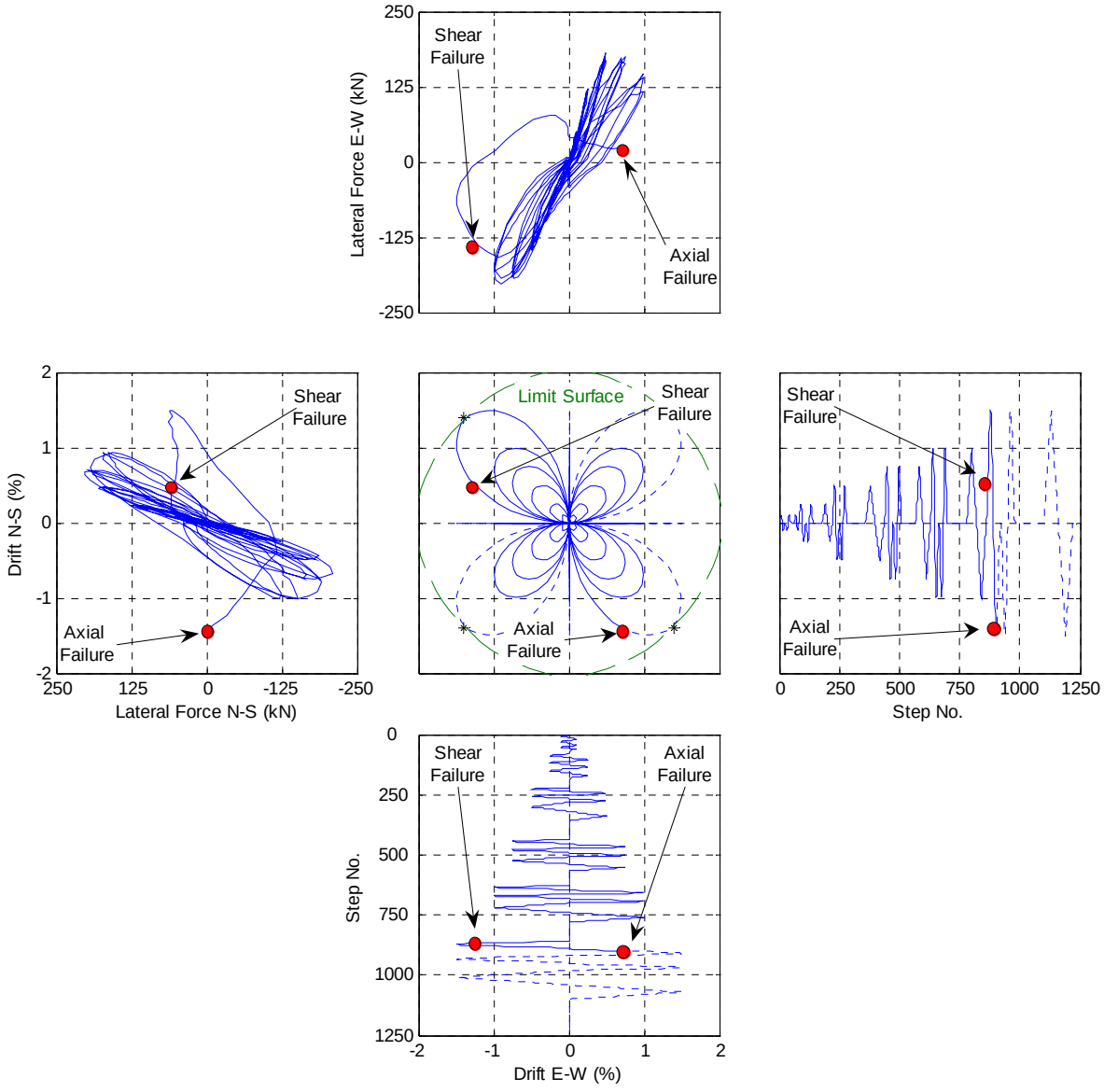

Figure 5-15 Limit Surface Model comparisons for specimen 24L-300-3D

Specimen 24L-300-3D-R has a reduced axial load, this results in separate limit curves for shear and axial failure drift as shown in Figure 5-16. Shear failure of the specimen occurs in the 1st 'leaf' of the drift cycles to 1.5%, whereas the Limit Surface model indicates that failure should occur in the cycles to 2.0% drift. However, for the model shear failure of the specimen is deemed to occur when section capacity reduces below 80% of the maximum capacity achieved as defined by Elwood and Moehle (2005b). They recognised that this definition is somewhat arbitrary and that a shear failure plane has not necessarily formed. Axial failure of the specimen also exceeds the modelled limit quite significantly with failure occurring on the 3rd 'leaf' to 3.0% drift. However this is the first drift level imposed that exceeds the modelled limit.

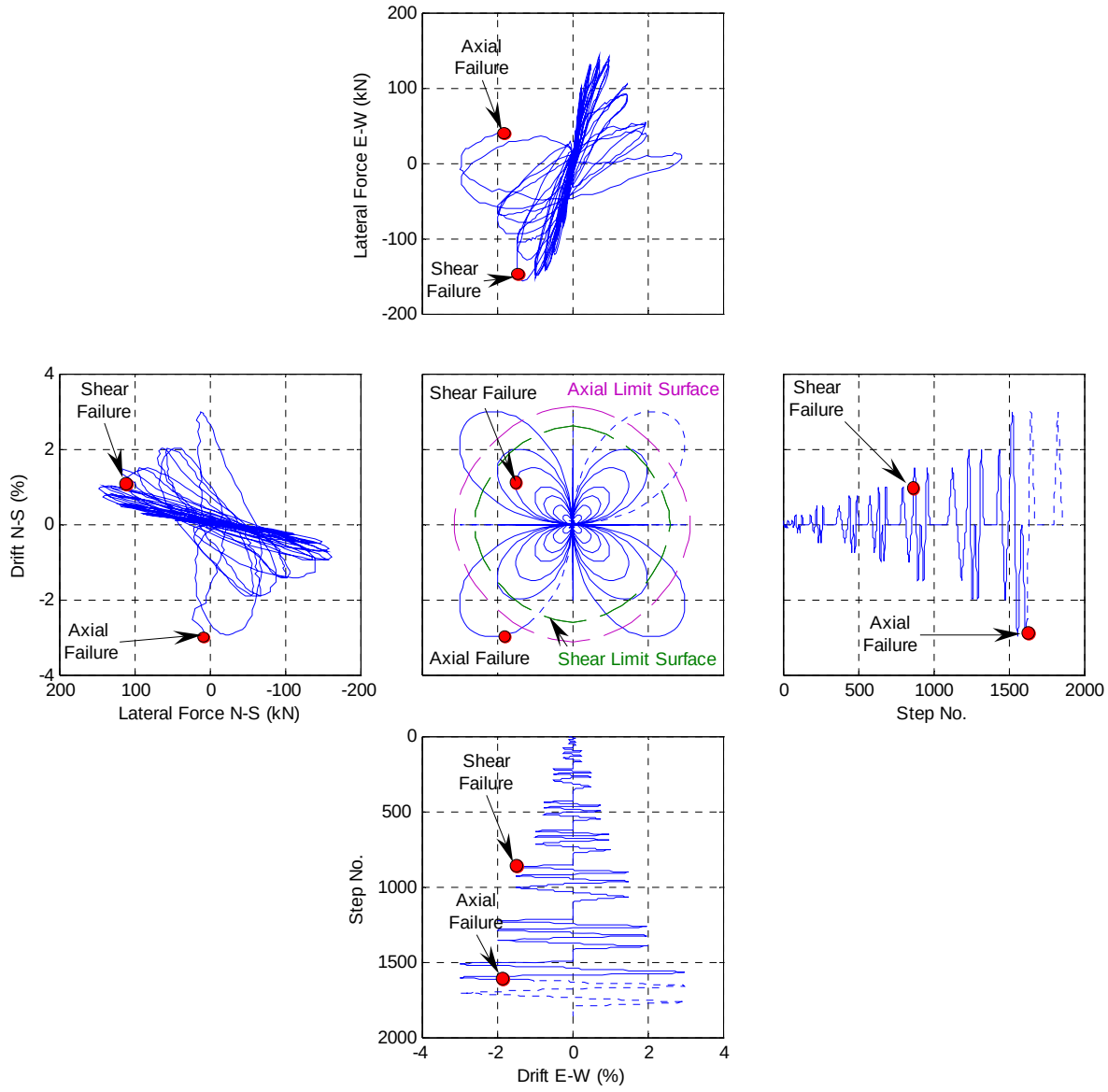

Figure 5-16 Limit Surface Model comparisons for specimen 24L-300-3D-R

A Comparison between the Limit Surface model and the experimental results for specimen 30L-300-3D is shown in Figure 5-17. Clearly, the model predicts the shear and axial failure adequately.

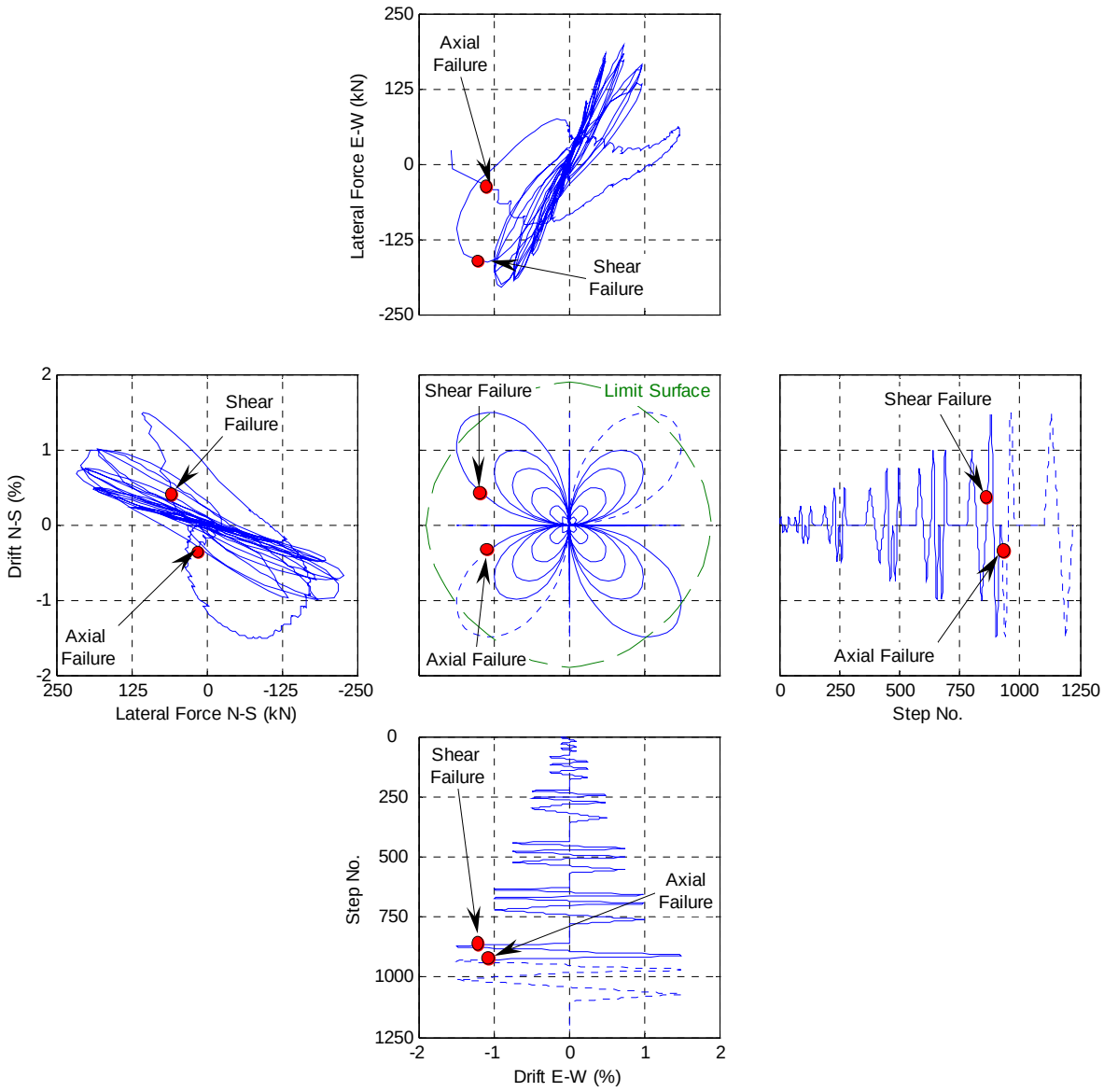

Figure 5-17 Limit Surface Model comparisons for specimen 30L-300-3D

As can be seen from the comparisons' above, the additional hysteretic demands imposed by bi-directional quasi-static loading protocol result in shear failure occurring at drift levels marginally lower than predicted. This effect is reduced for the specimen with the additional lap-splice length. However there is a belief among researchers that these protocols impose unrealistic demands upon test specimens and this will be explored further in the Chapter 6.0, which investigates performance under a more realistic quasi-earthquake drift protocol.

5.7.3 Simplified Backbone Model for Bi-Directional Loading

Due to the fact that it would be overly expensive and inefficient to comprehensively assess all existing buildings using NLTHA to determine potential collapse prone structures, there is a need for a 'desktop' assessment model for these inadequately detailed RC columns. Typically initial assessment programs involve determining the structural performance in each of the principal axes of the building (using Equivalent Static Analysis or similar simple procedures). Consequently the initial assessment model would necessarily be conservative and be able to assess the full bi-directional performance of these columns, represented in the principal axes of the structure.

Conservatively it is proposed that the drift limits be calculated for loading at a 45° angle which corresponds to the minimum effectiveness of the transverse reinforcement. These calculated limits are then resolved into the in-plane component as illustrated in Figure 5-18 below. Consequently, each in-plane backbone (in orthogonal directions) represent loading angles ranging from 0° to 45°, and it follows that the maximum backbone shear capacity is increased to the corresponding in-plane loading. An illustration of the simplified backbone model for bi-directional loading (resolved to the in-plane representation) is provided in Figure 5-19. Details from specimen 24L-300-3D are used to calculate the simplified backbone model.

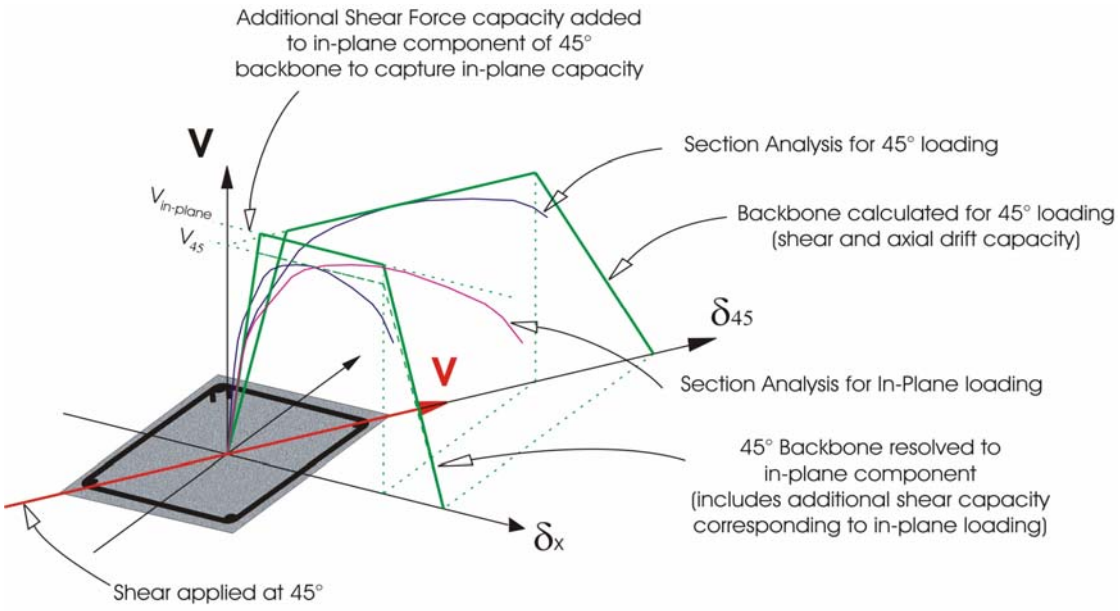

Figure 5-18 Backbone for 45° loading resolved to in-plane component

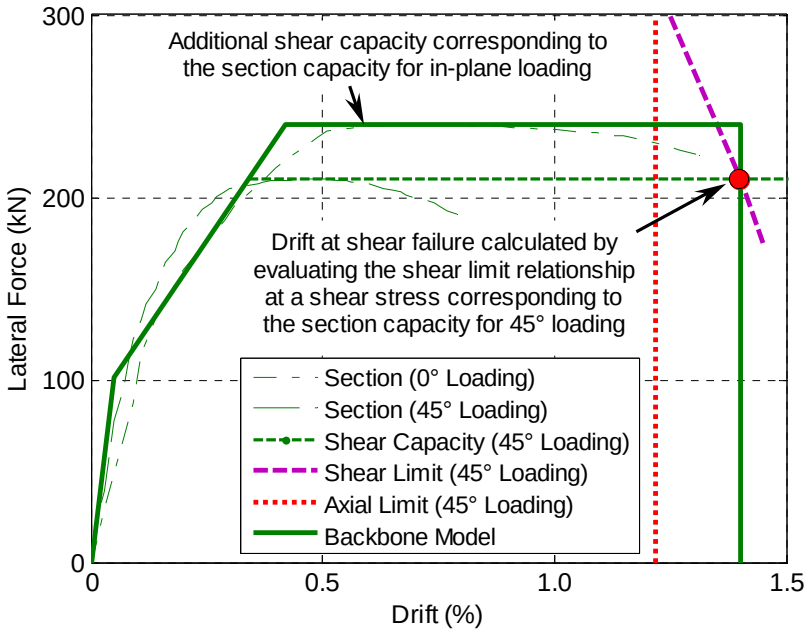

Figure 5-19 Derivation of simplified backbone model using Specimen 24L-300-3D

5.7.4 Simplified Backbone Model Comparisons

Experimental results and comparison with the simplified model for the bi-directional loading tests are shown on the following page in Figure 5-20 to Figure 5-22. Looking at the relationships for specimens 24L-300-3D and 24L-300-3D-R it initially appears that the model overestimates the capacity of the specimens as the force-displacement relationship does not reach the in-plane capacity. However, if consideration is given to the path of the loading protocol and the high rate of degradation associated with the minimum splice length provided it is evident that full capacity is unlikely to occur. Specimen 30L-300-3D however sustains a shear force considerably closer to the backbone due to the enhanced performance of the splice provided.

Of greater importance to the applicability of the model is the accuracy to predict the drift level at shear and axial failure. Experimental results and the modelled backbone for specimen 24L-300-3D are shown in Figure 5-20. Shear failure occurs at a level of drift slightly below the modelled level and as for the uni-directional specimen with this lap-splice length the axial failure occurs on the subsequent loop of the drift protocol.

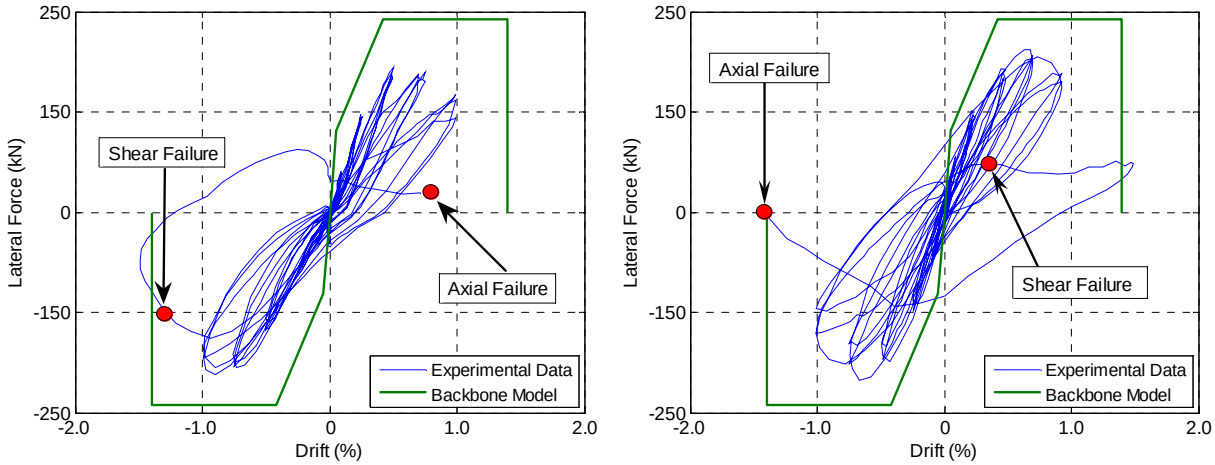

a) E-W Component direction **b) N-S Component direction**

Figure 5-20 Model comparisons for specimen 24L-300-3D

Figure 5-21 shows the comparisons for the second bi-directional specimen, 24L-300-3D-R (reduced axial load of 1000kN). It is clear that the backbone model captures the shear failure and the force-displacement behaviour adequately. The notable point of departure is with regard to the drift at axial failure, which exceeds the modelled limit by approximately 50%. However if the performance of previous tests performed by Melek (2003) is considered it is evident that cantilever column tests with axial load in this range lose axial capacity resulting from a flexural P-δ failure due to the test configuration. Whereas the model developed by Elwood et al. (2006) was calibrated using tests in double curvature and has shown to be valid for axial loads of this magnitude. Consequently, given the good fit of the experimental data prior to the modelled axial failure, the performance of this model applied to real double curvature columns can be considered adequate for low axial loads.

Comparisons for specimen 30L-300-3D are shown in Figure 5-22. Shear failure of the specimen occurs during the first 'leaf' to 1.5% drift, just prior to the modelled limit. The subsequent axial failure occurs during the third 'leaf' of the drift protocol, slightly later than modelled limit but this could be explained by the additional restraint at the failure plane by the dowel effect of the longitudinal bars and the reduced damage associated with increased splice length. As can be seen from the figures the simplified backbone model adequately captures the performance of these specimens subjected to the high demands of the bi-directional loading protocol and should provide a conservative model for the bi-directional limits resolved to in-plane components.

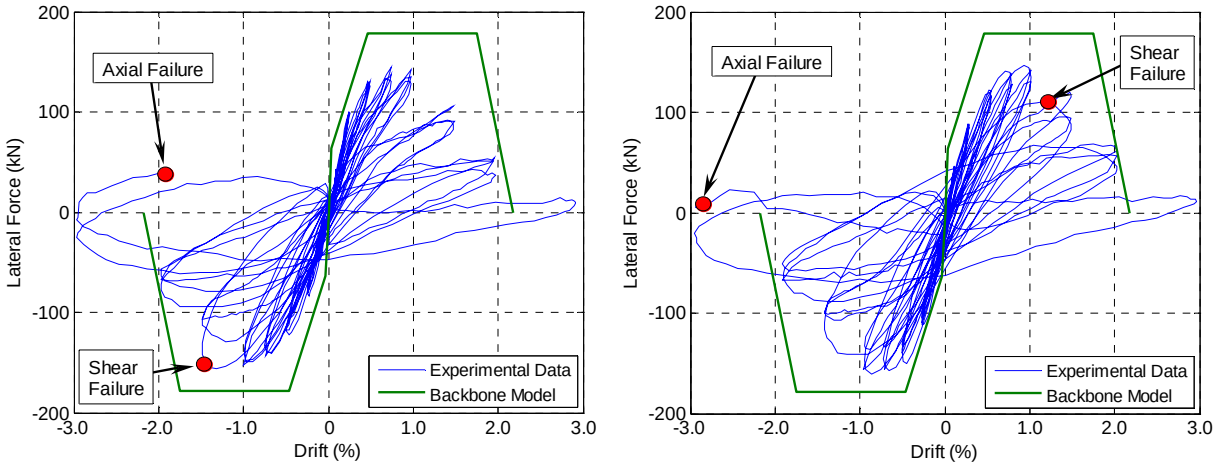

a) E-W Component direction **b) N-S Component direction**

Figure 5-21 Model comparisons for specimen 24L-300-3D-R

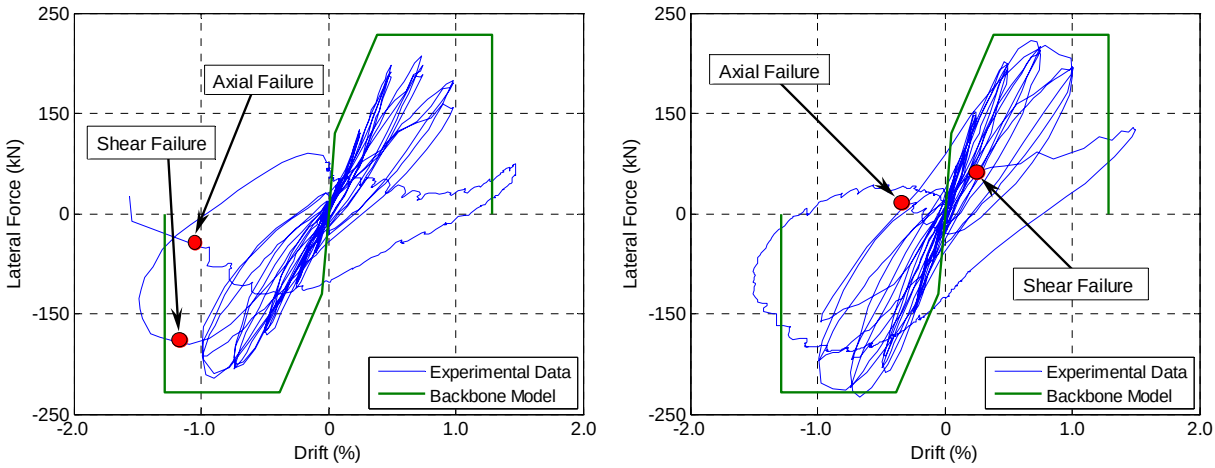

a) E-W Component direction **b) N-S Component direction**

Figure 5-22 Model comparisons for specimen 30L-300-3D

References

Elwood, K. J., and Moehle, J. P. (2005). "Drift Capacity of Reinforced Concrete Columns with Light Transverse Reinforcement." *Earthquake Spectra*, 21(1), 71-89.

Elwood, K. J., and Moehle, J. P. (2006). "Idealised Backbone Model For Existing Reinforced Concrete Columns and Comparisons With FEMA 356 Criteria." *Struct. Design Tall Spec. Build.*, 15, 553-569.

FEMA356. (2000). "Prestandard and Commentary for the Seismic Assessment of Buildings." FEMA.

Guidelines, N. (2006). "Assessment and Improvement of the Structural Performance of Buildings in Earthquakes." NZSEE Study Group Recommendations.

Melek, M., Wallace, J. W., and Conte, J. P. (2003). "Experimental Assessment of Columns with Short Lap Splices Subjected to Cyclic Loads." *PEER Report*, 04.

6.0 Experimental Results for Quasi-Earthquake Test

6.1 Quasi-Earthquake Protocol

Development of the quasi-earthquake protocol is undertaken to determine the likely performance of these 'gravity' columns under a realistic displacement history. Of particular interest is the commonly held belief that the quasi-static protocols with three cycles at each drift level are overly demanding when testing sub-assembly units designed prior to the modern codes. In order to further validate the Limit Surface Model a realistic earthquake displacement history is imposed on the final column in the test program. The steps taken in developing the protocol are outlined below:

1. Material tests were performed (refer to Table 6-1) and the measured properties used to calculate the Limit Curve for the specimen. Again, due to the high axial load the shear and axial failure drift limits coincide for both in-plane and 45° loading, as shown in Figure 6-1.

Table 6-1 Summary of material properties for the Quasi-Earthquake test specimen

Column Designation	f'_c (MPa)	N/f'_cA_g	f_y (MPa)	f_u (MPa)	f_{yt} (MPa)
24L-300-EQ	25.3	0.39	315	465	439

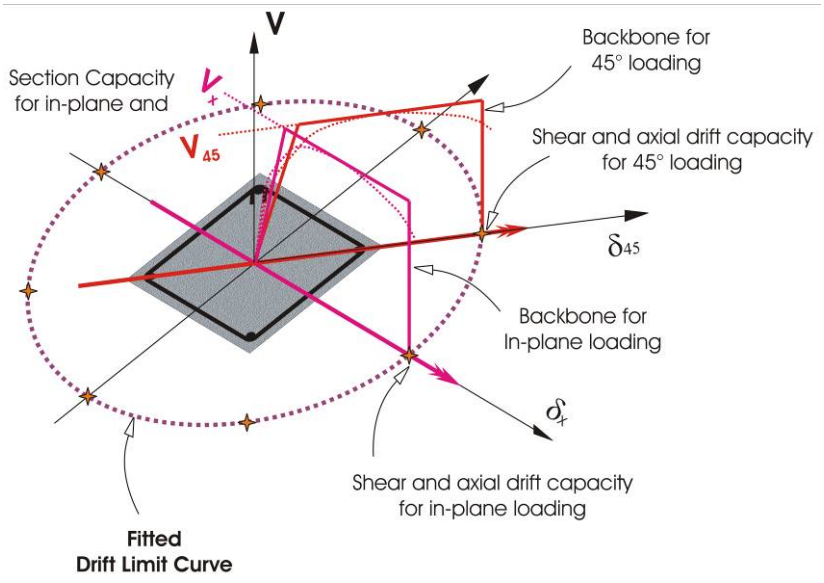

Figure 6-1 Illustration of Limit Surface for specimen 24L-300-EQ

2. A simplified model of the column is created (Figure 6-2) with the appropriate section properties, axial load, and calibrated hysteresis rule for bi-directional loading (Figure 6-3). Two orthogonal earthquake components are imposed to generate the displacement history.

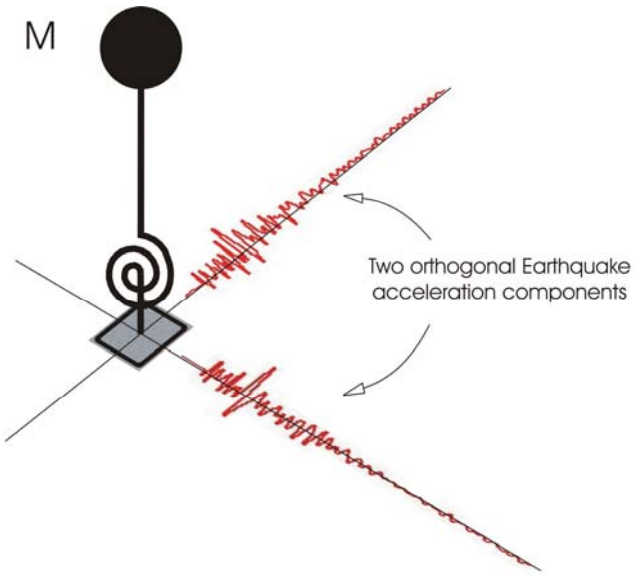

Figure 6-2 Model of specimen 24L-300-EQ

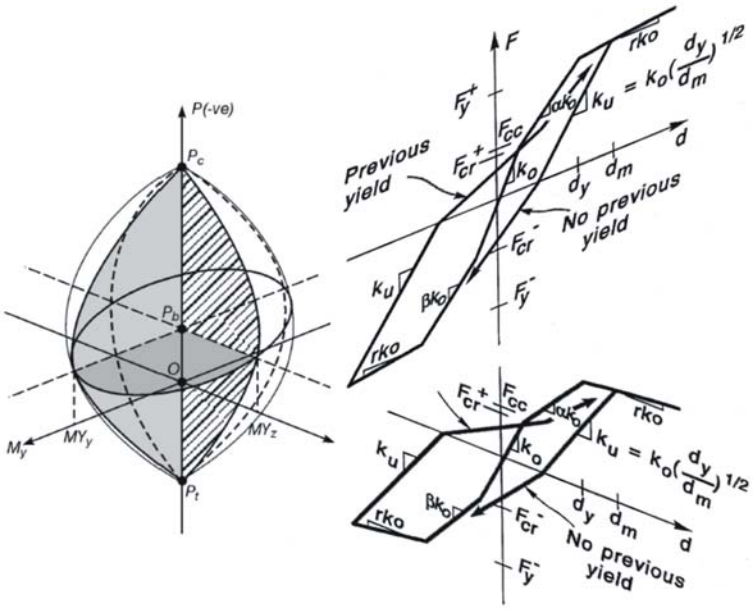

Figure 6-3 Hysteresis properties of the inelastic spring used in simplified model

3. To ensure appropriate excitation from the imposed earthquake record(s), the natural period of the column is required corresponding to the effective yielding of a structure incorporating columns with similar reinforcement details and applied axial load. The test columns were designed to correspond with a six-storey building with an inter-storey height of 3.6 metres. There exists considerable disparity between the relationships available in literature regarding estimating the natural period of a structure as outlined by Priestley et al. (2007). Equation (6-1) estimates the natural period as a function of the number of storeys whilst Equation (6-2) uses the total height of the structure. For the prototype structure this corresponds to estimations ranging from 0.6 to 1.8 seconds. Consequently, the period of the prototype structure was estimated to be 0.9 seconds, as this lies towards the conservative end of the range.

The effective stiffness of columns has been shown to be dependent on the axial load ratio as shown in Equation (6-3) (Elwood and Eberhard 2006). The effective mass of the model can be determined via Equation (6-4), using the target effective natural period and the calculated effective stiffness.

$$T_1 = 0.1n \tag{6-1}$$

$$T_1 = 0.1H_n \tag{6-2}$$

$$k_{eff} = \begin{cases} 0.2E_c I_{gross} & P \le 0.2 f_c' A_g \\ \left(\frac{5}{3}\frac{P}{f_c' A_g} - \frac{4}{30}\right) E_c I_{gross} & 0.2 f_c' A_g < P \le 0.5 f_c' A_g \\ 0.7E_c I_{gross} & P > 0.5 f_c' A_g \end{cases} \tag{6-3}$$

$$T_{eff} = 2\pi\sqrt{\frac{m_{eff}}{k_{eff}}} \tag{6-4}$$

4. Earthquake record selection was made using the GNS database records for Wellington, given a standard shallow earthquake, and ensuring that the displacement history was not too excessive in terms of a large number of peaks near the maximum demand. To these criteria the two orthogonal components of the F78201Z2 record of the 1978 Tabas earthquake are selected.

5. The imposed earthquake components are scaled to obtain a displacement history that coincides with the calculated drift limit surface as Figure 6-4 illustrates.

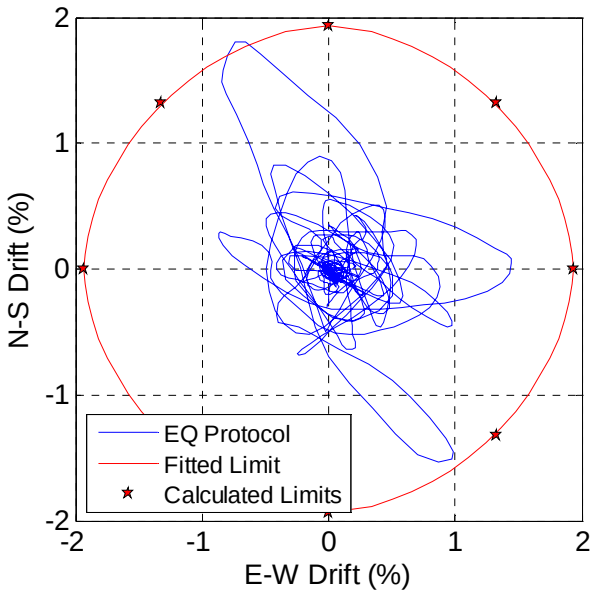

Figure 6-4 Quasi-earthquake protocol with modelled drift limit surface

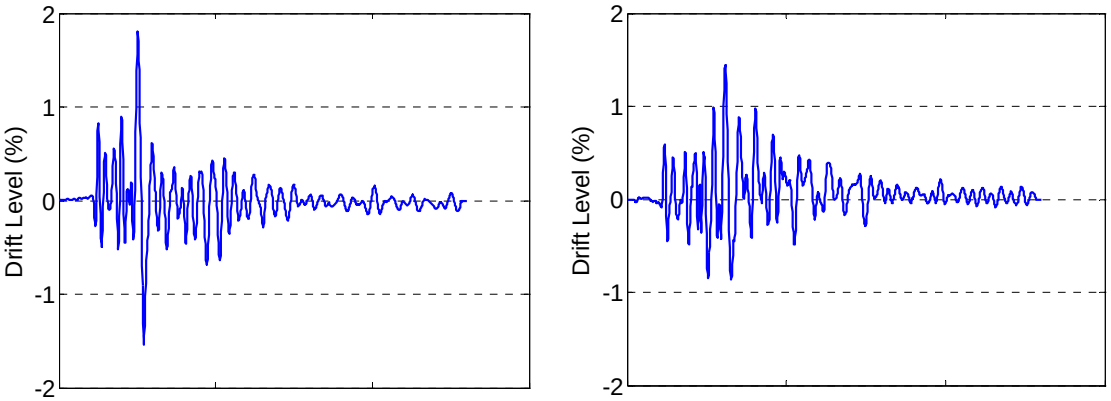

a) N-S Component of 3D Drift Protocol **b) E-W Component of 3D Drift Protocol**

Figure 6-5 Principal components of the Quasi-EQ protocol

6.2 Experimental Results for Specimen 24L-300-EQ

As can be seen from Figure 6-6 the demand imposed by the applied loading protocol is predominantly in the NW and SE quadrants, with a single notable excursion in the E direction. Also shown in this figure are 'markers', numbered to correspond with the selection of damage photographs presented in Section 6.2.1.

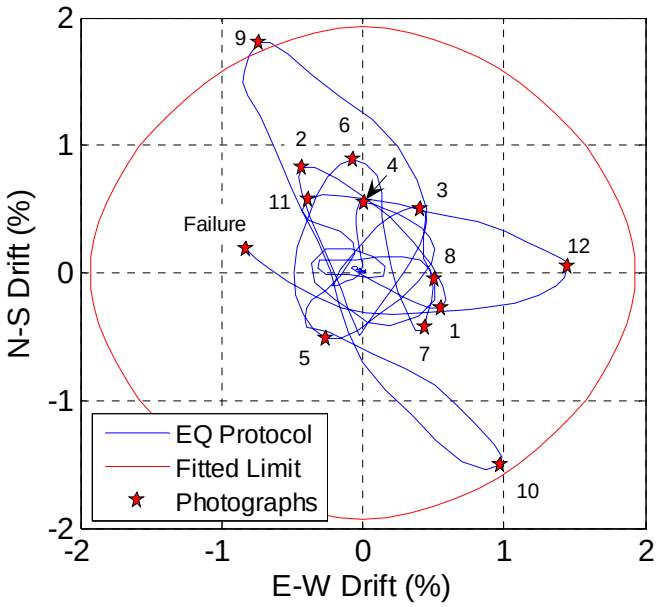

Figure 6-6 Loading protocol and photographic sequence for specimen 24L-300-EQ

6.2.1 Test Observations

Observations made during the testing of Specimen 24L-300-EQ are presented here. The progression of damage sustained by the specimen during testing is shown in the following sequence of figures (Figure 6-7 to Figure 6-11). Key stages during the imposed loading are outlined below with drift levels and associated damage highlighted.

Figure 6-7 illustrates the minor cracking appearing on the faces prior to the first significant drift demand. These damage photographs (1-8), all correspond to drift levels in the region of 0.5% to 1.0% (refer to Figure 6-6 above). The cracks are not uniformly distributed around the four column faces, due to the dominance of the NW and SE sectors in the imposed drift protocol. Consequently, the corresponding corners display the lap-splice splitting cracks shown in the previous bi-directional tests. Horizontal flexural cracks appear on all four faces, but the minor inclined shear cracks have two distinct orientations. The first shear crack

extends from the top of the lap-splice in the NW corner towards the base of the column in the SE corner, and the second crack extends from the top of the lap-splice in the SE corner and propagates towards the base in the NW corner.

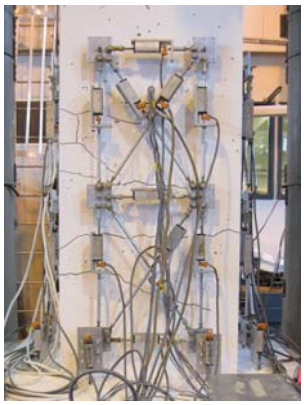

Photograph 1 (West Face)

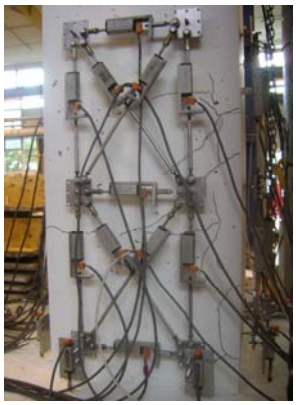

Photograph 2 (South Face)

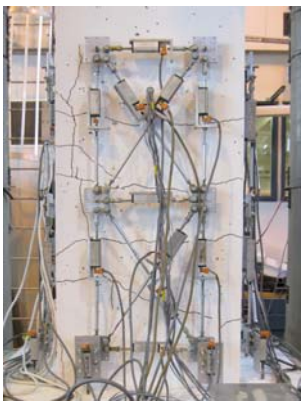

Photograph 3 (West Face)

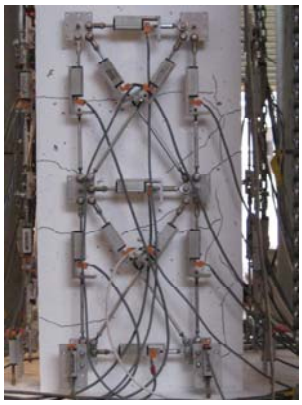

Photograph 4 (South Face)

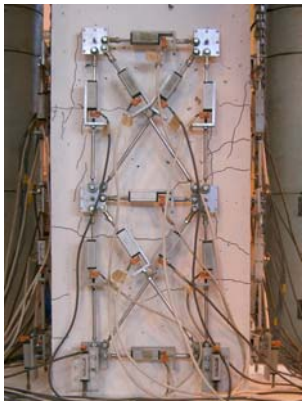

Photograph 5 (North Face)

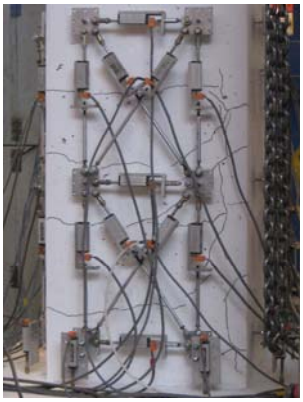

Photograph 6 (South Face)

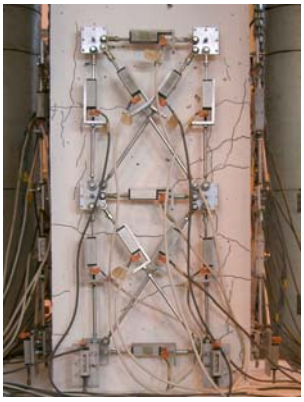

Photograph 7 (North Face)

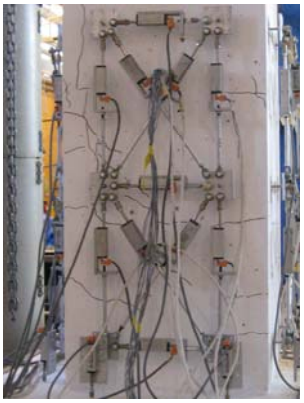

Photograph 8 (East Face)

Figure 6-7 Photographic sequence of damage sustained prior to 1st large drift 'peak'

The set of photographs below (shown in Figure 6-8) illustrate the damage sustained by the specimen as the 1st peak of the imposed protocol is attained. At this point in the loading the NW corner of the specimen is in compression, which is initiating the expulsion of the splice cover concrete. The shear crack extending from the top of the lap-splice in the SE corner has opened significantly at the upper end, and is associated with the reduced shear capacity exhibited by the specimen at this point.

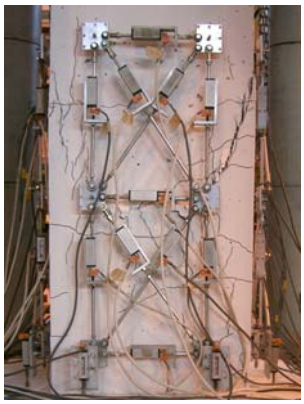

Photograph 9 (North Face)

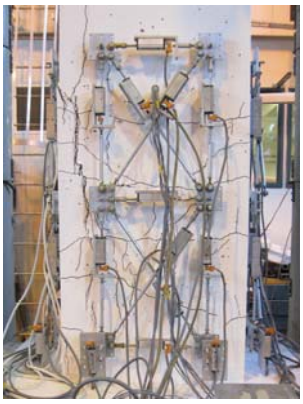

Photograph 9 (West Face)

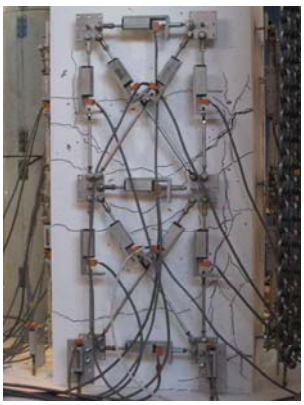

Photograph 9 (South Face)

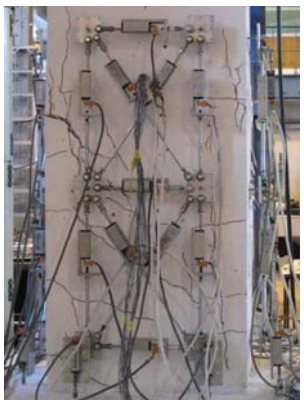

Photograph 9 (East Face)

Figure 6-8 Damage sustained by specimen at 1st large drift 'peak' (shear failure)

Figure 6-9 below, illustrates the damage to the specimen at the 2nd large drift 'peak'. At this point in the protocol the NW corner is in tension and further damage to the splice cover concrete in this corner is evident. Compression in the SE corner has closed the shear crack propagating from the top of the lap-splice in this corner and the splice cover concrete is beginning to be expelled.

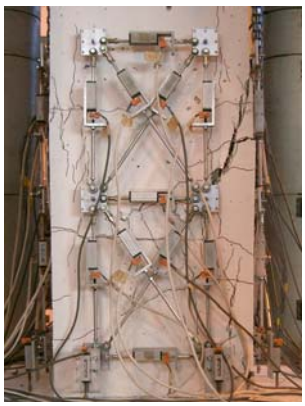

Photograph 10 (North Face)

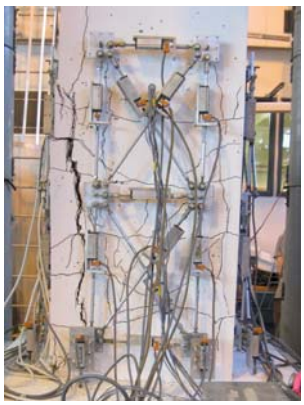

Photograph 10 (West Face)

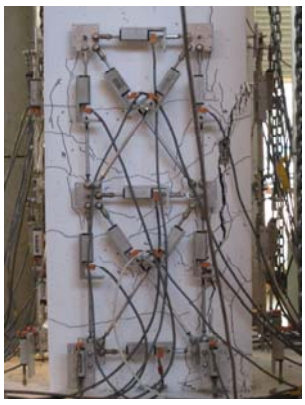

Photograph 10 (South Face)

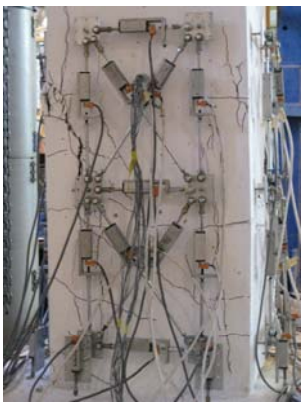

Photograph 10 (East Face)

Figure 6-9 Damage sustained by specimen at 2nd large drift 'peak'

The damage to the specimen at the 3rd large 'peak' is shown in Figure 6-10. At this point in the imposed drift protocol the cumulative effect of the large deformation demands has expelled the cover concrete adjacent to the lap-splices. In addition there is a new shear crack not previously seen on the East face of the specimen. Damage to the cover concrete over the entire East face of the specimen is induced by the compression this face is under at this point.

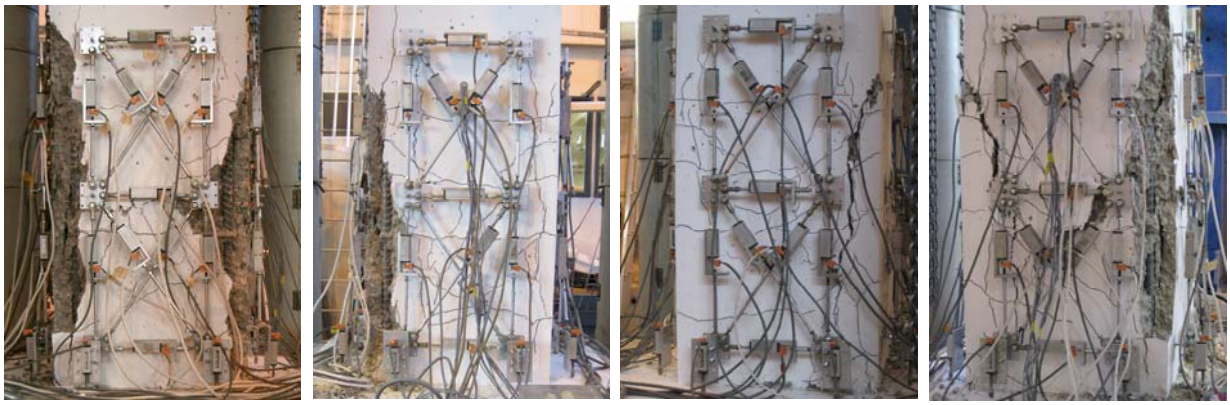

Photograph 12 (North Face) Photograph 12 (West Face) Photograph 12 (South Face) Photograph 12 (East Face)

Figure 6-10 Damage sustained by specimen at 3rd large drift 'peak'

The final set of damage photographs (shown in Figure 6-11), illustrate the various localised damage components the specimen underwent. Notably the splice cover concrete has been expelled in the NE an NW corners, the longitudinal bars have buckled at the poorly restrained crank, and the cover concrete has been seriously degraded and loosened on all four faces.

a) NE corner b) NW corner c) North Face d) West Face

Figure 6-11 Photographs of the damage the specimen sustained at axial failure

6.2.2 Relative Contributions to Displacement

Comparisons for the relative contributions to the total displacement are made in Figure 6-12 below. As was evident in the previous tests on specimens with the minimum allowable splice length the contribution from base rotation to the total displacement is initially small. Significant damage to the specimen occurs at the first major peak, this coincides with an increase in the contribution of base rotation to the total displacement. Beyond this point the damage incurred by the specimen results in significant divergence between the base rotation

and the imposed displacement. This did not occur to any significant degree in the previous bi-directional quasi-static testing due to the regularity of the imposed protocol, ensuring more uniformity in the damage sustained.

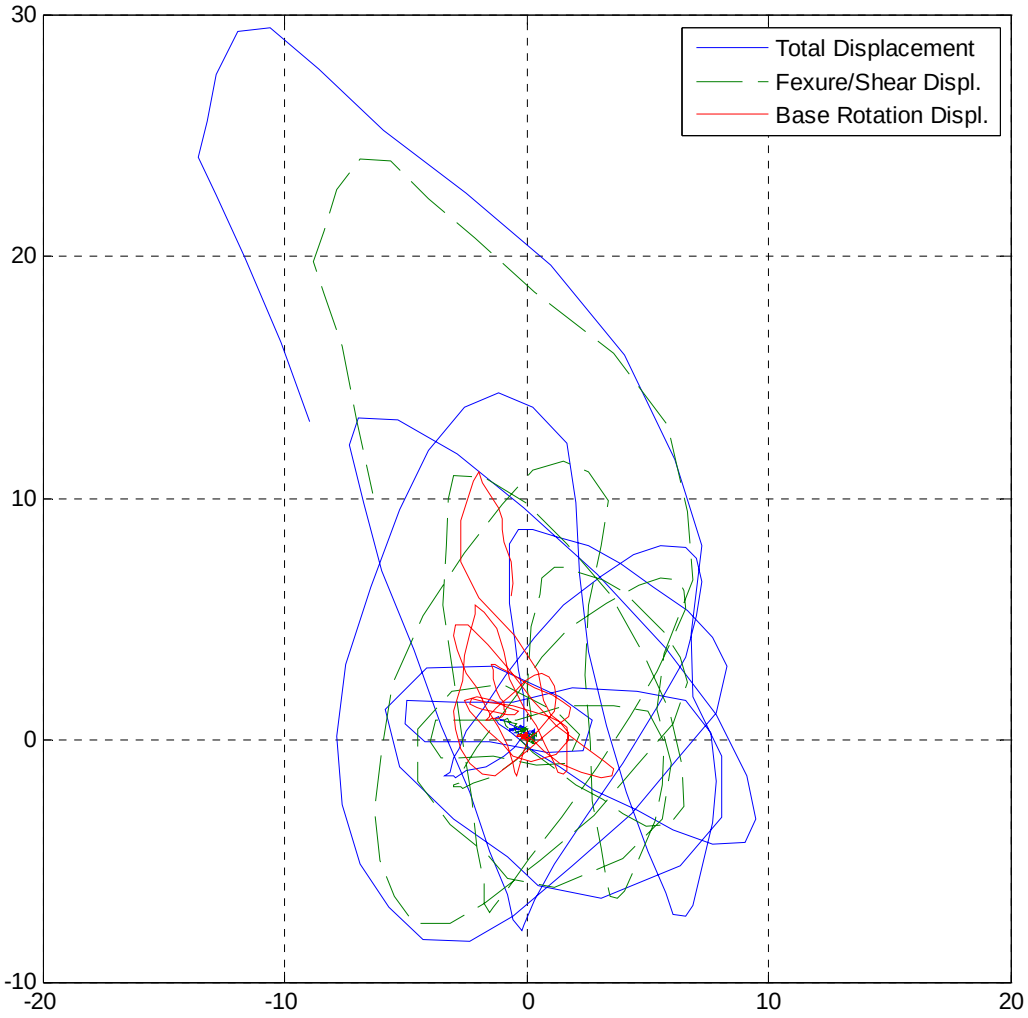

Figure 6-12 Contributions to Total Displacement for Specimen 24L-300-EQ

6.2.3 Force versus Drift Response and Comparison with Limit Surface Model

The force-drift relationship and the components of the imposed drift protocol for specimen 24L-300-EQ is shown below in Figure 6-13. The performance of the specimen is almost elastic until the first drift 'peak' is attained, however from this point on severe inelastic degradation occurs until subsequent loss of axial capacity after two more 'peaks'.

The test was terminated as the axial deformation of the specimen reached 15 mm, and at this point the residual axial capacity of the specimen had reduced to 990kN.

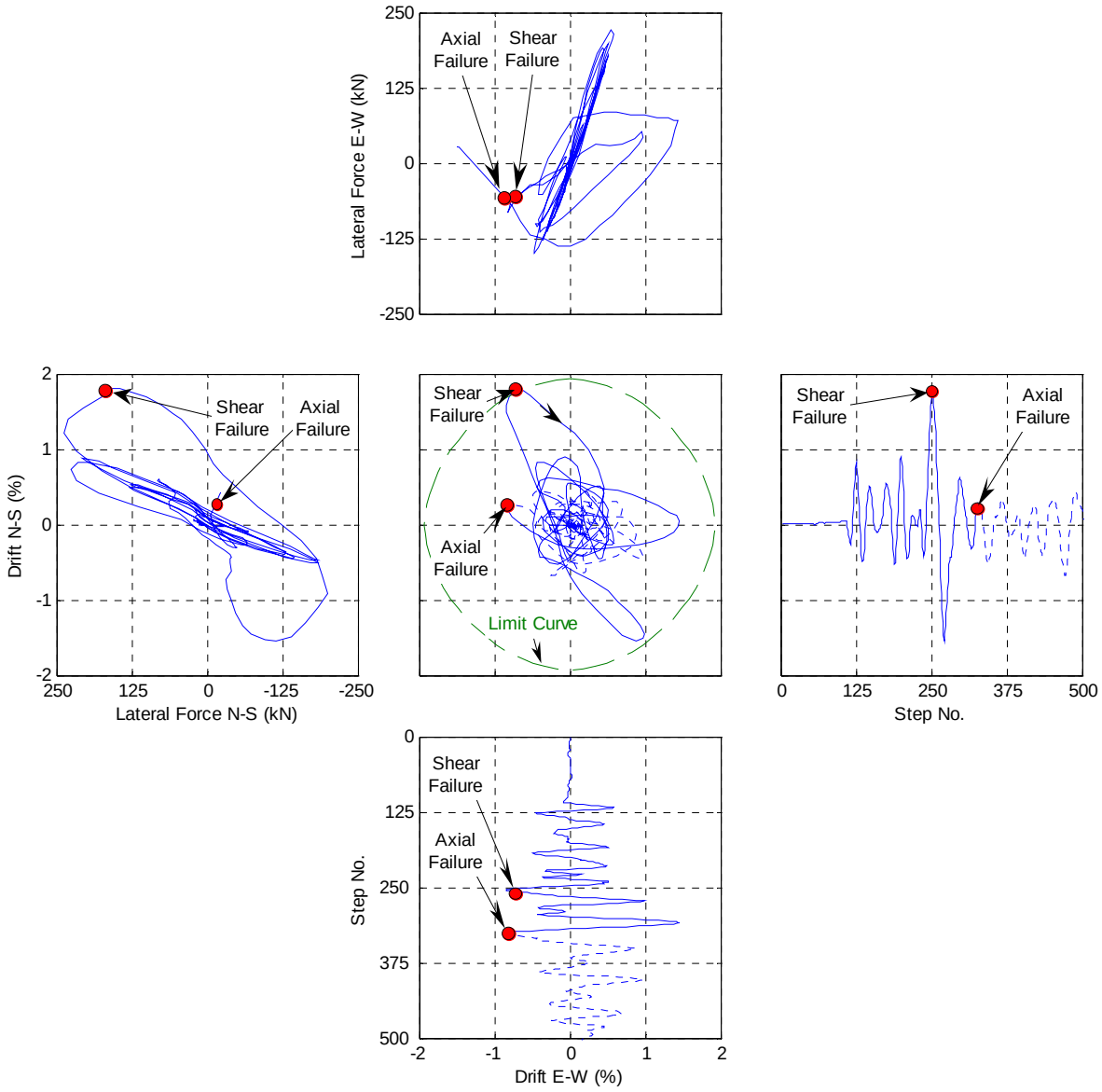

Figure 6-13 Experimental results for specimen 24L-300-EQ

Looking more closely at the force displacement relationship in the N-S direction at the point corresponding to the 1st drift 'peak', it is evident that the specimen sustained an increasing degradation in stiffness to this point. As the 'peak' was being approached the specimen underwent a sudden loss of lateral capacity in the E-W direction.

6.2.4 Simplified Backbone Model Comparisons

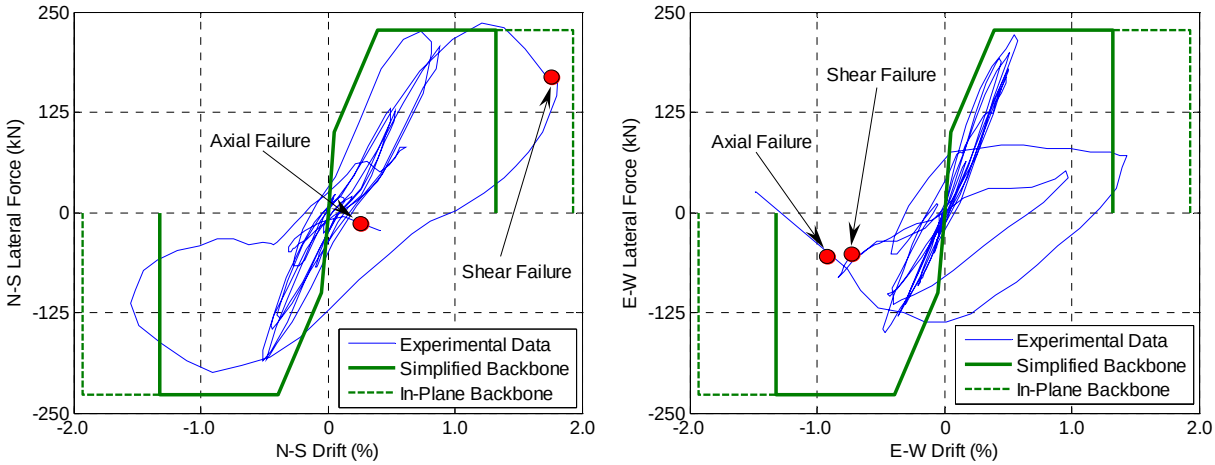

References

Elwood, K. J., and Eberhard, M. O. (2006). "Effective Stiffness of Reinforced Concrete Columns." Pacific Earthquake Research Centre.

Priestley, M. J. N., Calvi, G. M., and Kowalsky, M. J. (2007). *Displacement-Based Seismic Design of Structures*, IUSS Press.

7.0 Model Performance and Implementation

7.1 Model Performance

Chapter 4.0 illustrated clearly the inadequacy in the various shear strength capacity models, especially with regard to the impact of the assessed value of the yield drift. Any small variability in the calculation of the yield drift has a considerable affect on the ductility based degradation of shear capacity and hence the drift at which shear failure occurs. Similarly the NZSEE Guidelines ductility limit (2006) and the FEMA 356 backbone (2000), were shown to be overly conservative with regard to the available ductility in these inadequately detailed columns.

As Figure 4-16 and Figure 4-17 illustrate, the best estimation of the capacity 'backbone' of the columns tested uni-directionally is made by the model proposed by (Elwood and Moehle 2006) with the addition of a 'cracking' point added to the model. This cracking point is not entirely necessary for assessment of these columns but can further enhance the modelling of the hysteretic behaviour for use in NLTHA. The accuracy of this model is not unexpected as the model was calibrated using a large data base of similarly detailed columns. Extending the backbone model for bi-directional testing was necessary as real seismic events do not respect the in-plane nature of the uni-directional model. This was evident from the effective reduction of in-plane drift capacity displayed by the tests performed under the bi-directional loading protocol.

The limit surface model performed well in predicting the drift capacity of the bi-directional tests. One notable effect is that shear failure of the column occurred slightly earlier than expected for all three tests, significantly so for the test with reduced axial load. Considering the bi-directional protocol it is evident that additional degradation is sustained by the specimen. The 'path length' the specimen undergoes is nearly doubled for the each level of drift. However, the shear capacity is to a certain extent orientation specific and the associated degradation is not doubled. Explicit consideration of the performance/capacity of the lap-splices would further enhance the accuracy of the model. Additional tests are required with a variety of details to better calibrate the shear "failure" point, but overall the accuracy obtained is acceptable given the small number of experimental tests.

Axial failure is capture by the model with a greater degree of accuracy, with minimal additional displacement demands required after the limit is reached for failure to occur. Axial failure appears to be more independent of the additional demands imposed by the bi-directional loading, mostly due to the requirement for a failure plane to occur. As the failure plane is loading orientation specific it follows that the degradation associated with other loading angles is largely irrelevant. As noted in Chapter 5.7.2, the nature of the test with the reduced axial load was unlikely to sustain axial failure along a shear failure plane. Due to the cantilever test configuration axial failure occurred after sufficient core concrete was expelled to sustain a combined axial/P-δ failure.

The simplified backbone model for bi-directional loading performs well for the full quasi-static loading protocol due to the imposed displacements being equally distributed throughout the full 360°. For the quasi-earthquake test however the model illustrated the inherent conservatism, with the failure drift more closely approaching the equivalent in-plane drift than the assessed capacity for 45° loading. However as the orientation of an earthquake is uncertain with respect to the primary axes of the structure the conservatism is necessary. This emphasises the role of the simplified backbone as a preliminary assessment tool and highlights the need for full NLTHA of at risk structures with a full suite of appropriate earthquakes.

7.2 Consequences of Relative Stiffness

One limitation of the proposed drift limit models is the assumption that the point of contra-flexure is at the mid-height of the columns. This arises as a result of the nature of testing; either simple cantilever tests or double curvature tests with the head beam restrained from rotation were performed. However a more realistic column deformation profile takes into account the rotation of the beam-column joint at the top of the columns and the associated increased height to the point of contra-flexure. Consequently, the effective height of the column is increased and the effective level of imposed drift is reduced. This effective reduction of drift will impart a level of conservatism to the assessed failure limits. Figure 7-1 below illustrates the comparative deformation profiles and the increased effective height of the columns.

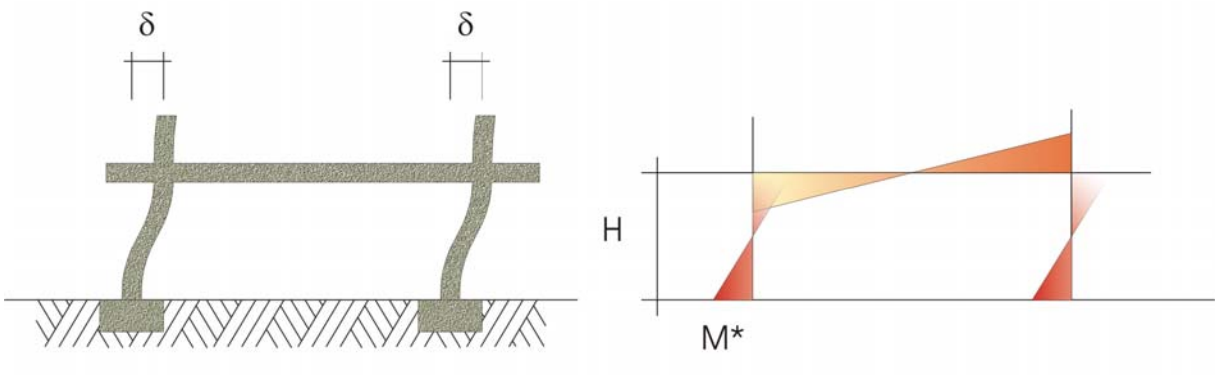

a) Illustration of assumed column deformation

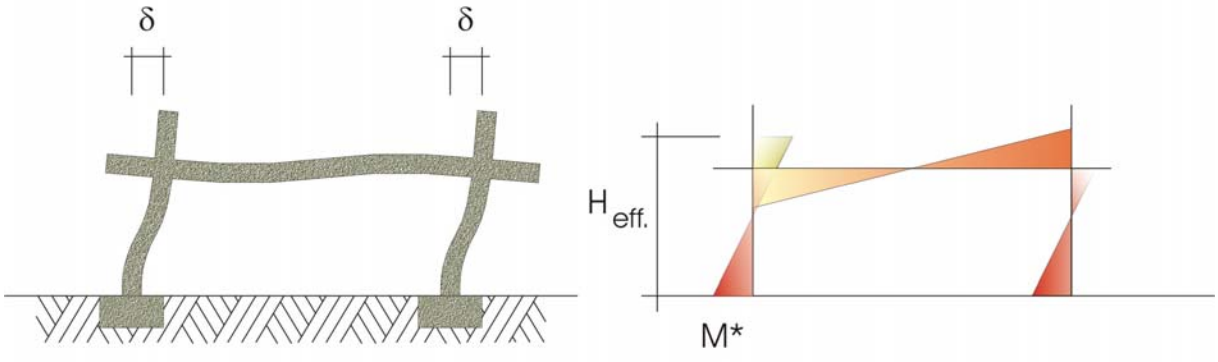

b) Illustration of realistic column deformation

Figure 7-1 Comparison between assumed and realistic displacement profile

The magnitude of the rotation of the beam-column joint will be largely due to the relative stiffness' of the column and the beams framing into the joint. For a typical one-way flooring system as predominantly found in NZ (i.e. double TT or hollow core decking units with topping) the beam stiffness will differ in the two directions. Perpendicular to the flooring direction large beams will be present to support the flooring, with smaller secondary beams parallel to the flooring units. As a consequence the rotation and the effective height of the columns will be different in each direction. The impact of this effect will need to be considered when using both the simplified backbone model and the limit surface model to assess the performance of existing structures.

7.3 Simplified Assessment of Existing Structures

The model can be used for a simplified desktop assessment of existing structures as a preliminary step to ascertain whether a more detailed approach is necessary. Basic information on the structure regarding the structural configuration, weights and seismic mass, and the primary lateral force resisting mechanism is required. These can then be used to determine the likely displacements that the structure will undergo during a given level of demand.

Basic properties of the structural materials are required for input into the drift capacity models for shear and axial failure. Ideally these properties would be determined by material testing as outlined in the various assessment guidelines published by the relevant authorities such as the NZSEE Guidelines(2006) and FEMA 356 (2000). In lieu of tested material properties being available estimations of the properties should be made as outlined in the published guidelines.

The level of accuracy to which the material properties are known and the level of complexity undertaken when modelling the structure will affect the degree of certainty resulting from the assessed likelihood of collapse. Likelihood of collapse is also extremely dependent on the level of imposed seismic force. Typically, the imposed level of seismic force is subject to regulation based requirements. In NZ there is a requirement that the lateral strength of the structure is able to withstand factored percentages of the current National Building Standards. This does not provide a guarantee that the structure will safely withstand a full design level event. This is especially important due to the brittle nature of the failure mechanisms highlighted in the previous chapters, such that a structure may safely withstand a 67% NBS event yet fail catastrophically with a minimal increase in the magnitude of demand.

Ideally, a given structure should be assessed using the full code imposed event and then a comparison made between the likely drift level the structure undergoes and the calculated drifts at shear and axial failure. Conservative assessments need to be made with regard to the threshold at which further analysis is deemed necessary and the structural configuration should be taken into account at this point. For example a shear wall building with intermediate ‘gravity’ columns is likely to be dominated by shear strength capacity as opposed to drift capacity. Whereas a MRF structure will sustain significant additional displacement with an increased level of lateral force and the drift capacity of the columns is likely to be critical.

Recognition of the 3D nature of earthquakes is also necessary, especially when assessing the performance using a simple equivalent static analysis in one direction, as was highlighted when comparing the 2D and 3D testing in the previous chapters. Typically assessment guidelines recognise this and impose a level of concurrency in the two orthogonal directions (100% in the primary direction and 30% in the secondary). However if the drift levels are assessed for the columns of interest at an angle of 45° and then resolved into the primary components as outlined in CH 5 a conservative estimation of the failure drift may be determined.

7.4 Assessment using Non-Linear Time History Analysis

7.4.1 Software Package

The implementation of the modelled limits to assess the structural performance of existing structures will be closely linked to the software package used for the assessment. Available software packages vary significantly in level of modelling complexity. These limits will affect the level of accuracy to which the NLTHA can perform. Typically the software will enable the user to define the structural geometry, member properties, and material properties in a similar manner. Differences lie mainly in the following areas:

1. The functional capacity of the software to simultaneously impose a single or two orthogonal acceleration records (vertical accelerations are neglected here but are included in many packages).
2. The ability of the user to select and define the hysteretic (non-linear) behaviour of the members at the critical sections. The range of modelling flexibilities range from the imposition of a simple bi-linear relationship, through to the availability of a suite of hysteresis rules with associated parameters to enable the user to capture complex inelastic behaviour.

Ideally the user would require the ability to impose two simultaneous orthogonal acceleration records and select and calibrate an appropriate hysteresis rule. If the acceleration record is imposed in a single direction the NLTHA loses the ability to assess the performance of the

inadequately detailed columns beyond the in-plane limits of the section assessed at a 45° loading angle. Consequently the additional information gained from the use of NLTHA is lost in the conservatism of the simplified limit implemented. As a result it is strongly recommended that two orthogonal acceleration records be used for every structural assessment.

7.4.2 Selection of Hysteresis Model

The complexity of the hysteresis rule utilised will dictate the level of calibration required. A simple bi-linear relationship needs only to be calibrated against the backbone curve for in-plane loading. The critical points include the yield point and the loss of shear capacity. Typically hysteresis rules are defined as functions of; initial stiffness, yield moment, post-yield stiffness, and a ductility limit, with additional parameters defining greater complexity (see Figure 7-2 (a) below). Also, the interaction of the axial load and the moment in the x- and y-directions are necessary (Figure 7-2 (b) below).

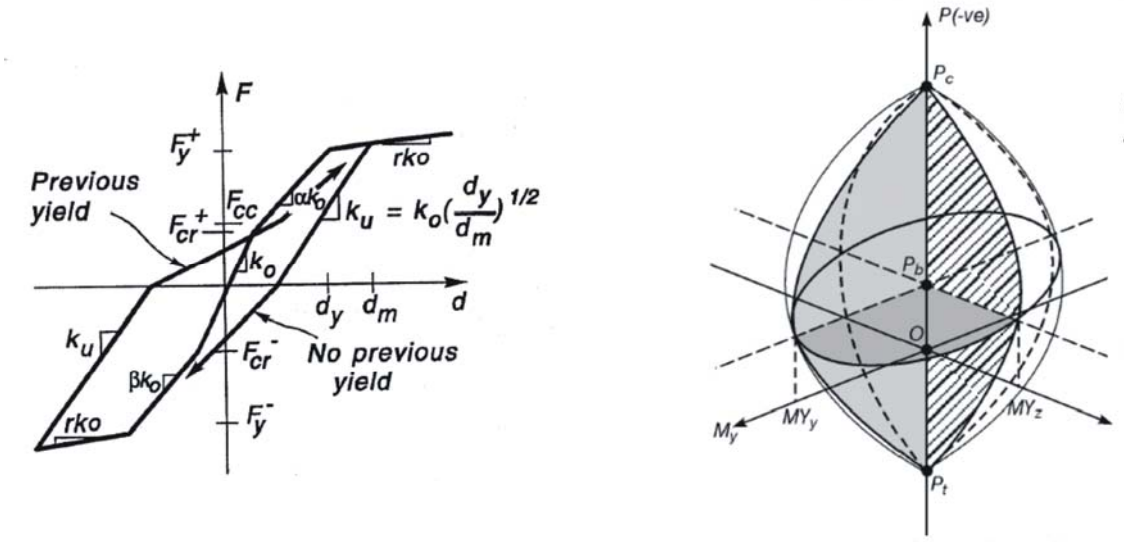

a) Typical Hysteresis Rule **b) Combined moment-axial interaction surface**

Figure 7-2 Typical hysteresis rule and moment-axial interaction surface for NLTHA (RUAUMOKO 2007)

Some open-source software packages such as OpenSees (McKenna et al. 2004) also enable the user to implement any number of discrete rules defining the structural behaviour of the inelastic members. However, the use of such software is not typical (or necessarily practical) for the consulting engineer. This is largely due to a combination of the level of programming ability required and the lack of an easily manipulated user interface.

7.4.3 Implementation of Shear and Axial Failure Springs

A further extension to the limit model is the possible implementation of shear and axial failure springs. This will allow the potential for axial load redistribution to be assessed, given the axial failure drift limit has been exceeded and loss of capacity has occurred. The uni-directional loading case has already been implemented in OpenSees by Elwood and Moehle (2008) and a simple representation is illustrated in Figure 7-3 below. Implementing the failure springs will require the shear and axial springs to act and interact over all orientations in the horizontal plane. A simple analogy for this would be similar to the extension from an in-plane moment-curvature interaction extrapolated to the three dimensional capacity surface shown above in Figure 7-2.

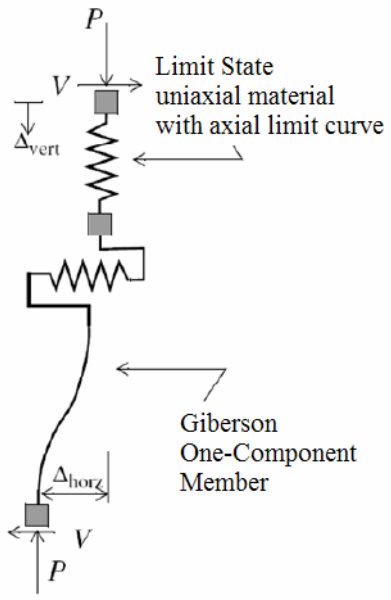

Components:

- Shear Spring

- Axial Spring

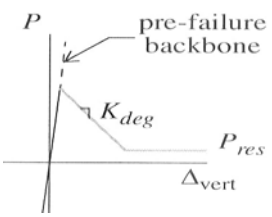

Figure 7-3 Representation of the shear and axial failure springs

References

Elwood, K. J., and Moehle, J. P. (2006). "Idealised Backbone Model For Existing Reinforced Concrete Columns and Comparisons With FEMA 356 Criteria." *Struct. Design Tall Spec. Build.*, 15, 553-569.

Elwood, K. J., and Moehle, J. P. (2008). "Dynamic collapse analysis for a reinforced concrete frame sustaining shear and axial failures." EARTHQUAKE ENGINEERING AND STRUCTURAL DYNAMICS.

FEMA356. (2000). "Prestandard and Commentary for the Seismic Assessment of Buildings." FEMA.

McKenna, F., Fenves, G., and Scott, M. (2004). *OpenSees: Open System for Earthquake Engineering Simulation*, Pacific Earthquake Engineering Research Center, University of California, Berkeley, CA.

NZSEE. (2006). "Assessment and Improvement of the Structural Performance of Buildings in Earthquakes." New Zealand Society for Earthquake Engineering.

RUAUMOKO. (2007).

8.0 Conclusions

8.1 Global Performance of Columns

The global performance of columns with inadequate detailing has been shown to be poor, with loss of axial capacity occurring at drift ratios as low as 1.5% for the bi-directional tests. The inadequate detailing investigated included, minimal transverse reinforcement, lap-splices in the potential plastic hinge zone, and cranked bars at the top of the lap splice. Of these parameters the transverse reinforcement ratio was critical (in combination with the axial load ratio). Both shear and axial load failure are proportional to the transverse reinforcement ratio and inversely proportional to the imposed axial load ratio.

As illustrated in the testing, the presence of the lap-splice in the plastic hinge only affected the rate of degradation of shear capacity but not the drift failure limits. Associated with the damage to the lap-splice was the expulsion of the cover concrete resulting from the splitting force imposed by tension in the spliced bars. Similarly, as the performance of the columns closely matched the model proposed by Elwood and Moehle (2006), the presence of cranked longitudinal bars at the top of the lap-splice did not significantly affect the global performance of the columns. Damage associated with the cranked bars was limited to local buckling of the bars as typically the cover concrete at the crank/splice had been expelled prior to the occurrence of buckling.

8.2 Adequacy of the Drift Based Failure Models

The Limit Surface Model achieved a good correlation with the tests performed. The two critical limits calculated by the model are the drifts at shear and axial failure. Drift at shear failure was minimally overestimated, due largely to the additional hysteretic demands imposed by the bi-directional loading. The modelled drift limit at axial failure was well captured by the models, with no discernible impact from the bi-directional loading. This is due to the required formation of an orientation specific shear failure plane for the axial failure to occur. Implementation of appropriate calibrated hysteresis rules into an NLTHA package in conjunction with the modelled limit surface provides the ability to assess the collapse potential for structures with inadequately detailed RC columns.

The Simplified Backbone Model also captures the performance of the columns well. Although the quasi-earthquake test illustrates the inherent conservatism due to the assumed worst case loading angle of 45°. However, as the simplified model is only intended as a preliminary desktop assessment this is appropriate as it will initiate a more detailed assessment of columns with the potential for failure.

8.3 Further Research Required

Additional research into the bi-directional performance of inadequately detailed columns is required. There are two facets to the information required to further advance the understanding of the performance of these columns:

1. Extend the detailing parameters and imposed axial load combinations. This will enable the bi-directional model to be validated for a greater range of detailing than the initial testing allowed.
2. Create a larger database of tests to enable a statistically significant assessment of the bi-directional drift limits for shear and axial failure. The proposed bi-directional model is based on the uni-directional model formulated by Elwood and Moehle (2006), which assesses the mean capacity of the column specimens and is calibrated using uni-directional tests. In addition a larger database will enable the model to provide probabilistic information regarding the likely failure drift, as illustrated for the uni-directional case in Figure 8-1 below.

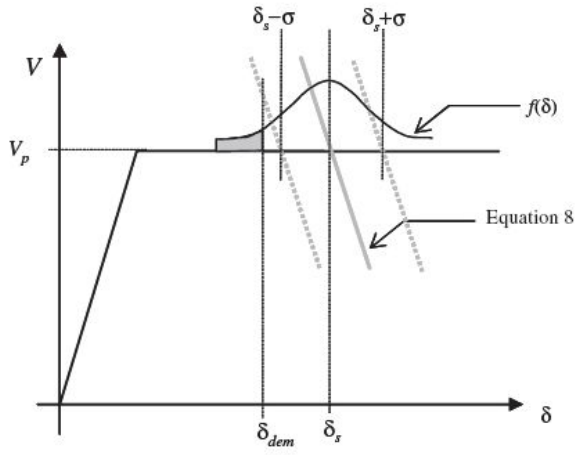

Figure 8-1 Probabilistic backbone model (Elwood and Moehle 2006)

Appendix A Material Testing

Longitudinal Reinforcement (Except Specimen 30L-300-2D)

Sample (#)	f_y (MPa)	f_u (MPa)
1	312.9	464.1
2	315.4	464.9
3	315.4	463.6
4	310.9	467.4
5	317.7	465.8
6	317.9	464.6
Average	**315**	**465**

Longitudinal Reinforcement for Specimen 30L-300-2D

Sample (#)	f_y (MPa)	f_u (MPa)
1	319.0	478.4
2	319.9	480.7
3	317.0	480.0
4	321.6	480.0
5	321.7	483.0
6	319.3	483.0
Average	**320**	**481**

Transverse Steel Reinforcement

Sample (#)	f_y (MPa)	f_u (MPa)
1	444.3	533.6
2	432.6	526.4
3	440.0	519.2
4	440.0	526.4
5	440.0	519.2
Average	**439**	**525**

Longitudinal Reinforcement (Except Specimen 30L-300-2D)

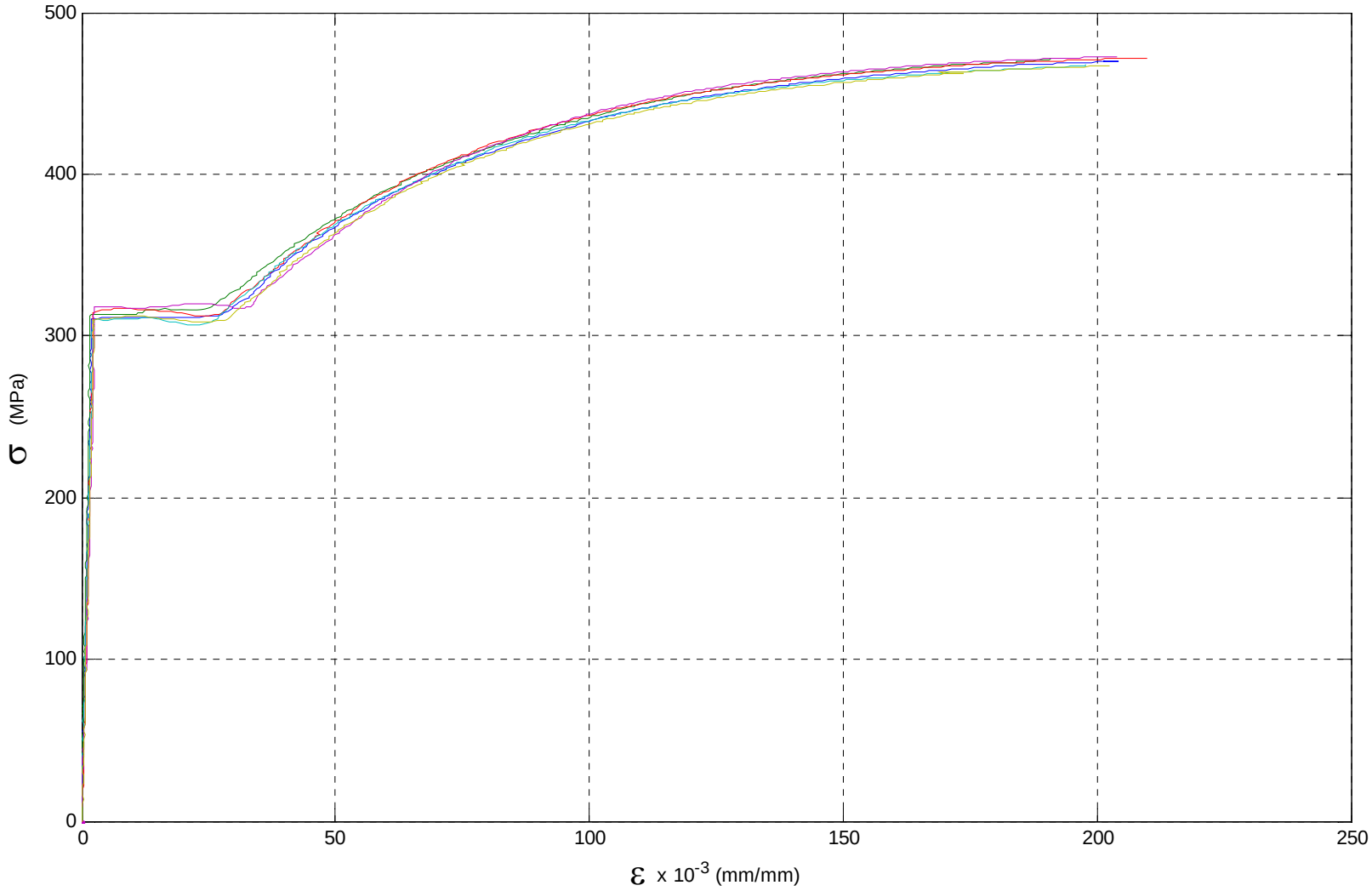

Longitudinal Reinforcement for Specimen 30L-300-2D

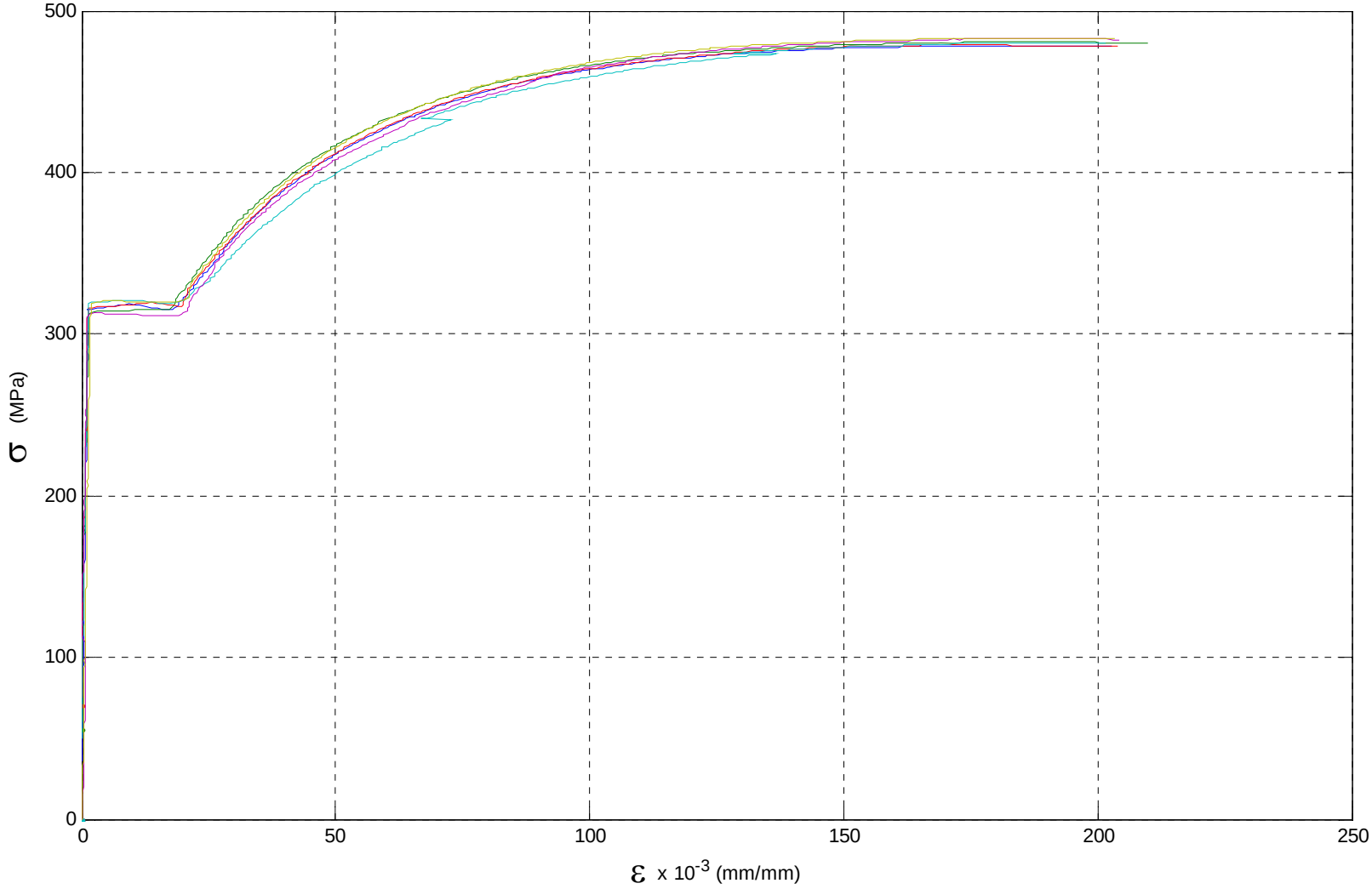

Transverse Steel Reinforcement

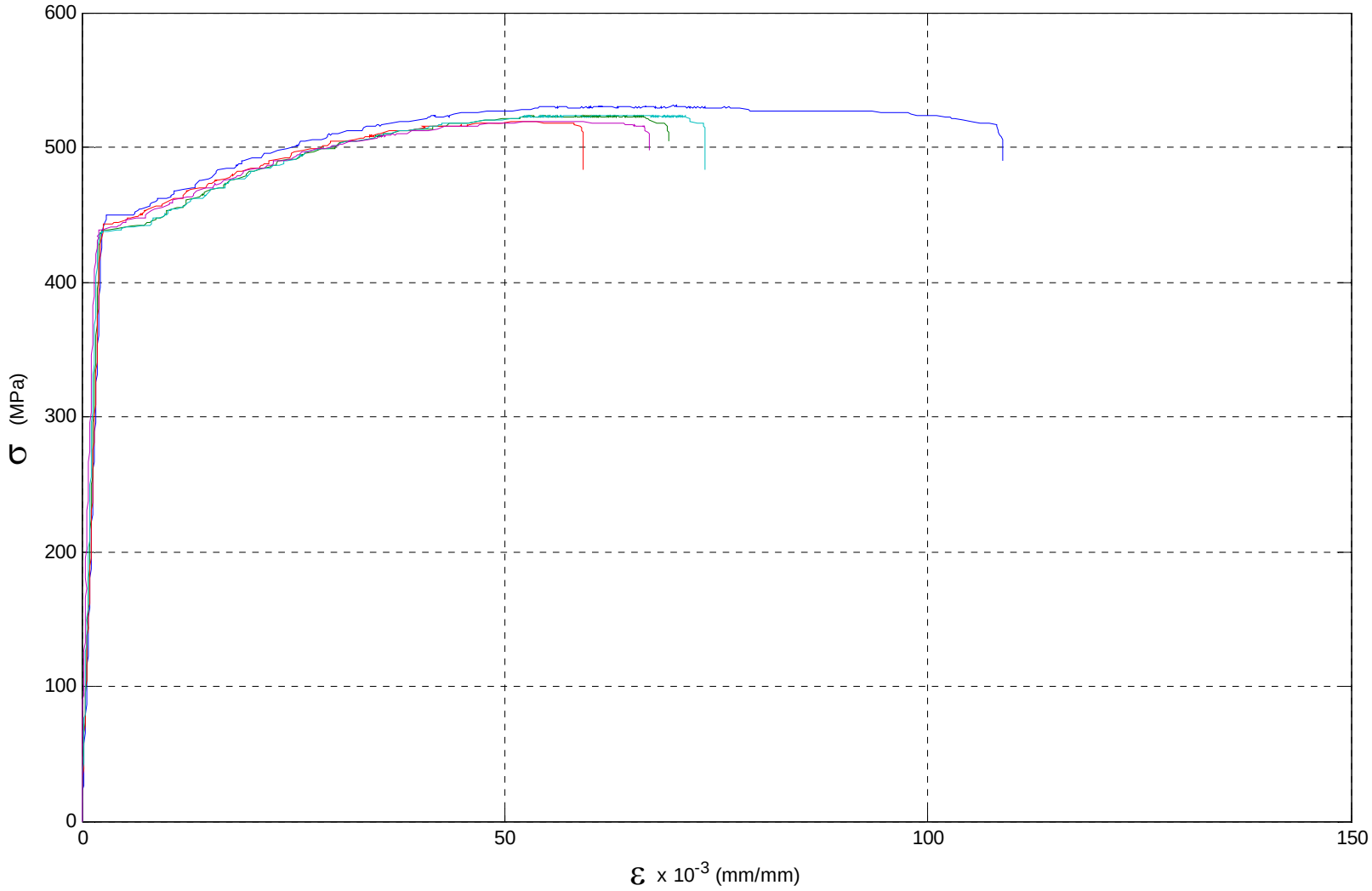

Appendix B Lateral and Axial Corrections

B.1 Lateral Force and Displacement Corrections

Due to the nature of the experimental setup with regard to the application of lateral load and the acquisition of data, a set of geometric corrections are necessary to enable the principal components of the displacement and force to be determined.

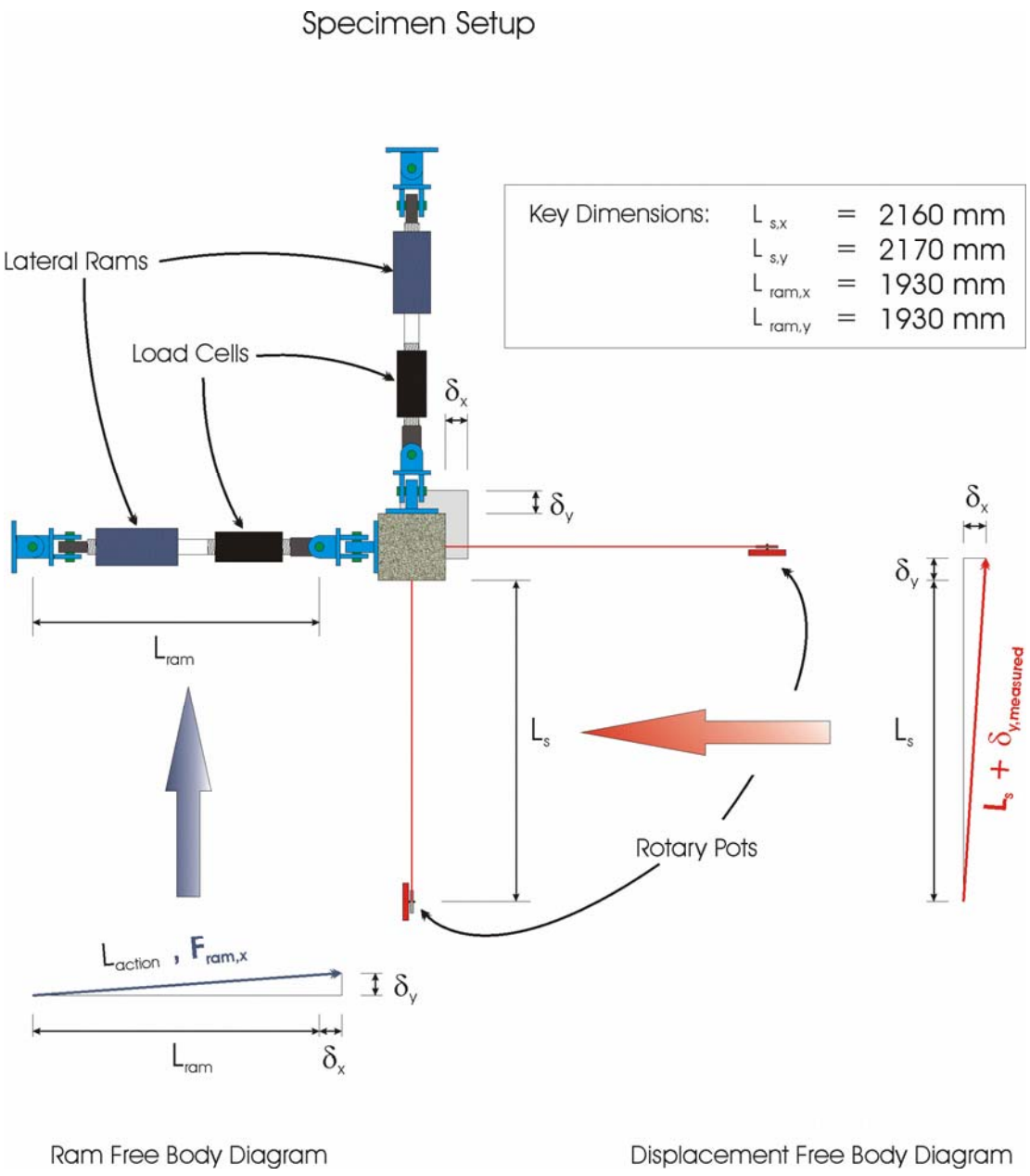

Displacement Correction	
X Component	Y Component
$\delta_x = \sqrt{(L_{s,x} + \delta_{x,measured})^2 - \delta_y{}^2} - L_{s,x}$	$\delta_y = \sqrt{(L_{s,y} + \delta_{y,measured})^2 - \delta_x{}^2} - L_{s,y}$

Note that the measured transverse displacement is used in the corrections as the string length is more than an order of magnitude larger, thus eliminating the need for an iterative solution.

Lateral Force Correction	
X Component	Y Component
$F_{X,(ram,x)} = F_{(ram,x)} \dfrac{L_{ram} + \delta_x}{\sqrt{(L_{ram} + \delta_x)^2 + \delta_y{}^2}}$	$F_{Y,(ram,x)} = F_{(ram,x)} \dfrac{\delta_y}{\sqrt{(L_{ram} + \delta_x)^2 + \delta_y{}^2}}$
$F_{X,(ram,y)} = F_{(ram,y)} \dfrac{\delta_x}{\sqrt{(L_{ram} + \delta_y)^2 + \delta_x{}^2}}$	$F_{Y,(ram,y)} = F_{(ram,y)} \dfrac{L_{ram} + \delta_y}{\sqrt{(L_{ram} + \delta_y)^2 + \delta_x{}^2}}$
$F_{X,TOTAL} = F_{X,(ram,x)} + F_{X,(ram,y)}$	$F_{Y,TOTAL} = F_{Y,(ram,x)} + F_{Y,(ram,y)}$

Note that for the bi-directional loading each Ram force can be reduced into x and y components, thus there are contributions from both Ram's to each of the resultant total x and y forces.

B.2 Axial Correction

Axial Force is applied to the columns as shown below. The implications of this experimental setup are illustrated along with the free-body diagram to enable the reduction of the inclined axial force into vertical and horizontal (both x and y) components.

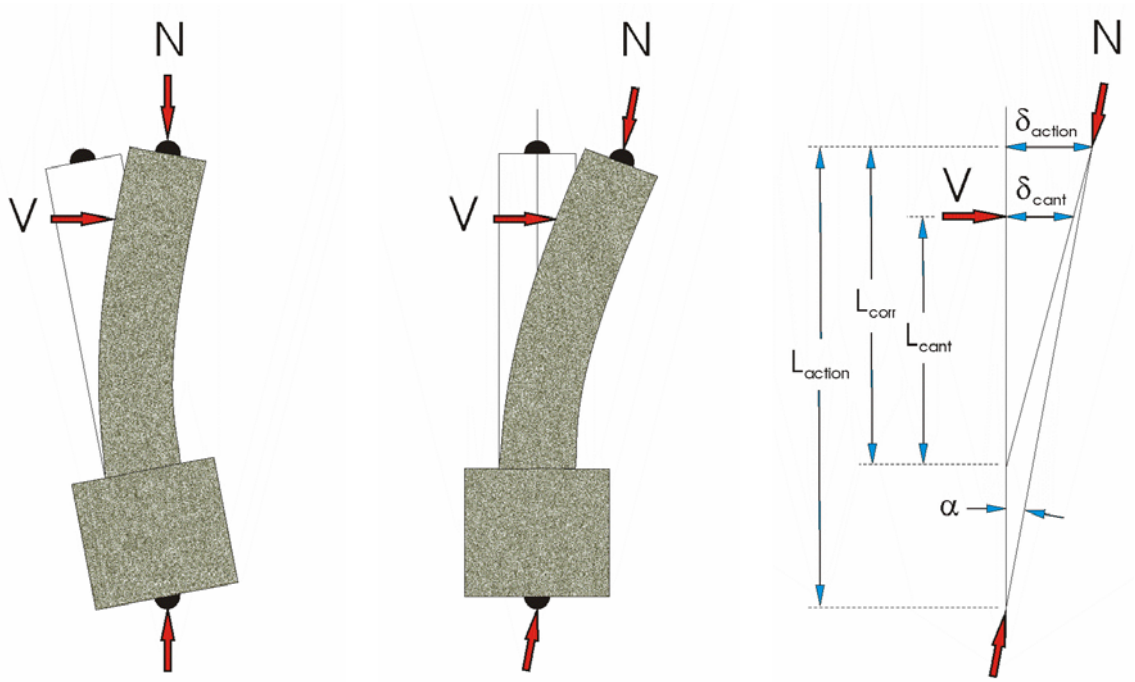

a)Test configuration **b) Equivalent representation** **c) Free-body diagram**

Assuming a linear displacement profile for the column (this assumption is explored subsequently), we have:

$$\delta_{action} = \delta_{cant.} \frac{L_{corr.}}{L_{cant.}} \qquad \alpha = \tan^{-1}\left(\frac{\delta_{action}}{L_{action}}\right)$$

Vertical Component	Horizontal Component
$N_V = N.Cos\alpha$	$N_H = N.Sin\alpha$

By assuming the linear displacement profile, an error is introduced in the calculated value of δ_{action} (as shown below). Considering the actual displacement profile, the rotation at the top of the column is greater than that assumed by the linear profile. The relative size of $\delta_{err}/\delta_{action}$ will be largest as the column begins to yield due to flexural curvature being developed over the height of the column without any plastic rotation at the base of the column. Also, the magnitude of the error is unlikely to increase significantly especially when the contributions from bond slip, splice degradation at the base and inelastic shear deformation are taken into account.

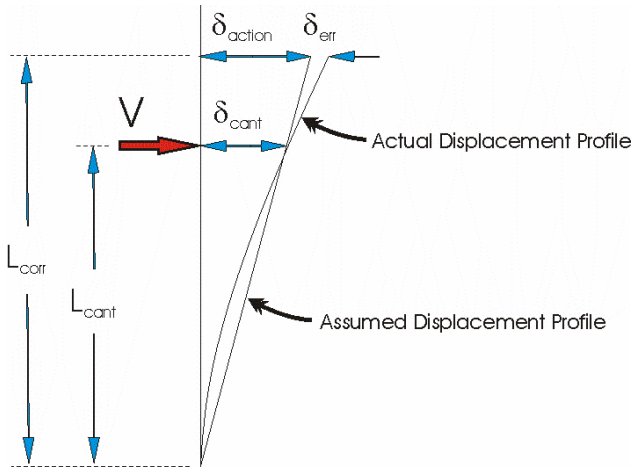

Assessment of Worst Case Consequences

Maximum displacement recorded: $\delta_{max} = 48mm$

Associated correction: $N_H = 60kN$

Likely magnitude of δ_{err}: $0.1 \times \delta_{max}$

Shear Force error associated: $V_{err} \approx 6kN$

Consequently this error is insignificant and can be neglected.

Appendix C Sample Model Calculations

C.1 Calculations for specimen 24L-300-2D

The following pages provide working examples of the typical calculations made throughout this thesis. The figure below is used to help with the geometric dimensions of the specimen.

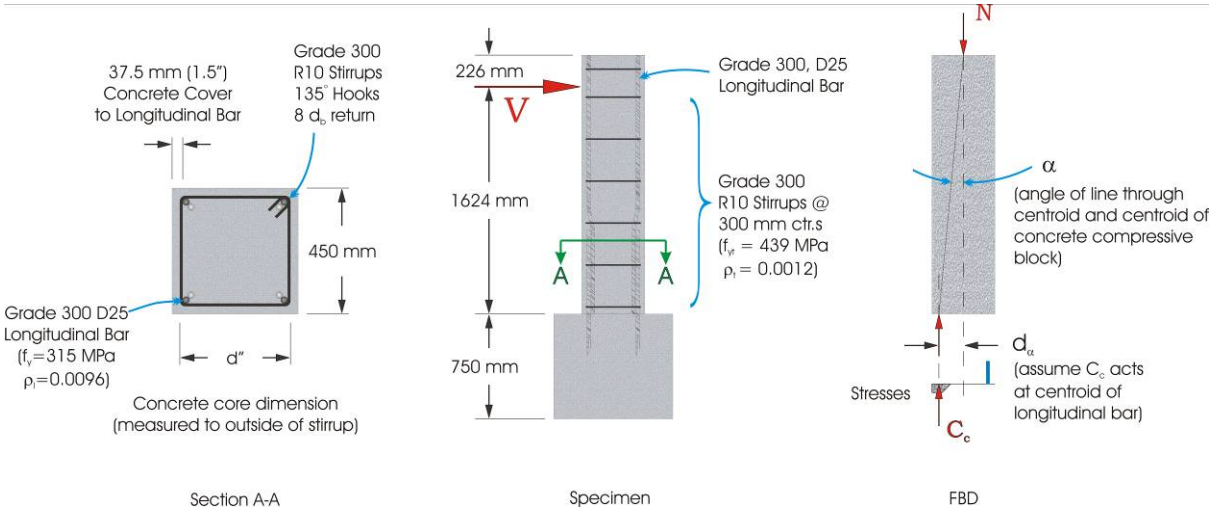

NZSEE Shear Capacity

$$V_{NZSEE} = 0.72(V_c + V_s + V_N) = 0.72\left(k\sqrt{f_c'}\,0.8A_g + \frac{A_v f_{yt} d''}{s}\cot 30° + N.\tan\alpha\right)$$

Where:

f'_c = *33.6 MPa*

A_g = *450 mm x 450 mm*

= *202500 mm^2*

A_v = *2 x π x (10 mm)^2/4*

= *157.1 mm^2*

f_{yt} = *439 MPa*

d'' = *450 mm – 2 x (37.5 mm - 10 mm)*

= *395 mm*

s = *300 mm*

$cot30°$ = *1.732*

N = *2000 kN*

α^N = $tan^{-1}((450/2-50)/(1624+226))$

= *5.40°*

And:

$1 \leq \alpha = M/VD \leq 1.5$ $\alpha = 1.624/0.45$ = *1.5*

$\beta = 0.5 + 20\rho_l \leq 1$ $\beta = 0.5+20 \times 0.0096$ = *0.69*

k = *αβ.k (α, β, defined above, and ductility dependent k from Figure below)*

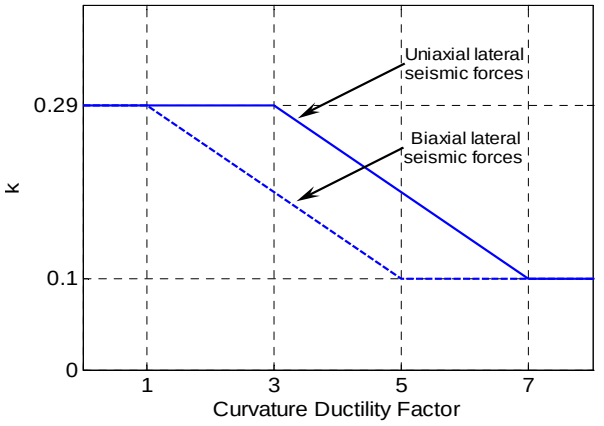

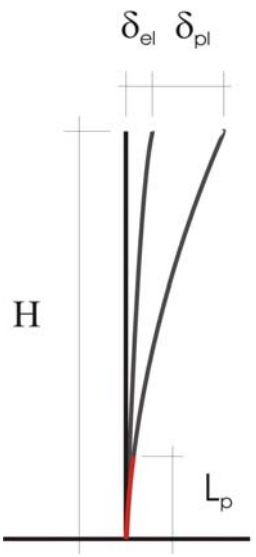

$$\mu_\varphi = \frac{\varphi}{\varphi_y}$$

$$\varphi_y = \frac{2.12\varepsilon_y}{h}$$

$$\delta = \delta_y + \delta_{pl}$$

$$\delta_y = \frac{\varphi_y H}{3}$$

$$\delta_{pl} = \frac{(\varphi - \varphi_y) L_p \left(H - {}^{L_p}/_{2}\right)}{H}$$

$$L_p = 0.08L + 0.022 f_y d_b$$

Where, displacement and related ductility are given by:

φ_y = *2.12 x 0.00158 / 450 mm*

= $7.44 \times 10^{-3}\ m^{-1}$

δ_y = $7.44 \times 10^{-3}\ m^{-1}$ *x 1.624 m / 3*

= *0.40%*

L_p = *0.08 x 1624 mm + 0.022 x 315 MPa x 25 mm*

= *303.2 mm*

δ = *0.40% + 275 x (φ- φ_y)*

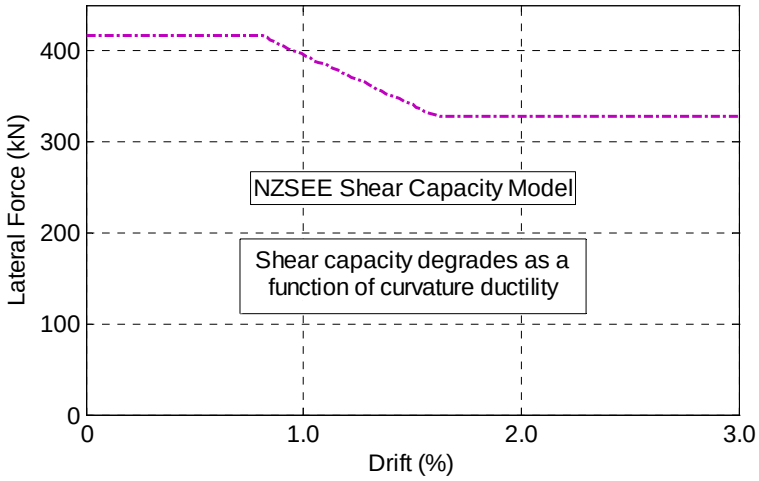

NZSEE Curvature Ductility Limit

Transverse reinforcement required:

$$\frac{A_{sh}}{S_h h''} = \left\{ \frac{A_g}{A_c} \frac{\left\{ \left(\varphi_u / \varphi_y \right) - 33\rho_t m + 22 \right\}}{111} \frac{f_c'}{f_{yt}} \frac{N^*}{\phi f_c' A_g} \right\} - 0.006$$

Rearranging to determine ductility capacity for reinforcement provided:

$$\frac{\varphi_u}{\varphi_y} = \left(\frac{A_{sh}}{s_h h''} + 0.006 \right) . \frac{A_c}{A_g} \frac{f_{yt}}{f_c'} \frac{\phi f_c' A_g}{N^*} . 111 + 33\rho_t m - 22$$

Where:

A_{sh} = *157.1 mm²*

s_h = *300 mm*

h'' = *395 mm* *(d'' from previous)*

A_c = d''^2

= *156025 mm²*

A_g = *202500 mm²*

f_{yt} = *439 MPa*

f_y = *315 MPa*

f'_c = *33.6 MPa*

ϕ = *0.85* *(Safety reduction factor)*

N^* = *2000 kN*

ρ_t = *0.0012*

m = $f_y/0.85f'_c$

= *11.03*

Results in an available curvature ductility:

φ_u/φ_y = *5.25*

Corresponds to a maximum drift of:

δ = $\delta_{el} + \delta_{pl}$

= *0.40% + 275 x (5.25-1) x 7.44 x* 10^{-3} m^{-1}

= *1.27%*

FEMA 356 Shear Limit

$$V_{356} = k_1 \frac{A_s f_{yt} d}{s} + \lambda k_2 \left(\frac{0.5\sqrt{f_c'}}{M/Vd} \sqrt{1 + \frac{N_u}{0.5\sqrt{f_c'} A_g}} \right) 0.8 A_g$$

Where:

A_s = *157.1* mm^2

f_{yt} = *439 MPa*

d = *0.8 x section depth*

= *0.8 x 450 mm*

= *360 mm*

s = *300 mm*

f'_c = *33.6 MPa*

M/V = *1.624*

N_u = *2000 kN*

A_g = *202500* mm^2

λ	=	*1.0*	*(for normal weight concrete)*
k_1	=	*0.5*	*(s > d/2)*
k_2	=	*(ductility dependent refer figure below)*	

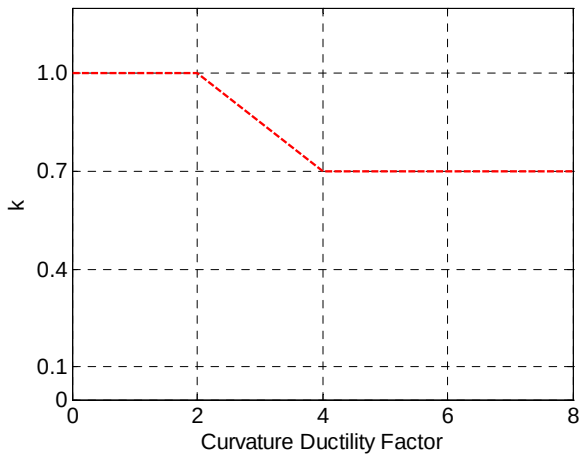

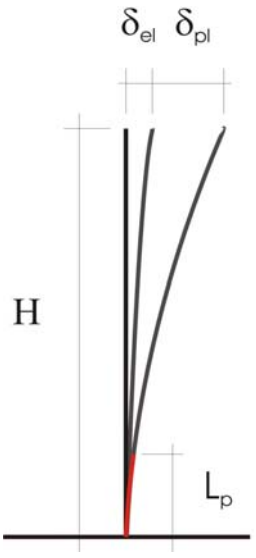

$$\mu_\varphi = \frac{\varphi}{\varphi_y}$$

$$\varphi_y = \frac{2.12\varepsilon_y}{h}$$

$$\delta = \delta_y + \delta_{pl}$$

$$\delta_y = \frac{\varphi_y H}{3}$$

$$\delta_{pl} = \frac{(\varphi - \varphi_y) L_p \left(H - {L_p}/{2} \right)}{H}$$

$$L_p = 0.08L + 0.022 f_y d_b$$

Where, displacement and related ductility are given by:

φ_y	=	*2.12 x 0.00158 / 450 mm*
	=	*7.44 x 10^{-3} m^{-1}*
δ_y	=	*7.44 x 10^{-3} m^{-1} x 1.624 m / 3*
	=	*0.40%*
L_p	=	*0.08 x 1624 mm + 0.022 x 315 MPa x 25 mm*
	=	*303.2 mm*
δ	=	*0.40% + 275 x (φ - φ_y)*

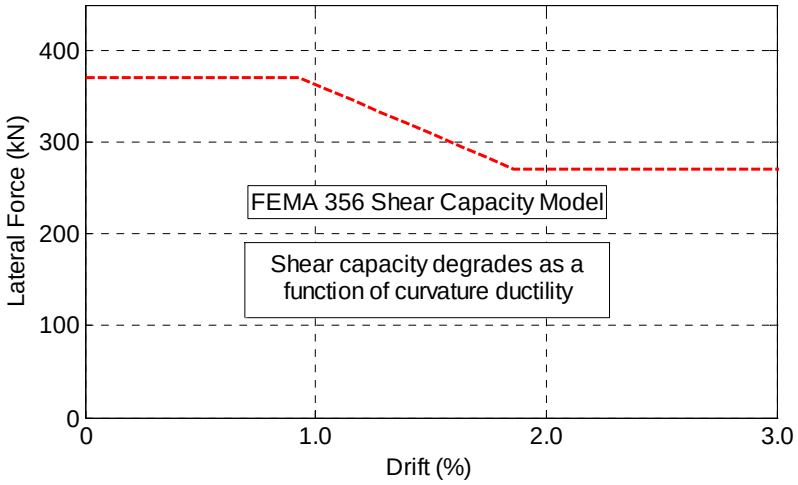

FEMA 356 Backbone

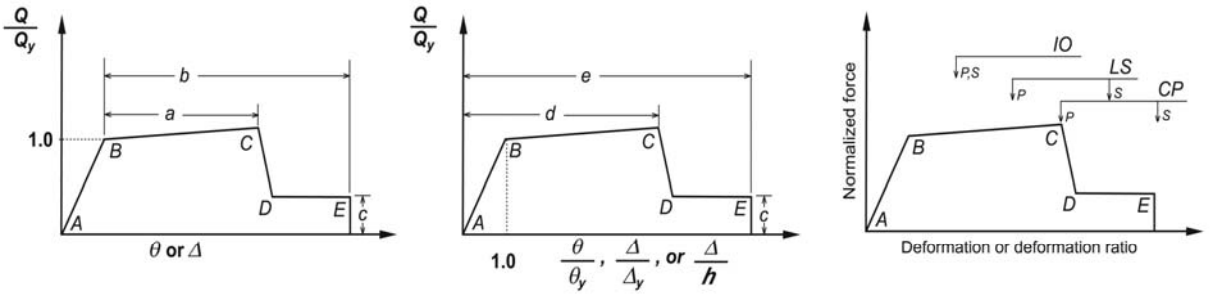

(a) Deformation (b) Deformation ratio (c) Component or element deformation acceptance criteria

Component	Flexural Rigidity	Shear Rigidity	Axial Rigidity
Beams—nonprestressed	$0.5E_cI_g$	$0.4E_cA_w$	—
Beams—prestressed	E_cI_g	$0.4E_cA_w$	—
Columns with compression due to design gravity loads ≥ 0.5 A	$0.7E_cI_g$	$0.4E_cA_w$	E_cA_g
Columns with compression due to design gravity loads ≤ 0.3 A or with tension	$0.5E_cI_g$	$0.4E_cA_w$	E_sA_s
Walls—uncracked (on inspection)	$0.8E_cI_g$	$0.4E_cA_w$	E_cA_g
Walls—cracked	$0.5E_cI_g$	$0.4E_cA_w$	E_cA_g
Flat Slabs—nonprestressed	See Section 6.5.4.2	$0.4E_cA_g$	—
Flat Slabs—prestressed	See Section 6.5.4.2	$0.4E_cA_g$	—

Note: It shall be permitted to take I_g for T-beams as twice the value of I_g of the web alone. Otherwise, I_g shall be based on the effective width as defined in Section 6.4.1.3. For columns with axial compression falling between the limits provided, linear interpolation shall be permitted . Alternatively, the more conservative effective stiffnesses shall be used.

Given the axial load ratio:

A_s = $157.1\ mm^2$

f_{yt} = $439\ MPa$

Conditions			Modeling Parameters[4]			Acceptance Criteria[4]				
			Plastic Rotation Angle, radians		Residual Strength Ratio	Plastic Rotation Angle, radians				
						Performance Level				
							Component Type			
							Primary		Secondary	
			a	b	c	IO	LS	CP	LS	CP
i. Columns controlled by flexure[1]										
$\frac{P}{A_g f_c}$	Trans. Reinf.[2]	$\frac{V}{b_w d \sqrt{f_c}}$								
0.1	C	3	0.02	0.03	0.2	0.005	0.015	0.02	0.02	0.03
0.1	C	6	0.016	0.024	0.2	0.005	0.012	0.016	0.016	0.024
0.4	C	3	0.015	0.025	0.2	0.003	0.012	0.015	0.018	0.025
0.4	C	6	0.012	0.02	0.2	0.003	0.01	0.012	0.013	0.02
0.1	NC	3	0.006	0.015	0.2	0.005	0.005	0.006	0.01	0.015
0.1	NC	6	0.005	0.012	0.2	0.005	0.004	0.005	0.008	0.012
0.4	NC	3	0.003	0.01	0.2	0.002	0.002	0.003	0.006	0.01
0.4	NC	6	0.002	0.008	0.2	0.002	0.002	0.002	0.005	0.008
ii. Columns controlled by shear[1, 3]										
All cases[5]			—	—	—	—	—	—	.0030	.0040
iii. Columns controlled by inadequate development or splicing along the clear height[1,3]										
Hoop spacing d/2			0.01	0.02	0.4	0.005	0.005	0.01	0.01	0.02
Hoop spacing > d/2			0.0	0.01	0.2	0.0	0.0	0.0	0.005	0.01
iv. Columns with axial loads exceeding $0.70P_o$[1, 3]										
Conforming hoops over the entire length			0.015	0.025	0.02	0.0	0.005	0.01	0.01	0.02
All other cases			0.0	0.0	0.0	0.0	0.0	0.0	0.0	0.0

1. When more than one of the conditions i, ii, iii, and iv occurs for a given component, use the minimum appropriate numerical value from the table.
2. "C" and "NC" are abbreviations for conforming and nonconforming transverse reinforcement. A component is conforming if, within the flexural plastic hinge region, hoops are spaced at $d/3$, and if, for components of moderate and high ductility demand, the strength provided by the hoops (V_s) is at least three-fourths of the design shear. Otherwise, the component is considered nonconforming.
3. To qualify, columns must have transverse reinforcement consisting of hoops. Otherwise, actions shall be treated as force-controlled.
4. Linear interpolation between values listed in the table shall be permitted.
5. For columns controlled by shear, see Section 6.5.2.4.2 for acceptance criteria.

Sezen et al. Shear Limit

$$V_{Sezen} = V_s + V_c = k\frac{A_v f_y d}{s} + k\left(\frac{0.5\sqrt{f'_c}}{a/d}\sqrt{1+\frac{P}{0.5\sqrt{f'_c}\,A_g}}\right)0.8A_g$$

Where:

A_v = *157.1 mm²*

f_{yt} = *439 MPa*

d = *Distance from extreme compression fibre to the centroid of tension steel*

= *450 mm – 50 mm*

= *400 mm*

s = *300 mm*

f'_c = *33.6 MPa*

a/d = *1624 mm / 400 mm*

= *4.0* *(2 ≤ a/d ≤ 4)*

P = *2000 kN*

A_g = *202500 mm²*

k = *ductility dependent refer figure below*

δ_y = *Secant stiffness of section at 70% of V_p extended to V_p*

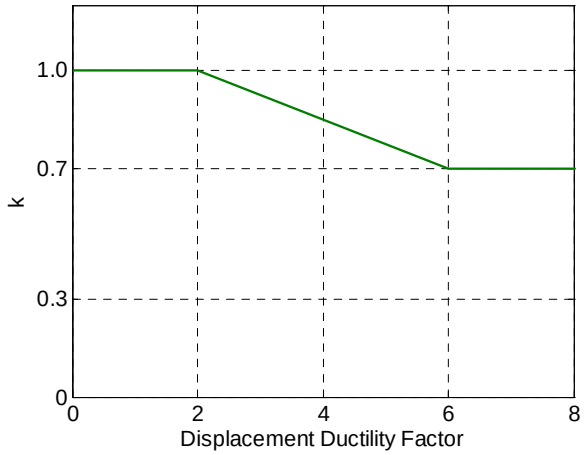

$$\delta_y = \frac{\varphi_y H}{3}$$

Where, displacement and related ductility are given by:

φ_y = $2.12 \times 0.00158 / 450\ mm$

= $7.44 \times 10^{-3}\ m^{-1}$

δ_y = $7.44 \times 10^{-3}\ m^{-1} \times 1.624\ m / 3$

= 0.40%

δ = $0.40\% + 275 \times (\varphi - \varphi_y)$

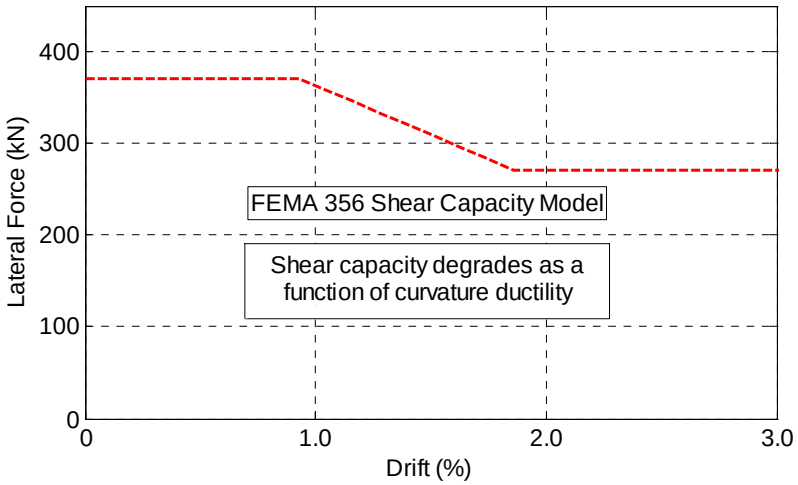

Elwood and Moehle Backbone

1) Shear capacity

(XTRACT section analysis)

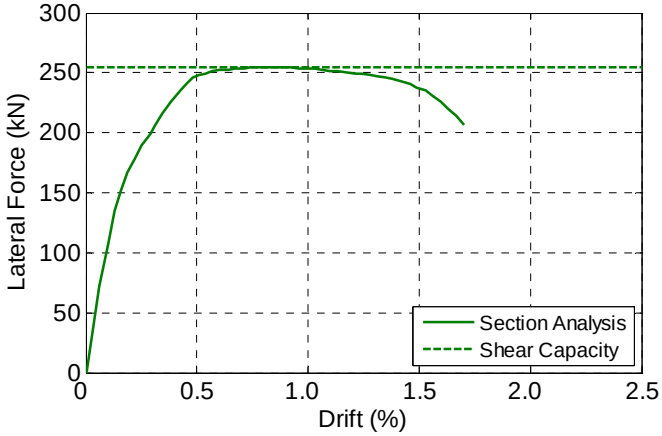

V_p = ***254.7 kN***

2) **Yield Drift** $\delta_y = \delta_{flex} + \delta_{shear} + \delta_{slip}$

Flexural Component: $\delta_{flex} = \frac{L}{3}\phi_y$ where: $\phi_y = \phi_{first\_yield} \cdot \frac{M_p}{M_{first\_yield}}$

$\phi_{first\ yield}$ is the minimum curvature corresponding to first yield of the steel or concrete (ε_y *or* $\varepsilon_c = 0.002$) and $M_{first\ yield}$ is the corresponding moment capacity.

From section analysis $\phi_{first\ yield} = 0.00875m^{-1}$, and $M_{first\ yield} = 400.4kN$

Thus:

ϕ_y = $0.00875m^{-1}$ x 254.7kN x 1.624m / 400.4kN

= $0.00904m^{-1}$

And:

δ_{flex} = 1.624m x $0.00904m^{-1}$ / 3

= 0.49%

Shear Component: $\delta_{shear} = \frac{V_p}{5/6 A_g G}$ where: $G = \frac{E}{2(1-\nu)}$ and $E = 4700\sqrt{f_c'}$

G is the Shear Modulus of the section, and ν is Poissons ratio (= 0.2)

Thus:

E = $4700 \times \sqrt{33.6MPa}$

= $27244\ MPa$

G = $27244\ MPa / 2(1-0.2)$

= $17027\ MPa$

δ_{shear} = $254.7\ kN / ((5/6) \times 202500\ mm^2 \times 17027\ MPa$

= 0.01%

Slip Component: $\delta_{slip} = \dfrac{d_b f_s \phi_y}{8u}$ where: $f_s = \begin{cases} f_y & \Leftarrow \quad P \le 0.2 f'_c A_g \\ f_y\left(\dfrac{5}{3} - \dfrac{10P}{3f'_c A_g}\right) & \Leftarrow \quad 0.2 f'_c A_g \le P \le 0.5 f'_c A_g \\ 0 & \Leftarrow \quad P \ge 0.5 f'_c A_g \end{cases}$

f_s is the axial load dependent stressing the tension, u is the bond stress capacity (take as $0.5\sqrt{f'_c}$) and $P/f'_c A_g$ is the axial stress ratio.

Given $N = 2000\ kN$, $f'_c = 33.6\ MPa$, and $A_g = 202500\ mm^2$

$P/f'_c A_g$ = $0.29\ MPa$

Thus:

f_s = $315 \times (5 - 10 \times 2000\ kN) / (3 \times 33.6\ MPa \times 202500\ mm^2)$

= $216\ MPa$

u = $0.5 \times \sqrt{33.6\ MPa}$

= $2.90\ MPa$

δ_{slip} = $25\ mm \times 216\ MPa \times 0.00904 m^{-1} / (8 \times 2.90\ MPa)$

= 0.21%

δ_y = $\delta_{flex} + \delta_{shear} + \delta_{slip}$

= *0.49 %+0.01 %+0.21 %*

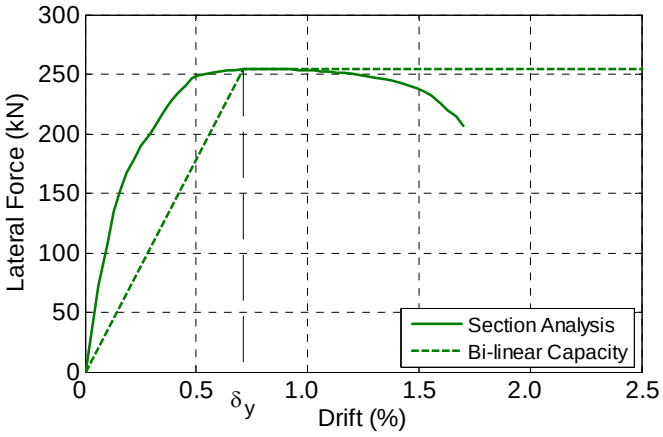

δ_y = ***0.71 %***

3) **Drift at Shear Failure**

$$\delta_s = \frac{3}{100} + 4\rho'' - \frac{1}{40}\frac{\upsilon}{\sqrt{f'_c}} - \frac{1}{40}\frac{P}{A_g f'_c} \geq \frac{1}{100}$$

Where ρ'' is the transverse reinforcement ratio (= *0.0012*), and υ is the nominal shear stress applied to the section.

υ = *254.7 kN / 202500 mm^2*

= *1.258 MPa*

δ_s = *0.03 + 4 x 0.0012 – 0.025 x 1.258 / √33.6 MPa – 0.025 x 0.29 (≥ 0.01)*

= *2.20 %*

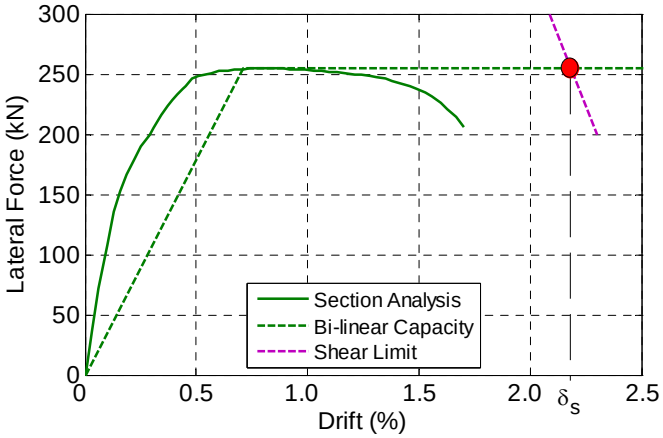

δ_s = ***2.20 %***

4) **Drift at Axial Failure**

$$\delta_a = \frac{4}{100} \frac{1 + \tan^2 65°}{\tan 65° + P\left(\frac{s}{A_{st} f_{yt} d_c \tan 65°}\right)}$$

Where d_c is the depth of the column core in the direction of the applied shear.

δ_s = *0.04 x (1 + tan² 65°) / (tan 65° + 2000 kN x (300 mm / ...*

(157.1 x 439 MPa x 395 mm x tan 65°)))

= *1.80 %*

As the calculated axial failure occurs at a lower level of drift than the drift at shear failure, and the axial failure model presupposes a shear failure plane the axial failure drift is corrected to coincide with the shear failure drift.

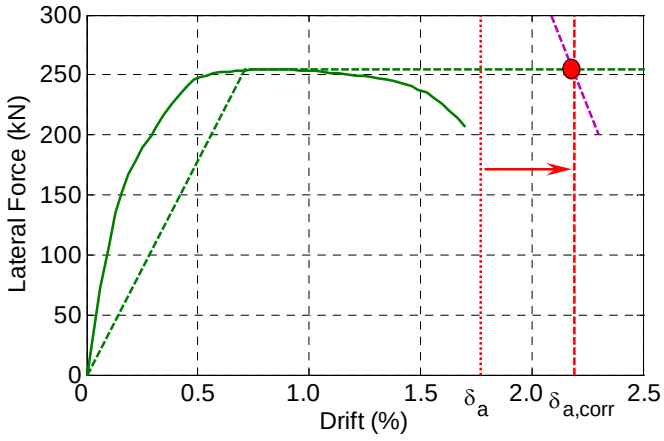

δ_a = ***2.20 %***

Backbone Model (Elwood and Moehle)

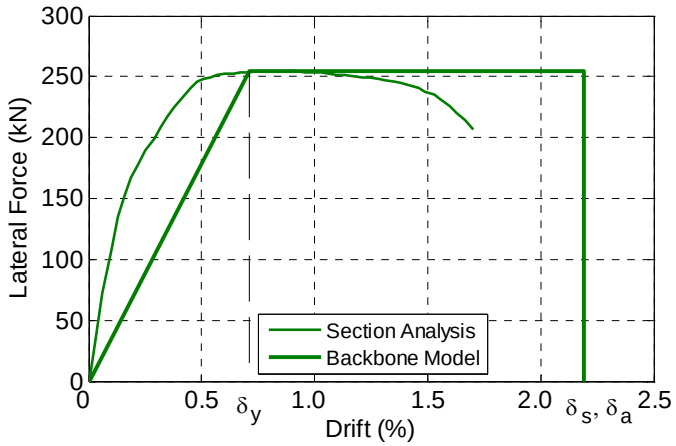

Appendix D Instrumentation Results

D.1 Strain-Gauges

This section of the appendices presents the measurements from the strain gauges attached to the longitudinal reinforcement. Measured data from each test specimen is presented in the six following graphs. Each graph contains the full recorded data for all 24 strain gauges, with sub-plots for the bar locations presented horizontally (starting from the SW corner and progressing clockwise), and the height of the gauges presented vertically. On each of the sub-plots the starter bar and longitudinal column bar data is presented comparatively. The figure below illustrates the labelling convention used.

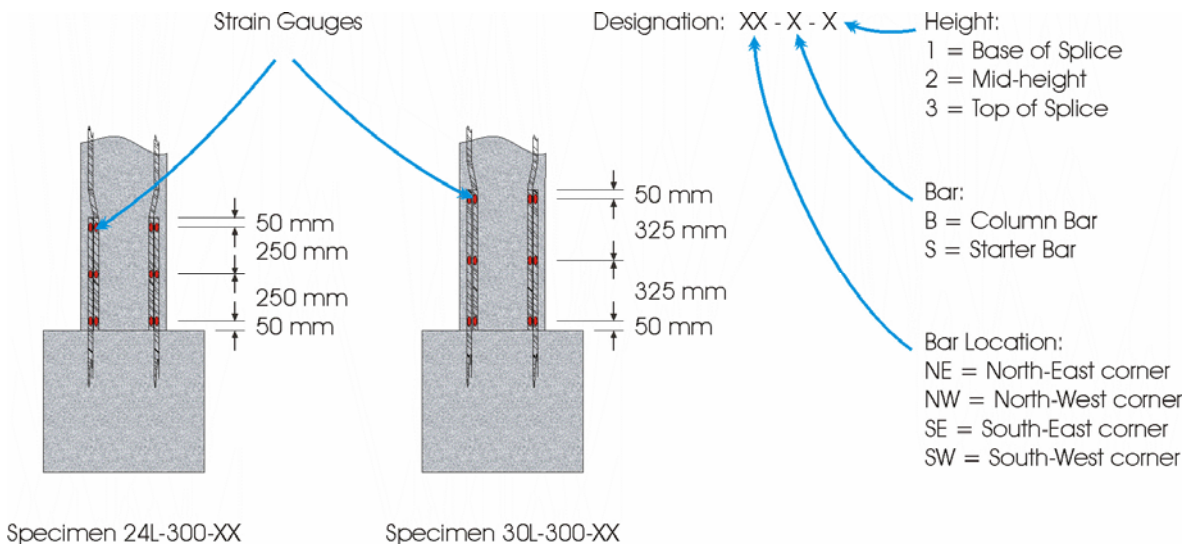

Where the strain gauge failed as a result of damage to the specimen the data presentation is terminated.

Specimen 24L-300-2D

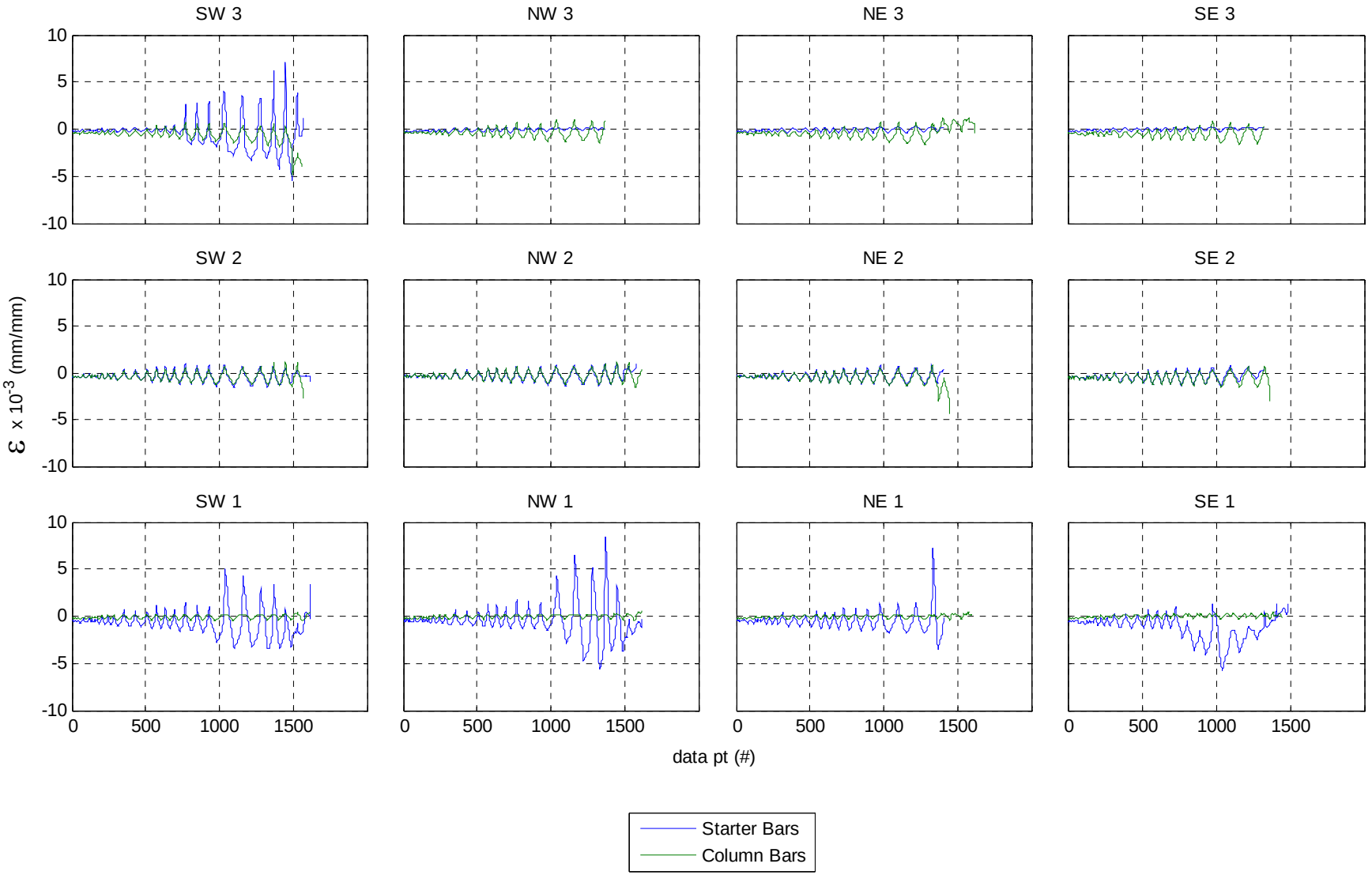

Specimen 24L-300-3D

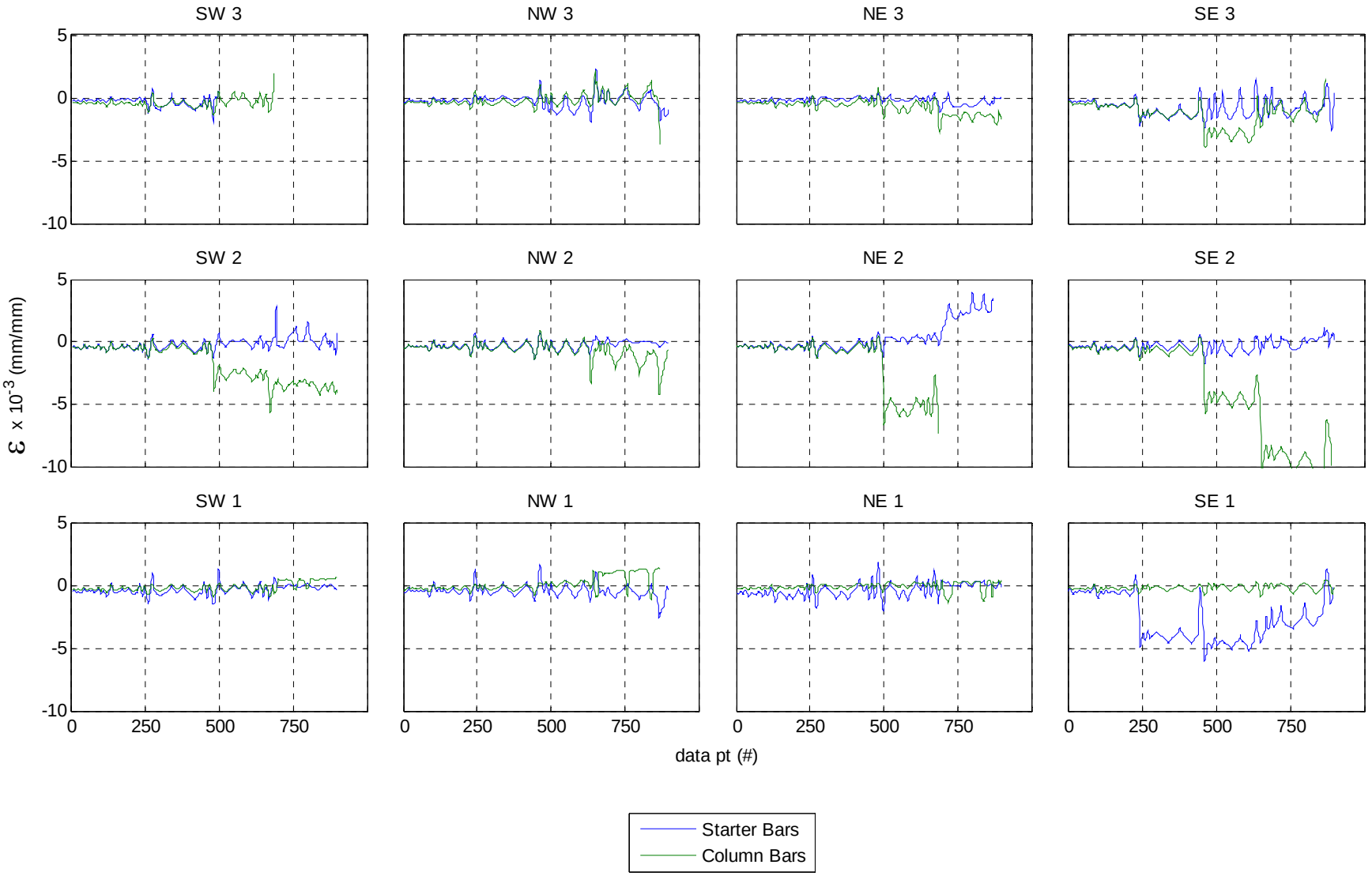

Specimen 24L-300-3D-R

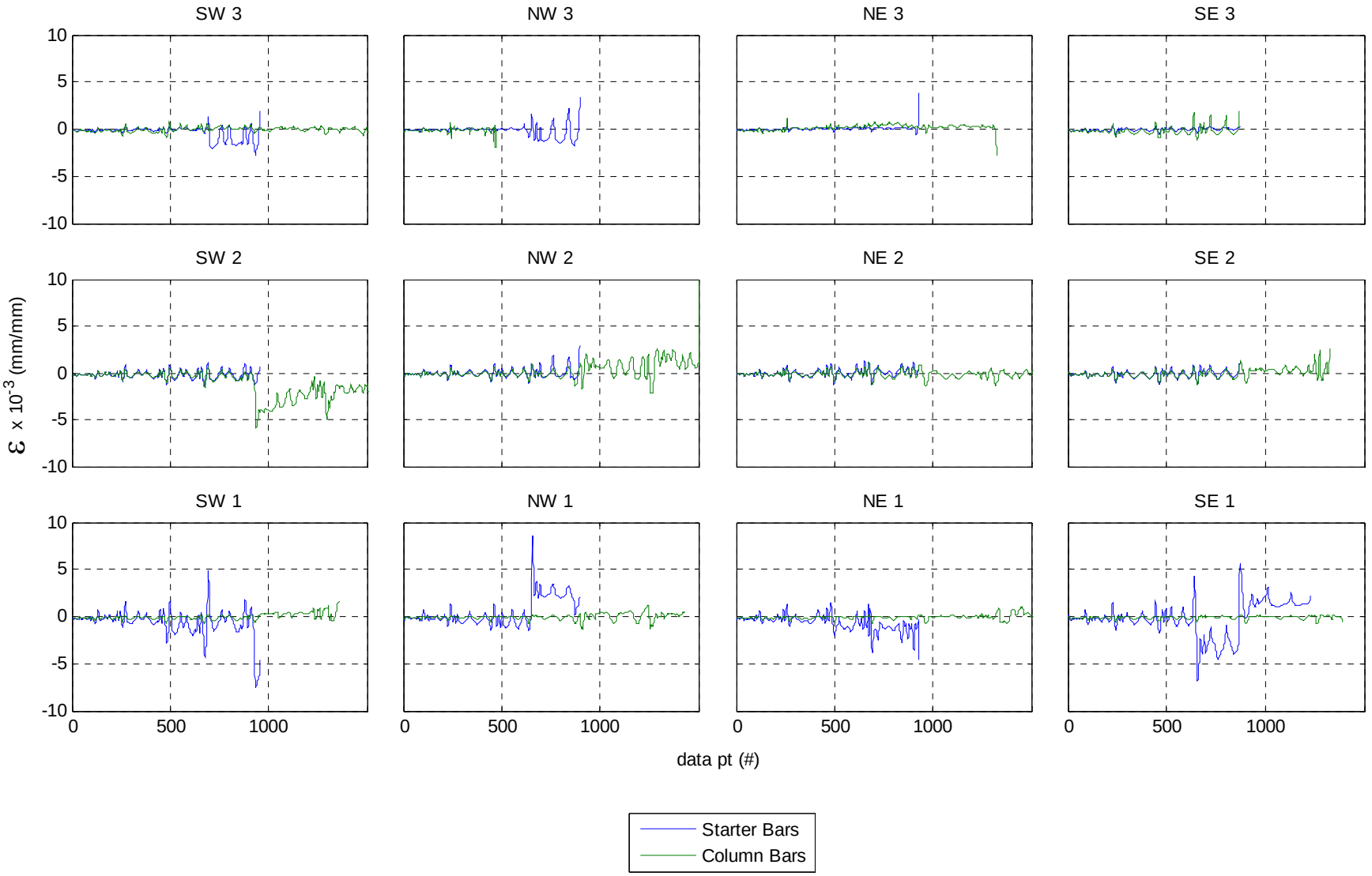

Specimen 30L-300-2D

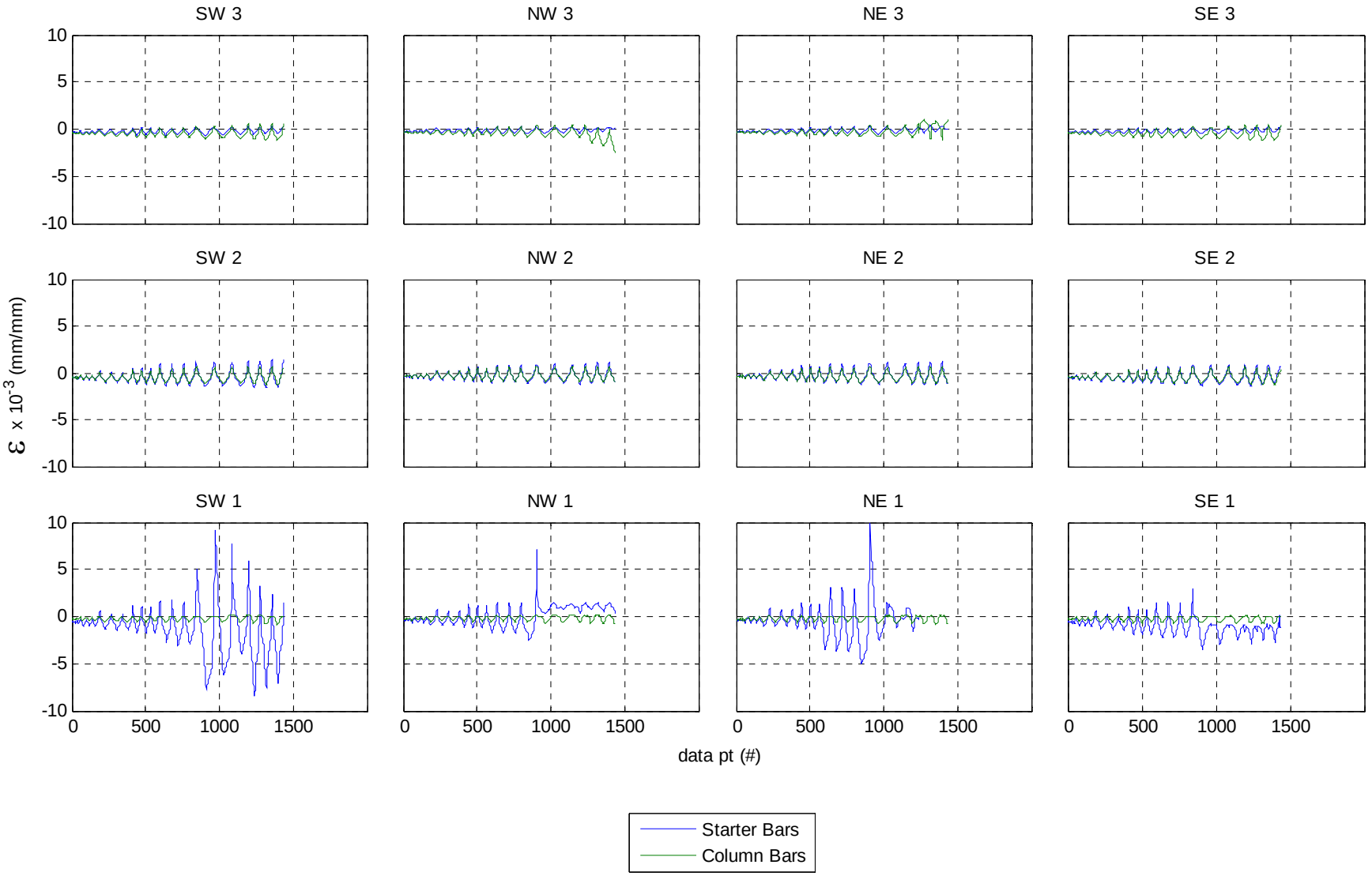

Specimen 30L-300-3D

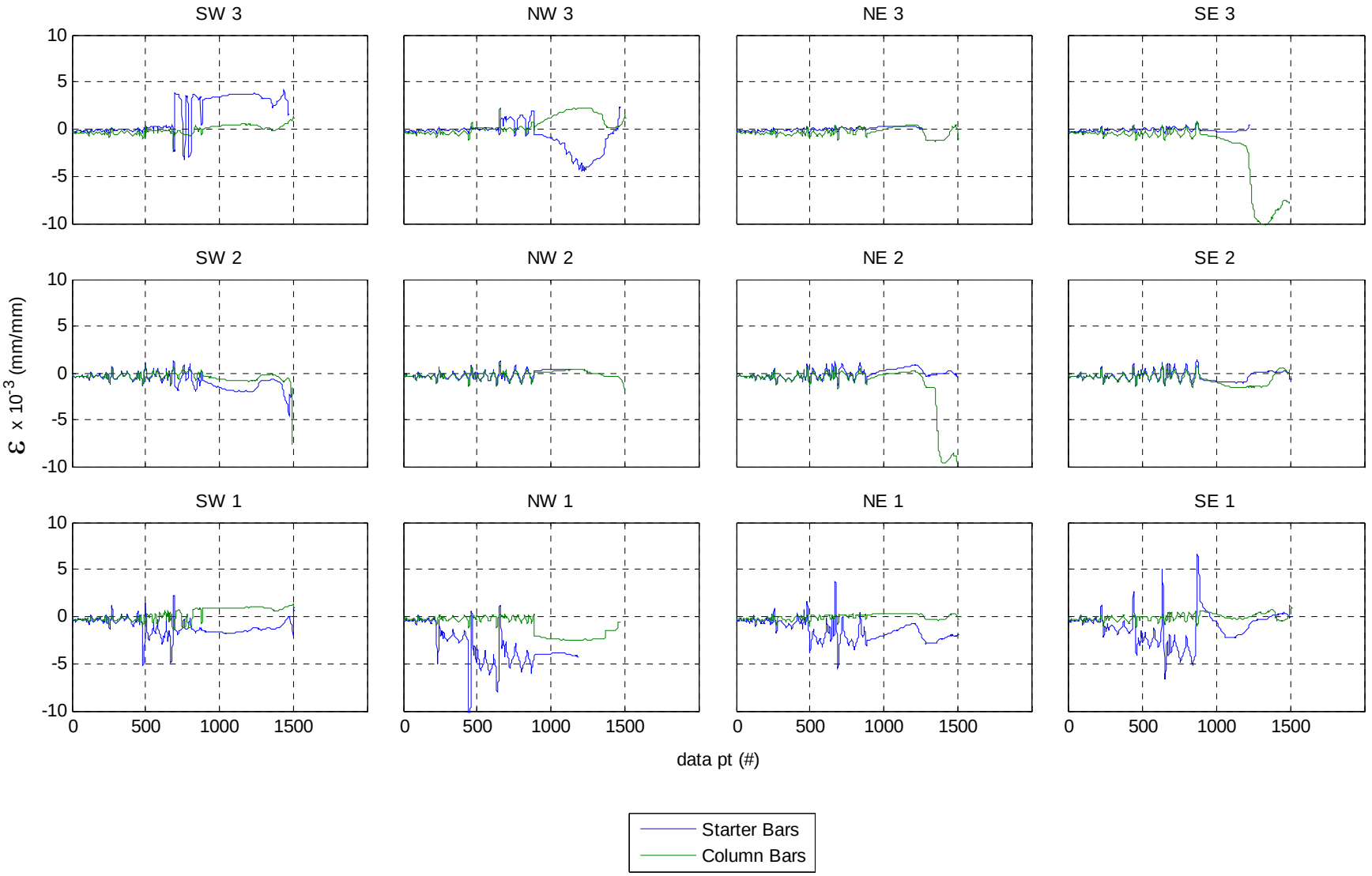

Specimen 24L-300-EQ

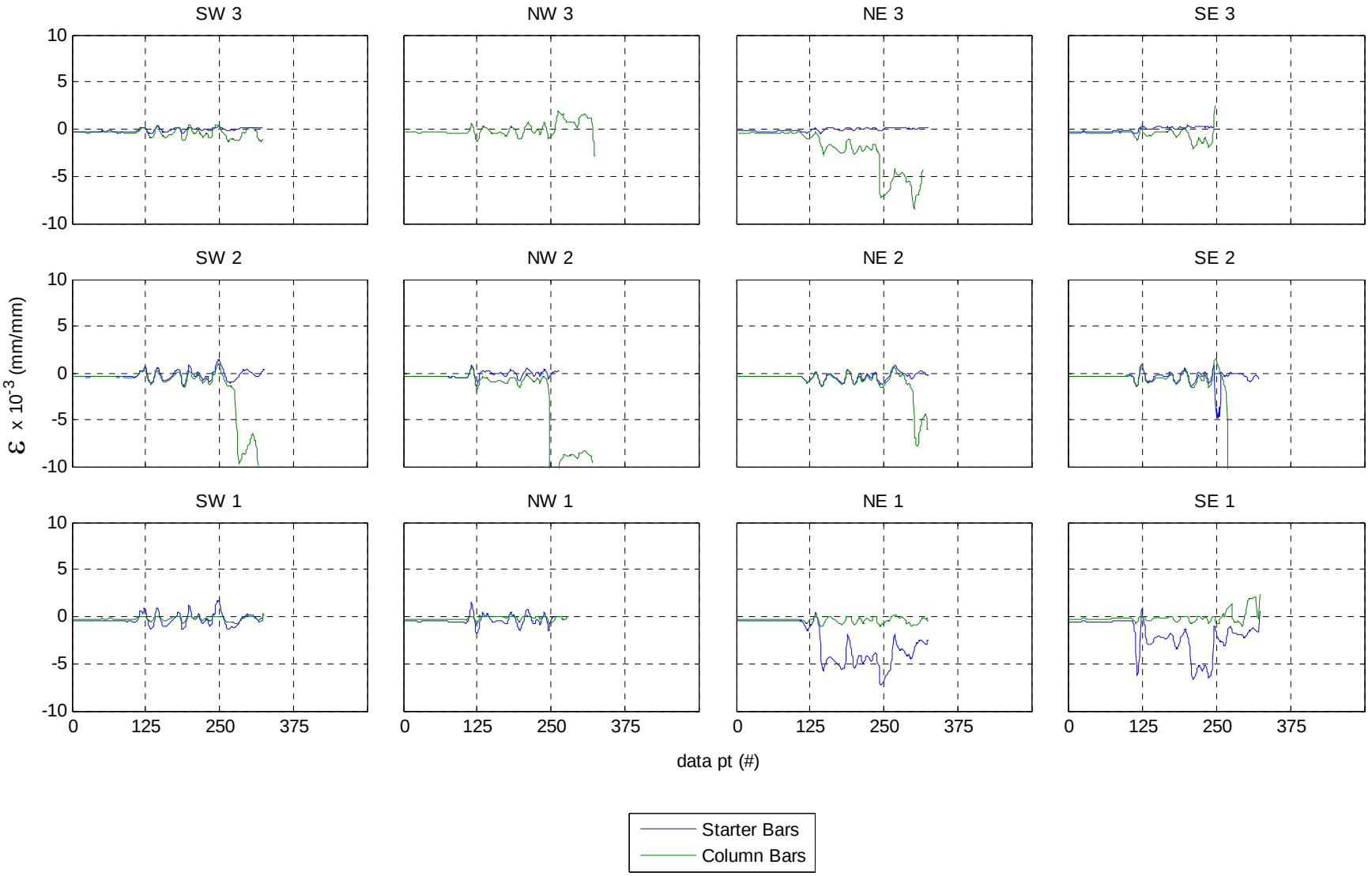

D.2 Potentiometer Data

This section of the appendices presents the measurements from the linear potentiometers attached to the base of the specimen as illustrated on the left in the figure below. Measured data from each test specimen is presented in the six following graphs. Each figure contains the full recorded data for each specimen, with the graphs for each individual potentiometer plotted in a position on the figure that represents their location as seen in plan. The two specimens tested in uni-directional bending have a reduced number of potentiometers sufficient to capture the rotation at the base.

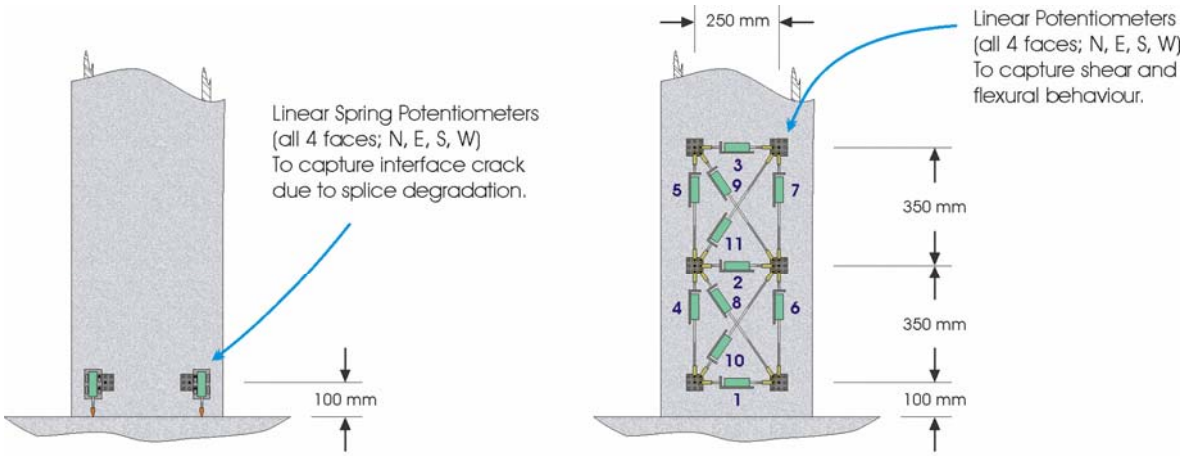

Note: The data collected from the instrumentation as shown on the right in the figure above (intended for calculation of the relative shear and flexural displacements) is not shown here as the acquisition was inadequate and incomplete due to progressive damage to the specimen and recording problems.

Specimen 24L-300-2D

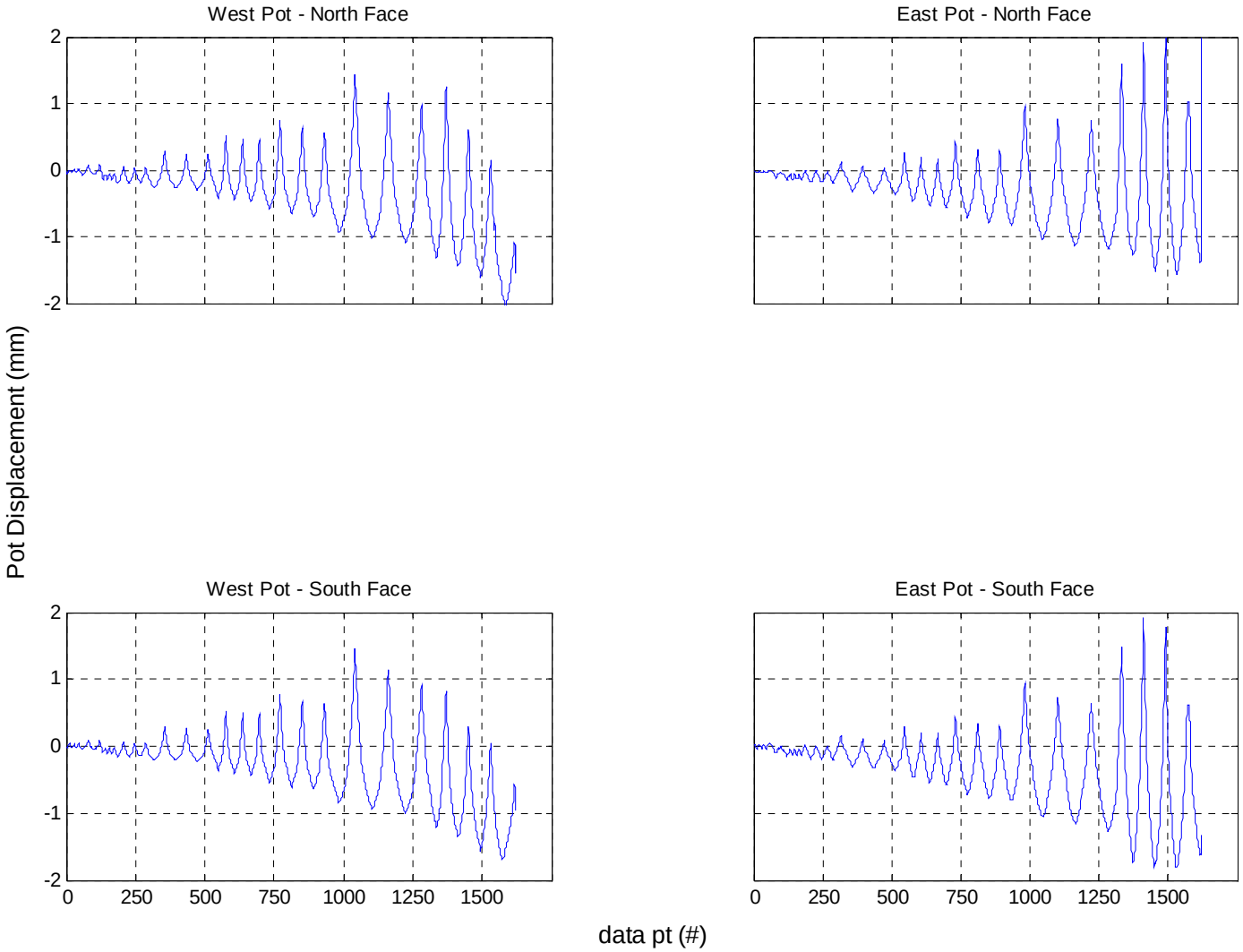

Specimen 24L-300-3D

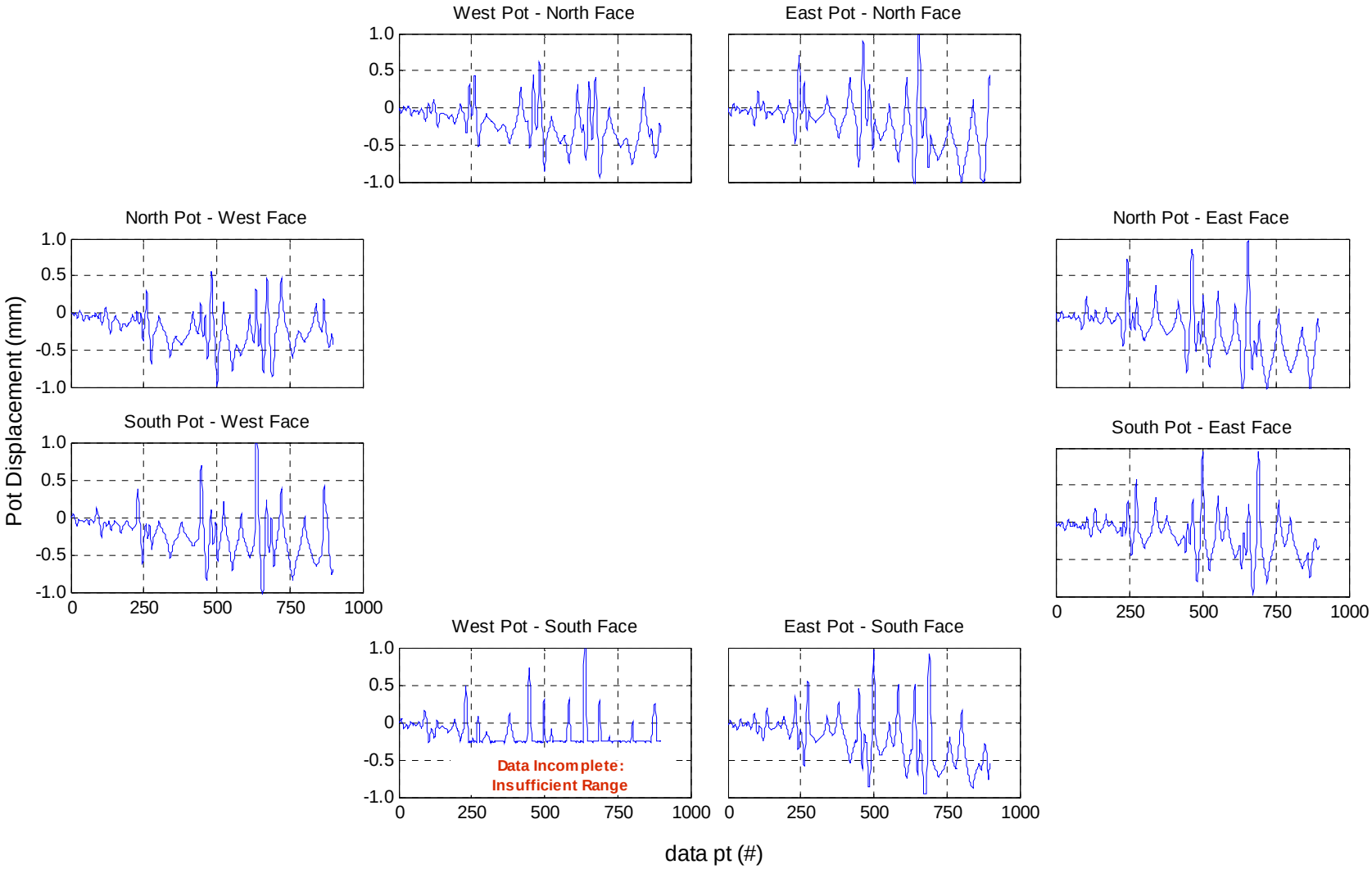

Specimen 24L-300-3D-R

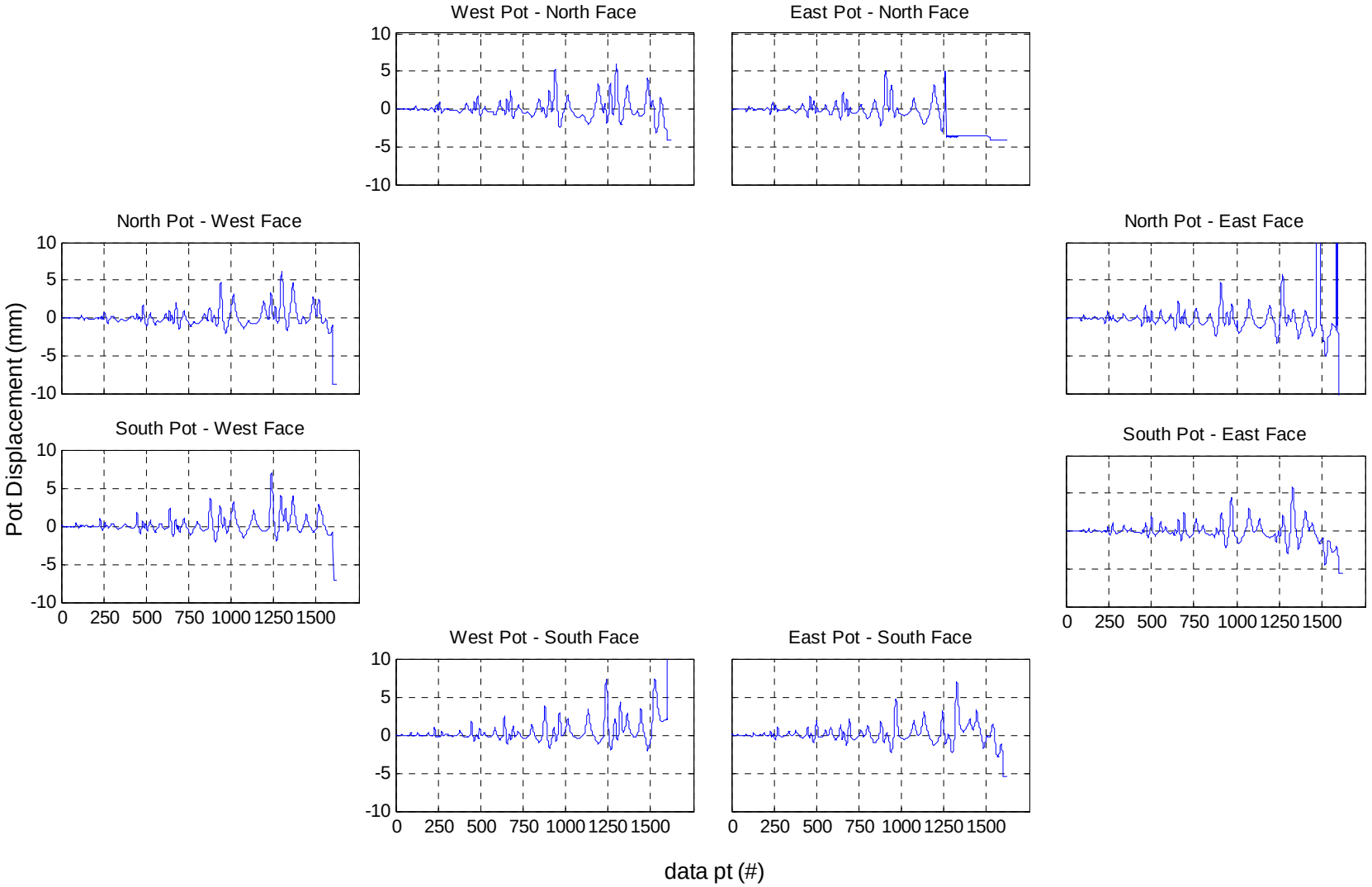

Specimen 30L-300-2D

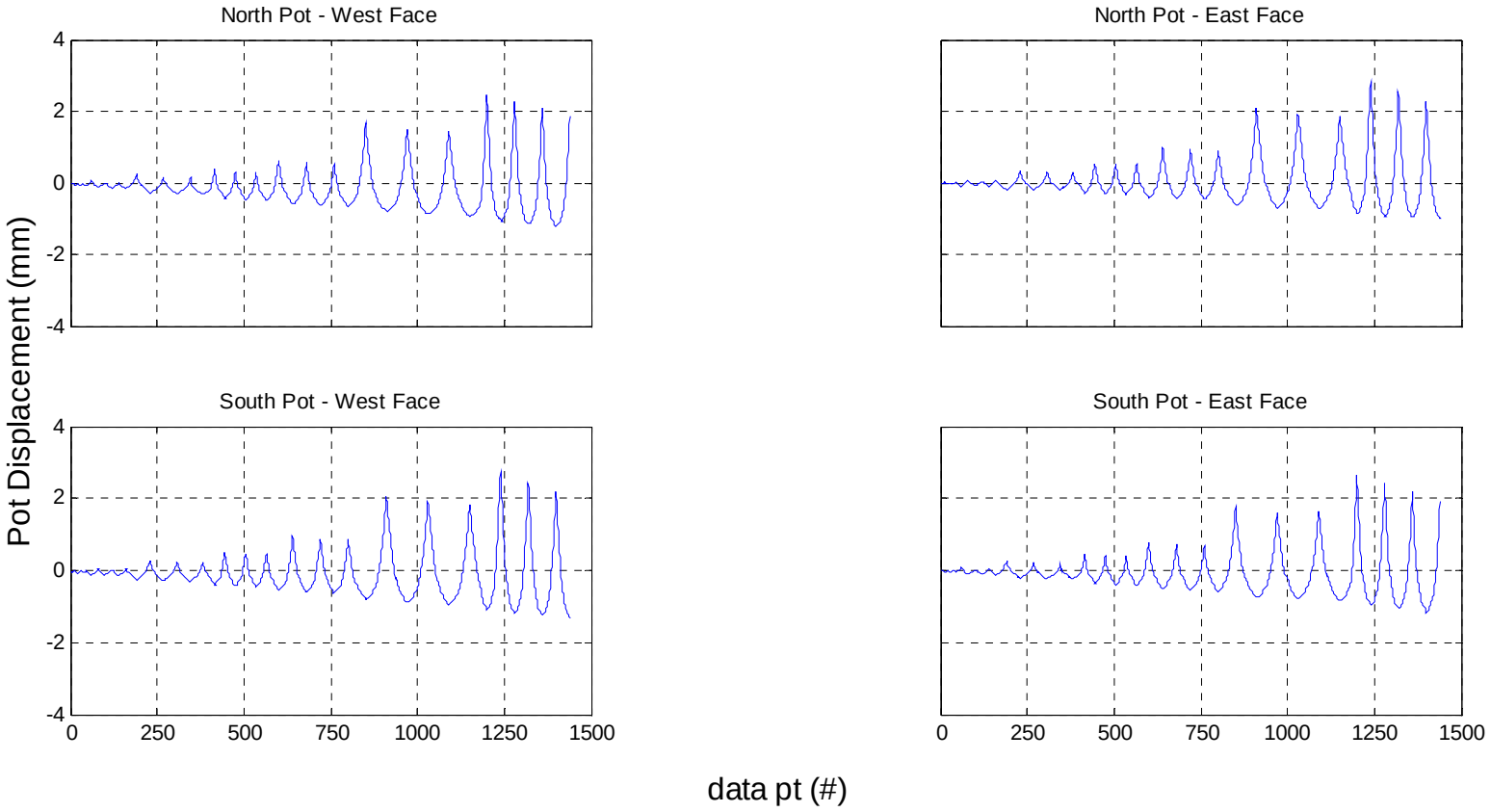

Specimen 30L-300-3D

(Note that data acquisition converted to time based sampling at end of test, resulting in the evident elongation)

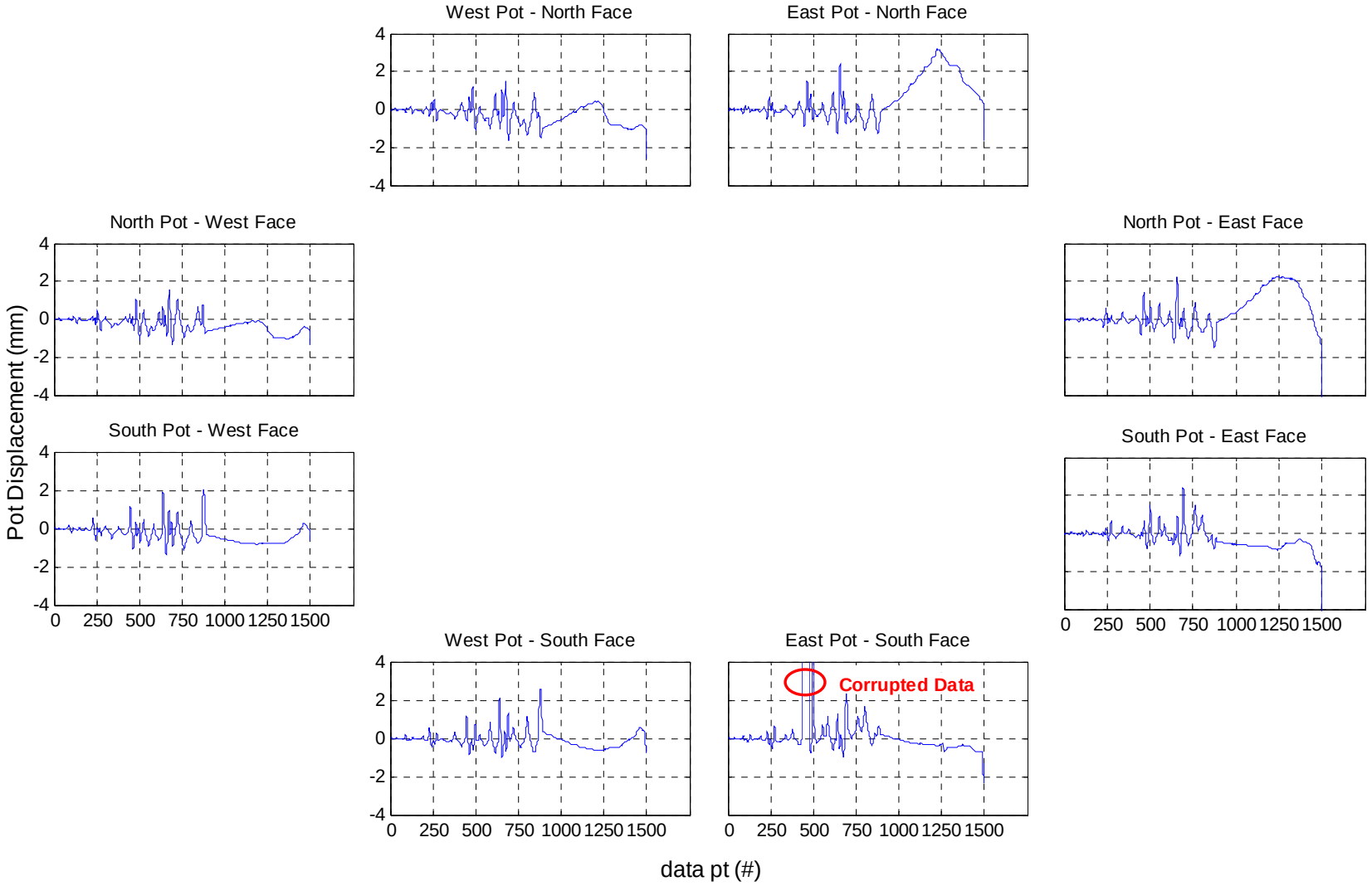

Specimen 24L-300-EQ

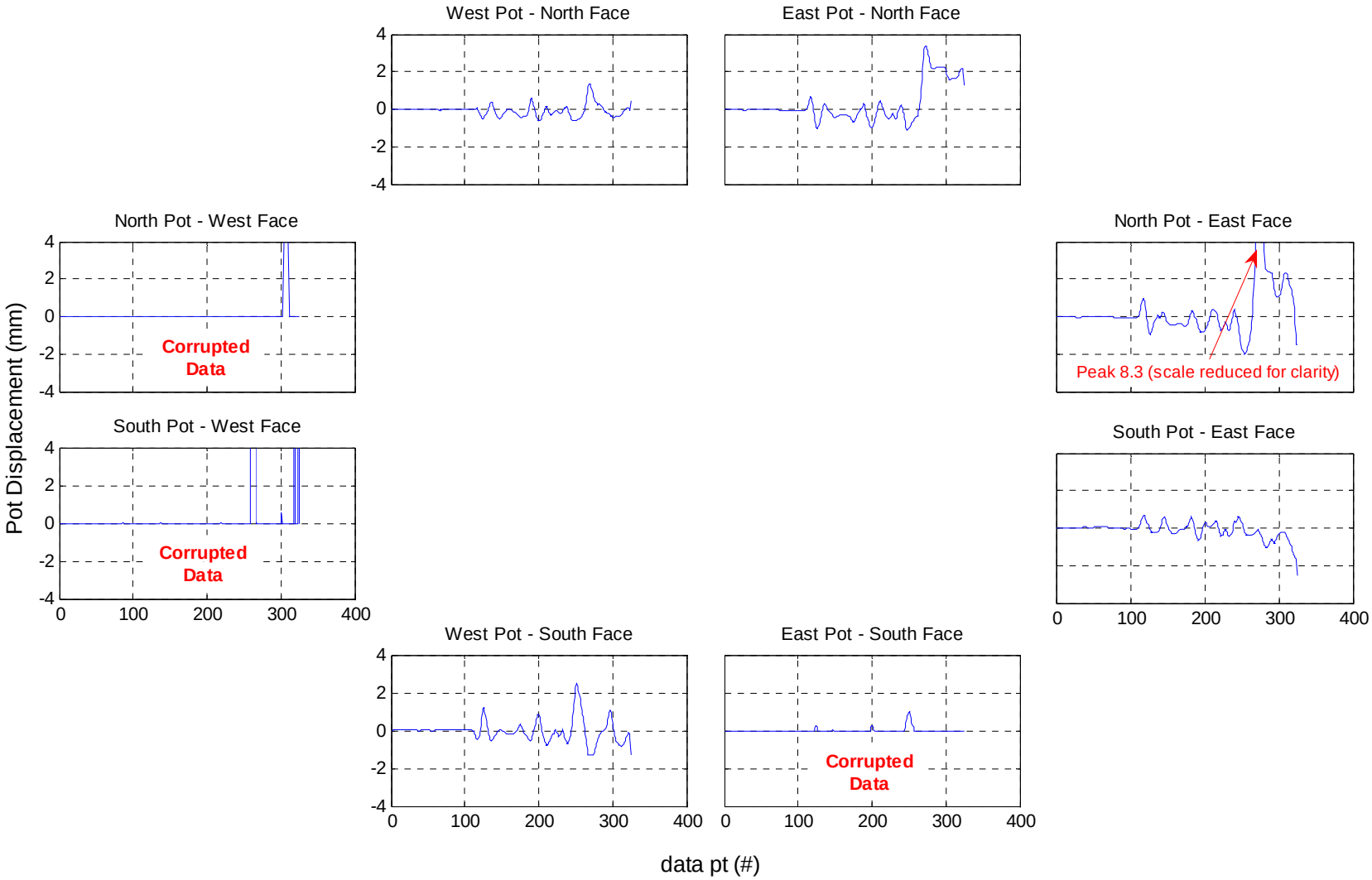

Appendix E Test Photographs

E.1 Construction

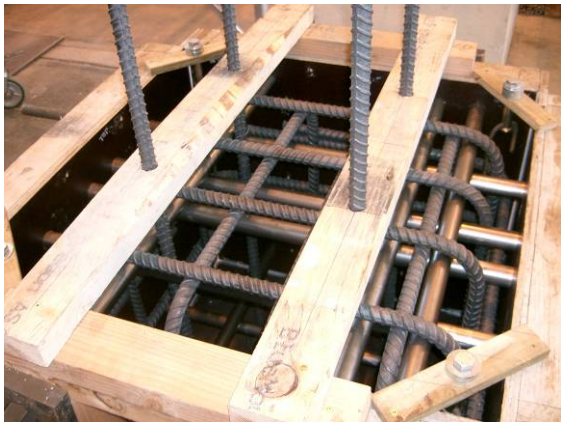

Base-block and formwork

Pouring base-block concrete

Lap-splice at base of column

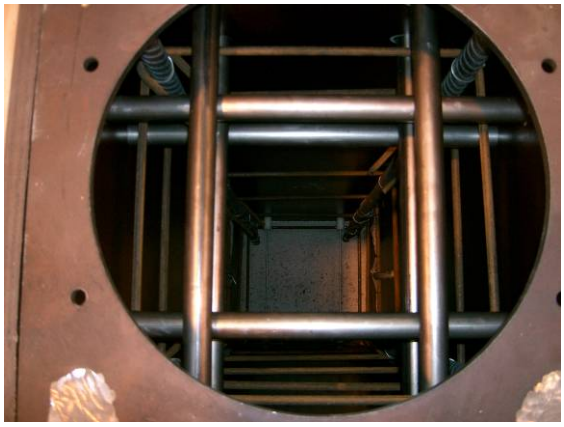

View down column before concrete pour

Lap-splice detail

Column formwork

Pouring column

E.2 Specimen 24L-300-2D

North Face

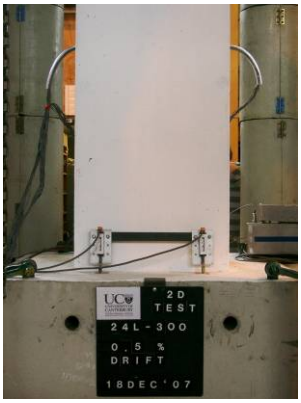

+ 0.5% Drift 1st Cycle

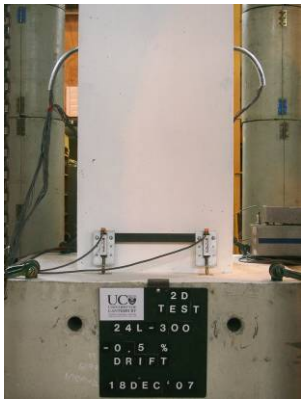

- 0.5% Drift 1st Cycle

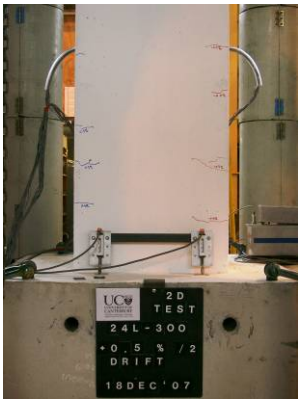

+ 0.5% Drift 2nd Cycle

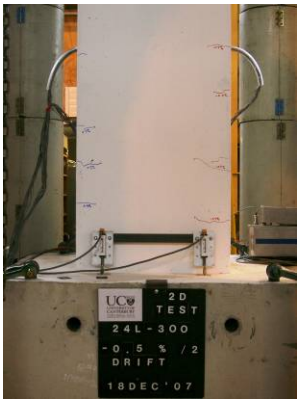

- 0.5% Drift 2nd Cycle

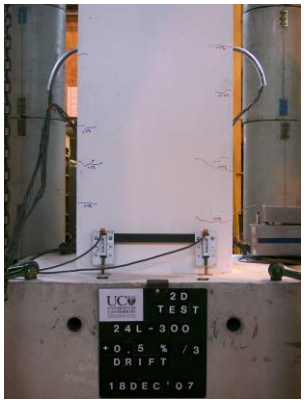

+ 0.5% Drift 3rd Cycle

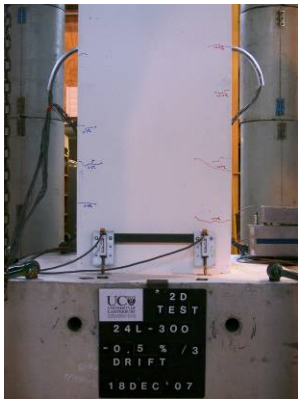

- 0.5% Drift 3rd Cycle

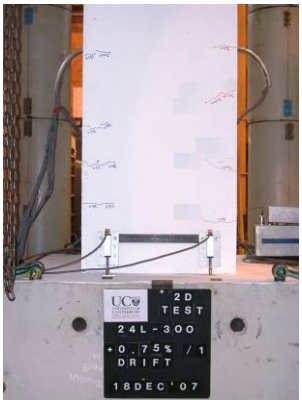

+ 0.75% Drift 1st Cycle

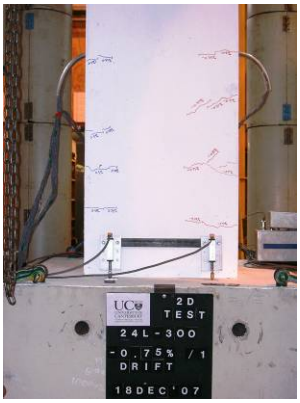

- 0.75% Drift 1st Cycle

+ 0.75% Drift 2nd Cycle

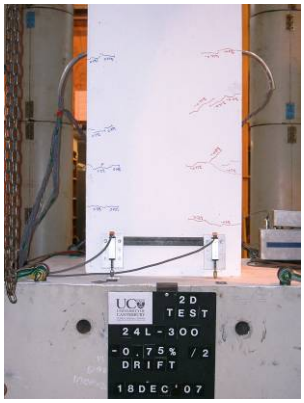

- 0.75% Drift 2nd Cycle

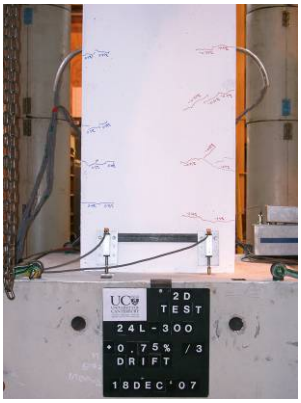

+ 0.75% Drift 3rd Cycle

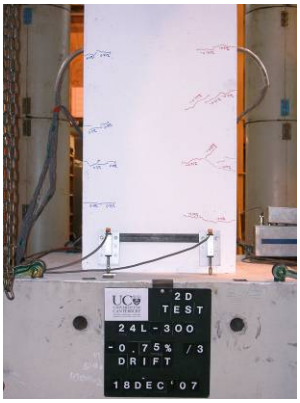

- 0.75% Drift 3rd Cycle

Specimen 24L-300-2D (Cont.)

North Face

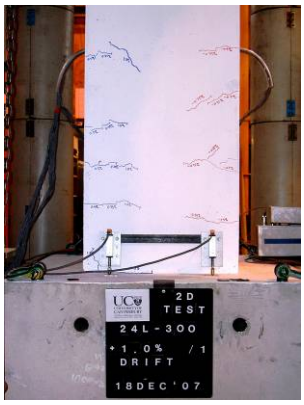

+ 1.0 % Drift 1st Cycle

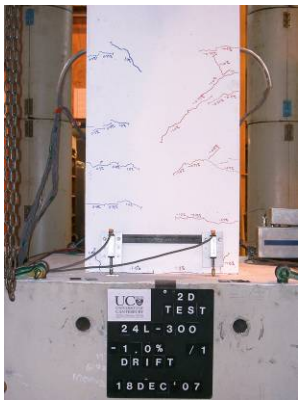

- 1.0 % Drift 1st Cycle

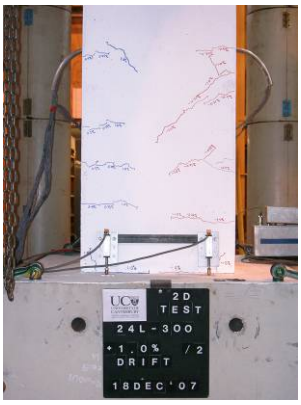

+ 1.0 % Drift 2nd Cycle

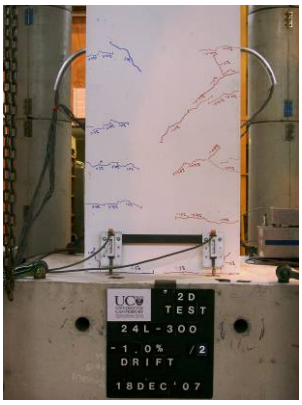

- 1.0 % Drift 2nd Cycle

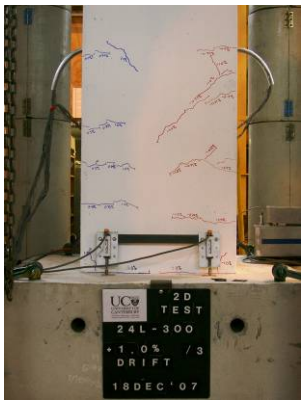

+ 1.0 % Drift 3rd Cycle

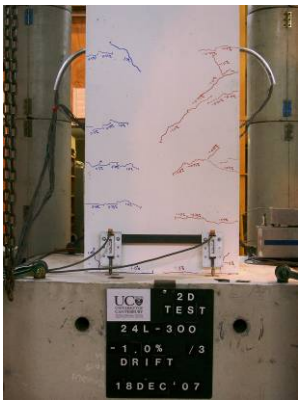

- 1.0 % Drift 3rd Cycle

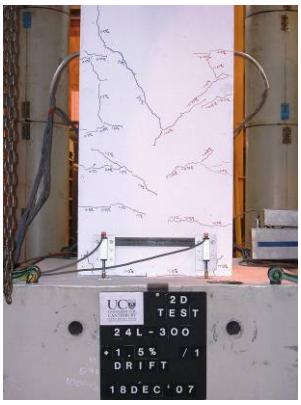

+ 1.5 % Drift 1st Cycle

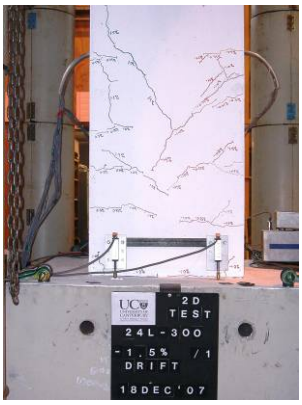

- 1.5 % Drift 1st Cycle

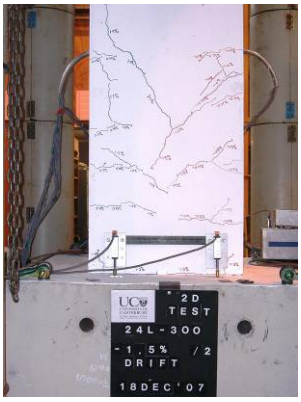

+ 1.5 % Drift 2nd Cycle

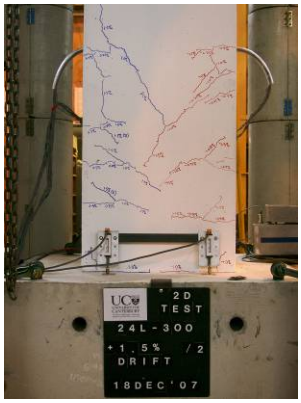

- 1.5 % Drift 2nd Cycle

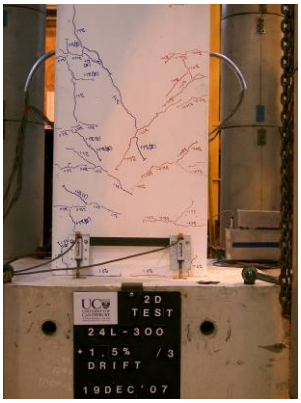

+ 1.5 % Drift 3rd Cycle

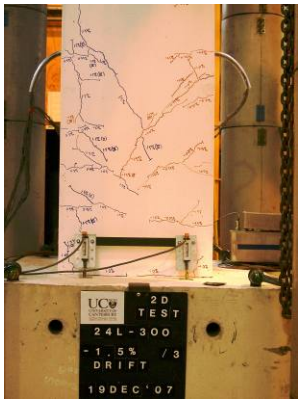

- 1.5 % Drift 3rd Cycle

Specimen 24L-300-2D (Cont.)

North Face

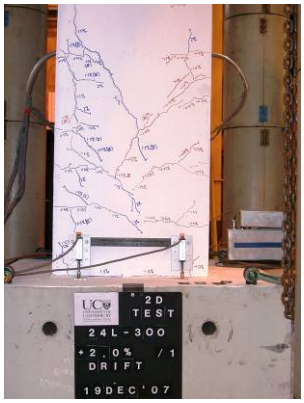

+ 2.0 % Drift 1st Cycle

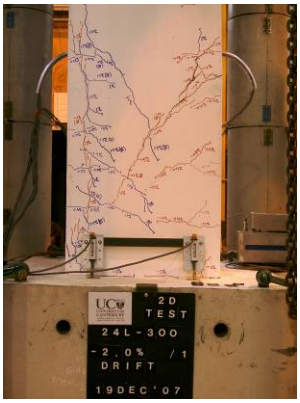

- 2.0 % Drift 1st Cycle

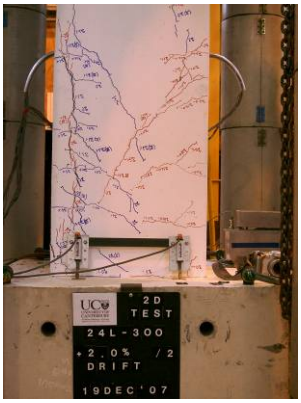

+ 2.0 % Drift 2nd Cycle

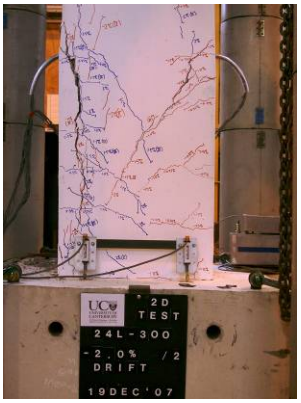

- 2.0 % Drift 2nd Cycle

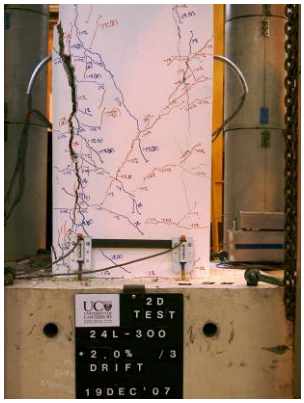

+ 2.0 % Drift 3rd Cycle

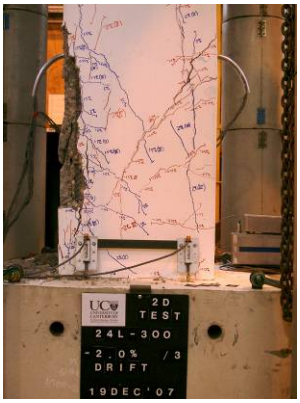

- 2.0 % Drift 3rd Cycle

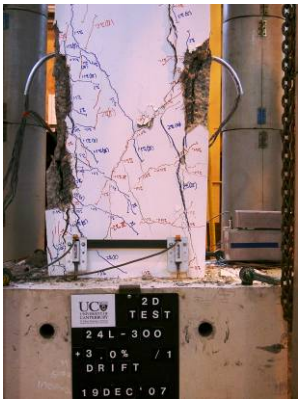

+ 3.0 % Drift 1st Cycle

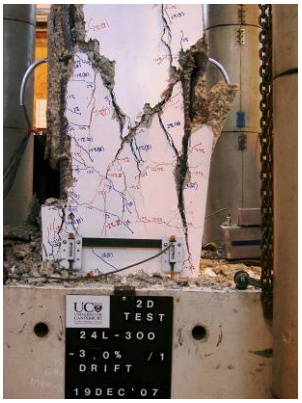

- 3.0 % Drift 1st Cycle

Failure Photographs

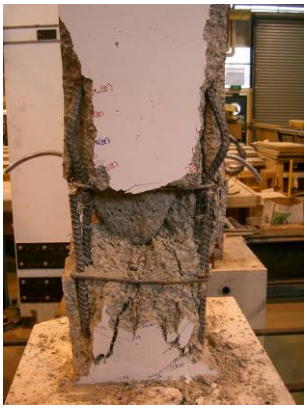

Buckled Bars and Shear Failure cone

Burst Stirrup and out-of-plane failure

E.3 Specimen 24L-300-3D

North Face

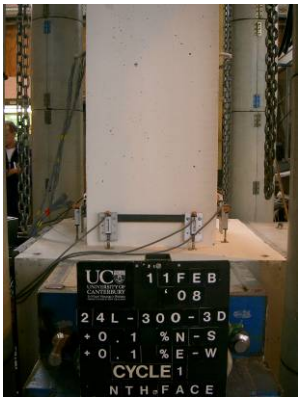

1st Loop of 0.1% Drift Cycles

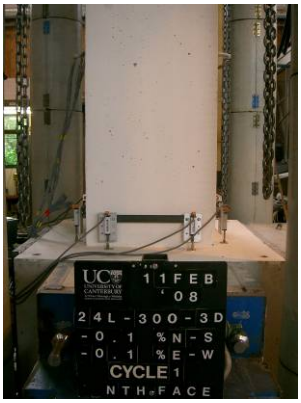

2nd Loop of 0.1% Drift Cycles

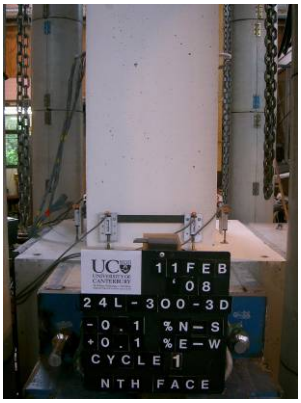

3rd Loop of 0.1% Drift Cycles

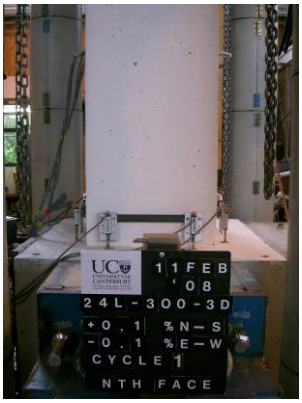

4th Loop of 0.1% Drift Cycles

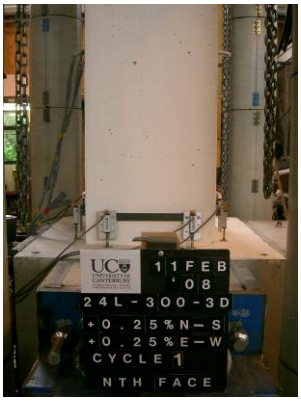

1st Loop of 0.25% Drift Cycles

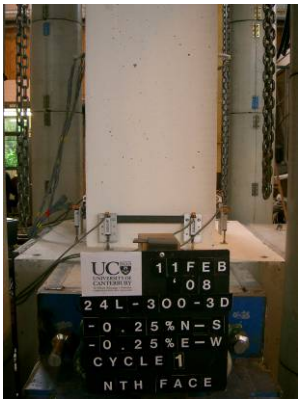

2nd Loop of 0.25% Drift Cycles

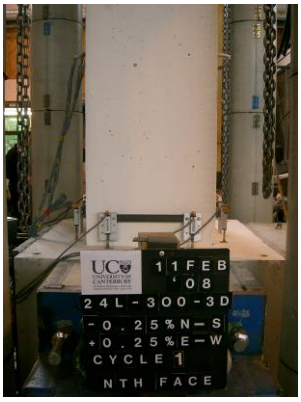

3rd Loop of 0.25% Drift Cycles

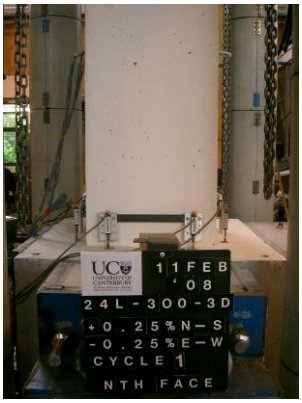

4th Loop of 0.25% Drift Cycles

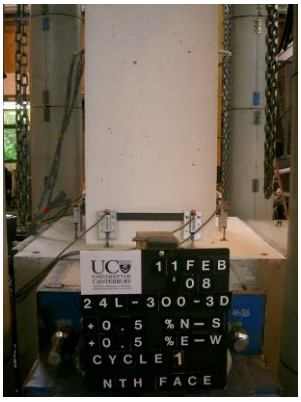

1st Loop of 0.5% Drift Cycles

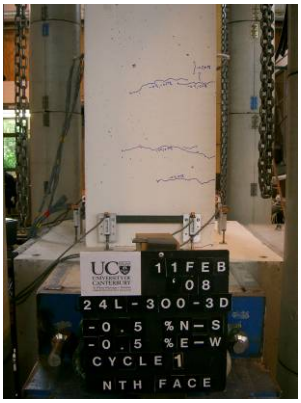

2nd Loop of 0.5% Drift Cycles

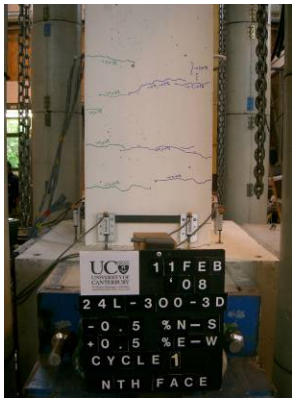

3rd Loop of 0.5% Drift Cycles

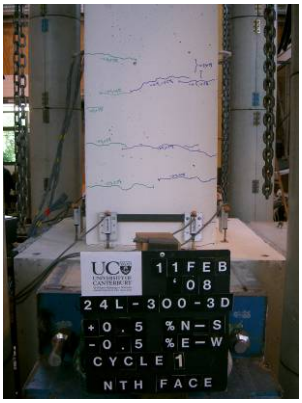

4th Loop of 0.5% Drift Cycles

Specimen 24L-300-3D (Cont.)

North Face

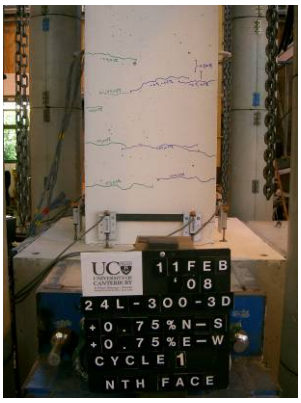

1st Loop of 0.75% Drift Cycles

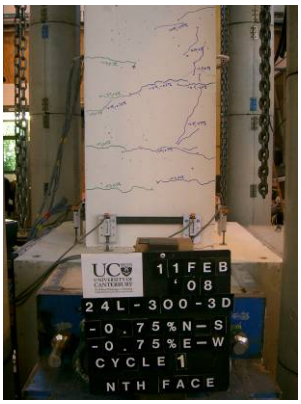

2nd Loop of 0.75% Drift Cycles

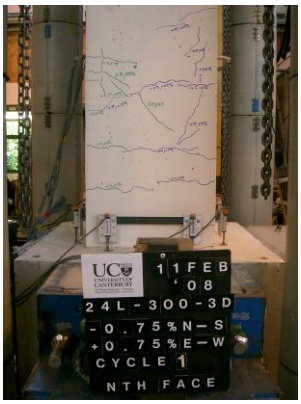

3rd Loop of 0.75% Drift Cycles

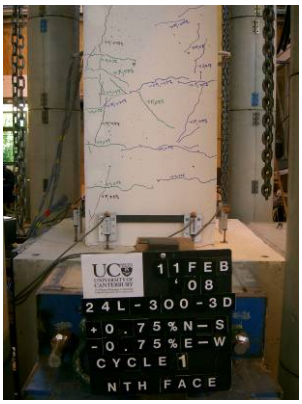

4th Loop of 0.75% Drift Cycles

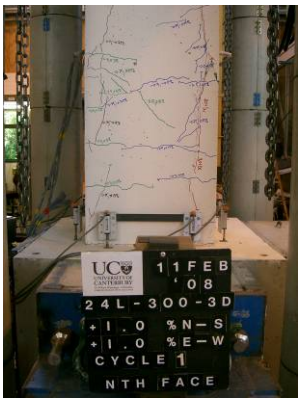

1st Loop of 1.0% Drift Cycles

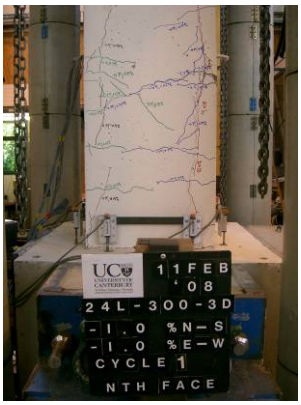

2nd Loop of 1.0% Drift Cycles

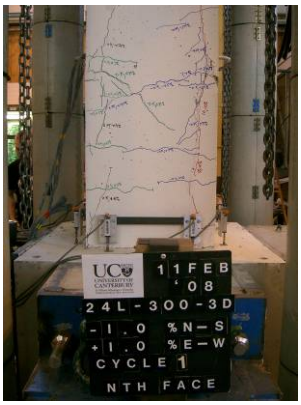

3rd Loop of 1.0% Drift Cycles

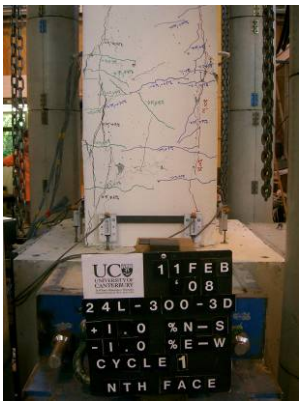

4th Loop of 1.0% Drift Cycles

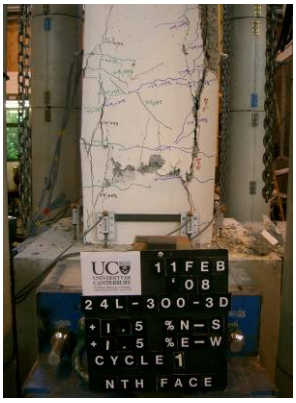

1st Loop of 1.5% Drift Cycles

2nd Loop of 1.5% Drift Cycles

Specimen 24L-300-3D (Cont.)

West Face

1st Loop of 0.1% Drift Cycles

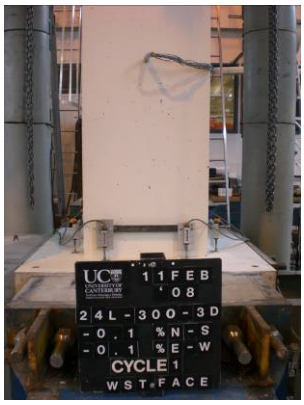

2nd Loop of 0.1% Drift Cycles

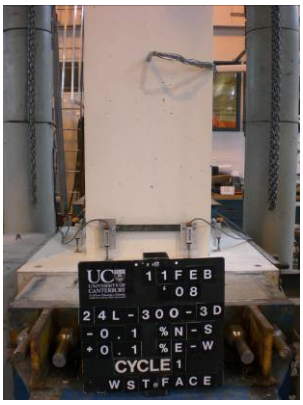

3rd Loop of 0.1% Drift Cycles

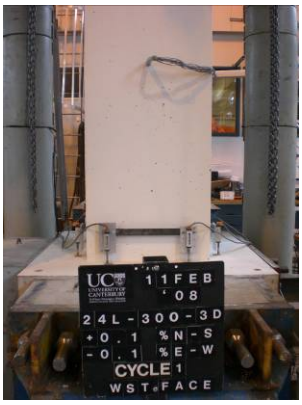

4th Loop of 0.1% Drift Cycles

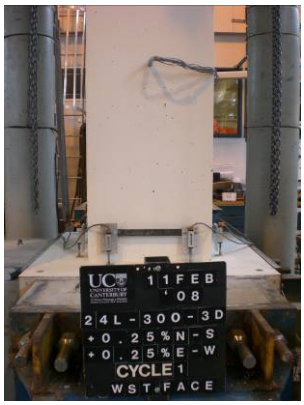

1st Loop of 0.25% Drift Cycles

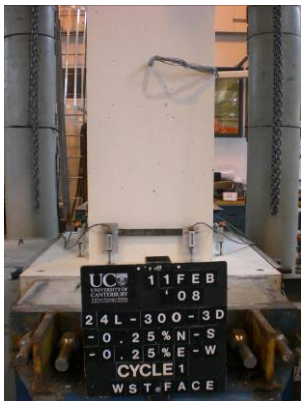

2nd Loop of 0.25% Drift Cycles

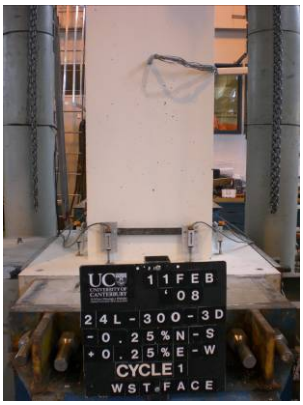

3rd Loop of 0.25% Drift Cycles

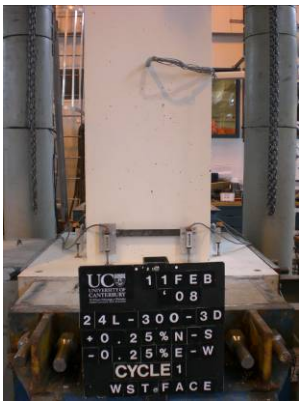

4th Loop of 0.25% Drift Cycles

1st Loop of 0.5% Drift Cycles

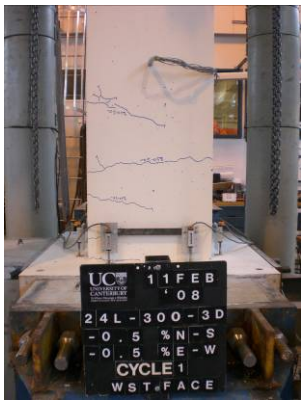

2nd Loop of 0.5% Drift Cycles

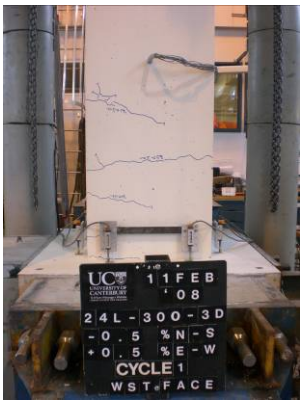

3rd Loop of 0.5% Drift Cycles

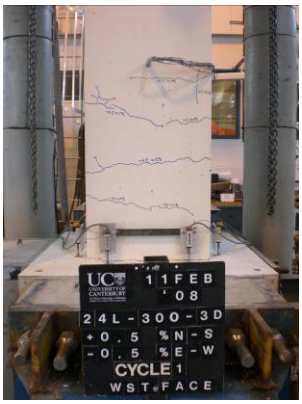

4th Loop of 0.5% Drift Cycles

Specimen 24L-300-3D (Cont.)

West Face

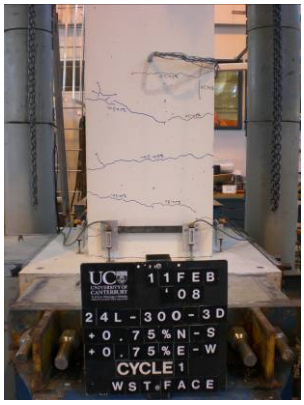

1st Loop of 0.75% Drift Cycles

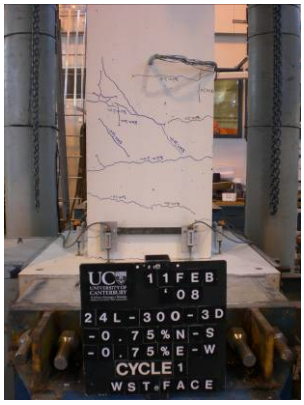

2nd Loop of 0.75% Drift Cycles

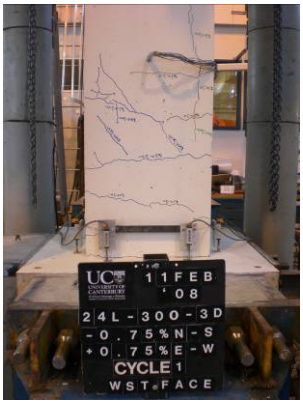

3rd Loop of 0.75% Drift Cycles

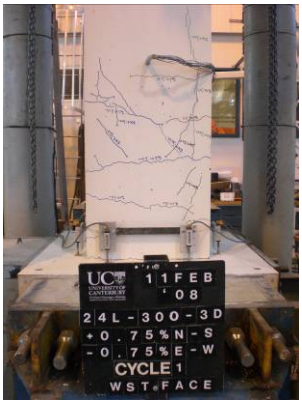

4th Loop of 0.75% Drift Cycles

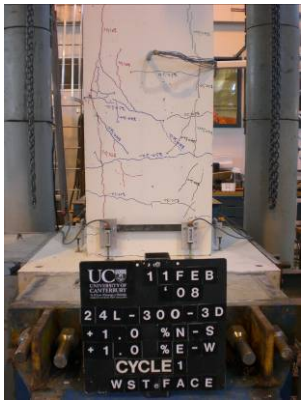

1st Loop of 1.0% Drift Cycles

2nd Loop of 1.0% Drift Cycles

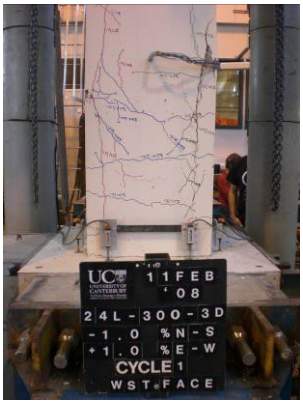

3rd Loop of 1.0% Drift Cycles

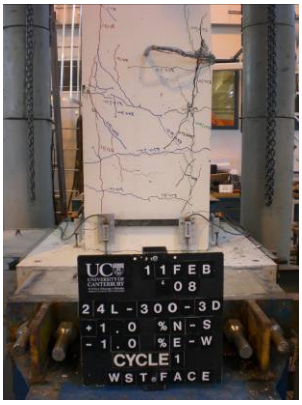

4th Loop of 1.0% Drift Cycles

1st Loop of 1.5% Drift Cycles

2nd Loop of 1.5% Drift Cycles

Specimen 24L-300-3D (Cont.)

Failure Photographs

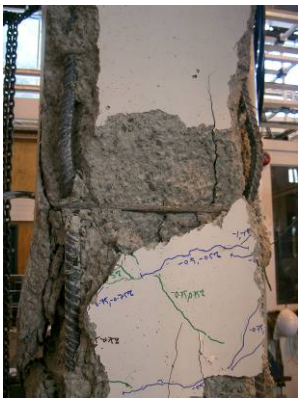

Close-up of buckled bars

Cover concrete removed

Shear-Failure plane

Residual deformation

Experimental apparatus and specimen post failure

E.4 Specimen 24L-300-3D-R

North Face

1st Loop of 0.1% Drift Cycles

2nd Loop of 0.1% Drift Cycles

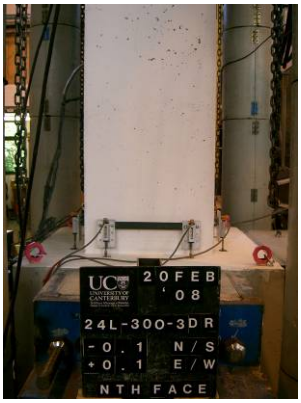

3rd Loop of 0.1% Drift Cycles

4th Loop of 0.1% Drift Cycles

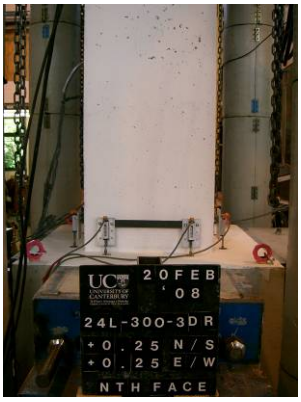

1st Loop of 0.25% Drift Cycles

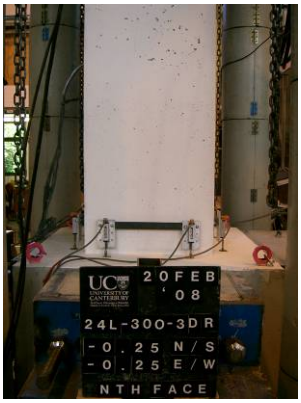

2nd Loop of 0.25% Drift Cycles

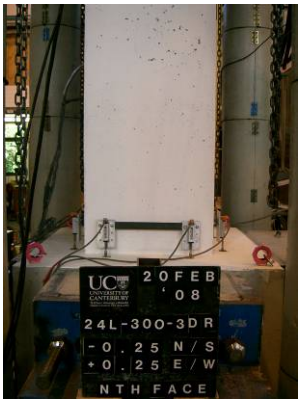

3rd Loop of 0.25% Drift Cycles

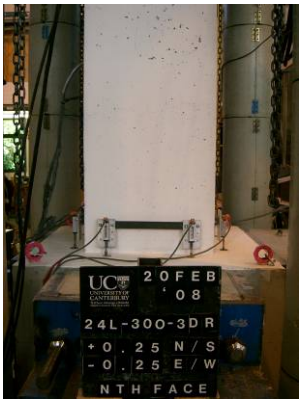

4th Loop of 0.25% Drift Cycles

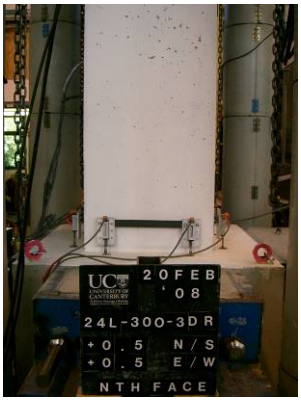

1st Loop of 0.5% Drift Cycles

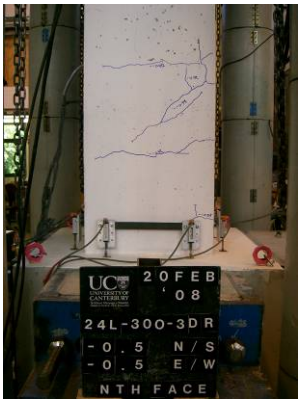

2nd Loop of 0.5% Drift Cycles

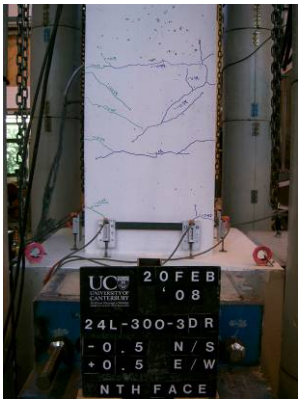

3rd Loop of 0.5% Drift Cycles

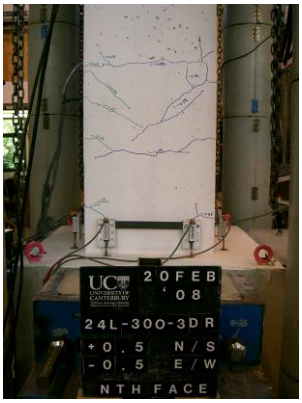

4th Loop of 0.5% Drift Cycles

Specimen 24L-300-3D-R (Cont.)

North Face

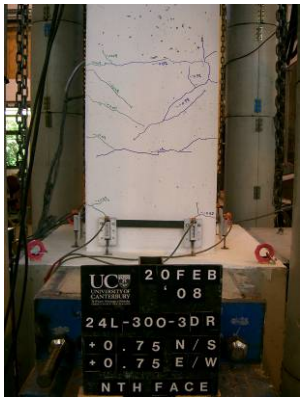

1st Loop of 0.75% Drift Cycles

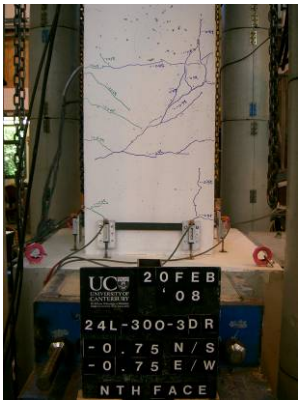

2nd Loop of 0.75% Drift Cycles

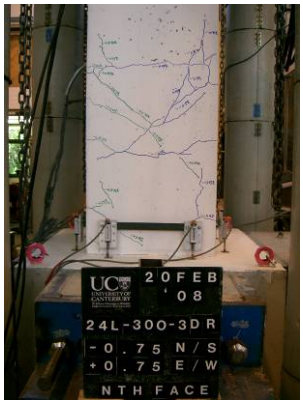

3rd Loop of 0.75% Drift Cycles

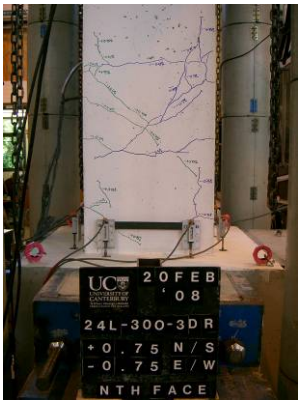

4th Loop of 0.75% Drift Cycles

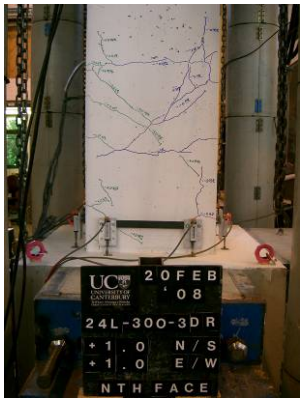

1st Loop of 1.0% Drift Cycles

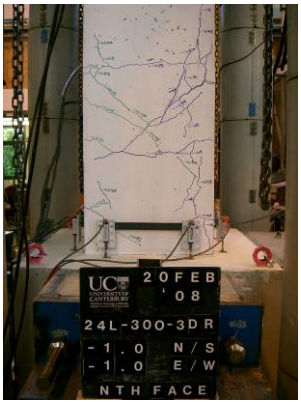

2nd Loop of 1.0% Drift Cycles

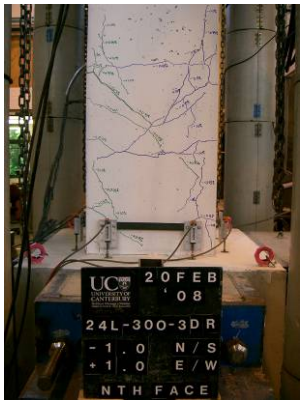

3rd Loop of 1.0% Drift Cycles

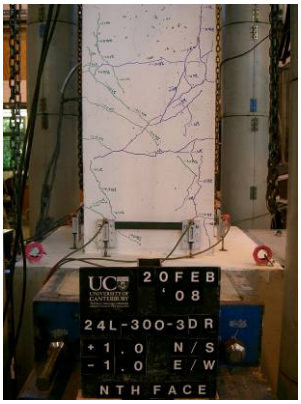

4th Loop of 1.0% Drift Cycles

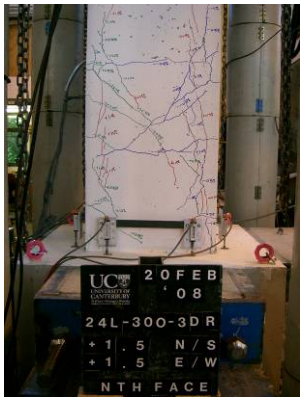

1st Loop of 1.5% Drift Cycles

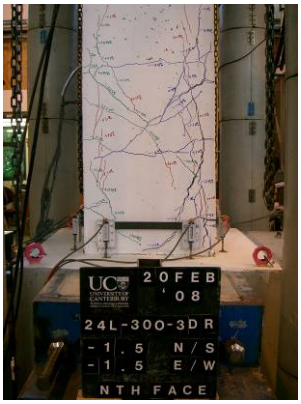

2nd Loop of 1.5% Drift Cycles

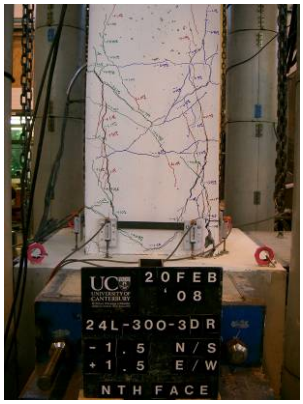

3rd Loop of 1.5% Drift Cycles

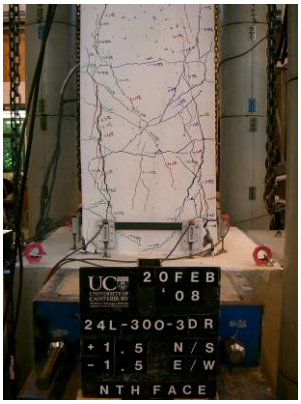

4th Loop of 1.5% Drift Cycles

Specimen 24L-300-3D-R (Cont.)

North Face

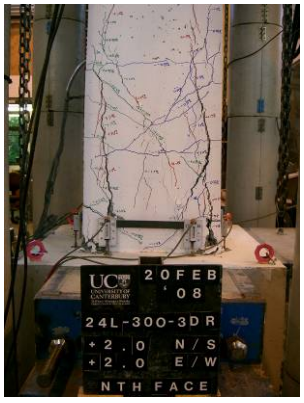

1st Loop of 2.0 % Drift Cycles

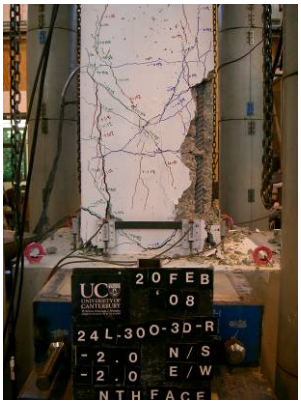

2nd Loop of 2.0 % Drift Cycles

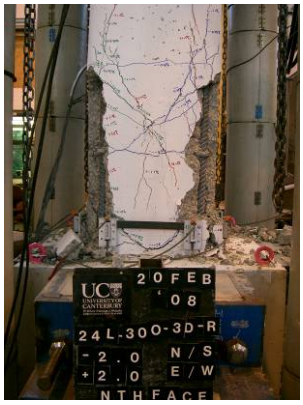

3rd Loop of 2.0 % Drift Cycles

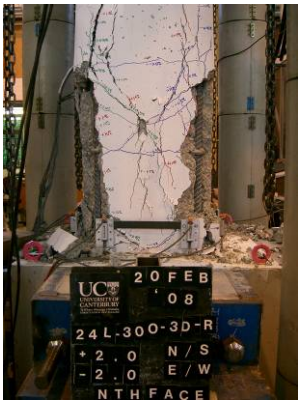

4th Loop of 2.0 % Drift Cycles

1st Loop of 3.0% Drift Cycles

missing

2nd Loop of 3.0% Drift Cycles

missing

3rd Loop of 3.0% Drift Cycles

4th Loop of 1.0% Drift Cycles

Specimen 24L-300-3D-R (Cont.)

West Face

1st Loop of 0.1% Drift Cycles

2nd Loop of 0.1% Drift Cycles

3rd Loop of 0.1% Drift Cycles

4th Loop of 0.1% Drift Cycles

1st Loop of 0.25% Drift Cycles

2nd Loop of 0.25% Drift Cycles

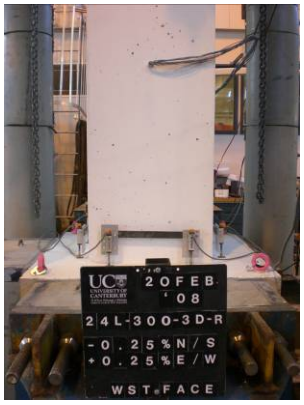

3rd Loop of 0.25% Drift Cycles

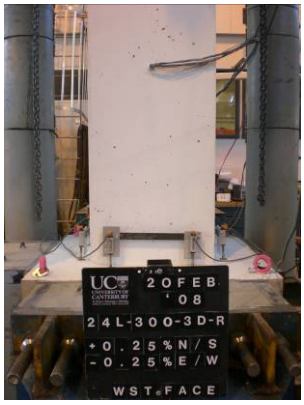

4th Loop of 0.25% Drift Cycles

1st Loop of 0.5% Drift Cycles

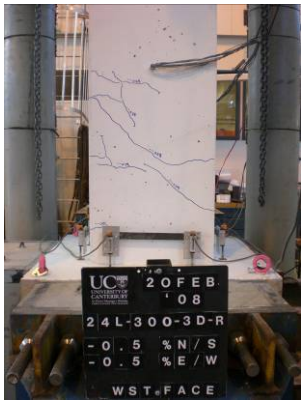

2nd Loop of 0.5% Drift Cycles

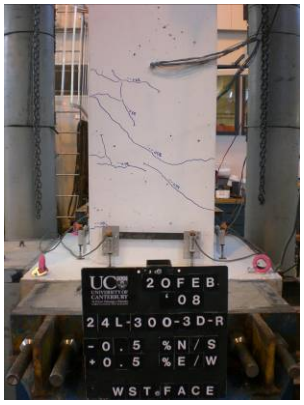

3rd Loop of 0.5% Drift Cycles

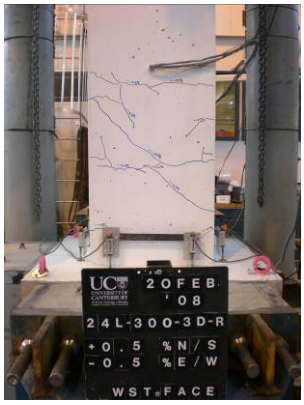

4th Loop of 0.5% Drift Cycles

Specimen 24L-300-3D-R (Cont.)

West Face

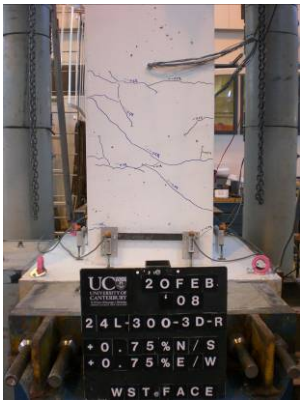

1st Loop of 0.75% Drift Cycles

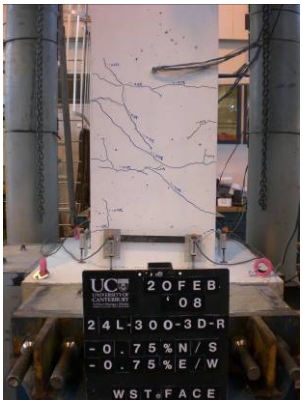

2nd Loop of 0.75% Drift Cycles

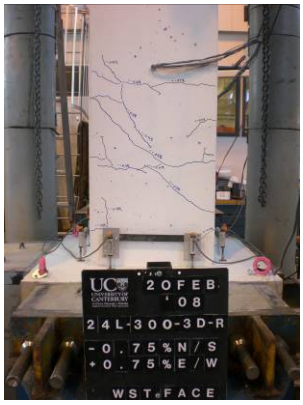

3rd Loop of 0.75% Drift Cycles

4th Loop of 0.75% Drift Cycles

1st Loop of 1.0% Drift Cycles

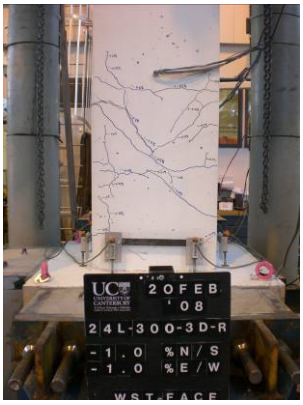

2nd Loop of 1.0% Drift Cycles

3rd Loop of 1.0% Drift Cycles

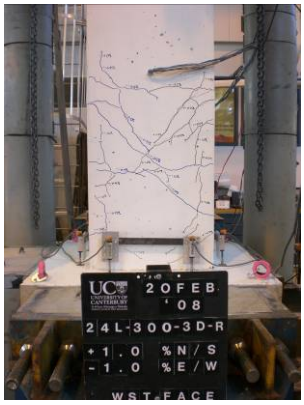

4th Loop of 1.0% Drift Cycles

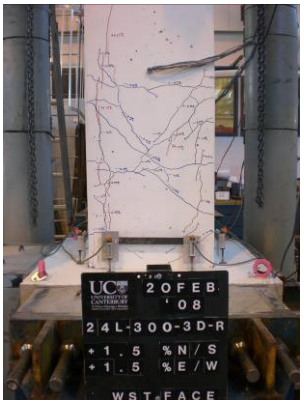

1st Loop of 1.5% Drift Cycles

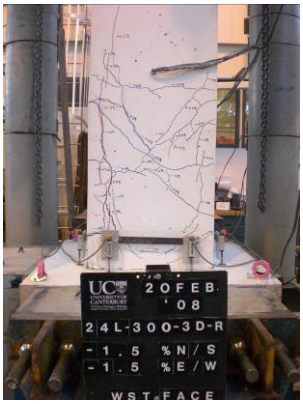

2nd Loop of 1.5% Drift Cycles

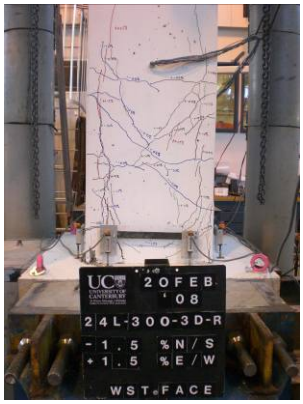

3rd Loop of 1.5% Drift Cycles

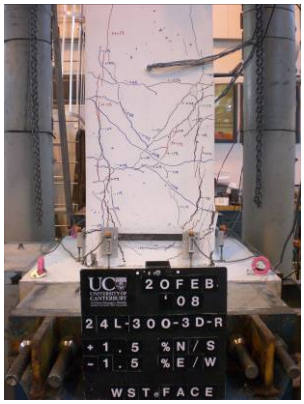

4th Loop of 1.5% Drift Cycles

Specimen 24L-300-3D-R (Cont.)

West Face

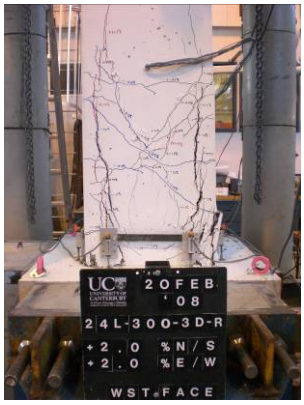

1st Loop of 2.0% Drift Cycles

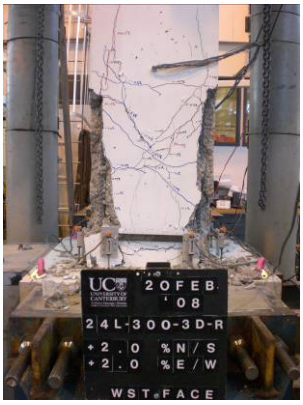

2nd Loop of 2.0% Drift Cycles

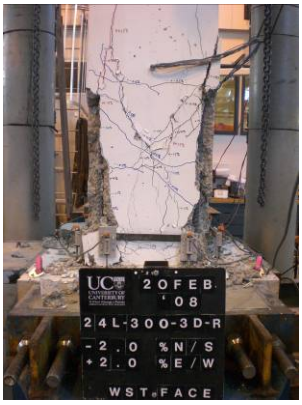

3rd Loop of 2.0% Drift Cycles

4th Loop of 2.0% Drift Cycles

1st Loop of 3.0% Drift Cycles

2nd Loop of 3.0% Drift Cycles

3rd Loop of 3.0% Drift Cycles

Failure Photographs

Post-failure 1

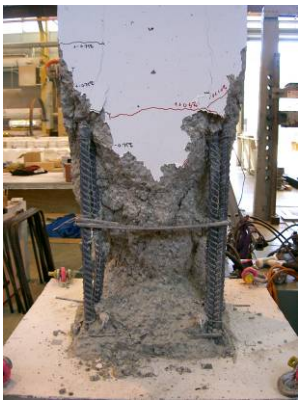

Post-failure 2

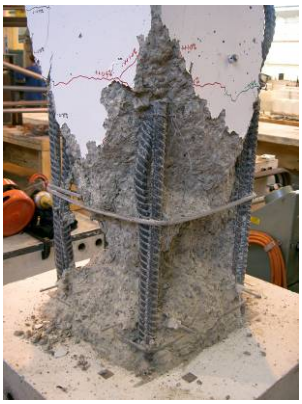

Post-failure 3

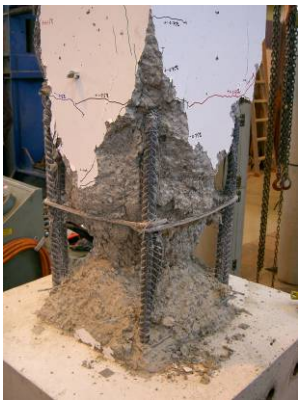

Post-failure 4

E.5 Specimen 30L-300-2D

West Face

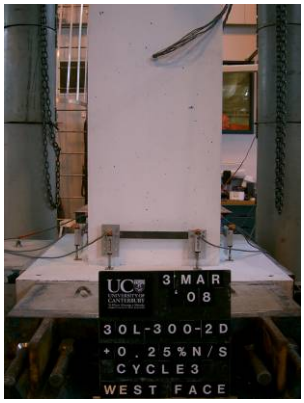

+ 0.25% Drift 3rd Cycle

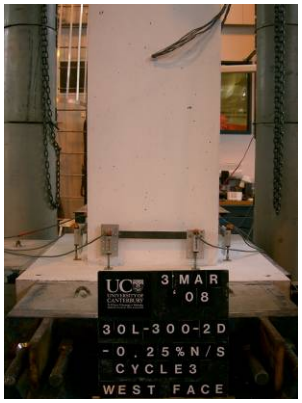

- 0.25% Drift 3rd Cycle

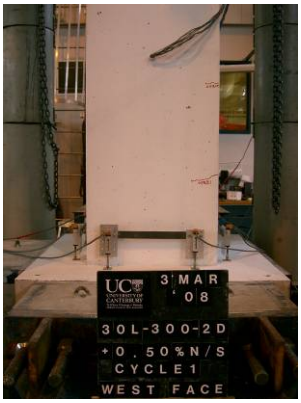

+ 0. 5% Drift 1st Cycle

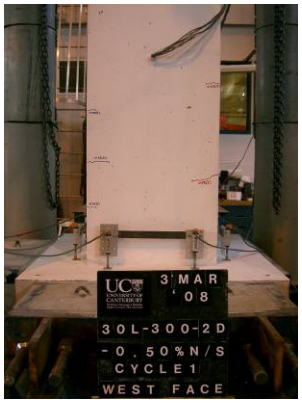

- 0. 5% Drift 1st Cycle

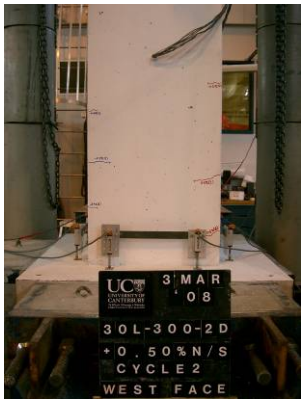

+ 0. 5% Drift 2nd Cycle

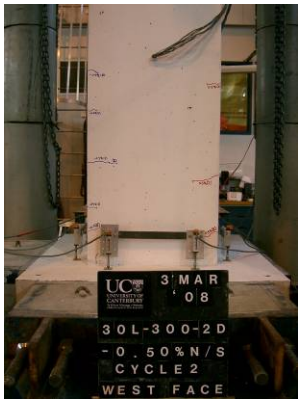

- 0. 5% Drift 2nd Cycle

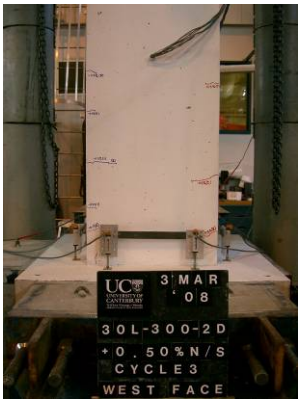

+ 0. 5% Drift 3rd Cycle

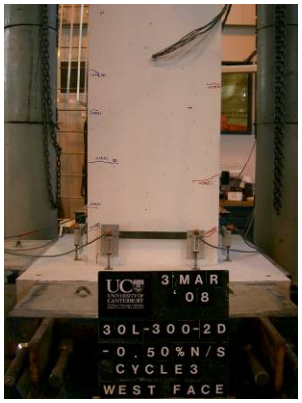

- 0. 5% Drift 3rd Cycle

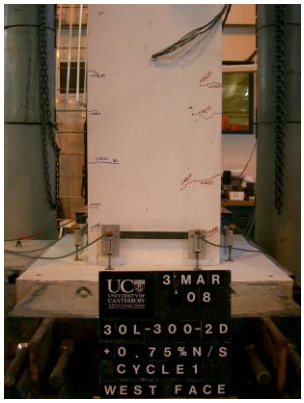

+ 0.75 % Drift 1st Cycle

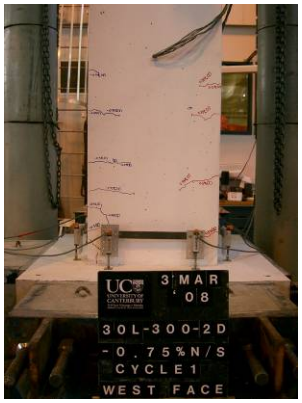

- 0.75 % Drift 1st Cycle

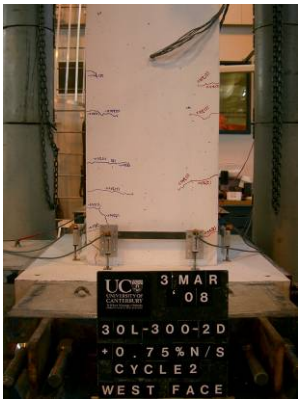

+ 0.75 % Drift 2nd Cycle

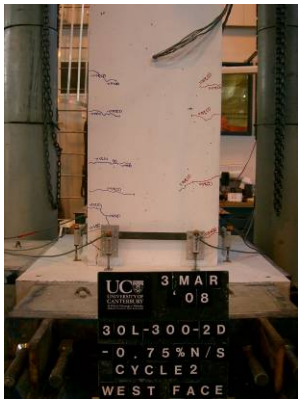

- 0.75 % Drift 2nd Cycle

Specimen 30L-300-2D (Cont.)

West Face

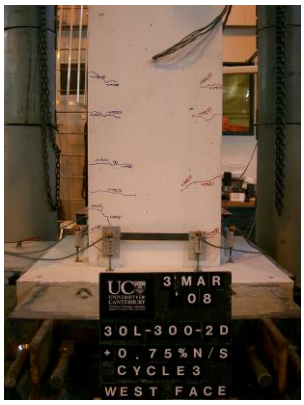

+ 0.75 % Drift 3rd Cycle

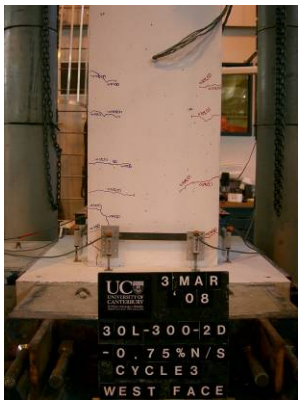

- 0.75 % Drift 3rd Cycle

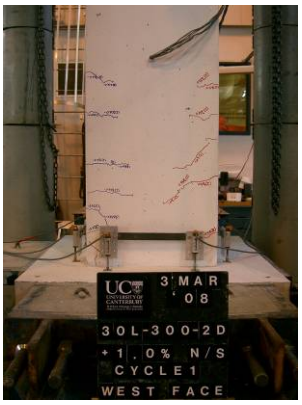

+ 1.0 % Drift 1st Cycle

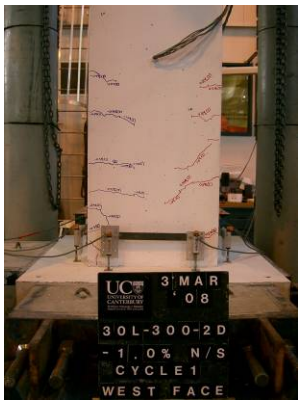

- 1.0 % Drift 1st Cycle

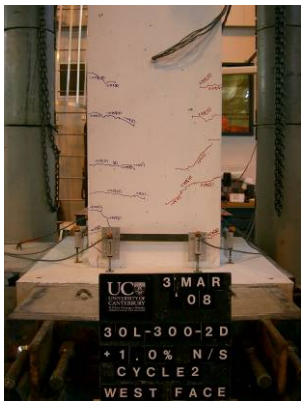

+ 1.0 % Drift 2nd Cycle

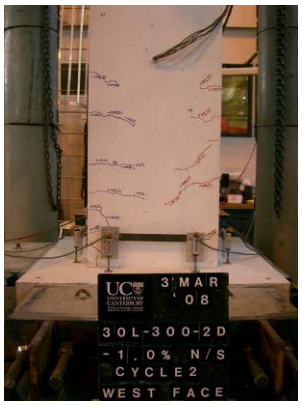

- 1.0 % Drift 2nd Cycle

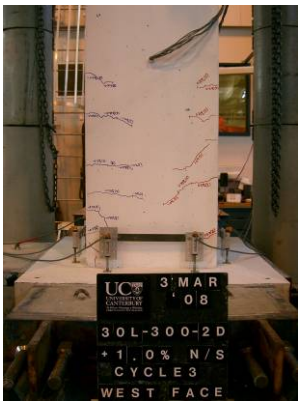

+ 1.0 % Drift 3rd Cycle

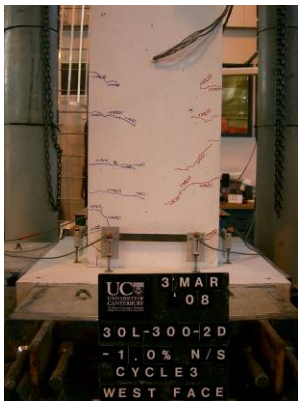

- 1.0 % Drift 3rd Cycle

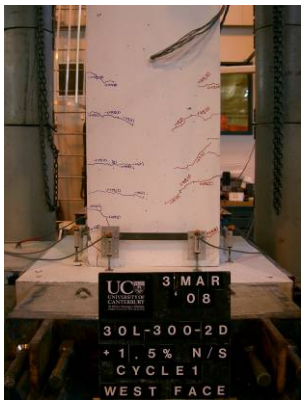

+ 1.5 % Drift 1st Cycle

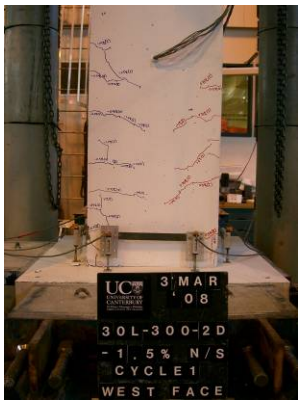

- 1.5 % Drift 1st Cycle

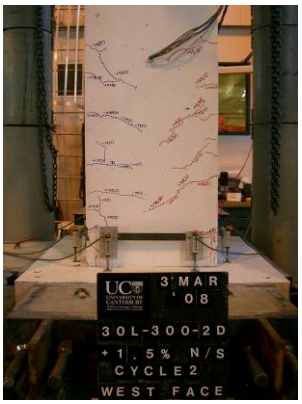

+ 1.5 % Drift 2nd Cycle

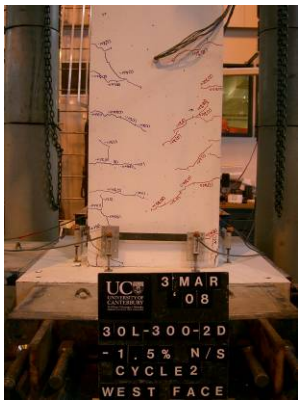

- 1.5 % Drift 2nd Cycle

Specimen 30L-300-2D (Cont.)

West Face

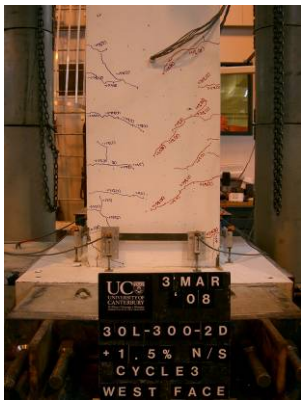

+ 1.5 % Drift 3rd Cycle

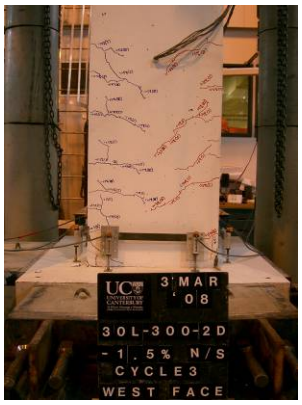

- 1.5 % Drift 3rd Cycle

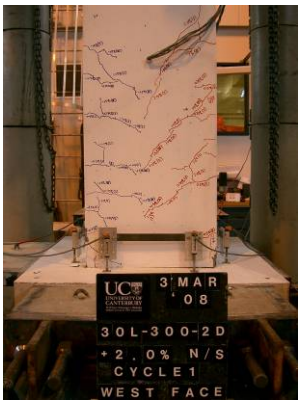

+ 2.0 % Drift 1st Cycle

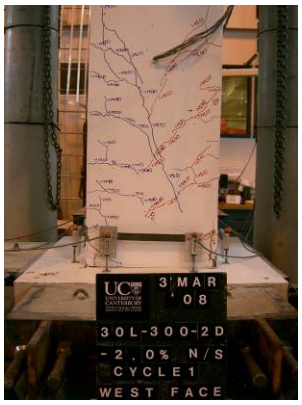

- 2.0 % Drift 1st Cycle

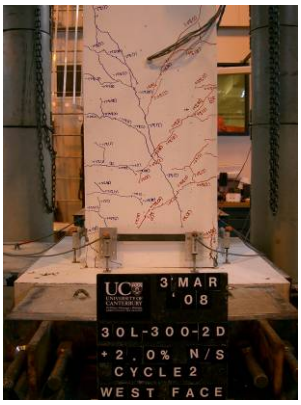

+ 2.0 % Drift 2nd Cycle

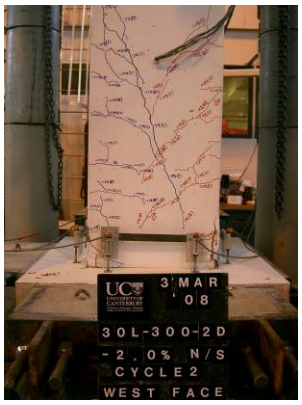

- 2.0 % Drift 2nd Cycle

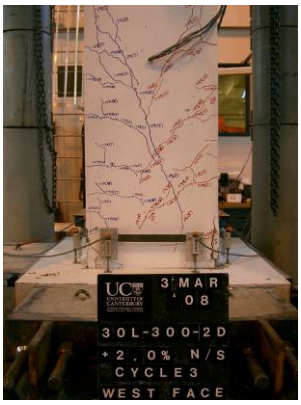

+ 2.0 % Drift 3rd Cycle

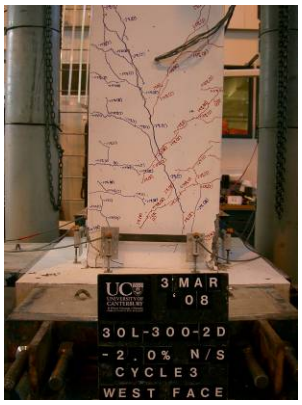

- 2.0 % Drift 3rd Cycle

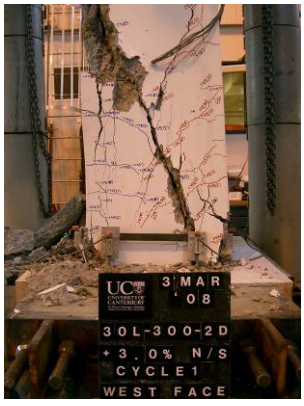

+ 3.0 % Drift 1st Cycle

Crank Buckling

Shear-Failure plane (West)

Shear-Failure plane (East)

E.6 Specimen 30L-300-3D

North Face

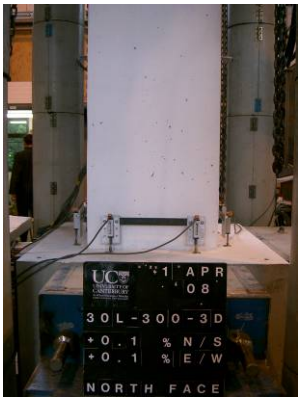

1st Loop of 0.1% Drift Cycles

2nd Loop of 0.1% Drift Cycles

3rd Loop of 0.1% Drift Cycles

4th Loop of 0.1% Drift Cycles

1st Loop of 0.25% Drift Cycles

2nd Loop of 0.25% Drift Cycles

3rd Loop of 0.25% Drift Cycles

4th Loop of 0.25% Drift Cycles

1st Loop of 0.5% Drift Cycles

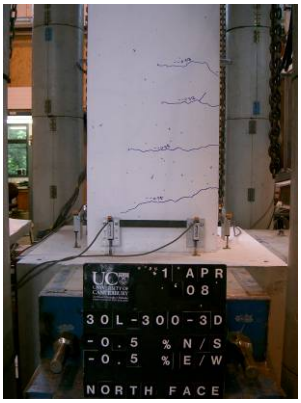

2nd Loop of 0.5% Drift Cycles

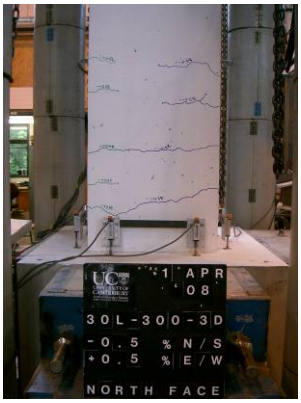

3rd Loop of 0.5% Drift Cycles

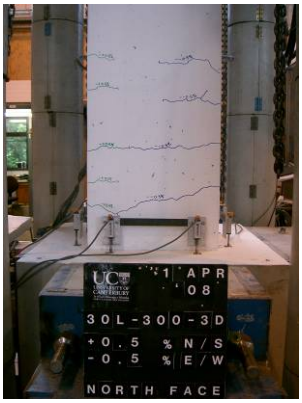

4th Loop of 0.5% Drift Cycles

Specimen 30L-300-3D (Cont.)

North Face

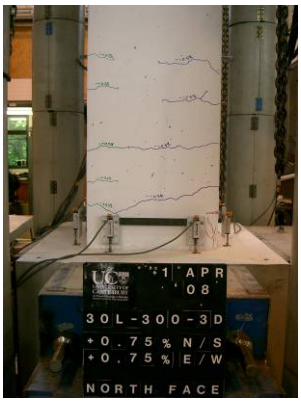

1st Loop of 0.75% Drift Cycles

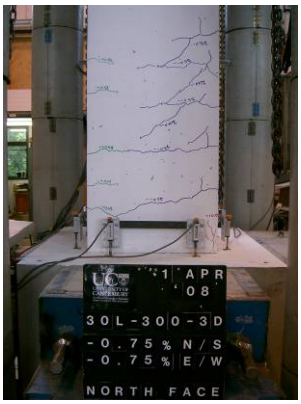

2nd Loop of 0.75% Drift Cycles

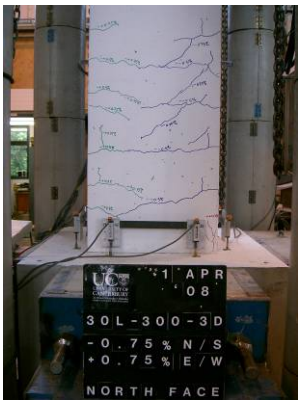

3rd Loop of 0.75% Drift Cycles

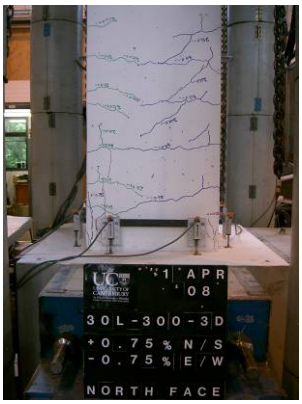

4th Loop of 0.75% Drift Cycles

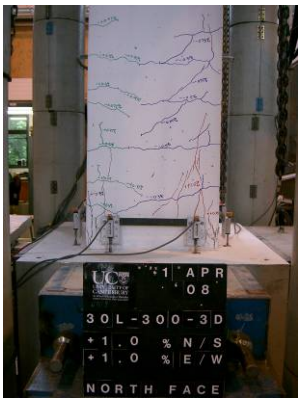

1st Loop of 1.0% Drift Cycles

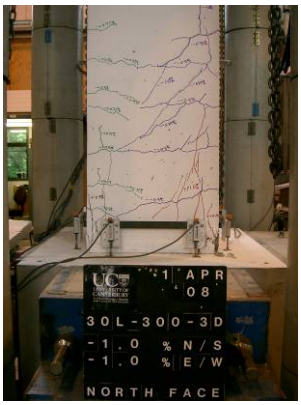

2nd Loop of 1.0% Drift Cycles

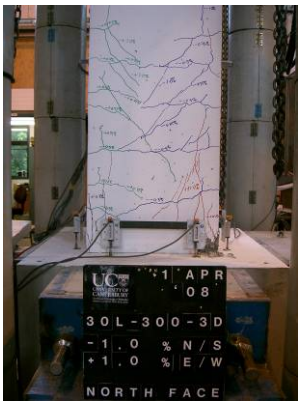

3rd Loop of 1.0% Drift Cycles

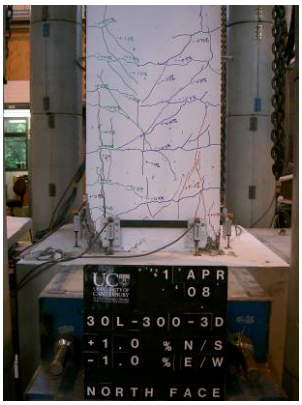

4th Loop of 1.0% Drift Cycles

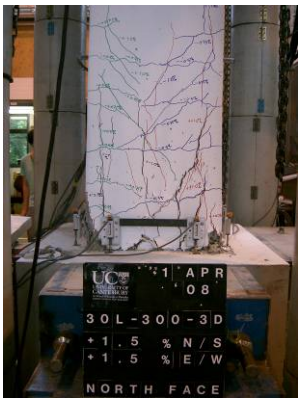

1st Loop of 1.5% Drift Cycles

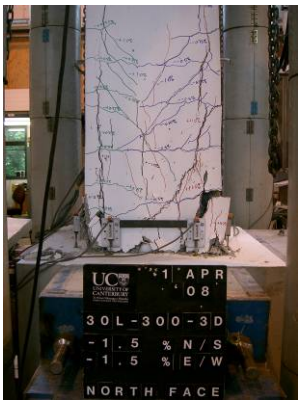

2nd Loop of 1.5% Drift Cycles

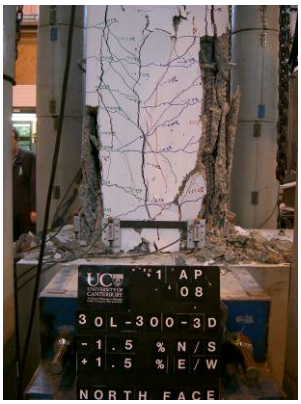

3rd Loop of 1.5% Drift Cycles

Specimen 30L-300-3D (Cont.)

West Face

1st Loop of 0.1% Drift Cycles

2nd Loop of 0.1% Drift Cycles

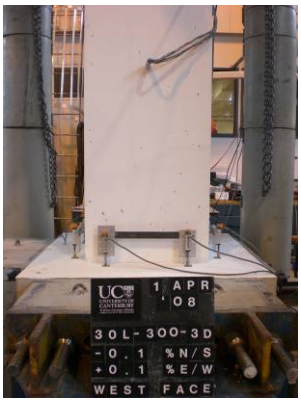

3rd Loop of 0.1% Drift Cycles

4th Loop of 0.1% Drift Cycles

1st Loop of 0.25% Drift Cycles

2nd Loop of 0.25% Drift Cycles

3rd Loop of 0.25% Drift Cycles

4th Loop of 0.25% Drift Cycles

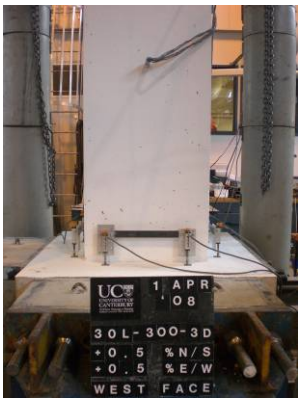

1st Loop of 0.5% Drift Cycles

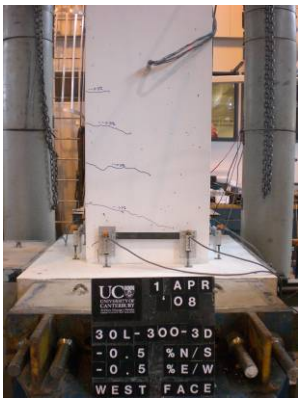

2nd Loop of 0.5% Drift Cycles

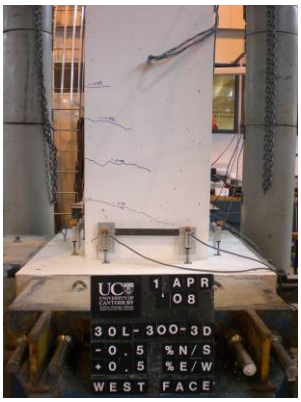

3rd Loop of 0.5% Drift Cycles

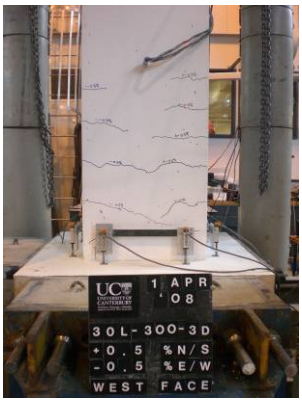

4th Loop of 0.5% Drift Cycles

Specimen 30L-300-3D (Cont.)

West Face

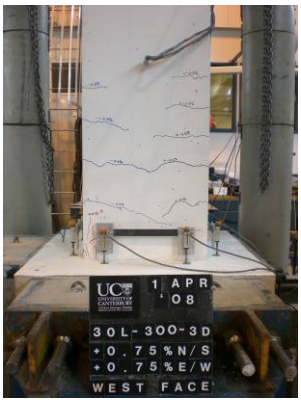

1st Loop of 0.75% Drift Cycles

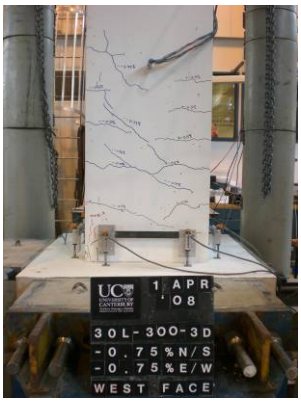

2nd Loop of 0.75% Drift Cycles

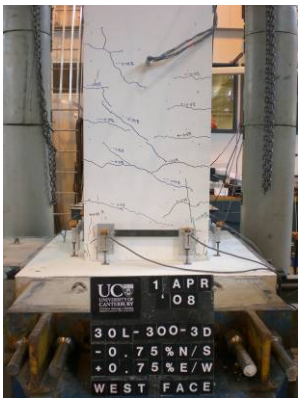

3rd Loop of 0.75% Drift Cycles

4th Loop of 0.75% Drift Cycles

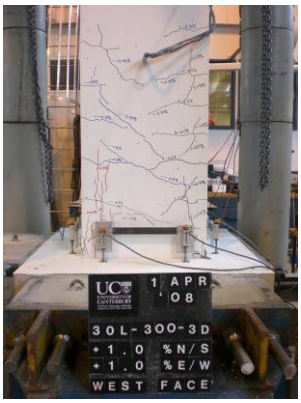

1st Loop of 1.0% Drift Cycles

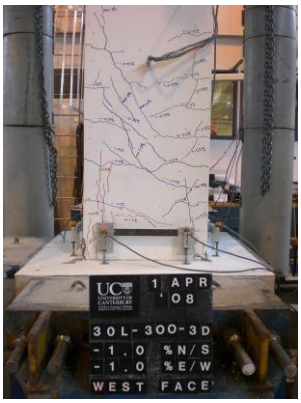

2nd Loop of 1.0% Drift Cycles

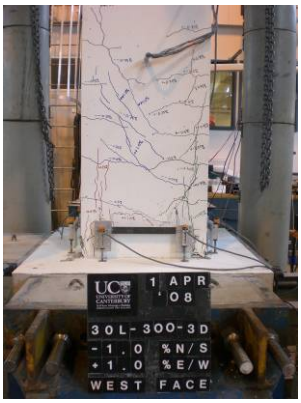

3rd Loop of 1.0% Drift Cycles

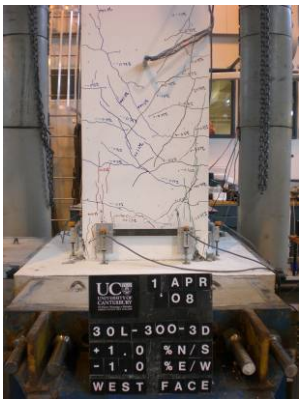

4th Loop of 1.0% Drift Cycles

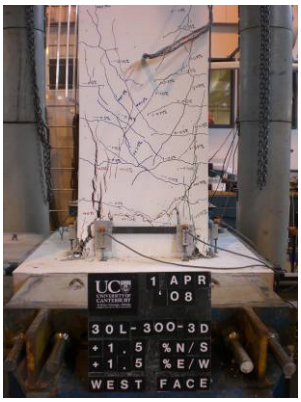

1st Loop of 1.5% Drift Cycles

2nd Loop of 1.5% Drift Cycles

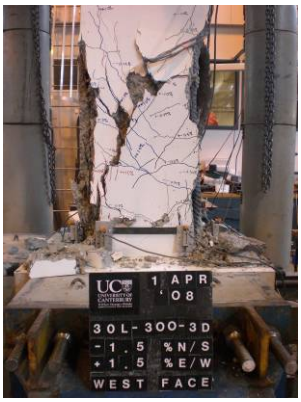

3rd Loop of 1.5% Drift Cycles

Specimen 30L-300-3D (Cont.)

Failure Photographs

1st Loop of 0.75% Drift Cycles

2nd Loop of 0.75% Drift Cycles

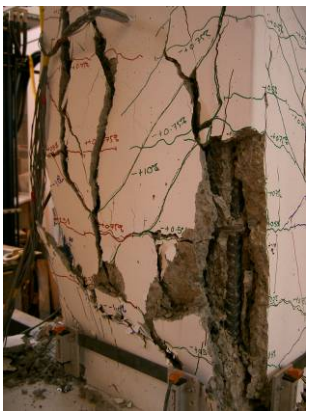

3rd Loop of 0.75% Drift Cycles

1st Loop of 1.0% Drift Cycles

2nd Loop of 1.0% Drift Cycles

3rd Loop of 1.0% Drift Cycles

E.7 Specimen 24L-300-EQ

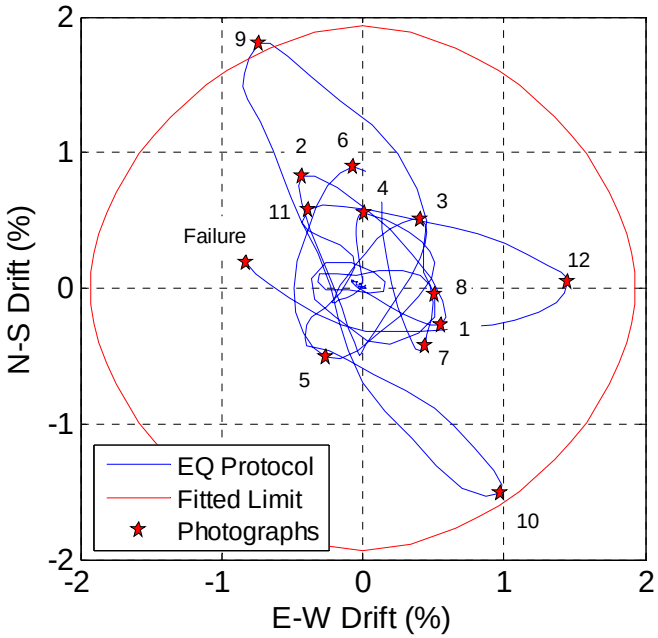

Loading protocol with photographic sequence for specimen 24L-300-EQ

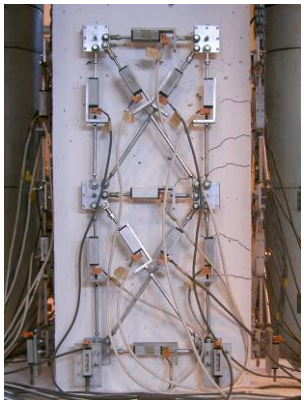

Photograph 1 (North Face)

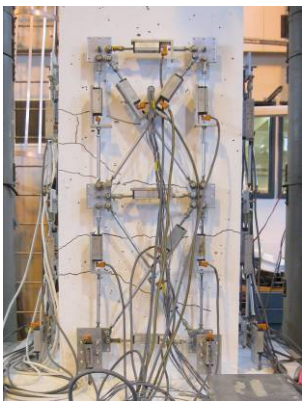

Photograph 1 (West Face)

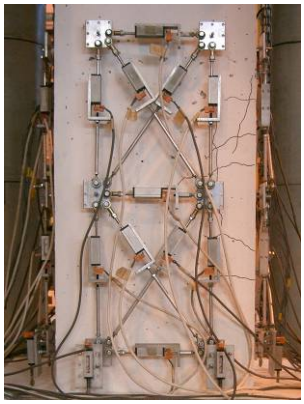

Photograph 2 (North Face)

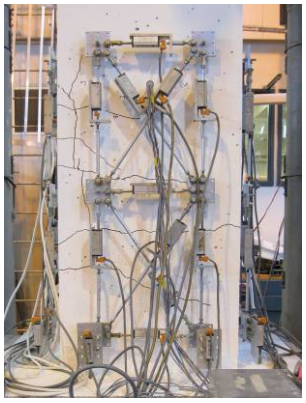

Photograph 2 (West Face)

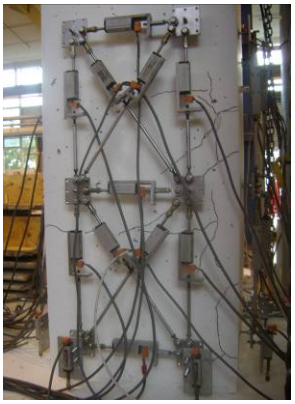

Photograph 2 (South Face)

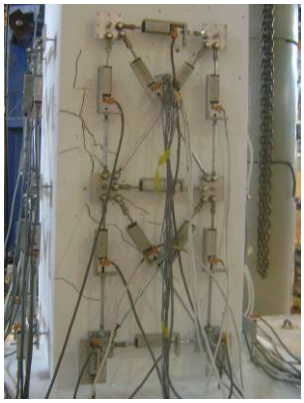

Photograph 2 (East Face)

Specimen 24L-300-EQ (Cont.)

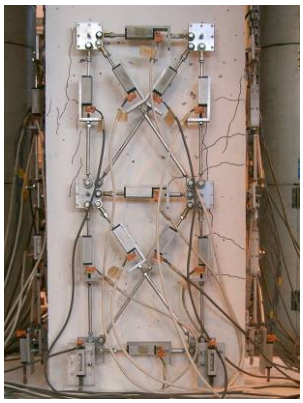

Photograph 3 (North Face)

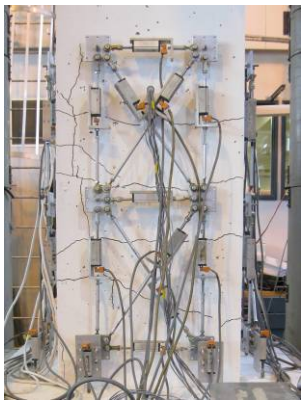

Photograph 3 (West Face)

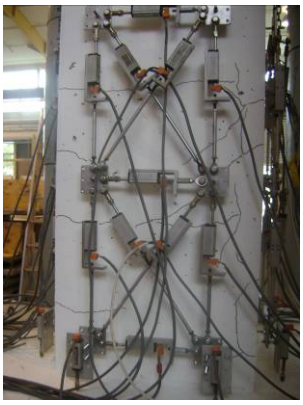

Photograph 3 (South Face)

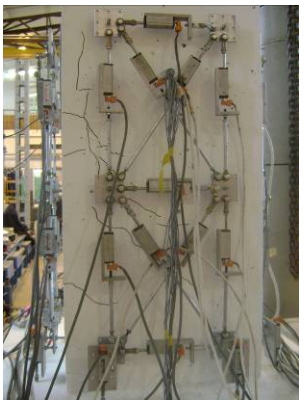

Photograph 3 (East Face)

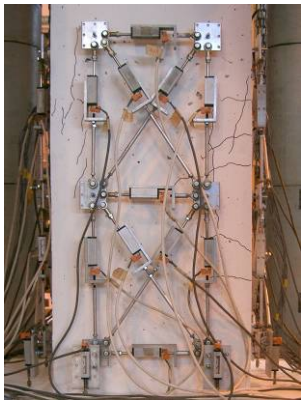

Photograph 4 (North Face)

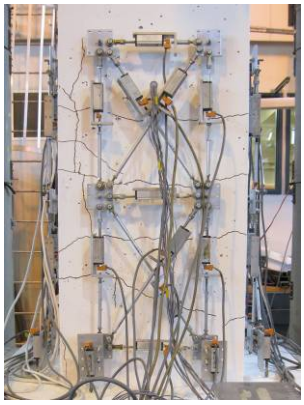

Photograph 4 (West Face)

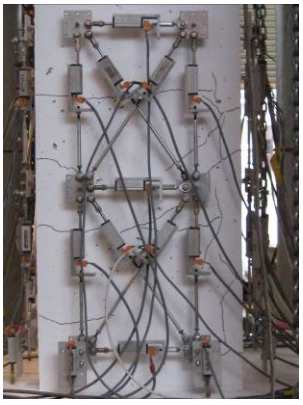

Photograph 4 (South Face)

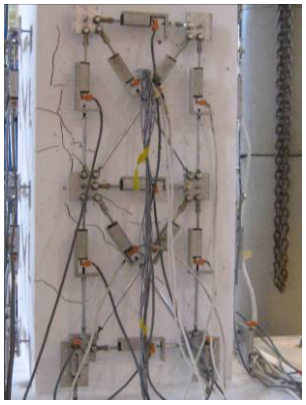

Photograph 4 (East Face)

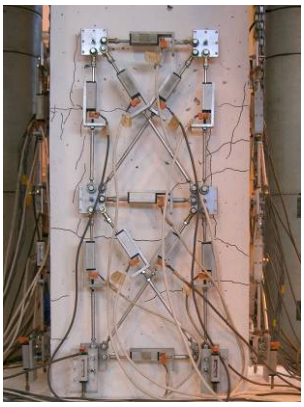

Photograph 5 (North Face)

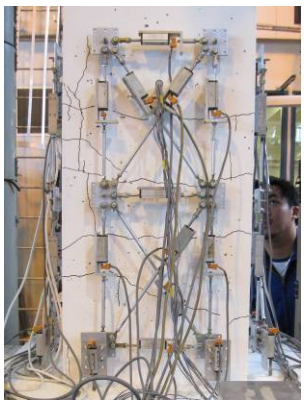

Photograph 5 (West Face)

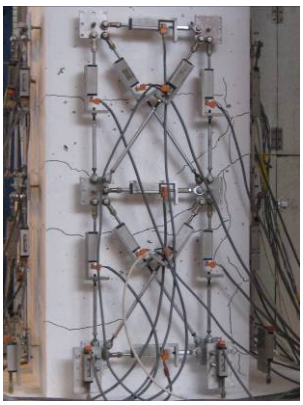

Photograph 5 (South Face)

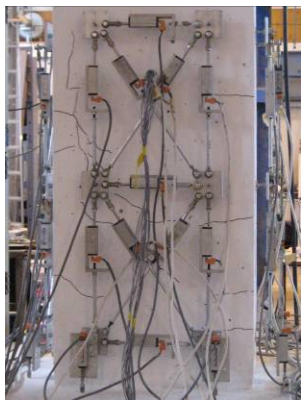

Photograph 5 (East Face)

Specimen 24L-300-EQ (Cont.)

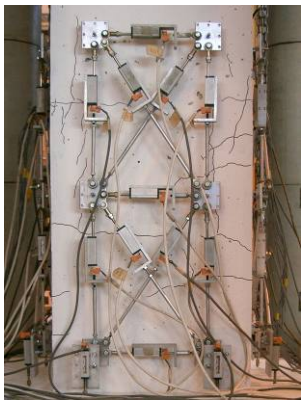

Photograph 6 (North Face)

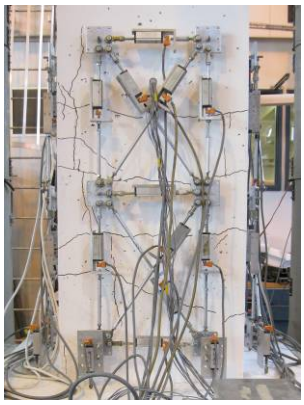

Photograph 6 (West Face)

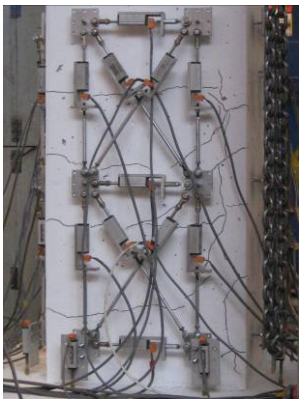

Photograph 6 (South Face)

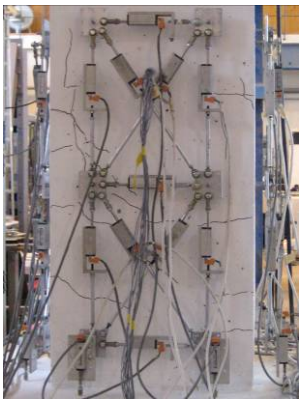

Photograph 6 (East Face)

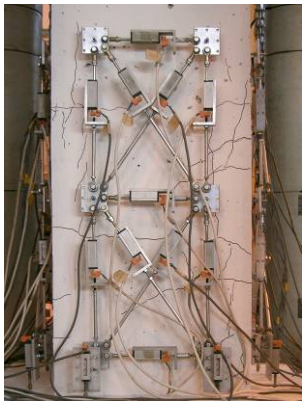

Photograph 7 (North Face)

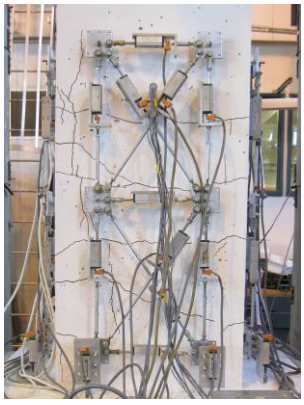

Photograph 7 (West Face)

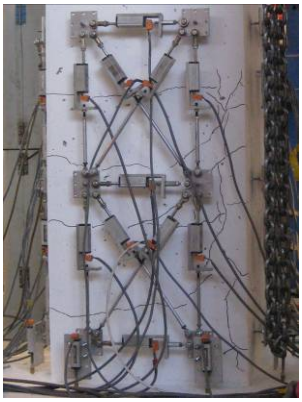

Photograph 7 (South Face)

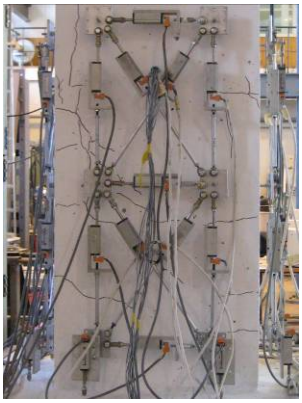

Photograph 7 (East Face)

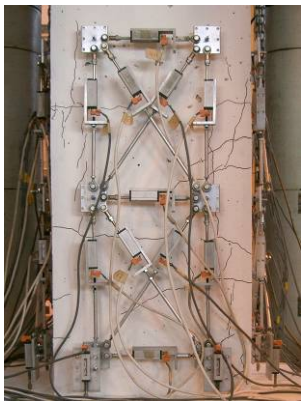

Photograph 8 (North Face)

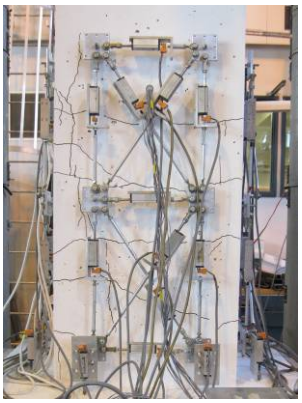

Photograph 8 (West Face)

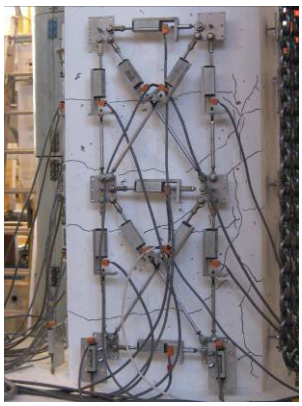

Photograph 8 (South Face)

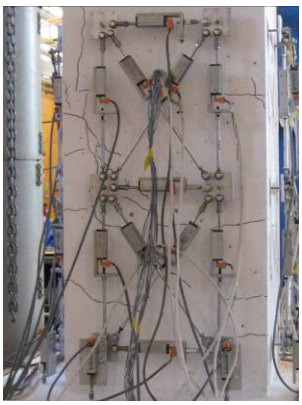

Photograph 8 (East Face)

Specimen 24L-300-EQ (Cont.)

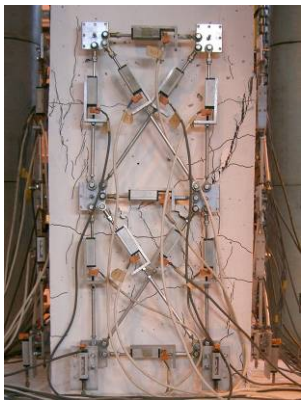

Photograph 9 (North Face)

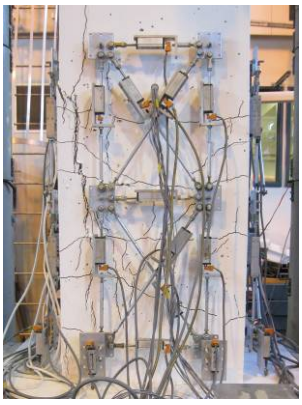

Photograph 9 (West Face)

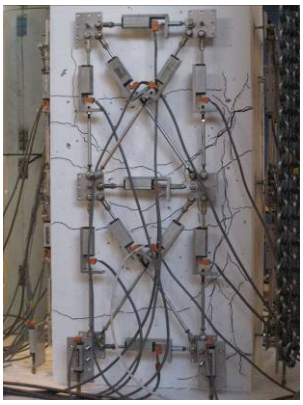

Photograph 9 (South Face)

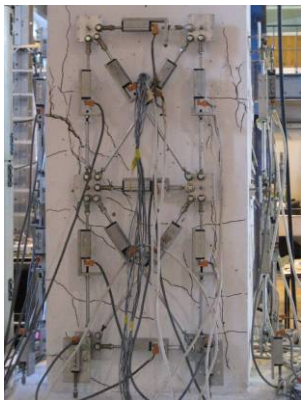

Photograph 9 (East Face)

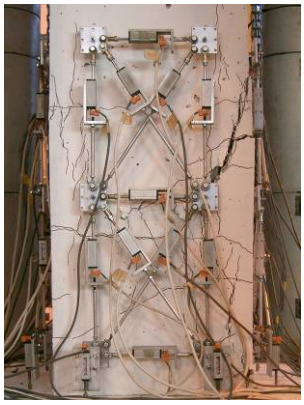

Photograph 10 (North Face)

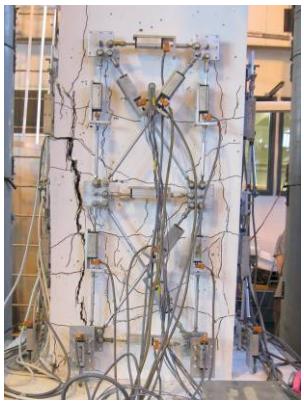

Photograph 10 (West Face)

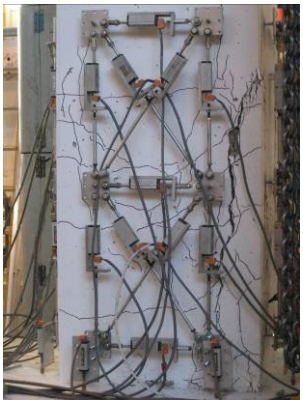

Photograph 10 (South Face)

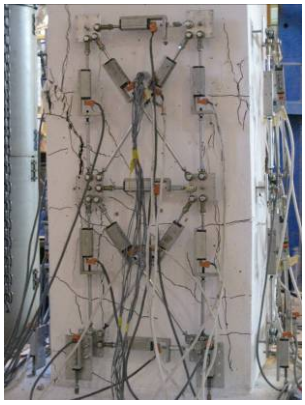

Photograph 10 (East Face)

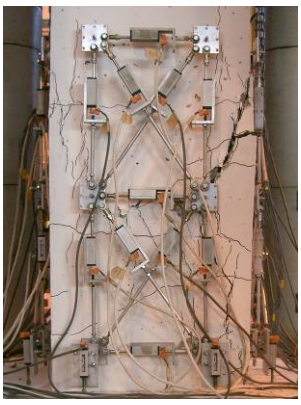

Photograph 11 (North Face)

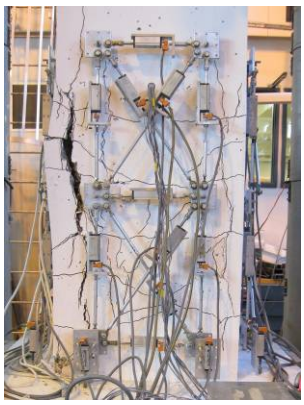

Photograph 11 (West Face)

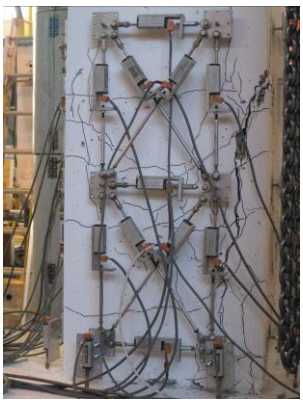

Photograph 11 (South Face)

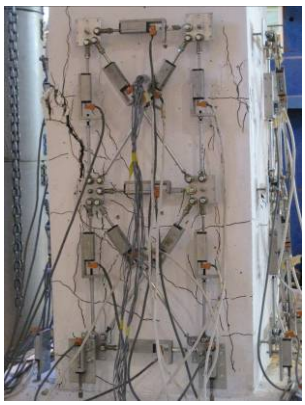

Photograph 11 (East Face)

Specimen 24L-300-EQ (Cont.)

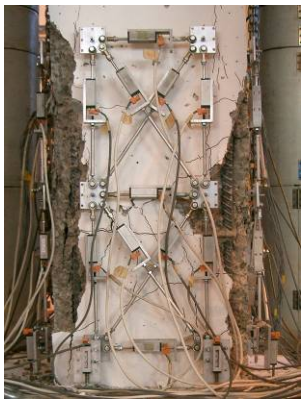

Photograph 12 (North Face)

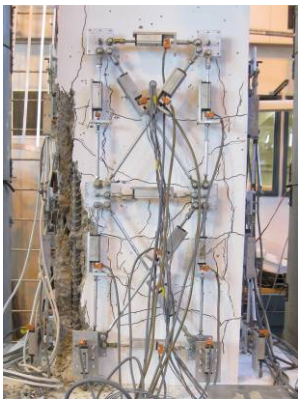

Photograph 12 (West Face)

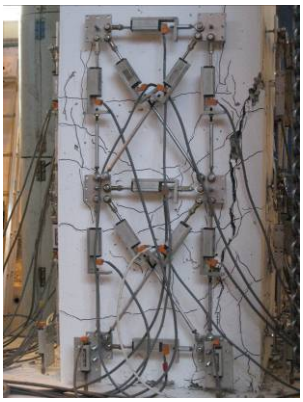

Photograph 12 (South Face)

Photograph 12 (East Face)

Failure Photographs

Failure (North Face)

Failure (West Face)

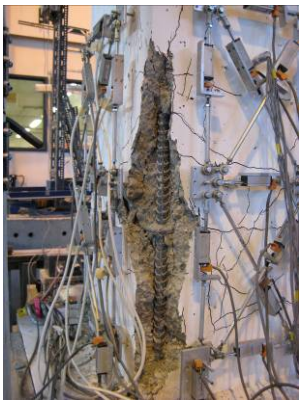

Failure (NW Corner)

Failure (NE Corner)

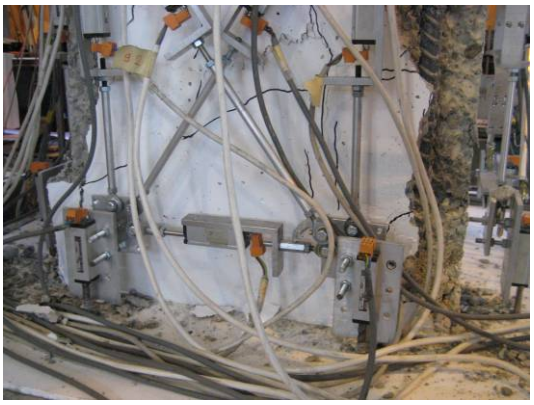

Failure (Close-up North Base)

Failure (Close-up East Base)